공학박사 학위논문

Experimental Study on Unsteady Kinematics of Shrouded Multistage Axial Compressor Flow

다단 슈라우드형 축류 압축기 유동의 비정상 운동학에 대한 실험적 연구

2019 년 8 월

서울대학교 대학원

기계항공공학부

이 재 형

다단 슈라우드형 축류 압축기 유동의 비정상 운동학에 대한 실험적 연구

Experimental Study on Unsteady Kinematics of Shrouded Multistage Axial Compressor Flow

지도 교수 송 성 진

이 논문을 공학박사 학위논문으로 제출함

2019 년 4 월

서울대학교 대학원

기계항공공학부

이 재 형

이재형의 공학박사 학위논문을 인준함

2019 년 6 월

위 원 장 **(인)**

부위원장 **(인)**

위 원 **(인)**

위 원 **(인)**

위 원 **(인)**

Abstract

An experimental investigation has been conducted to identify the unsteady kinematics of shrouded stator of a low-speed multistage axial compressor. Unsteady velocity distributions have been measured at upstream and downstream of 3rd shrouded stator using single-element 45° slanted hot-wires. The data have been ensemble-averaged to obtain the timewise variation of velocity vectors upstream and downstream of the shrouded 3rd stator.

The width and velocity disturbances of 3rd stator wake varied by the merge with 3rd rotor wakes. Between the two 3rd rotor wakes, a pseudo-wake region is observed, which is presumed to be created by the recirculation due to the negative jet of the 3rd rotor wakes. This velocity disturbance is attenuated by the viscous mixing and wake stretching as the 3rd wakes are transported downstream. Because of the velocity disturbances, the aerodynamic properties downstream of the stator blade vary.

The hubside corner separation of the multistage shrouded stator alters the unsteady kinematics of the hubside shrouded stator flow. The attenuation of the wake is lower at the hubside due to the reduced effective passage width by the corner separation. In addition to this, this hub corner separation triggers the hubside positive radial movements at the upstream and downstream of hubside of the 3rd stator. This increases the timewise variation of the hubside aerodynamic properties, deviating the shrouded stator off from its designed flow condition further compared with the midspan region.

Changing the operating conditions have affected the hubside unsteady flow structures. At near stall cases, the widths of wakes and hub corner separation are increased, but the hubside unsteady flow structure is qualitatively similar to that of the design cases.

For the higher flow rate cases, the width and the magnitude of the corner separation are reduced, resulting in the disappearances of a positive radial movement inside the corner separation.

Keywords: Axial Compressor, Shrouded Stator, Rotor, Unsteady Kinematics, Wake, Hubside, Corner Separation

Student Number: 2012-23183

Acknowledgments

This thesis summarizes the activities having been done in the six and a half years of my graduate school life. Without extensive guidance, supports, encouragements, and advice from the other people, this thesis would not have existed. I would like to express my deepest gratitude to those who have supported me.

First, I would like to appreciate my thesis advisor Professor Seung Jin Song for his thoughtful guidance throughout the entire graduate school period. His constant suggestions, motivations, and discussions have founded the very basics of this research.

Second, I would like to express my gratitude to Doctor Hyoun-Woo Shin for his advice. His extensive knowledge in measuring techniques and turbomachines have been very helpful for the construction of the apparatus used in the experiments, and detailed measuring methods.

Third, I would like to appreciate those who have helped in making the experimental apparatus. I present my gratitude to Doctor Sungho Yoon for his advice on designing the apparatus. Also, I would like to thank Mr. Kijae Choi, who has made the experimental apparatus used in the study, for his diligent and marvelous manufacturing skills. I also like to thank my colleague Keibyoung Lee for participating in the design process of the apparatus.

I would also like to thank my graduate school colleagues, especially Juhyun Im, Juhyun Shin, Jieun Song, Junho Kim, Heechan Jeong, Keibyoung Lee, Suyong Kim, Sungkyung Lim, and Hongseong Moon. Memories with those people encouraged me to withstand my life in graduate school.

Finally, I would like to gratitude the unconditional love I have taken from my beloved father Dohee, mother Kyungsuk Gu, sister Suyeon, and my beloved wife Euiseul Ro. This thesis is dedicated to them.

Table of Contents

List of Figures

List of Tables

Nomenclature

Variables

a	Acceleration of SNU compresso [m/s^2]
A	Area of the measuring plane [m^2]
A_b	Blocked area [m^2]
AH	Absolute humidity [kg/m^3]
b	Systemic uncertainty
c	Labyrinth seal clearance [mm]
c_f	Friction coefficient
c_p	Heat capacity of air [J/K]
C	Chord [mm]
C_b	Bearing load rating [N]
C_d	Discharge coefficient
C_p	Total pressure coefficient ($\frac{P_{t,2}-P_{t,1}}{P_t-P_s}$)
$CF_{\dot{m}}$	Mass flow rate correction factor
CF_N	Rotation speed correction factor
D_{vis}	Decay rate of wake by the viscous dissipation
D_{stator}	Decay rate of wake inside the stator passage

e_{res}	Residual specific unbalance [g·mm/kg]
E	Raw voltage from a hot-wire sensor [V]
G	Balancing grade [mm/s]
h	Labyrinth seal height [mm]
H	Enthalpy [J]
i	Relative flow angle [°]
k^+	Nondimensionalized roughness number
k_s	Equivalent sandgrain roughness [μm]
L	Pitchwise Fluid segment length
L_g	Life span of grease [hr]
$\dot{m}$	Compressor mass flow rate [kg/s]
$\dot{m}_c$	Corrected mass flow rate [kg/s]
$\dot{m}_c^*$	Corrected mass flow rate, including humidity effect [kg/s]
M	Mass of rotating parts [kg]
N	Rotation speed [rev/min]
N_c	Corrected rotation speed [rev/min]
N_c^*	Corrected rotation speed, including humidity effect [rev/min]
N_{max}	Maximum rotation speed of bearing [rev/min]
N_t	Number of labyrinth seal teeth

p	Labyrinth seal axial distance [mm]
P	Stator Pitch [mm]
P_{atm}	Atmospheric pressure [Pa]
P_b	Equivalent bearing load [N]
P_{ij}	Two-dimensional production rate of turbulent kinetic energy
P_{ref}	Reference pressure [101.3 kPa]
P_s	Static pressure [Pa]
P_t	Total pressure [Pa]
ΔP	Pressure difference [Pa]
r	Variable
R	Gas constant of air [J/kg K]
R_a	Centerline-averaged roughness height [μm]
R_i	Labyrinth seal inner radius [mm]
R_o	Labyrinth seal outer radius [mm]
s	Random uncertainty
S	Span [mm]
t	Labyrinth seal teeth thickness [mm]
T	Time [s]
T_0	Time for 1 rotor passage rotation [s]

T_{atm}	Atmospheric temperature [K]
T_b	Temperature of bearing [°C]
T_i	Tolerance of each component [mm]
T_{ref}	Reference temperature [288.15 K]
T_{sum}	Accumulated tolerance of assembled parts [mm]
T_t	Total temperature [K]
u	Uncertainty of variable r at 95% interval
U	Velocity [m/s]
U_{res}	Residual unbalance [g·mm]
U_t	Velocity at rotor tip [m/s]
U'	Velocity disturbance [m/s]
W	Relative velocity [m/s]
X_i	Parameters constituting the variable r
y_i	Deviation of surface profile from the averaged position [mm]
α	Absolute flow angle [°]
γ	Heat capacity ratio of air
δ^*	Displacement thickness [mm]
ϵ	Resonance margin rate

η Efficiency ($\frac{\dot{m}c_p T_{t,in}\left\{\left(\frac{P_{t,out}}{P_{t,in}}\right)^{\frac{\gamma-1}{\gamma}}-1\right\}}{\tau\dot{\theta}}$)

θ Momentum thickness [mm]

θ_0 Angle of slanted hot-wire filament [°]

θ_p Flow pitch angle [°]

θ_y Flow yaw angle [°]

θ_α Angle between hot-wire filament and flow direction [°]

$\dot{\theta}$ Rotation speed [rad/s]

ν Kinematic viscosity of air [m^2/s]

ρ Density [kg/m^3]

τ Torque [N·m]

ψ Pressure coefficient ($\frac{P_{s,out}-P_{t,in}}{1/2\rho U_t^2}$)

ϕ Flow coefficient ($\frac{U_{x,in}}{U_t}$)

ω Vorticity [1/s]

Subscripts

0 Initial value

1 Inlet

2 Outlet

$\|avg, E\|$	Time-averaged, area averaged of entire passage
b	Blocked Region
c	Corrected at reference t
d	Design condition
eff	Effective component
Hub	Hub region (25 ~ 75% *S*)
in	Inlet of Compressor
leak	Labyrinth seal leakage flow
Max	Maximum
Mid	Midspan
Min	Minimum
out	Outlet of Compressor
p	Perpendicular to streamwise direction
Pas	Passage region (25 ~ 75% *S*)
r	Radial direction
s	Streamwise direction
t	Rotor tip velocity component
Tip	Tip region (75 ~ 96% *S*)
x	Axial direction

δ	Boundary between blocked and passage region
θ	Tangential direction

Superscripts

M	Mass-averaged
P	Pitchwise-averaged
$\bar{}$	Time-averaged
$\vec{}$	Velocity vector
$\hat{}$	Unit vector

Abbreviations

BLD	Boundary layer distortion
CV	Clockwise vortex
CCV	Counter-clockwise vortex
CRV	Counter-rotating vortex
IGV	Inlet guide vane
LDA	Laser Doppler anemometry
LE	Blade leading edge
PIV	Particle image velocimetry

PS	Blade pressure side
PV	Passage vortex
RANS	Reynolds averaged Navier-Stokes
Re	Reynolds number ($\frac{CU_t}{\nu}$)
RH	Relative humidity
RPM	Rotation per minute [revolution/min]
RW	Rotor wake
SS	Blade suction side
SW	Stator wake
TCV	Tip clearance vortex
T/C	Tip clearance
TE	Blade trailing edge

1. Introductions

1.1 Overview of the Study

1.1.1 Multistage Axial Compressor

Turbomachines are flow-driven mechanical devices, which add or subtract energy from working fluid. They are composed of turbines and compressors; turbines extract the energy from the working fluid, and compressors raise the energy of the fluid by increasing the pressure of the fluid. Internal combusting devices (gas turbines), external heat sources (boilers, nuclear reactors or renewable energies) or external power sources (industrial compressors, pumps) supply the energy required to power turbomachines. Because of their compactness and higher power output compared with conventional reciprocating combustion engines, turbomachines are widely used for power generations, aviation and marine propulsions, and industrial applications.

Axial compressors are a type of compressors that compress the axially driven working fluid. They are composed of rotating rotors, which add energy by increasing the

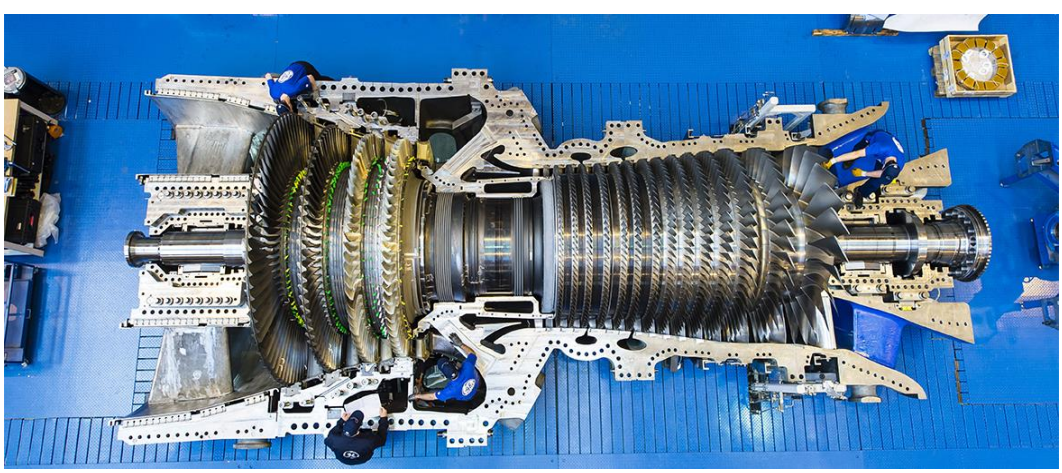

Figure 1.1 A Picture of an H-Class Gas Turbine [1]

velocity of the fluid, and stationary stators, which pressurize the fluid by decreasing the fluid velocity. Axial compressors are composed of multi-stages (a rotor row and a stator row consist of a single 'stage') to acquire desired pressure rise. These have an advantage of higher mass flow compared with radial compressors [2]; because of their high mass flow rate, most gas turbines for power generation and propulsion adopt the axial configuration.

1.1.2 Unsteady Nature of Flow inside the Blade Rows

As flow passes through blade rows, upstream blade rows generate wakes, which are low-momentum areas created at the behind of the blades due to blade surface boundary layers. In addition, additional flow structures, such as 1) hub and tip clearance vortices, generated by the clearance flow, [3-5], 2) corner separation, a common three-dimensional separation at the corner between the casing and the blade, [6] and 3) horseshoe vortices, which are generated due to the impingement of a boundary layer on blunt bodies [7], are also created behind each blade. These are transported downward, creating periodic unsteadiness inside the passages of turbomachines.

The wakes of upstream rotors in the relative frame (or stators in the absolute frame) have lower streamwise velocity, but their directions are identical. However, in a downstream absolute stator frame (or relative rotor frame), both the direction and the magnitude of the upstream rotor wakes are different, as shown in the velocity triangle of Figure 1.2. Due to this, the magnitude and the direction of incoming fluids vary timewise, which have been observed by numerous previous researches [4, 8-20]; for example, measurements of Sanders and Fleeter [12], which were conducted at a 1.5 stage axial compressor at subsonic case, reported that the relative Mach number deficit was ranged from 13.2% to 17.7% by rotor wakes, and the variation of downstream stator incidence angle was ranged from -15° to +1.9°. These caused the variation of the averaged incidence

angle of the downstream stator by 2.8°. In addition, Lange et al. [4] adopted the method of Khalid et al. [21] to obtain the unsteady blockage, which is defined as $A_b = \iint \left(1 - \frac{\rho U_x}{\rho_\delta U_{x,\delta}}\right) dA$ to quantify the deficit of axial velocity generated by rotor tip clearance flow and rotor wakes. Sinusoidal variation of 0.6~0.7% variation of the blockage was observed.

These upstream rotor wakes enter downstream stator passages, and are first chopped by the leading edges (LE) of stator blades [8]. The velocity difference between the absolute rotor wake vector and the absolute velocity vector of the passage flow shown in Figure 1.2 is called the "slip velocity [9]," which pushes the wake components towards

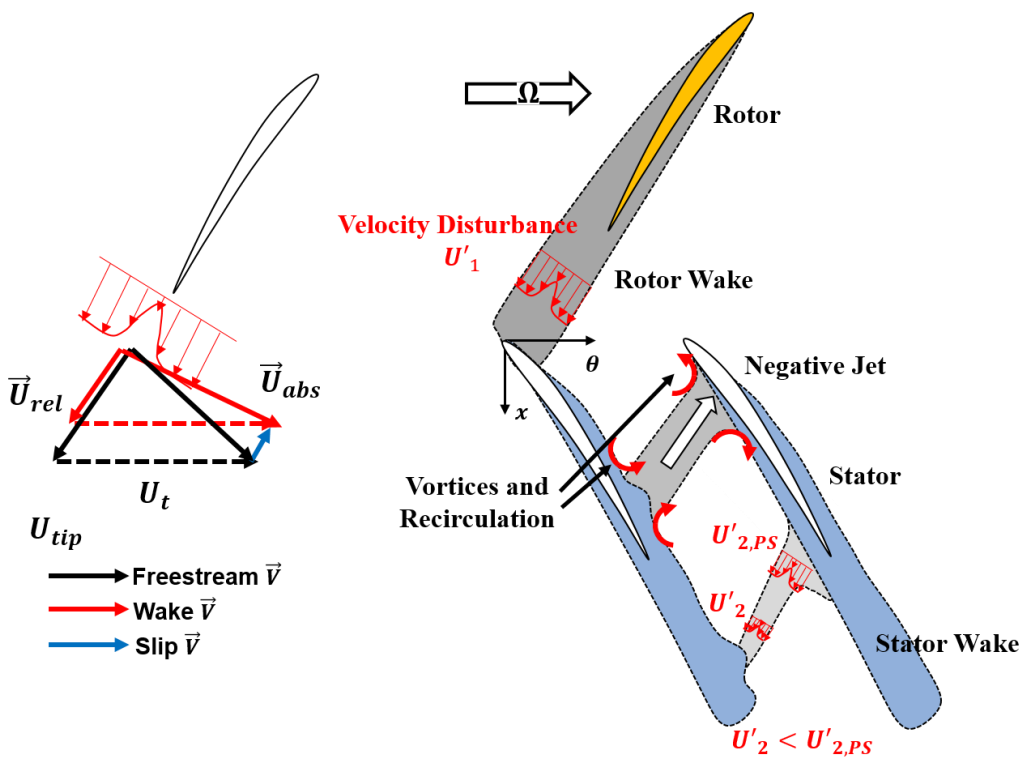

Figure 1.2 Schematic of Upstream Rotor Wakes inside a Stator Passage

the pressure side (PS) of the downstream stator blades. This phenomenon is called the "negative jet," which is the typical behavior of midspan unsteady flow structures inside blade passages. Due to this phenomenon, rotor wakes are concentrated at the stator PS as the wakes were transported downstream. In addition, by this relative movement inside the passage, clockwise and counter-clockwise vortices (CV, CCV) is generated near the PS of stator passage, and recirculation is generated between the two rotor wakes. This distorts the boundary layer of the suction side (SS) of the stator blade (boundary layer distortion), yielding higher boundary layer thickness and increased stator profile loss [22, 23].

As the wakes from the upstream blade row are transported downstream, the velocity disturbances, the timewise variation of aerodynamic properties and unsteady kinematics, created by the upstream blades are attenuated. Typical viscous mixing attenuates the velocity disturbances at the axial gap between the rotor and stator [10, 19, 22-24], increasing the wake mixing loss. However, inside the downstream blade row passage, the velocity disturbances are attenuated due to the increase of the stator passage width, which is known as "wake stretching." This phenomenon reduced the velocity disturbances without the increase of entropy, yielding higher stage efficiency and lower loss compared with rotor only cases.

1.1.3 Configurations of Axial Compressors and Their Flow Structures

Because turbomachines are composed of rotating parts and stationary parts, radial clearances between the two parts should exist. Minimizing these clearances is ideal, but due to mechanical tolerances, centrifugal forces and thermal expansions, it is difficult to reduce these below a certain level. As a result, tip clearance exists between the rotor blades and external casings. Tip leakage flow is generated through the clearances by the pressure difference between PS and SS, reducing the compressor performance and operating range

by triggering a compressor stall [3].

For a cantilevered stator configuration, which has hub clearances between the stationary stator blades and rotating rotor disk, hub clearance flow flows through the hub clearances. The hub clearance flow creates hub clearance vortex, which acts as a hubside blockage with a low momentum region near the PS of an adjacent blade. In addition, the hubside corner separation is swept away by the clearance flow; its hubside behavior of the cantilevered stator is similar to rotor tip clearance flow.

Another type of stator configuration is called a shrouded stator; a toroidal structure called a shroud covers the stator hub to eliminate the hub clearances. However, there still exists a radial clearance between the shroud and the rotating hub disk. Teeth-shaped objects called labyrinth seals are installed between the shroud and the rotor disk to reduce the radial clearance. Due to the pressure difference between the stator upstream and downstream, the passage flow is sucked into the downstream cavity, creating labyrinth seal leakage flow. This labyrinth seal leakage flow is re-introduced to the passage via the upstream cavity. Due to the leakage flow, low-momentum fluid is concentrated at hubside SS of the shrouded stator blade. In addition, the absence of the hub clearance flow permits the concentration of the low-momentum fluid at the hubside, SS of stator blade, widening the hubside corner separation compared with the cantilevered configuration. [25-27].

These two stator configurations have their advantages and disadvantages. The cantilevered configuration has a higher operating range and better stator efficiency; the hub clearance flow sweeps away the low-momentum fluid, reducing the possibility of the stall. However, the hub clearance flow increases incidence angle of downstream flow, reducing the overall stage performance depending on the compressor configuration, such as the width of the hub clearance, the degree of reaction and solidity [27, 29].

1.1.4 Effect of Stator Configuration on Hubside Unsteady Kinematics

Depending on the configuration of the stator, the hubside unsteady kinematics of stator passage flow differ. For the cantilevered type stator, the stator hub clearance flow reoriented the upstream rotor wake more parallel to stator blade, stretching the rotor wake 15% longer than the midspan cases [5].

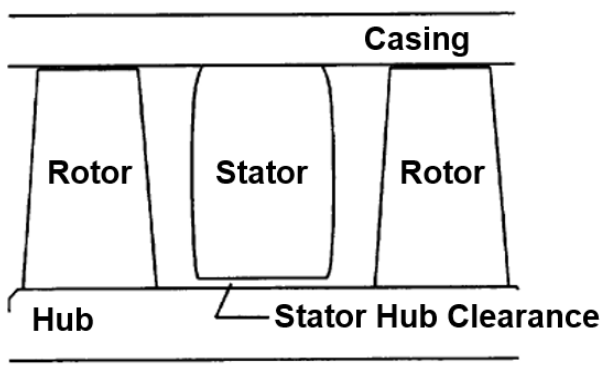

(a) Cantilevered Stator Configuration

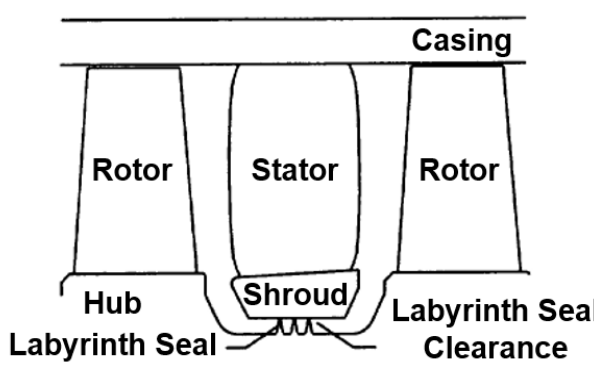

(b) Shrouded Stator Configuration

Figure 1.3 Schematics of the Two Stator Configurations of Axial Compressors [28]

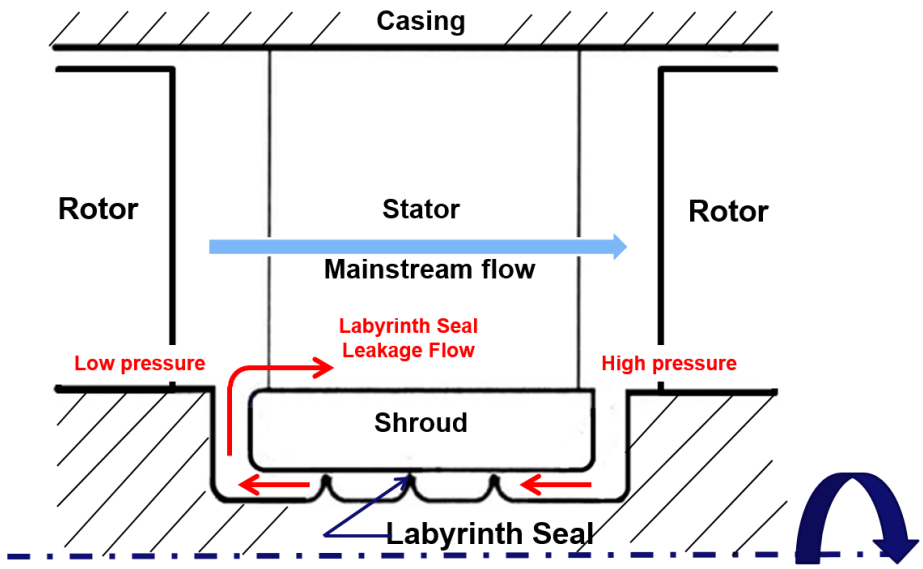

Figure 1.4 Schematic of the Meridional View of the Labyrinth Seal Leakage Flow of Shrouded Stator

For the shrouded stator configuration, experiments at an annular cascade with rotating cylinder rows [15, 16] observed the higher fluctuation of velocity components at the periphery of the corner separation. This indicates that the periphery of the hubside corner separation was disturbed by the upstream rotor wake, similar to the boundary layer distortion at the midspan. However, the frequency analysis of the measured velocity at the core of corner separation showed no wake passing frequency, which suggested that the hubside corner separation blocked the upstream rotor wake. This implies that the attenuation of the wake by the wake stretching inside the blade passage is affected by the hubside corner separation because the corner separation blocks the hubside passage [30]. However, no previous researches focused on the effect of the corner separation on the hubside unsteady kinematics of the shrouded stator flow configuration.

In addition to that, many of the previous researches have dealt with the unsteady

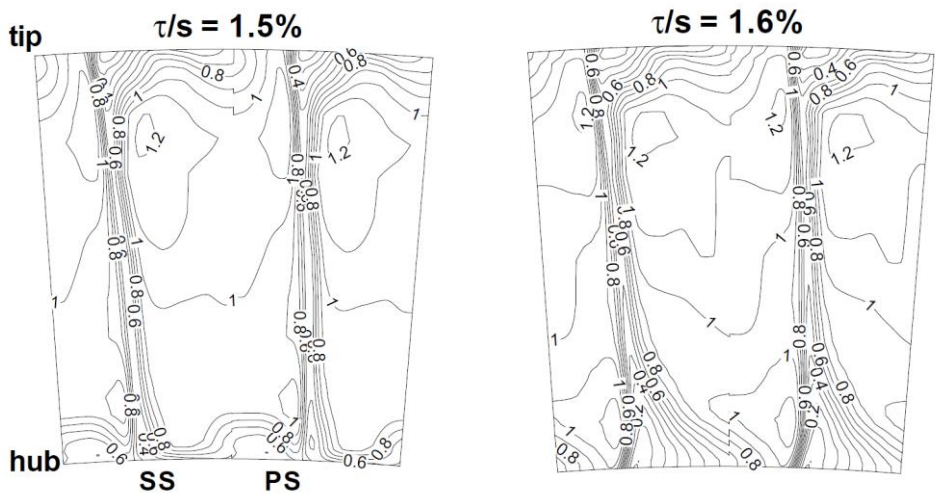

(a) Cantilevered **(b) Shrouded**

Figure 1.5 Contours of Non-Dimensional Total Pressure Coefficient C_p of Different Stator Configurations at Design Point [27]

kinematics of passage flow created by upstream rotor wakes in two-dimensional configurations, or individual single aerodynamic properties such as U_x or P_t, which have not dealt with the possible the radial movements created by the interaction between rotor and stator wakes.

Therefore, this study will aim to answer the unsteady kinematics of a multistage shrouded axial compressor flow, focusing on the 1) impact of the hubside corner separation on the unsteady flow structure of shrouded stator and 2) its impact on the variation of aerodynamic properties.

1.2 Literature Review

1.2.1 Unsteady Behavior of Aerodynamic Properties by the Upstream Wakes

It has been known that the periodic unsteady wakes generated by the upstream rotors (or stationary stators) vary the aerodynamic properties of the inlet of downstream stator passages (or rotor passages) [4, 8-20], due to the different magnitude and direction of the velocity vectors of wakes and passage flow, as shown in Figure 1.2. For example, Sanders and Fleeter [12] showed that maximum 17.7% variation of relative Mach number and ~10° variations of absolute flow angle were observed at the downstream of a rotor row of 1.5 stage axial compressor at the subsonic case, causing the averaged incidence angle of downstream angle varied by 2.8°. Dring and Spear [31] compared the experimental data of Stauter et al. [19] and two-dimensional throughflow analysis including the effect of the wake mixing, showing the mixing of wake induced 13° flow angle, 30% dynamic pressure variation and increased efficiency.

In addition, Mailach and Vogeler [32, 33] conducted measurements using unsteady pressure transducers at both the rotor and the stator midspan surfaces, and hot-film arrays at the stator midspan surfaces, which showed the variation of the surface unsteady pressure due to the periodical unsteadiness by the upstream stator wake. As a result, the boundary layer was affected by the upstream wakes. The upstream rotor wakes promoted the transition of LE boundary layer of downstream stator surfaces, altering the entire chordwise boundary layer.

The variations of velocity components and flow angle by the upstream wake can be recognized as “blockage,” which hinders the transportation of passage flow by reducing the effective flow area [21, 30]. Khalid et al. [21] suggested a method to quantify the blocked area created by the endwall boundary layer and tip clearance flow, as shown in equation 1.1.

$$A_b = \iint \left(1 - \frac{\rho U_x}{\rho_\delta U_{x,\delta}}\right) dA \tag{1.1}$$

δ is the boundary of the blocked region, and the boundary was distinguished by the value of the gradient of velocity; the method is analogous to displacement thickness of two dimensional flat plate boundary layer. Lange et al. [4] adopted the method of Khalid et al. [21] to obtain the unsteady blockage to quantify the deficit of axial velocity generated by rotor tip clearance flow and rotor wakes. Sinusoidal variation of 0.6~0.7% variation of the blockage was observed. In addition, Sirakov and Tan [34] adopted the method of Khalid et al. [21] to calculate the blockage downstream of a rotor row created by upstream stator wakes and tip clearance flow. They found out that 27% of the blockage was reduced for time-averaged blockage from unsteady simulations compared with steady simulation.

1.2.2 Behavior of Upstream Wakes inside the Midspan of Downstream Blade Row

In the early stages, Smith [8] measured the unsteady velocity downstream of a midspan 1st rotor row at six different pitchwise locations using a single-element hot-wire to investigate the behavior of upstream inlet guide vane (IGV) wakes passing through the 1st rotor passages. His measurements found that the upstream IGV wakes appeared at different locations and at the same time, suggesting that the leading edge (LE) of the 1st rotor chopped the IGV wake, and the two chopped segments did not reunite at the trailing edge (TE) of the 1st rotor. In addition, he proposed that as the upstream IGV fluid passed the 1st rotor, the pitchwise length L of the wake segment increased, leading to the attenuation of velocity disturbances by the IGV wake due to the preservation of the magnitude of vorticity. This phenomenon is later known as “wake stretching.”

Kerrebrock and Milokajczak [9] proposed a model explaining the behavior of the rotor wakes inside the stator passage. They suggested that there is a velocity difference

between the rotor wake and the passage flow at the stator absolute frame, called the "slip velocity," as shown in Figure 1.2. This velocity vector pushed the upstream rotor wake fluid toward the pressure side (PS) of the downstream stator, which is later known as "negative jet." As a result, the rotor wake was concentrated at the stator PS. Helium-tracing measurements were performed at the 1st stage of an axial compressor to validate their assumptions, which showed the increased helium concentration rate at the stator PS. Pitchwise variations of stagnation temperature were also measured in a single stage transonic compressor; higher stagnation temperature was observed at the downstream of the stator PS, owing to the migration of the upstream rotor wake by the slip velocity.

Van Zante et al. [10] suggested an analytical model of viscous dissipation and inviscid stretching of a rotor wake inside a cantilevered stator row. In addition, experiments with laser fringe anemometer (LFA) technique and numerical calculations at the mid-span of the cantilevered stator passage were performed to assess the model. They found that irreversible viscous dissipation and reversible wake stretching were the dominant mechanisms of the attenuation of the rotor wake. Inside the stator passage, the inviscid wake decay by the wake stretching was the dominant factor of the rotor decay mechanism inside the stator row; the magnitude of viscous mixing was negligible inside the stator passage. However, for the axial clearances between the rotor and the stator row, the irreversible viscous dissipation dominated the attenuation of the rotor wake, leading to an increase of the wake mixing loss. Reducing the axial clearance decreased the portion of the viscous mixing loss due to the increased reversible wake stretching inside the stator passage, and reduced irreversible wake mixing loss at the axial clearance.

Similar results were achieved by Sanders et al's particle image velocimetry (PIV) measurements at the midspan of a cantilevered stator of a multistage axial compressor [11]; they found that 1) the inviscid wake stretching and the viscous dissipation enhanced the

attenuation of the rotor wake, and 2) the negative jet phenomenon pushed the rotor wake towards the PS of the stator.

Mailach et al. [13] investigated the behavior of upstream stator wakes inside a midspan rotor passage at a multistage compressor using 2D laser Doppler anemometer (LDA) technique and unsteady pressure transducers on the surface of a midspan rotor blade. Measurements found 1) the chopping of the stator wake by the rotor blade, 2) the attenuation of the stator wake inside the rotor passage, 3) the negative jet phenomenon and 4) clockwise, counter-clockwise vortices near the PS of rotor, and recirculation by the migration of the stator wakes towards the rotor PS. It is expected that by these vortices and recirculation, static pressure and streamwise velocity at the surface of blade surface vary as suggested by potential flow calculations of Meyer [35]. Similar unsteady flow structures were observed at the single stage stator passage unsteady simulations performed by Sirakov and Tan [34], Valkov and Tan [23]. However, due to the limitation of laser technique near surfaces (surfaces reflect laser near the wall, which hinders measurements near surfaces) velocities near the rotor blades could not be resolved.

Valkov [22], Valkov and Tan [23] further investigated the behavior of the upstream rotor wakes inside the stator passage using steady and unsteady Reynolds averaged Navier-Stokes (RANS) simulations. Five different numerical configurations were used to identify the mechanism of the behavior of the rotor wakes inside stator passages: 1) 2D configuration, 2) 3D inviscid flow (ID) with an interaction of a streamwise vortex (SW) (ID/SW), 3) 3D inviscid flow (ID) with an interaction of a tip leakage flow (TL) (ID/TL), 4) 3D viscous flow (VD) with an interaction with a streamwise vortex (SW) (VD/SW) and 5) 3D viscous flow (VD) with a interaction with tip leakage vortex (TL) (VD/TL). Inlet disturbances, such as the upstream rotor wakes, the rotor tip leakage flow or streamwise vorticity, were classified into two categories: 1) rotor P_t/blockage

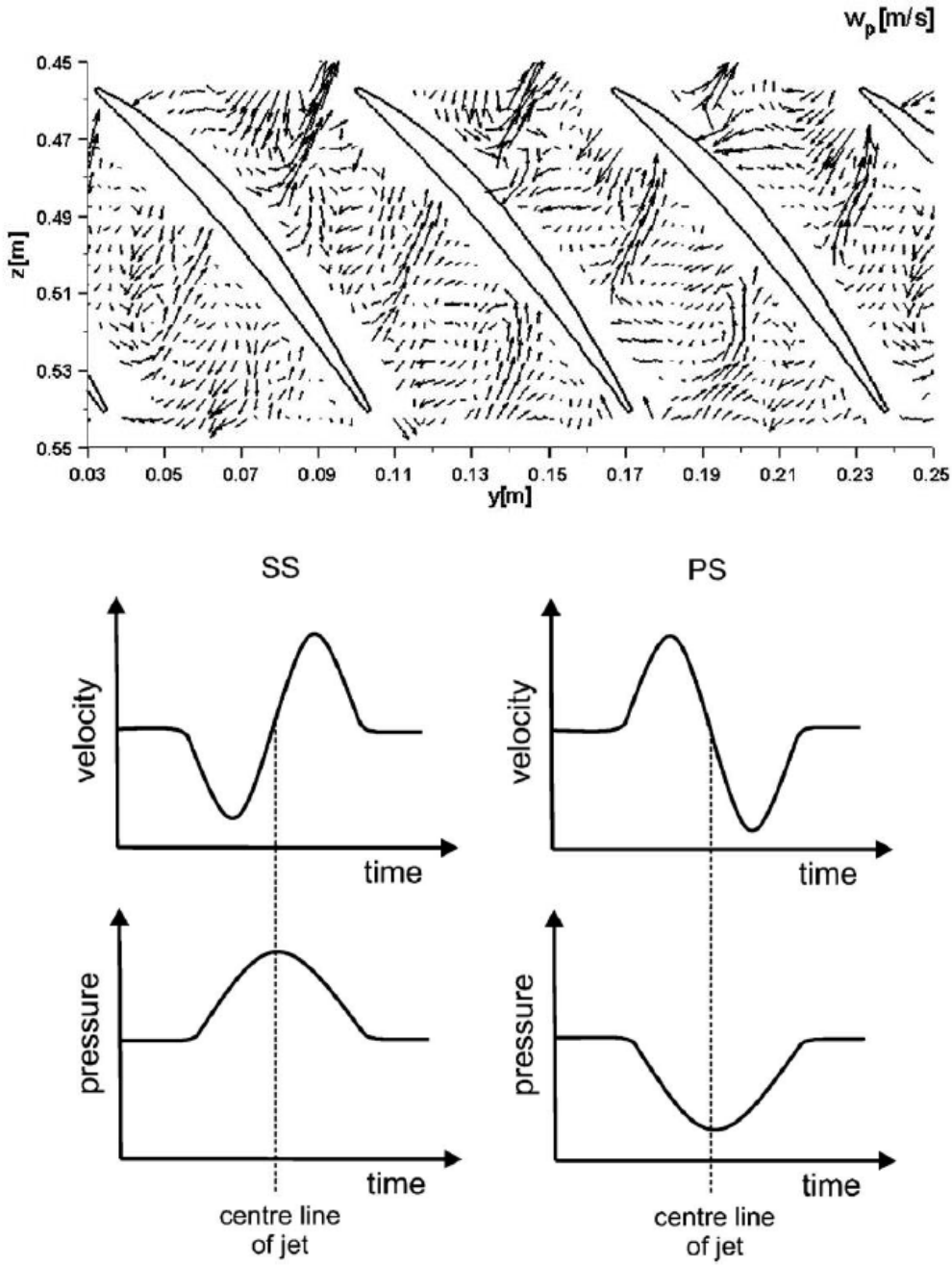

Figure 1.6 Measured Secondary Flow Vectors inside Rotor Passages and the Variation of Pressure and Velocity on the Surface of a 3rd Rotor, Reference Rotor-Stator Position, Midspan, Design Point [13]

disturbances which were perpendicular to streamlines, such as wakes and tip leakage vortex core, 2) rotor crossflow disturbances, which were parallel to streamlines, such as streamwise vortex and tip leakage flow. Gaussian velocity defect profile was used to imitate the rotor wakes, and peak relative velocity defect and the pitchwise thickness of wakes were varied to change the wake profile. Two generic mechanisms affected the attenuation of these inlet disturbances and unsteady performances. The first was the beneficial reversible two-dimensional recovery of energy by the wake stretching, which had been also observed by previous researches [8, 10, 11]. By the virtue of Kelvin's theorem, the velocity defect by the upstream rotor wake was reduced without entropy generation, reducing the mixing loss of the rotor wake (equal to rotor profile loss). However, depending on the direction of the vortices, the magnitude of incoming vortices can be amplified. In addition, the frequency of the fluctuation of the upstream rotor wake affected the level of benefit from the wake recovery. The second one was detrimental non-transitional boundary layer distortion; the negative jet and the resulting recirculation lifted the low momentum SS boundary layer vortical fluid into the passage flow, increasing the stator profile loss. Compared with the steady simulations, ~10% increase of stator profile loss was observed by the boundary layer distortion.

Montomoli et al. [5] performed unsteady RANS simulations of a four-stage, low-speed cantilevered configuration axial compressor to investigate the periodic unsteady behavior created by the rotor-stator interaction. Both steady and unsteady simulations were performed to assess the difference created by the unsteady simulation, which showed a higher operating range for the unsteady cases; the negative jet phenomenon pushed the low-momentum fluid towards the stator PS, thus stall was delayed at the stator SS. Velocity vector, vorticity and total pressure distributions of 1st stator passage were presented, showing that 1) the rotor wakes were headed to the PS of stator blade by negative jet phenomenon and 2) the rotor wakes were attenuated inside the stator passage.

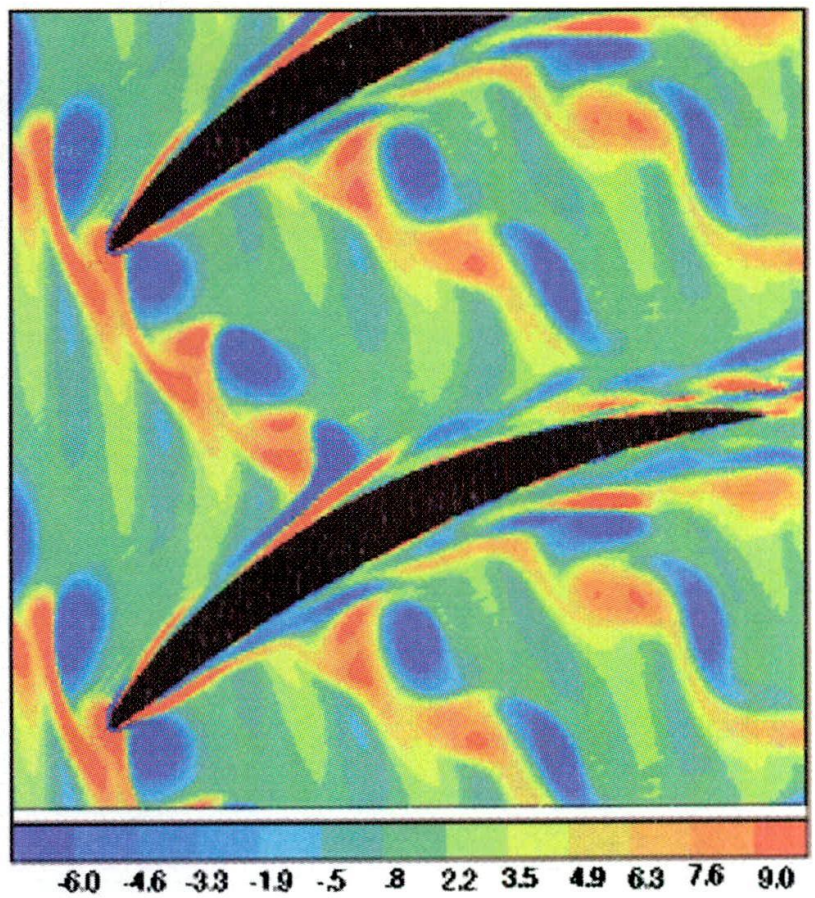

Figure 1.7 Instantaneous Numerical Color Contour of Radial Vorticity of Stator Passages with Upstream Wakes [23]

Soranna et al. [36] performed 2D PIV measurements at a low-speed axial compressor to investigate the effect of upstream IGV wakes on the downstream unsteady rotor passage flow structure, including the PS and SS boundary layer. The measurement showed that the orientation of strain varied across a rotor passage, indicating the anisotropic stretching of the fluid element. This caused the negative production rate of Reynolds stress term, which was expressed as $P_{ij} = -\overline{U_i' U_k'} \frac{\partial \overline{U_J}}{\partial x_k} - \overline{U_J' U_k'} \frac{\partial \overline{U_i}}{\partial x_k}$. As a result,

the high turbulent kinetic energy of upstream IGV wakes was reduced and converted into total pressure. Similar result was observed at LES simulations of a low-speed multistage axial compressor by Hah [24]; two different axial gaps were calculated to check the effect of the axial clearance on pressure rise. It was observed that reducing the axial gap from 112% C_x to 29% C_x increased the pressure loss by 0.5%; 22% of this was by the wake stretching, and 63% was due to the unsteady non-uniform pressure field at the rotor exit. In addition, higher loss areas were observed at the PS, midspan of stator exit plane; lower pressure recovery and longitudinal curvature effect, created the lower anisotropic strain rate. As a result, higher pressure loss near the stator PS was created.

1.2.3 Unsteady Kinematics of Downstream Stator Tip Flow

At the tip region of the stator passages, the tip clearance flow of the upstream rotor blades is added, creating additional unsteady flow structures compared with those of the midspan stator passage.

Valkov and Tan [37] simulated the unsteady flow structure of the tip region of a stator blade row using RANS simulations, following the technique of Valkov [22]. The velocity profile of the tip clearance vortex was extracted from the results of Khalid [21]. The calculations showed that the tip clearance flow acted as a core of steady, slowly-swirling low-energy fluid; the most important aspect of the tip vortex was the relative total pressure and velocity defect. Thus, the tip clearance flow was perceived as widened rotor wake, which was attenuated by the two-dimensional wake stretching phenomenon. Identical results were obtained by Montomoli et al [5]; the attenuation of tip clearance flow by the wake stretching was observed. However, increased passage loss by the interaction of tip leakage vortex and casing boundary layer was also observed.

Sirakov and Tan [34] simulated the unsteady interaction between the upstream stator wakes and the rotor tip clearance flow of a low-speed axial compressor using steady and unsteady RANS simulations. A single rotor was calculation domain, and the upstream stator wakes were artificially constructed using Gaussian profile characterized by peak velocity defect and wake width. Inviscid casing wall boundary condition was adopted to remove the interaction between the tip clearance flow and the casing boundary layer, which was reported by Shin et al. [38]. The calculations showed that double leakage flow (the passage of tip clearance flow through the neighboring tip clearance gap) was created. This double leakage lowered stagnation pressure further, reducing the compressor performance. However at unsteady simulations, the inclusion of upstream stator wakes increased the stagnation pressure; the stator wakes had higher relative stagnation pressure, diverting the double tip leakage flow away from the rotor PS. As a result, the amount of the double leakage flow was reduced, yielding higher compressor performance of the time-averaged unsteady case compared with the steady simulations.

Mailach et al. [14] investigated the unsteady tipside flow structure of a rotor passage at a low-speed multistage axial compressor. LDA measurements at the rotor tip region (98.8% span from the hub) were performed to acquire meridional velocity distribution. The results have shown that the negative jet phenomenon and the counter-rotating vortices created by the upstream stator wake affected the periodical fluctuation of the magnitude and the direction of downstream rotor tip clearance vortex, as can be seen in Figure 1.8; the distribution of axial velocity U_x downstream of were varied by the fluctuation of the tip leakage vortex.

Lange et al. [4] further investigated the unsteady tipside flow structure of the multistage axial compressor, which had been used by Mailach et al. [13, 14]. Unsteady pressure measurements downstream of a rotor row, and casing static pressure measure-

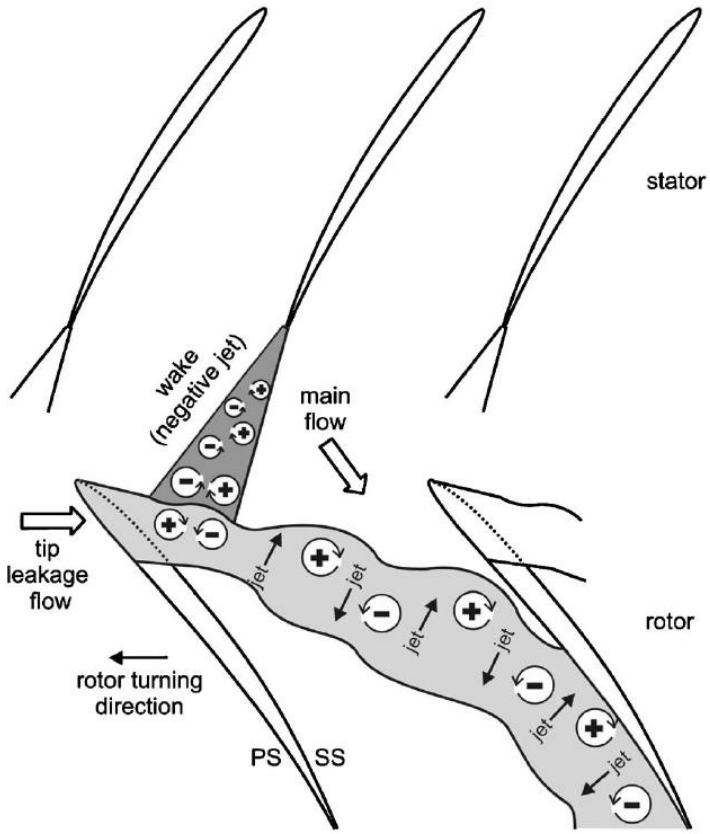

Figure 1.8 Schematic of Tip Clearance Vortex Influenced by Upstream Stator Wakes [14]

ments were performed and compared with the unsteady numerical non-linear harmonic (NLH) simulations to analyze the interaction between the upstream stator wakes and the rotor tip clearance flow. They found that the impingement of the stator wake at the LE of the rotor blade varied the incidence angle, leading to rotor tipside pressure fluctuation. This lead to the variation of the pressure gradient between the rotor PS and SS, varying the mass flow rate of tip leakage flow. As a result, the magnitude of blockage, following the method of Khalid et al. [21], showed sinusoidal variation.

1.2.4 Unsteady Kinematics of Downstream Stator Hub Flow

Unlike the other regions, the unsteady kinematics of hubside stator flow varies based on two stator configurations: a cantilevered and a shrouded stator. The cantilevered stator configuration (Figure 1.9 (a)) has a hubside clearance between the rotating hub disk and the stationary stator blade. Through the clearance, hub clearance flow is flowing from the PS to the SS of the stator blade, similar to the tip clearance of the rotor. On the contrary, the shrouded stator configuration (Figure 1.9 (b)) has a hubside toroidal structure called the shroud covering the hubside of the stator to eliminate the hub clearance. However, a radial clearance still exists between the shroud and rotating hub disk. A tooth-shaped object called a labyrinth seal is installed between the shroud and the rotating disk to minimize the clearances, but due to the mechanical tolerances, thermal expansions, etc., the radial clearances cannot be eliminated. As a result, the pressure difference between the upstream and the downstream of the stator row pushes the hubside passage flow into the downstream cavity, creating the labyrinth seal clearance flow passing through the labyrinth seal clearance. This clearance flow re-enters the mainstream passage via the upstream cavity of the shrouded stator configuration.

The two stator configurations create different compressor characteristics and the hubside flow structure of the stator passage [25-27]. Jefferson and Turner [39] first investigated the effect of the shroud clearance and the tip clearance on the performance of a shrouded multistage axial compressor. Four rotor and stator blade configurations were tested; the combinations of a shrouded, an unshrouded stator, shroud clearances, twisted and untwisted blades (which are obsolete for modern axial compressors) were tested in their experiments. The performances of each configuration were measured, and steady measurements with a pneumatic probe were performed to identify the velocity and the flow angle distribution inside the compressor. By adopting the shroud, the compressor used in

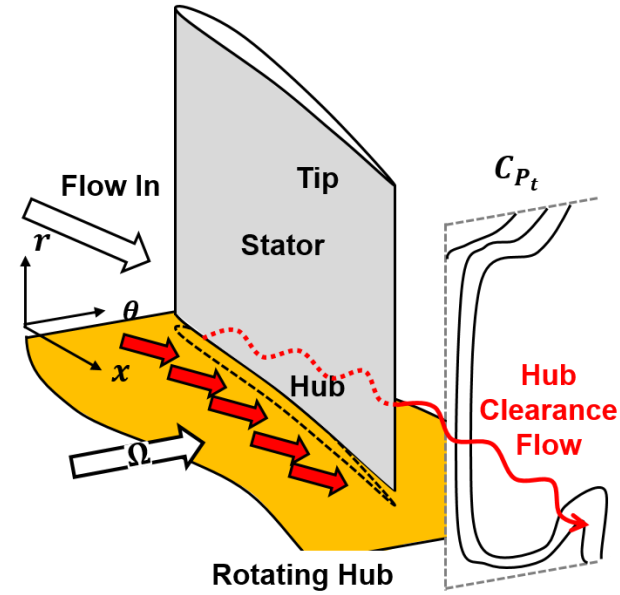

(a) Schematic of Cantilevered Stator and Steady Flow Structure

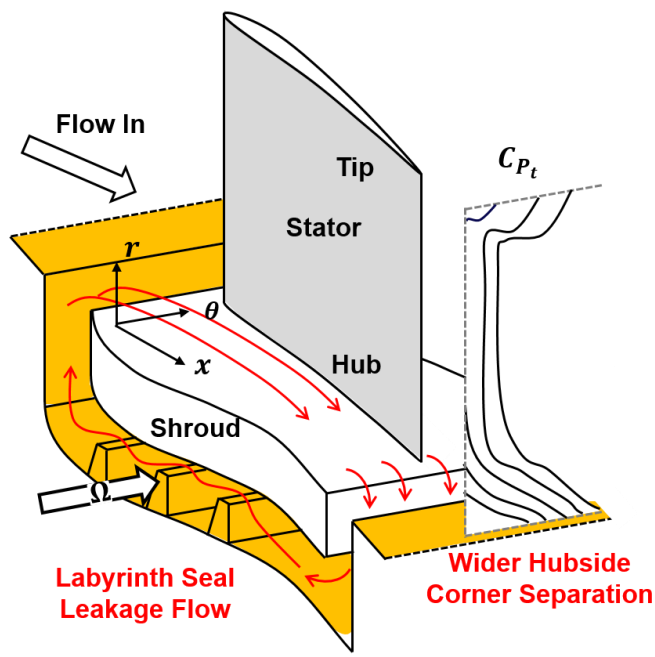

(b) Schematic of Shrouded Stator and Steady Flow Structure

Figure 1.9 Schematics of the Two Stator Configurations and Flow Structures [25-27]

the experiment were more susceptible to the stall, thus lower stall onset point was achieved. In addition, increasing the shroud labyrinth seal clearance decreased compressor performance.

Swaboda et al. [25] experimentally compared the flow distributions inside a low-speed multistage axial compressor with a shrouded and a cantilevered stator. The performances of each configuration were compared, and a pneumatic cobra probe was traversed tangentially and radially to obtain flow angle and total pressure distributions downstream of the stators. Measurements found that the shrouded configuration had slightly higher work coefficients, but lower stall margin; the hub clearance flow of the cantilevered configuration removed the hub corner separation, stabilizing the flow field. Thus, the cantilevered stator configuration had a lower stator loss. However, due to the hub clearance vortex, rotor inlet condition was changed, yielding the higher stage loss compared with the shroud configuration. Similar to the Swaboda et al.'s research, Campobasso et al. [26] and Lange et al. [27] experimentally and numerically compared the performances and flow structures of a low-speed multistage axial compressor with a shrouded and a cantilevered stator. Higher efficiency, lower operating range, and wider hub corner separation were observed at the shrouded configuration; the hub leakage flow reduced the stator loss by sweeping the low momentum fluid near the hub, SS of the cantilevered stator. However, due to the hub clearance flow, a low axial momentum and high loss region existed near the PS of the adjacent stator blade, which was similar to the behavior of the rotor tip leakage flow.

These different hubside flow structure of each stator configurations affect the unsteady kinematics of hubside stator flow. For the cantilevered stator configurations, numerical simulation by Montomoli et al. [5] observed that the hub clearance flow of the cantilevered stator reoriented the direction of the upstream rotor wake inside the

downstream stator passage, making the rotor wake more parallel to the streamline. This increased the stretching of the hubside rotor wake by 15%, as shown in Figure 1.10; the attenuation of the wake by the wake stretching can be higher at the hubside of the cantilevered configuration.

However, for the shrouded configuration, the low momentum fluid was concentrated at the hubside, resulting in wider hubside corner separation compared with cantilevered cases. Schultz et al. [15] and Poensgen and Gallus [18] performed experiments conducted at an annular cascade with rotating cylindrical rotor rows to imitate the upstream wake. Hubside corner separation was observed at the hubside SS of blades, reducing the momentum at the region.

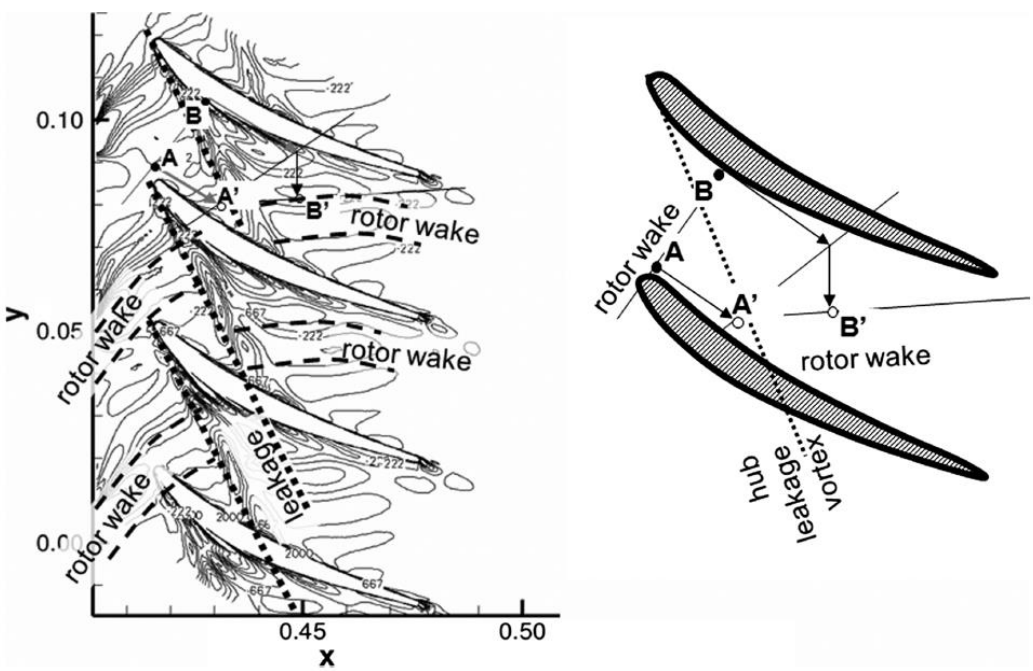

Figure 1.10 Instantaneous Numerical Vorticity Contour at 5% Span and the Schematic of Hubside Wake Behavior of a Cantilevered Stator [5]

Joslyn and Dring [30] conducted experiments at a low-speed multistage shrouded stator axial compressor using a pneumatic 5-hole probe to investigate the steady kinematics of hubside shrouded stator flow. The result showed the existence of wider hubside corner separation at the shrouded stator, similar to the results of Schultz et al. [15] and Poensgen and Gallus [18]. The hubside corner separation increased the hubside blockage, deflecting the hubside passage flow radially. As the flow rate was reduced the width of the corner separation was significantly increased.

In addition, the labyrinth seal leakage flow of the shrouded stator configuration further widens the width of the hub corner separation. The effect of the labyrinth seal leakage flow on compressor performance has been investigated since late 1950; Jefferson and Turner [39] first investigated the effect of the shroud clearance and the tip clearance on the performance of a shrouded multistage axial compressor, followed by Mahler [40] and Freeman [41]. Mahler's [40] experimental result with a two-lipped inter-stage labyrinth seal showed reduced compressor efficiency as the seal clearance was increased. Freeman's [41] experiments at a two-stage axial compressor with varying labyrinth seal clearances, Heidegger et al.'s [42] numerical calculations, Wellborn and Okiishi's [28, 43] experiments at a low-speed multistage axial compressor configuration, and cascade experiments by Demargne and Longley [44] also showed the reduced compressor efficiency by the increased labyrinth seal clearance due to the increased labyrinth seal leakage flow. Freeman [41], Wisler [45] and Ludwig [46] quantified the effect of the labyrinth seal clearance on compressor performances; for a 1.0 percent increase in the clearance to blade span, 1.5 [41, 46] percent of the efficiency was reduced, and the stall margin was reduced to a maximum 6 percent [45].

Furthermore, the labyrinth seal clearance flow creates the unique flow structure of the shrouded stator configuration. Wellborn and Okiishi [28, 43] investigated the effect

of labyrinth seal clearance and rotation speed on the flow properties upstream and downstream of a shrouded stator of a low-speed four stage axial compressor. Measurements were conducted with five different labyrinth seal clearances. In addition, numerical simulations were conducted to vary the rotating speed of the compressor, but the boundary conditions derived from the experiments were kept constant regardless of the rotating speed. Increasing the clearance increased the incidence, deviation, diffusion factor and loss at the stator hub region, spoiling the flow properties near the stator hub. Numerical simulations showed that the increase of the rotation speed increased the tangential momentum of the leakage flow, yielding less leakage flow collected on the hubside SS of stator blade, and reduced stator loss. Based on these results, they proposed the behavior of leakage flow inside the stator blade row, as shown in Figure 1.11; when the amount of leakage flow was large due to higher labyrinth seal clearance, the leakage flow with low momentum cannot withstand the pressure gradient between the PS and the SS inside the stator passage. As a result, the streamline of the leakage flow was turned towards the SS of the stator passage, collecting the low-momentum fluid near the hubside SS of the shrou-

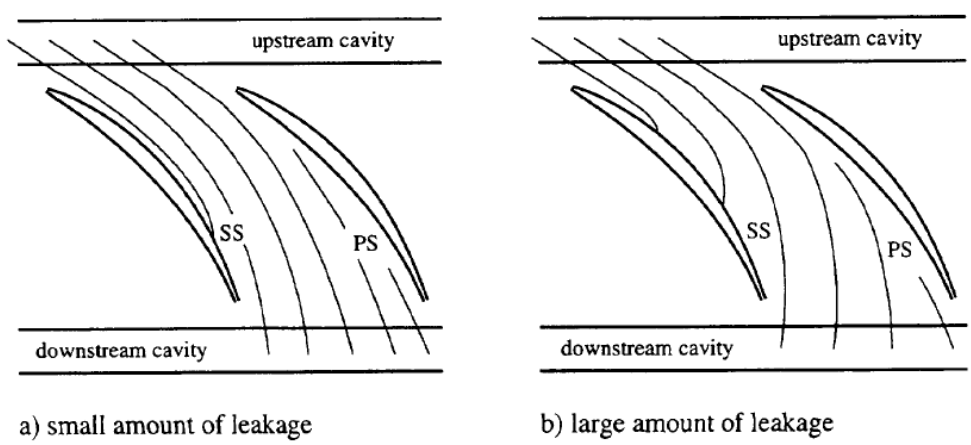

Figure 1.11 Idealized Hubside Streamlines of Shrouded Stators for Small and Large Leakage Flow [28]

ded stator passage; the hubside SS boundary layer was worsened, and the hubside SS passage flow was overturned.

Demargne and Longley [44] experimentally and numerically investigated the effect of the mass flow rate and tangential velocity of labyrinth seal leakage flow on the flow characteristics of a shrouded stator cascade. A circumferential slot was installed at the upstream of the stator blade, and the leakage flow was injected through the slot, thus the mass flow rate and the tangential velocity of the leakage flow could be controlled separately. Similar to Wellborn and Okiishi [28, 43], increasing the tangential velocity of the leakage flow reduced the overall loss and the concentration of leakage flow near the hubside SS of the stator. In addition, they proposed the effect of the leakage flow on the boundary layer thickness of the hubside casing, stating that the low-momentum leakage flow increased the axial and tangential displacement thickness and the momentum thickness of the hubside casing, as shown in equations 1.2 and 1.3.

$$\Delta\delta_x^* = \Delta\theta_x = \frac{\dot{m}_{leak}}{\rho U_x} \tag{1.2}$$

$$\Delta\theta_\theta = \frac{\dot{m}_{leak}}{\rho U_x}\left(1 - \frac{U_{\theta,leak}}{U_\theta}\right) \tag{1.3}$$

Kim [47] numerically investigated the steady flow structure of a shrouded stator cascade using steady RANS k-ω turbulence model. The entire shrouded stator passage of a low-speed axial compressor cascade passage including the upper, lower cavities and labyrinth seals was calculated and validated by the experimental results of the cascade rig. Three different levels of leakage flow tangential velocity were chosen, while the leakage flow mass flow rate was fixed to assess the effect of leakage flow tangential velocity on the flow structure of the shrouded stator. Numerical results showed that the streamlines of the leakage flow first left the upper cavity and headed towards the PS of the downstream blade, and shifted towards the SS due to the pressure gradient between the PS and the SS;

identical behavior of the leakage flow by the PS-SS pressure gradient was observed at the simulation results of Marty and Aupoix [48]. As a result, low momentum fluid was concentrated near the hubside corner separation, creating wider low momentum region at the stator hubside SS. Similar to the results of Wellborn and Okiishi [28, 43] and Demargne and Longley [40], increasing the leakage flow tangential velocity reduced overall loss; additional tangential momentum surpassed the pressure gradient between the PS and the SS, therefore less low-momentum fluid was concentrated at the hubside SS, reducing the width of hubside corner separation. This labyrinth seal leakage flow created the additional vortex other than the typical passage vortex and horseshoe vortices. In addition, the flow structures of upstream and downstream cavities were also investigated; a local egress (flow coming out from the cavity) was observed at the downstream cavity. Meridional structures of upstream and downstream cavities showed the recirculations by the ingress and the egress.

This different hubside steady flow structure of shrouded stator would definitely create the different hubside unsteady kinematics of hubside shrouded stator flow compared with that of the cantilevered configurations. Schultz et al. [15, 16] performed experiments at an annular cascade with rotating cylinder rows to investigate the incoming periodic unsteady flow on downstream flow structures. The structure of the annular cascade was similar to that of the shrouded stator; stationary hub casing enabled the concentration of the low momentum fluid at the hubside SS of the blades. They found that the existence of the wake enhanced transition near the leading edge. In addition, the laminar separation bubble was disappeared. This reduced the hub corner separation by ~40% compared with no rotor cases due to the energized hub, by high turbulence intensity and oscillation. However, the blade profile loss was also increased by ~30%. Furthermore, the frequency analysis of the measured velocity at the core of the corner separation showed no wake

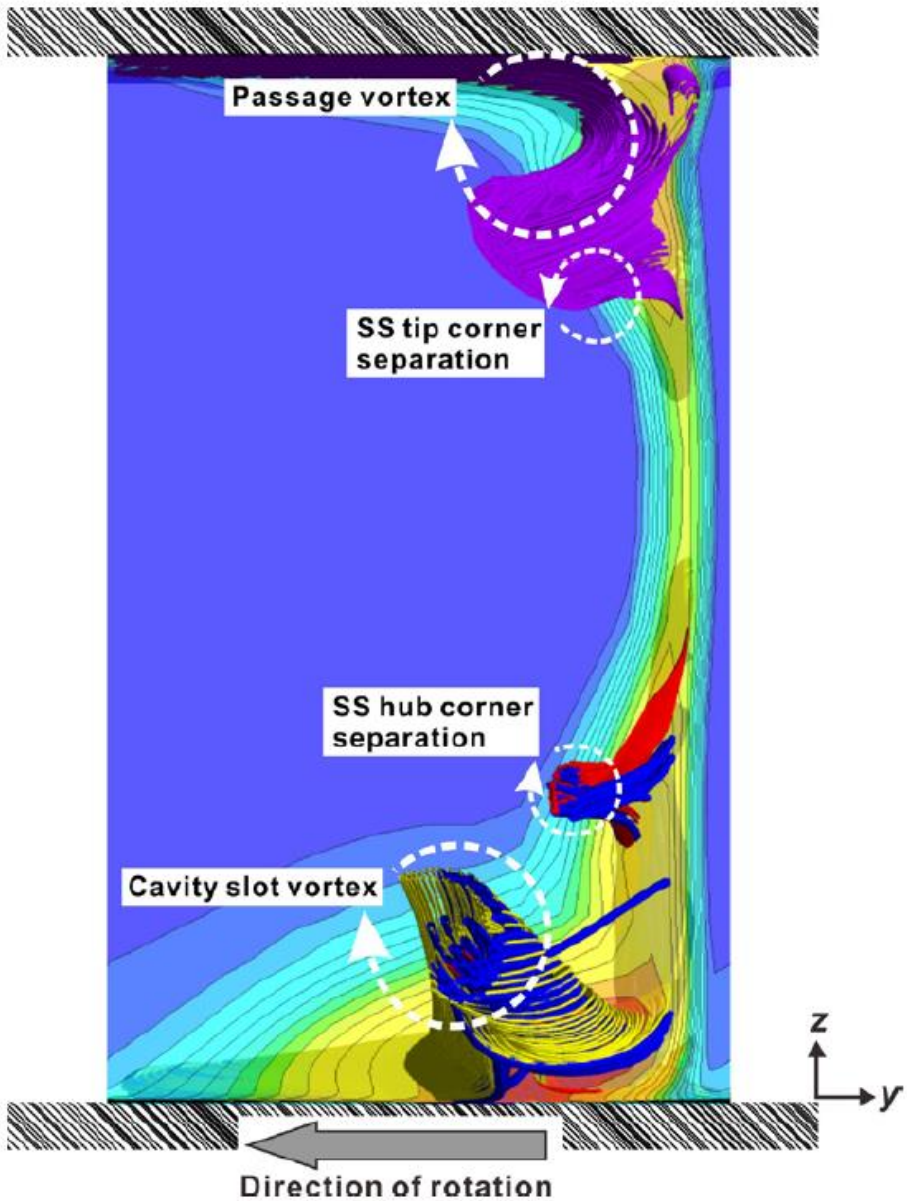

Figure 1.12 Numerical Total Pressure Loss Color Contour and Vortical Motion at the Downstream of a Shrouded Stator [47]

passing frequency, while the unsteadiness of the velocity at the periphery of the corner separation was increased. These suggest that 1) the rotor wake could not pass the center of the corner separation, and 2) the periphery of the corner separation would also be affected by the upstream rotor wake, similar to the midspan boundary layer distortion.

Poensgen and Gallus [17, 18] performed experiments using the annular cascade used by Schultz et al. [15, 16] to measure the three-dimensional unsteady velocity vectors using a three-axis hot-wire. They found that with the existence of downstream blades, the wake profile and the turbulent intensity of the rotor decayed faster compared with the configuration without downstream blades. The effect of the unsteadiness by the upstream wakes was small at the center of the tip clearance region and corner separation region, while the effect was large at the periphery of the corner separation. In addition to that, they found the amplification of the velocity disturbances created by the upstream wake at increased loading condition. This indicates that the variation of the hubside corner separation can affect the hubside unsteady kinematics of the shrouded stator configuration.

Ernst et al. [20] measured the unsteady total pressure and the velocity distributions upstream and downstream of a shrouded multistage transonic compressor stator with unsteady pressure transducers and laser techniques to assess the rotor-stator interaction by the frequency analysis of the measured signals. The unsteady total pressure P_t distributions showed the wakes of upstream IGV and rotor rows. In addition, the magnitude of the P_t was varied by the superposition of rotor and stator wakes. The frequency analysis of the P_t signal showed that the blade passing frequencies of the upstream and downstream rows were observed, which suggested that both the upstream and downstream rows affect the unsteady kinematics of a certain blade passage flow. The static pressure measurements at the casing were also performed, which showed the variation of the shock intensity by the periodic tip clearance vortex.

Kato et al. [49] calculated unsteady RANS simulations of the entire stage, 1/10 of the pitch of a transonic multistage axial compressor with and without shroud cavity to investigate the effect of labyrinth seal leakage flow on the compressor performance. The cavities were modeled to produce the leakage flow mass flow rate derived from an empirical model to reduce computational costs. The loss generated at the shrouded stator passage was divided and categorized based on the source of the loss. It was found that the inclusion of the cavity into the calculation domain yielded the 1.7% of efficiency drop; the interaction between the leakage flow and the periodic upstream rotor wakes was responsible for the decrease. In addition, it was observed that the ejected leakage flow from the cavity produced hubside blockage, enhanced secondary flow, and the hubside corner separation.

Wellborn [50] further investigated the unsteady kinematics of the upstream and the downstream of a shrouded stator flow at a low-speed four stage axial compressor. A hot-film sensor and a steady pneumatic probe were used to measure the total, static and velocity vector inside the 3rd stator cavities. Numerical simulations were also performed to analyze the cavity flow structures in detail. The meridional measurements of velocity vector showed that recirculations were observed at the upstream cavity due to the labyrinth seal leakage flow, which was similar to the secondary flow structures observed in a shrouded turbine [51]. The labyrinth seal leakage flow first impinged on the upstream rotor disk. After the collision, it migrated radially outward and exited the upstream cavity. The recirculations were varied pitchwise; the location of the recirculation was shifted radially inward (towards the axis), and negative radial velocity was observed near the LE of the stator. The potential effect of the stator LE was responsible for these phenomena; increased static pressure by the stator potential effect created the pitchwise variations. A similar result was obtained by the Kim's [47] numerical calculations. The upstream rotor also affected the upstream cavity flow structure; the pitchwise variation of the ensemble-averaged

velocity components at -5.7% span observed a local ingress behind a rotor TE. For the downstream cavity, the calculation showed that the passage flow experienced sudden expansion, creating the separation inside the cavity. As a result, another recirculation was generated inside the separation region. The passage flow impinged the downstream rotor disk and was sucked into the downstream cavity. In addition, a local egress was observed near the SS of the downstream stator at increased loading condition, which was presumed to be generated by stator secondary flow.

1.3 Motivations and Objectives of the Study

As discussed in the previous sections, the unsteady kinematics of the rotor and stator passage flow have been extensively studied by many researchers [4, 5, 8, 9, 10-20, 22-24, 32-34, 36-38, 49-51]. Unsteady flow structures inside the midspan blade passage have been studied experimentally, numerically and analytically since 1960's, which have found out the negative jet phenomenon by the slip velocity [9], CV, CCV and recirculation between the two different wakes inside the blade passage [11, 13, 22, 23, 34], the wake stretching [8] and the local anisotropic stretching of wake components [24, 36]. At the tip region, a numerical study by Valkov and Tan [37] showed that the tip clearance flow was attenuated by the wake stretching inside a stator passage, similar to the midspan region. In addition to that, the interaction of rotor tip leakage flow and stator wake fluctuated the direction and width of tip clearance flow [14]. Because of these phenomena, the aerodynamic properties of the multistage axial compressors vary timewise.

However, the unsteady kinematics of hubside stator flow is different depending on the stator configurations of the axial compressor due to their different hubside flow structures. Experimental investigation of Swaboda et al. [25], Campobasso et al. [26] and Lange et al. [27] showed that the cantilevered type created the hub clearance through the

hub clearance of cantilevered stator; this hub clearance flow swept away the low momentum fluid near hubside SS, reducing the loss at the region. By the hub leakage vortex, high loss region was generated near the PS of the adjacent stator blade. Numerical research by Montomoli et al. [5] showed that the stator hub clearance flow reoriented the upstream rotor wake more parallel to stator blade, stretching the rotor wake 15% longer than the midspan cases, which can affect the hubside wake stretching phenomenon.

At the shrouded stator configuration, low momentum fluid was concentrated at the hubside SS of stator blade, resulting in wider hubside corner separation compared with cantilevered cases [25-27, 30]. In addition, Wellborn and Okiishi [28, 43], Demargne and Longley [44], Kim [47], Marty and Aupoix [48] experimentally and numerically showed that the labyrinth seal leakage flow widened the hubside corner separation further due to the concentration of labyrinth seal leakage flow at the hubside SS. In addition, experiments at an annular cascade with rotating cylinder rows by Schultz et al. [15, 16] observed the higher fluctuation of velocity components at the periphery of the corner separation. This indicates that the periphery of the hubside corner separation was disturbed by the upstream rotor wake, similar to the boundary layer distortion on the midspan region. However, the wake passing frequency was not detected at the center of corner separation, suggesting that the hubside corner separation blocked the upstream rotor wake. This implies that the attenuation of the wake by the wake stretching inside the blade passage can be affected by the hubside corner separation.

In addition, the effect of hubside corner separation on the unsteady kinematics of hubside shrouded stator passage flow can be altered by the variation of the operating condition. It is well known that as the flow rate decreases, the area covered by the hubside corner separation widens [30]. Not only that, Poensgen and Gallus [17, 18] showed that the velocity disturbances created by the upstream wake were amplified when the operating

condition was changed to near stall. This indicates that the variation of the hubside corner separation can affect the hubside unsteady kinematics of the shrouded stator configuration.

However, no previous researches focused on the effect of the corner separation on the unsteady kinematics of the hubside shrouded stator flow. An experimental investigation by Ernst et al. [20] did measure the unsteady total pressure variation inside the shrouded stator passage, yet they did not deal with the hubside unsteady kinematics. Furthermore, most of the unsteady researches focus on two-dimensional axial-tangential distributions or the variation of aerodynamic properties, which have not dealt with the possible the radial movements created by the interaction between rotor and stator wakes, such as the radial movements as mentioned by Sanders and Fleeter [12]. It is possible that additional radial movements can be generated by the interaction between rotor and stator wakes, especially at the hubside of the shrouded stator where wider corner separation deflected the passage flow [30].

Hence, the primary objective of this research is to experimentally investigate the unsteady kinematics of multistage shrouded axial compressor flow and assess the impact of the hubside corner separation on the hubside unsteady kinematics of shrouded stator flow. Specifically, this study aims to answer the following questions.

I. How does the unsteady kinematics of the multistage shrouded stator passage flow generated by the upstream rotor wake?

II. How does the corner separation of shroud stator affect the behavior of hubside rotor wake inside the hubside stator?

III. How does the corner separation of shrouded stator affect the attenuation of the upstream rotor wake?

IV. Do the radial movements created by the interaction between rotor and stator

wake exist? If so, why do the movements created?

V. How does the variation of the operating conditions affect the unsteady kinematics of the multistage shrouded stator flow?

To answer these questions, experiments have been conducted at a shrouded multistage axial compressor. A low-speed multistage shrouded axial compressor has been designed and built for the experiment. Experiments have been conducted at the 3rd stage of the compressor; unsteady three-dimensional velocity distributions at the upstream and the downstream of the 3rd shrouded stator have been measured using single-element 45° degree slanted hot-wires. Radial and tangential planar unsteady velocity distributions have been acquired to investigate the unsteady kinematics of multistage shrouded axial compressor flow and assess the impact of the hubside corner separation on the unsteady kinematics of hubside shrouded stator flow.

1.4 Thesis Organization

This thesis consists of five following chapters.

Chapter 1 introduces the motivation of the study. Previous researches which have dealt with the unsteady flow kinematics of blade passage flow are discussed. The motivation and the objective of the study are set based on the previous researches.

Chapter 2 presents the renewal process of a low-speed multistage shrouded axial compressor, instrumentations and measuring techniques used in the study. The design concepts, the engineering parameters, the configurations, the instrumentations and the operating parameters of the compressor are presented. The detailed instrumentations of the compressor, the techniques for measuring three-dimensional velocity vector distributions inside the compressor, the uncertainty analysis of the data, and the measuring conditions are followed.

Chapter 3 presents the measurement results. Unsteady flow kinematics upstream and downstream of the 3rd stator flow at designed flow condition are discussed using the timewise variation of the color contour of unsteady three-dimensional velocity components.

Chapter 4 presents the effect of the hubside corner separation on the unsteady kinematics of the shrouded stator flow. The impact of the hubside corner separation on the wake stretching, and the radial movement of the hubside passage flow will be discussed.

Chapter 5 presents the unsteady kinematics of the shrouded stator flow at off-design conditions to assess the impact of the operating condition on the unsteady flow structures.

Chapter 6 and 7 summarize the results of the study. Discussions, conclusions, contributions of the study and the recommended future works are presented.

2. Experimental Configurations

2.1 Overview of Turbomachines for Research Purposes

To improve efficiency, maximize pressure rise and extend the operating range of turbomachines, it is necessary to investigate the detailed flow properties inside turbomachines. Measuring flow properties inside the turbomachines is ideal, but due to the spatial and capital limitations, direct measurements inside the machines are difficult. To elaborate these efforts, previous research adopted experiments on cascades [15-18, 44, 47] or computational fluid dynamics [22-24, 37, 42, 47-49] to investigate the flow structures inside the turbomachines. However, these researches have limitations resulting from the inherently different two-dimensional stationary structure of cascade compared with three-dimensional rotating configurations, and the drawbacks of CFD techniques, which produce inaccurate flow structures [52]. Therefore, measuring flow structures inside the actual multistage rotating machinery is necessary to understand the detailed physical mechanisms.

Various institutions have turbomachines for research purposes to investigate fundamental flow structures inside the passage [53-58]. Their configurations usually have 1) large dimensions (Diameter $\geq$ 1m) to ease the access of the blade passage and 2) low speed to focus on basic flow structures and reduce operating costs. Recently, a transonic configuration is adopted to study transonic flow characteristics [57].

GE LSRC [53] is a low-speed axial compressor for research purposes, imitating the rear stage of axial compressors to focus on the verification of various design configurations. It is composed of four identical stages with IGV, and the shrouded stator configuration with variable rotor and stator stagger angle, large optical access windows for laser and flow visualization techniques. It has radial, circumferential and yaw traversing equipment for sensor movements, and steady and unsteady probes for measurements bet-

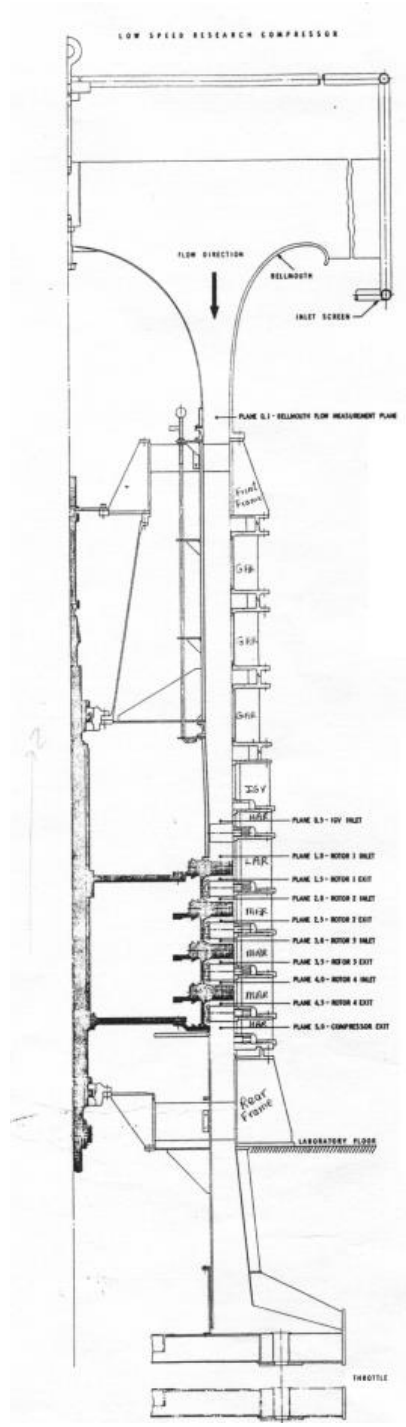

Figure 2.1 Configuration of GE LSRC [53]

ween the rotor and stator, and on the blade surfaces. The diameter of the GE LSRC is 1.542 m (60 inches), and it is vertically aligned open-type compressor with an inlet circular filter, a bellmouth and an ogjve, a compressor section and an outlet throttle. The aim of the compressor is to test various blade configurations such as stagger, aspect ratio, the solidity of blade row, different blade shape.

NASA LSRC [54] is a low-speed axial compressor for research purposes, similar to the configuration of GE LSRC: four identical stages with IGV, shrouded stators with variable rotor and stator stagger angle, large optical access windows for laser and flow visualization techniques, radial, circumferential and yaw traversing equipments for sensor movements, steady and unsteady probes for measurements inside the compressor. The 1.22 m diameter LSRC is an open-type compressor. It is positioned horizontally, and at the inlet of the compressor, a 2.4 m diameter circular filter is installed to prevent foreign object injection. A bellmouth and an ogive are located at the downstream of the filter, followed by a long inlet duct with the length to radius ratio higher than 3, and a compressor section. The mass flow rate is controlled by a downstream throttle section. The NASA LSRC is

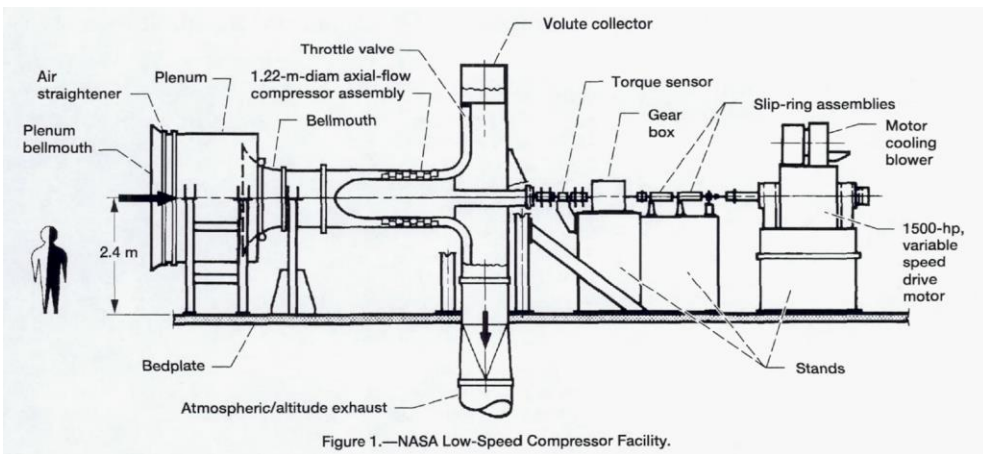

Figure 2.2 Configuration of NASA LSRC [54]

powered by a 1,500 hp (1,103 kW) motor.

Dresden LSRC [55] is a low-speed axial compressor for research purposes, operated by TU Dresden in Germany. This compressor shares similar configuration with GE LSRC and NASA LSRC: four identical stages with IGV, variable rotor, and stator stagger angle, optical access windows for laser and flow visualization techniques, radial, circumferential and yaw traversing equipments for sensor movements, steady and unsteady probes for measurements inside the compressor. The compressor adopted the cantilevered stator configuration. Its primary objective of the study is the unsteady flow kinematics of the blade passage flow, focusing on the rotor-stator interaction by the upstream wake. [4, 13, 14, 27, 32, 33].

LISA (Leakage Interaction in Shrouded Axial) turbine located at ETH Zurich is a closed- loop 2-stage axial turbine designed to investigate the effect of shroud leakage flow on turbine performances and the unsteady kinematics of the turbine flow [56]. A 750 kW power radial compressor drives 800 mm diameter turbine up to maximum 1,500 RPM. A 400 kW generator absorbs the power from the turbine, and a gearbox connects the turbine and the generator. To prevent the rotating parts from the sudden stop, two safety couplings are installed between the rotating parts to prevent the failure of the entire system. Unsteady fast response aerodynamic probes are installed at the turbine to measure unsteady flow field inside the turbine passage.

Darmstadt Transonic Compressor is a 1.5 stage transonic compressor with variable inlet guide vanes, an upstream settling chamber, and optical access windows for laser techniques [57]. The compressor is operated by an 800 kW motor. It is specialized for measurements at rotor tip region and inside a casing treatment passage using laser techniques.

Previous LSRC at Seoul National University [58] follows the configurations of

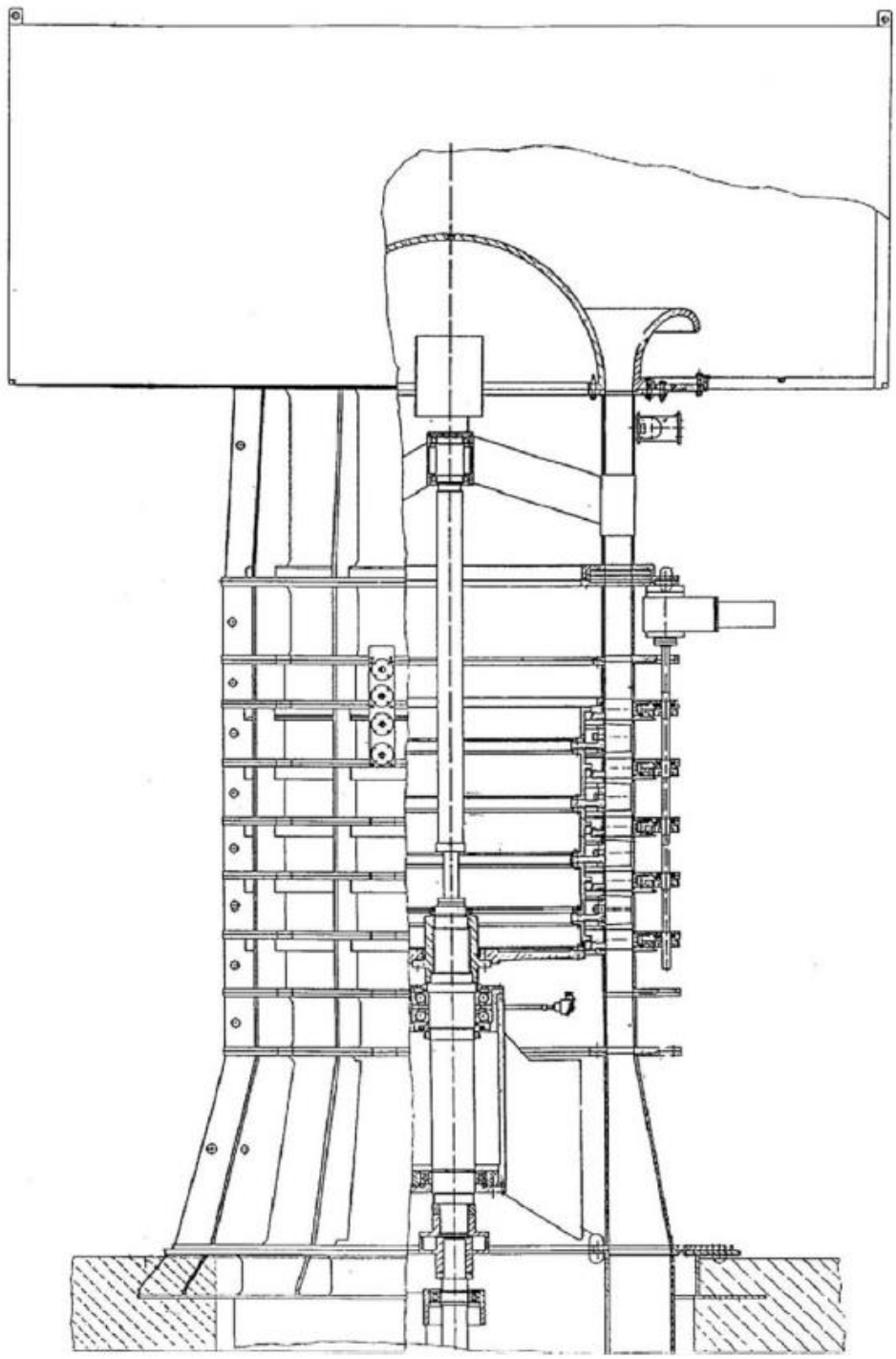

Figure 2.3 Configuration of TU Dresden LSRC [55]

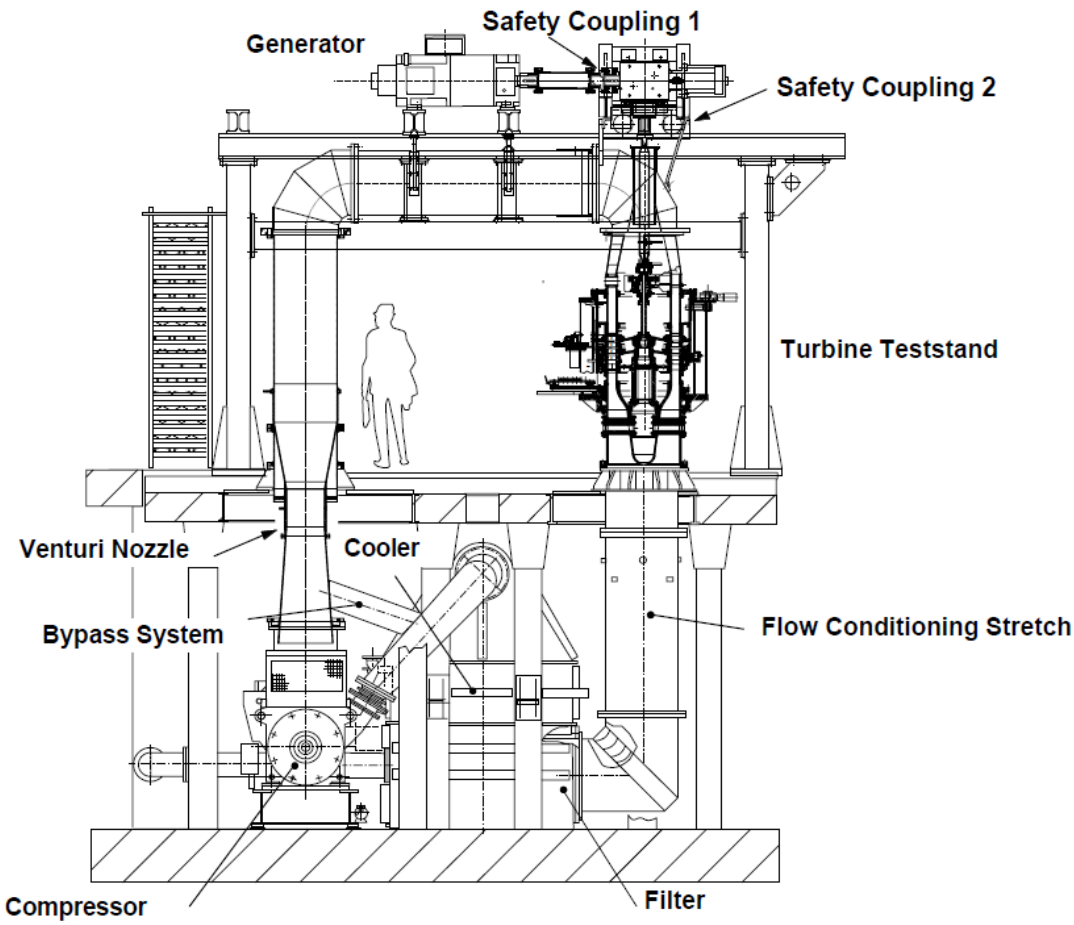

Figure 2.4 Configuration of ETH Zürich LISA Turbine [56]

the GE LSRC: four repeating shrouded configuration stages, an open-type axial compressor with an inlet filter system, operated by a motor with a gearbox between. It is 2/3 reduced configuration of the GE LSRC and equipped with a radial traversing system, optical access windows, steady and unsteady sensors for the operations and stall characteristics. Table 2.1 summarizes turbomachines installed at other institutions for research purposes; compared with the other institutions' equipment, the basic configuration of SNU LSRC is similar to those of other institutions. However, it has low Reynolds num-

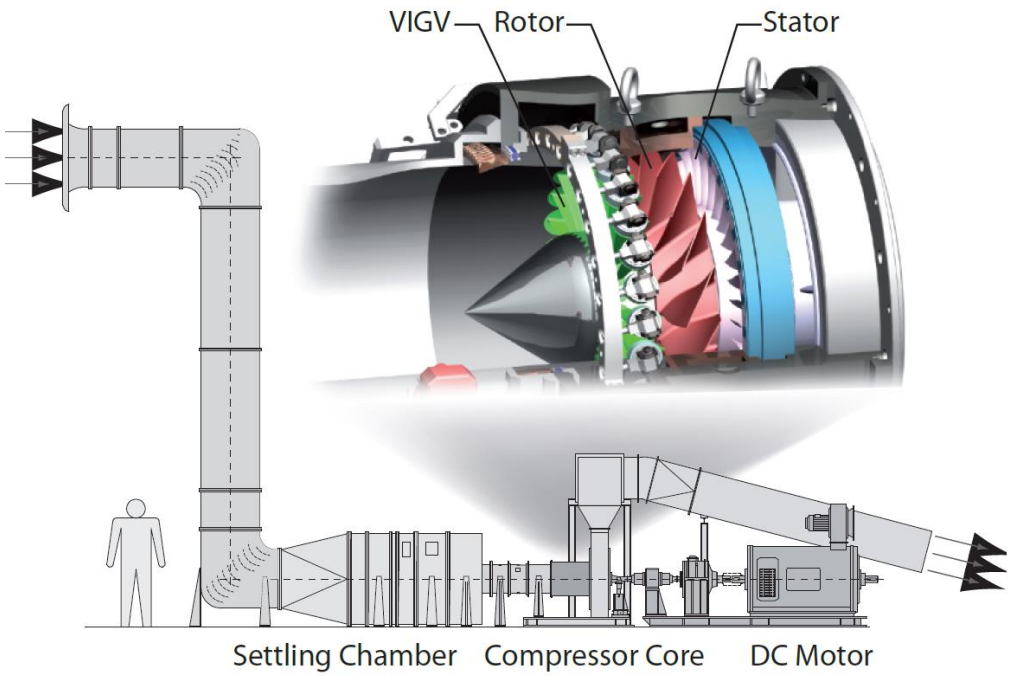

Figure 2.5 Configuration of TU Darmstadt Transonic Compressor [57]

bers and higher tip clearance ratio. Furthermore, its level of mechanical accuracy is low, reducing the compressor efficiency. In addition to this, a manual circumferential traversing and a throttle system are installed. As a result, its operating flexibility, such as measuring configurations or digitalized control, is limited compared with other institution's equipment. Therefore to improve the compressor efficiency, the operating flexibility, and the measuring configurations, a new SNU compressor has been built and tested at Turbomachinery Laboratory of Seoul National University.

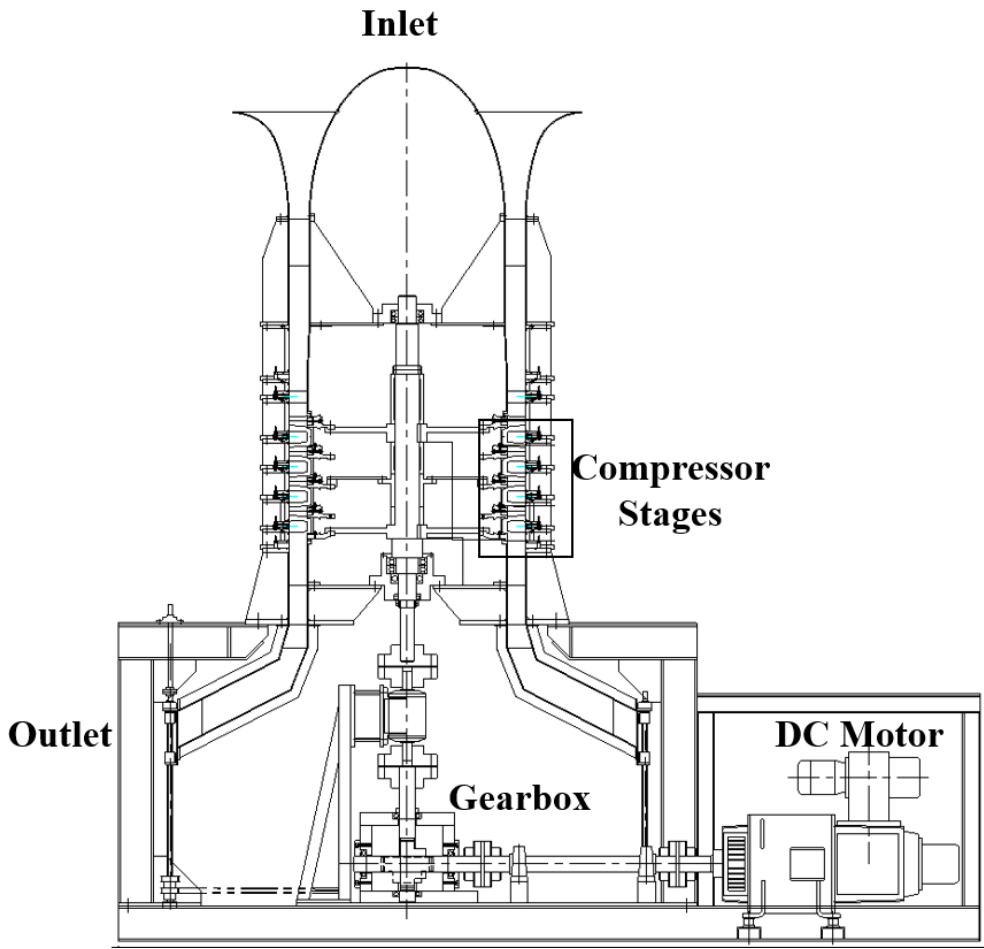

Figure 2.6 Configuration of Previous Seoul National University LSRC [58]

2.2 Design Procedure of SNU Compressor

To design and manufacture a low-speed multistage axial compressor (SNU compressor), the following procedures have been implemented. Figure 2.7 illustrates the design steps of the new SNU compressor. First, design parameters and basic configuration of SNU compressor, such as surface roughness, mechanical tolerance, and balancing grade have been decided. Based on those parameters and configurations, detailed drawings of

Table 2.1 Summary of Turbomachines for Research Purposes

Parameter	SNU [58]	GE [53]	NASA [54]	Dresden [55]	Darmstadt [56]	ETHZ [57]
Re (CU_t/ν)	174,500	360,000	406,667	570,000	N/A	130,000
RPM	800	1,000	980	1,000	20,000	Max 1,500
Diameter (mm)	1,000	1,525	1,220	1,260	N/A	800
$\dot{m}$ (kg/s)	5.00	14.37	12.30	25.35	N/A	Max 12.00
Stage #	4	4	4	4	1	2
Motor Power (kW)	55	308.0	1103.3	500.0	800.0	750.0
T/C (% S)	2.6%	1.36%	1.4%	1.25%	N/A	
Type	Open	Open	Open	Open	Open	Closed
Safety Coupling	N	Y	N/A	N/A	N/A	Y

each part has been drawn using CAD software. In this stage, the selection of powertrain parts (bearings, a gearbox, and a motor), and instrumentations for measuring the operating conditions of the compressor and flow inside the compressor have been selected and considered to implement the system inside the compressor. The structural analysis of each components and assembled parts, the interference between each part have been assessed and analyzed using CAD software and the discussion with the manufacturer. The detailed drawings have been modified according to the analysis. The entire compressor parts have

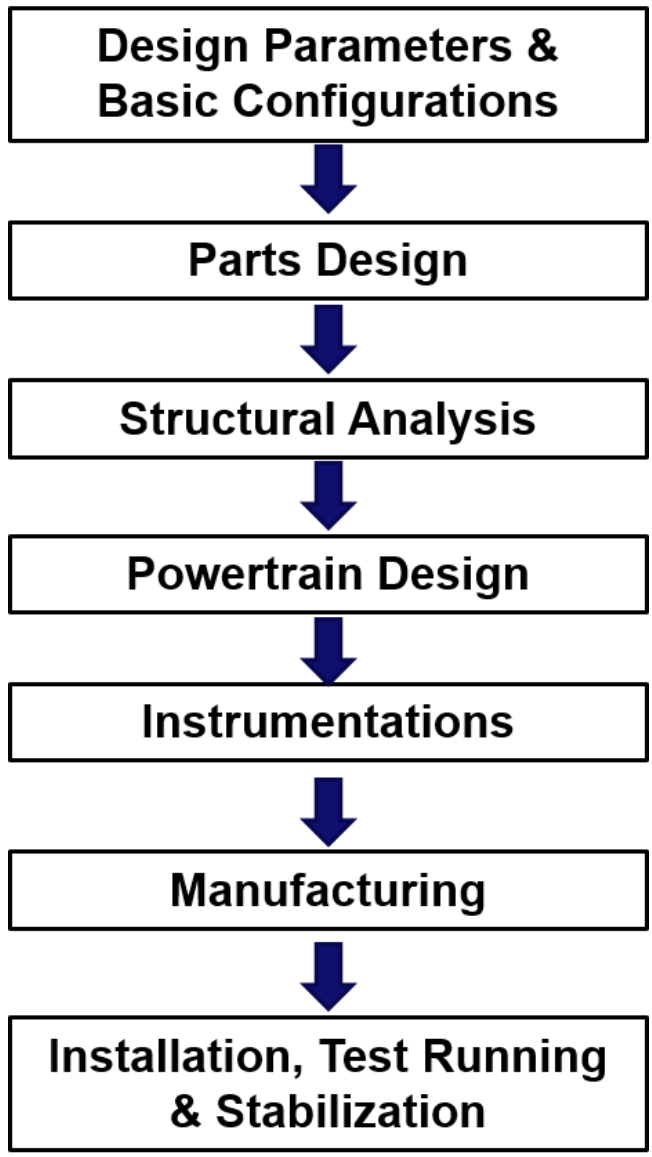

Figure 2.7 Design Procedure of SNU Compressor

been manufactured and supervised by Daehyun Protec located at Guro-gu, Republic of Korea. The compressor has been installed at Turbomachinery Laboratory of Seoul National University, Republic of Korea, and it has been tested for several months to verify

performances, flow qualities and stability of the compressor.

2.2.1 Design Parameters and Basic Configurations of SNU Compressor

Similar to the previous SNU LSRC, GE LSRC, NASA LSRC, and TU Dresden LSRC, the new SNU compressor is an open-type compressor, having four repeating stages including IGV, an inlet filter system with a bellmouth and an ogive. It is powered by a DC motor and a gearbox. The configuration of the SNU compressor is illustrated in Figure 2.8, and the parameters of the SNU Compressor is presented in Table 2.2. To improve the stability, a steel plate having a 30 mm thickness has been placed on the horizontally flattened surface. Eight circumferentially equally spaced, vertically aligned supporting beams have been installed to support the vertically aligned compressor system. At the inlet of the compressor, a circular filter system has been installed to prevent foreign object ingestions. Inside the filter, 24 flow-straightening plates have been installed at the upstream of the bellmouth and the ogive to eliminate inlet swirl. A throttle system has been placed downstream of the compressor section to control mass flow rate. A horizontally aligned 55 kW DC motor powers the compressor, and a gearbox transfers the power to the vertically aligned compressor section. To prevent damage by the mechanical failure of rotating parts, two safety couplings have been installed between each powertrain components.

To improve the dimensional accuracy and the stability of the compressor, three mechanical parameters have been set and controlled during the manufacturing process. The dimensional accuracy of each part has been set according to the level of tip clearances, which is 1.4% of span or 1.05 mm. To obtain the overall tolerance of the compressor, the RMS average of each part's tolerance has been calculated using equation 2.1 [59].

$$T_{sum} = \sqrt{\sum_{i=1}^{n} T_i^2} \tag{2.1}$$

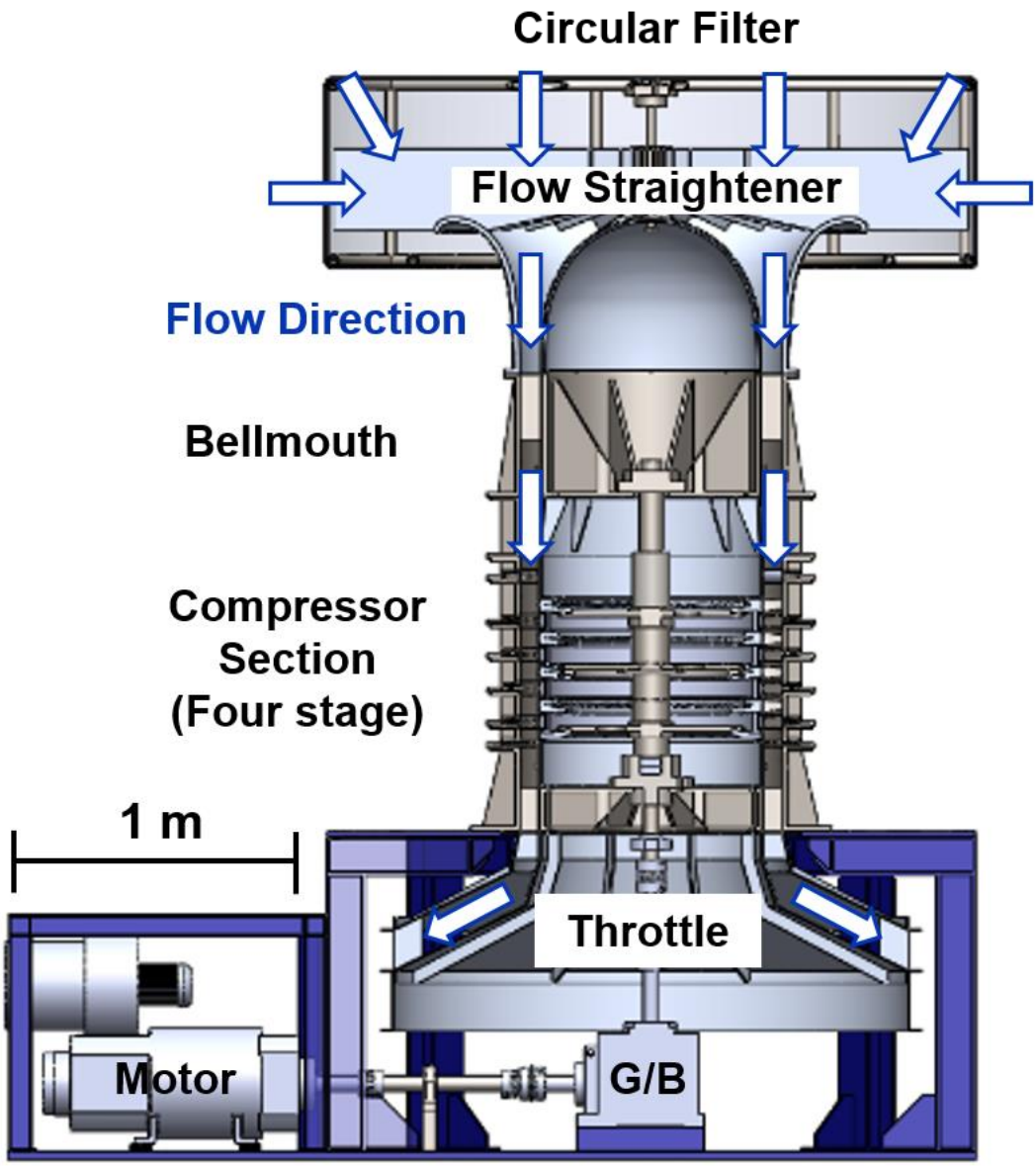

Figure 2.8 Configuration of New SNU Compressor

At the radial direction, four-rotor components (main axis, two rotor disk components, and rotor blades) plus one external casing are related to tip clearances, which

Table 2.2 Parameters of SNU Compressor

Parameters	Numbers
Design Mass Flow Rate	5 kg/s
Diameter	1,000 mm
Hub to Tip Ratio	0.85
Number of Blades (IGV/Rotor/Stator)	53/52/88
Rotor Chord	56 mm
Span	75 mm
Tip claearance (% *S*)	1.40%
Labyrinth Seal Clearance (% *S*)	0.93%
Motor Power	55 kW
Design RPM	1,000
Reynolds Number	195,500
Dimensional Accuracy of each Part	< 0.05 mm
Surface Roughness	< 3.2 μm
ISO 1940-1 Balancing Grade	< G 2.5

results in $\sqrt{5}$ times of individual tolerance T_i. Based on this, the tolerance level of each components for all directions are set to be ± 0.05 mm.

Surface roughness also affects the aerodynamic properties of turbomachines [60]. Increasing the surface roughness thickens blade wake, increases blade profile loss and alters blade loading. Therefore, the surface roughness of the blade, rotating disk, and casing surface must be smooth enough to increase the overall performance. Equations 2.2 ~ 2.5 defines the criteria for determining the smoothness of the blade surface [61]:

$$R_a = \frac{1}{N}\sum_{i=1}^{N}|y_i| \tag{2.2}$$

$$k_s \approx 6.2\, R_a \tag{2.3}$$

$$c_f = \left[2.87 + 1.58\, log\frac{C}{k_s}\right]^{-2.5} \tag{2.4}$$

$$k^+ = Re\frac{k_s}{C}\sqrt{\frac{c_f}{2}} \tag{2.5}$$

The range of roughness number (k+) for the real compressor is between 20 and 150 [62], and the compressor is considered aerodynamically smooth at the k^+ value around 2 [61]. If the target R_a value is 3.2 um, with the rotor chord length of 56 mm and Reynolds number of 195,500, then k^+ is calculated to be 3.46, which can be considered aerodynamically smooth. Therefore, the surface roughness R_a of the components facing the blade passages (rotor and stator blades, casing and rotor disk) has been controlled to be within 3.2 μm.

The grade of the balancing of rotating parts also affects the stability of the compressor; misaligned rotating parts have a center of mass discordance with the rotating axis, creating centrifugal force acting on rotating parts, and increasing the system instability. Therefore, this mass residual must be controlled within certain levels. Equation 2.6 represents the international criteria for determining the grade of balancing [63]:

$$U_{per} = 1{,}000\frac{(e_{res}\dot{\theta})M}{\dot{\theta}} \tag{2.6}$$

According to the ISO 1940-1 criterion [63], the grade of the compressor system is G 2.5, thus the value of $e_{res}\dot{\theta}$ should be less than 2.5.

Based on these designed mechanical parameters, components of SNU compressor have been designed. First, to improve the experimental versatility of SNU compressor, rotor disks and blades have been designed to vary the incidence and the blade solidity, which are illustrated in Figure 2.9. Rotor blades have been designed to have a supporting cylinder with a drilled screw hole for locking bolt, which is located at the center of rotor blades. By doing this rotor blades can be rotated to alter the stagger angle. Horizontally-

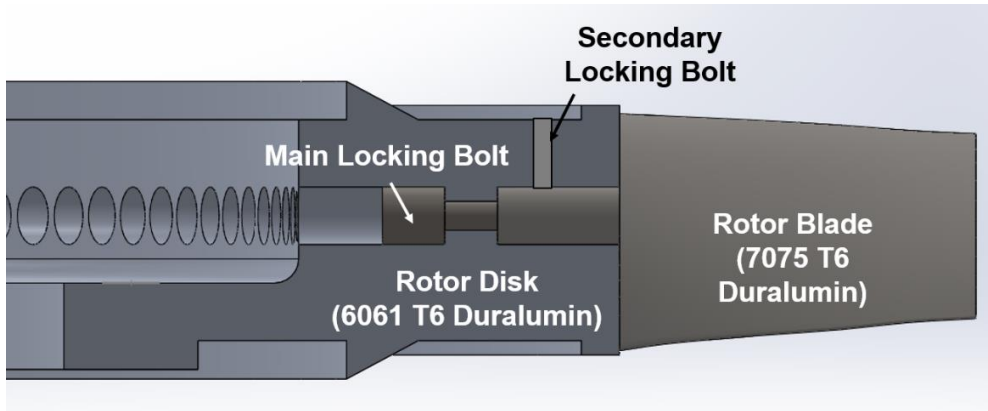

Figure 2.9 Cross-Sectional View of the Designed Rotor Disk and the Rotor Blade

aligned secondary locking bolts have been designed to hold the rotor blade firmly during the operation. Blades have been made of Duralumin 7075 T6, and rotor disks have been made of 6061 T6 to guarantee high mechanical strength with reduced weight. The geometries of rotor, stator, and IGV have been provided by Doosan Heavy Industries & Constructions.

Figure 2.10 shows the structure of the designed compressor section. It has been designed to have four repeating stages with upstream IGVs, the shrouded stator configuration with labyrinth seal structure, and external casings covering the compressor section. External casings have been modified to enable the rotation of stator rows for circumferential traversing, which will be presented in section 2.4.

The geometry of the labyrinth seal and the cavity have been designed to control the mass flow rate of the labyrinth seal leakage flow. Figure 2.11 and 2.12 shows the geometric parameters of labyrinth seal geometry [42, 64]; 1) the number of labyrinth seal teeth N_t, 2) the thickness of labyrinth seal t, 3) the height of the seal h, 4) labyrinth seal gap height c, 5) the axial distance between the seals p, 6) the radius of the gap R_i and

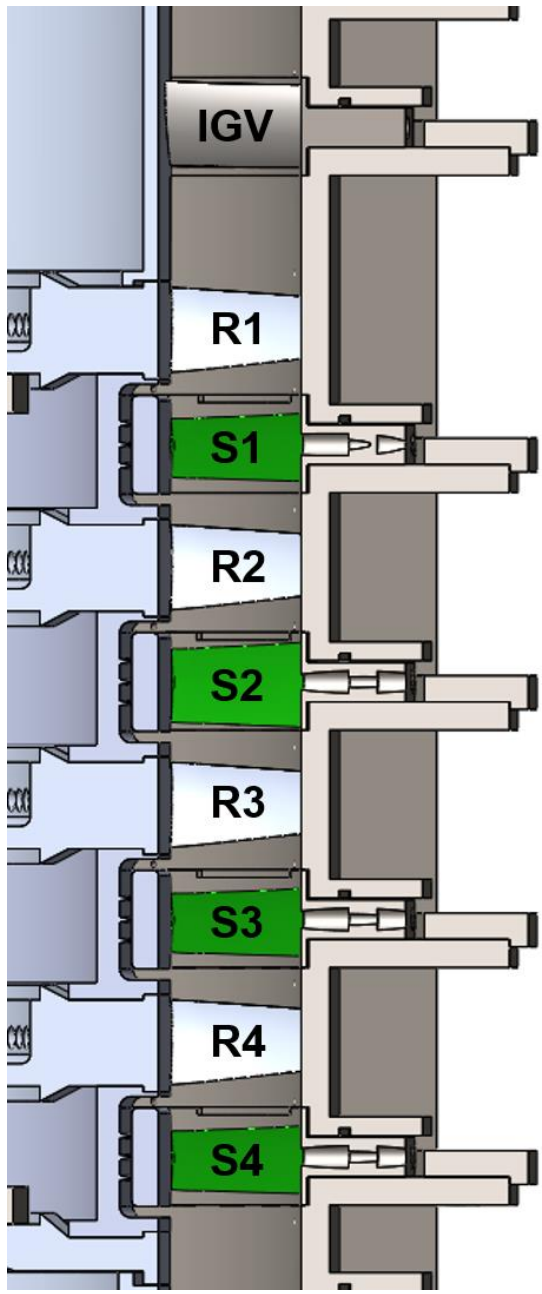

Figure 2.10 Cross-Sectional View of Compressor Stages and Casings

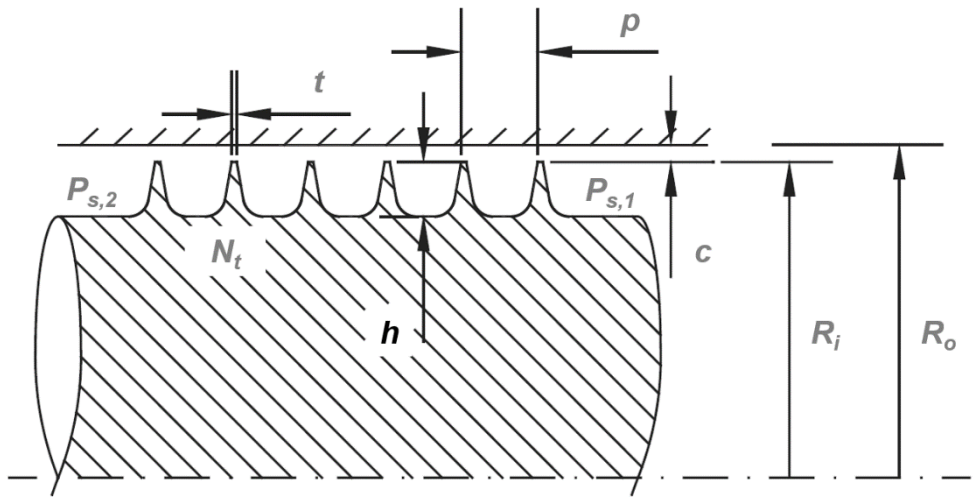

Figure 2.11 Factors Affecting Labyrinth Seal Geometry [64]

R_o, 7) inlet and outlet pressure $P_{s,1}$ and $P_{s,2}$, 8) the shape of the labyrinth seal, 9) the shape of cavity geometries affect the labyrinth seal leakage flow mass flow rate $\dot{m}_{leak}$ of a labyrinth seal. Generally, decreasing c decreases $\dot{m}_{leak}$ and increasing N_t decreases $\dot{m}_{leak}$. However, c is limited by the accumulated mechanical tolerance, and increasing N_t increases the flexibility and the manufacturing costs. Therefore, these parameters have to be decided according to the targe $\dot{m}_{leak}$. It has been decided according to the comparison with other institutions; Table 2.3 summarizes the $\dot{m}_{leak}$ of other experimental apparatuses with shrouded stator configuration. The maximum $\dot{m}_{leak}/\dot{m}$ is 2.50%, and the minimum $\dot{m}_{leak}/\dot{m}$ of axial compressors when the shroud cavity is not blocked ranges between 0.48 ~ 0.52%. Therefore, the target $\dot{m}_{leak}/\dot{m}$ of SNU Compressor has been decided to be less than 0.5%.

Based on the target $\dot{m}_{leak}/\dot{m}$, the detailed labyrinth seal geometries have been designed. Table 2.4 summarizes the *c/S* of other experimental apparatuses; c/S ratio is estimated to be less than 1%. Considering the absolute value of c and accumulated

Table 2.3 List of Leakage Flow Mass Flow Rates of Previous Research

Previous Research	Type	$\dot{m}_{leak}/\dot{m}$ (%)
Heidegger et al. [42]	Axial, CFD	0.60 ~ 2.50
Wellborn and Okiishi [43]	Axial, Experiment	0.00 ~ 1.20
Demargne and Longley [44]	Cascade, Experiment	0.00 ~ 0.90
Kato et al. [49]	Axial, CFD	0.48
Flores and Seume [66]	Axial, CFD	0.00 ~ 0.84

Table 2.4 List of Labyrinth Seal Clearance of Previous Research

Previous Research	Type	c/S (%)
Wisler [53]	Axial, Experiment	0.78
Wasserbauer et al. [54]	Axial, Experiment	0.78
Heidegger et al. [42]	Axial, CFD	3.20
Wellborn and Okiishi [43]	Axial, Experiment	0.25 ~ 1.90
Kato et al. [49]	Axial, CFD	1.00
Flores and Seume [66]	Axial, CFD	1.10

tolerance, the *c/S* of SNU Compressor has been decided to be 0.93%. Trapezoidal shape labyrinth seal teeth have been selected for their structural safety and discharge coefficients [67]. Other parameters, such as the seal height, the seal pitch have been selected according to the proposed scheme of Denecke et al. [65].

According to Heidegger et al [42], 1) decreasing the axial cavity gap from 10% *S* to 8%, *S* resulted in a 2.4% decrease of P_t drop at cavity region, and 2) decreasing seal cavity depth from 60% S to 30% *S* resulted in a 3.7% decrease of $\dot{m}_{leak}$ and a 4.1%

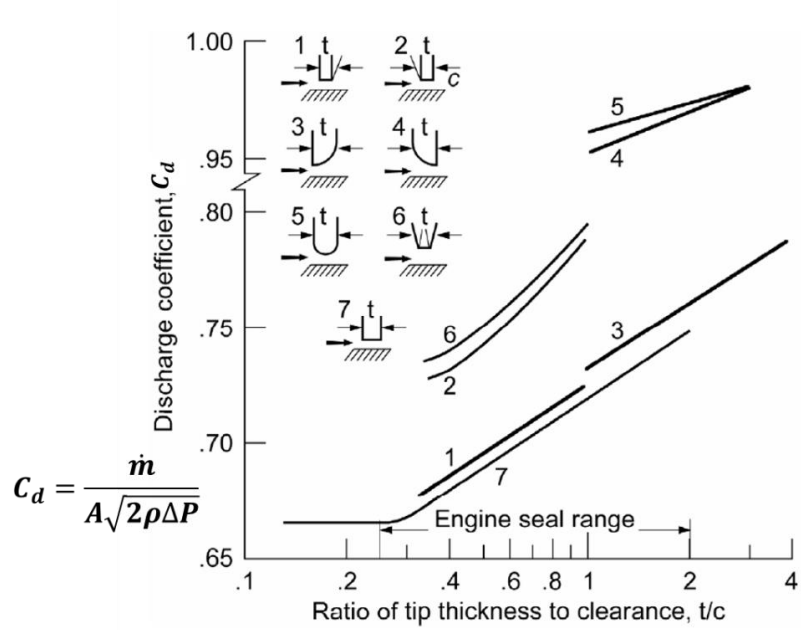

Figure 2.12 Discharge Coefficients versus the Ratio of Tip Thickness to Clearance Ratio of Different Labyrinth Seal Geometries [67]

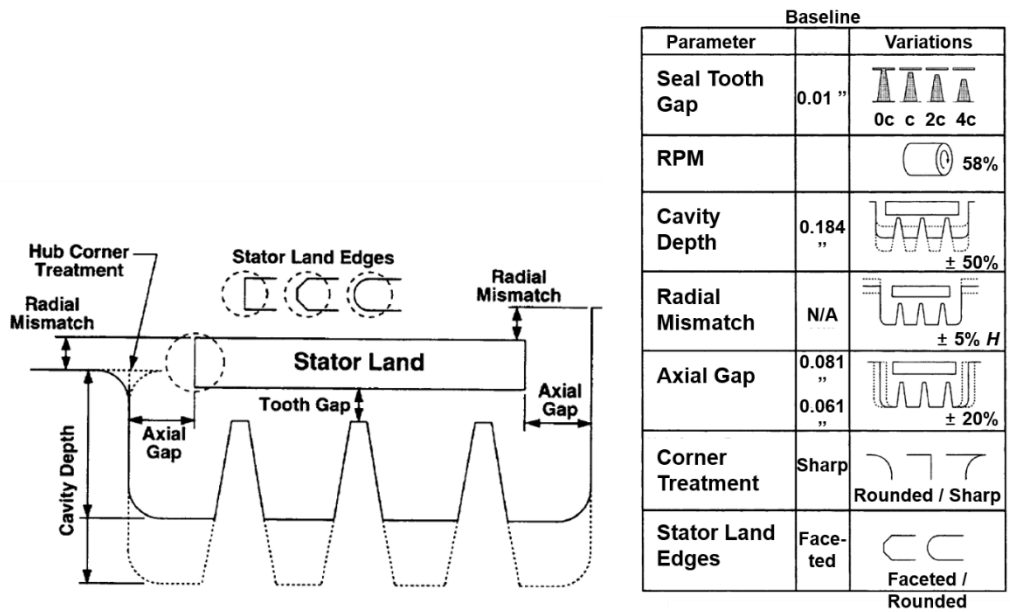

Figure 2.13 Schematic of the Modifications of Labyrinth Seal Cavity Geometry by Heidegger et al. [42]

increase in P_t drop at cavity region. Considering the result of Heidegger et al. [42] and the level of the mechanical tolerances of the SNU compressor, the cavity axial gap and the depth have been selected to be 8.00% S and 27.45% S, respectively. The corner of the shroud and the labyrinth seal passage have been designed to have curvatures to prevent corner separation. For this designed labyrinth seal geometries, $\dot{m}_{leak}/\dot{m}$ has been estimated to be 0.65%, 0.46% and 0.38% for 1, 2 and 3 N_t, using the formula of Childs [64]. Therefore, N_t has been decided to be 3. Figure 2.14 illustrates the geometry of the labyrinth seal and the shroud cavity of the SNU compressor, and Table 2.5 summarizes the geometric parameters of the labyrinth seal and the shroud cavity the SNU compressor.

2.2.2 Designing Parts of SNU Compressor

After the basic configurations of the SNU Compressor have been decided, detailed designs of the part of SNU Compressor have been conducted. Drawings of all components composing SNU Compressor are drawn, as shown in Figure 2.15. The total

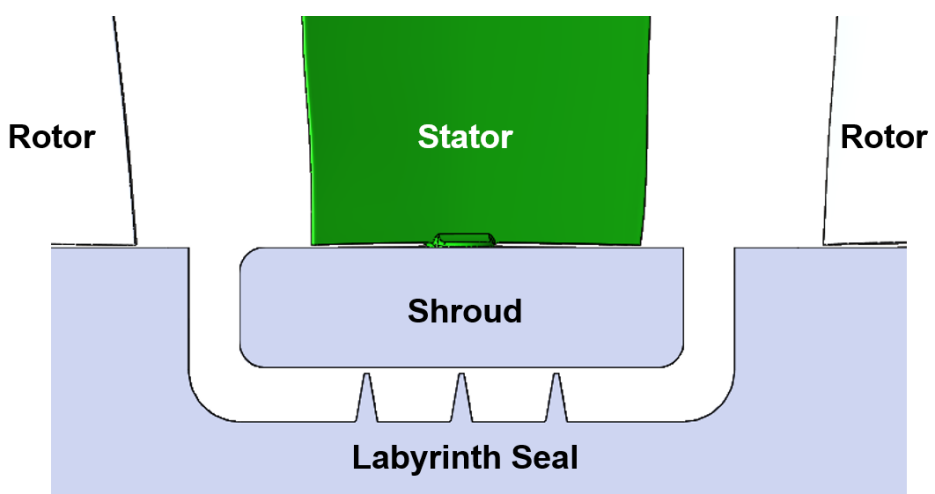

Figure 2.14 Cross-Sectional View of the Designed Labyrinth Seal Geometry

Table 2.5 Geometric Parameters of the Labyrinth Seal and the Cavity of SNU Compressor

Geometric Parameters	Values
c	0.93% S
h	7.47% S
p	14.93% S
R_o	411.00 mm
N_t	3
Cavity Axial Gap	8.00% S
Cavity Depth	27.47% S

weight of the designed compressor is estimated to be 6,359.63 kg: 5,908.30 kg for stationary parts and 451.33 kg for rotating parts. To install, disassemble and re-assemble those heavy compressor parts, two mechanical hoists with 1,000 kg capacity each have been installed at the ceiling of the room where SNU Compressor has been installed.

2.2.3 Structural Analysis of SNU Compressor

To estimate the mechanical safety of the designed compressor components, the structural analyses of the SNU Compressor have been performed using the ANSYS Mechanical. Three calculations have been performed: 1) static load of the entire compressor system, 2) dynamic load of the rotating parts, 3) modal analysis of rotating parts. The assembly of each part has been constructed using the Solidworks. This assembly has been transferred to ANSYS meshing tools; unstructured mesh with fine mesh gridding option has been used. To reduce computational costs, complex geometries such as access

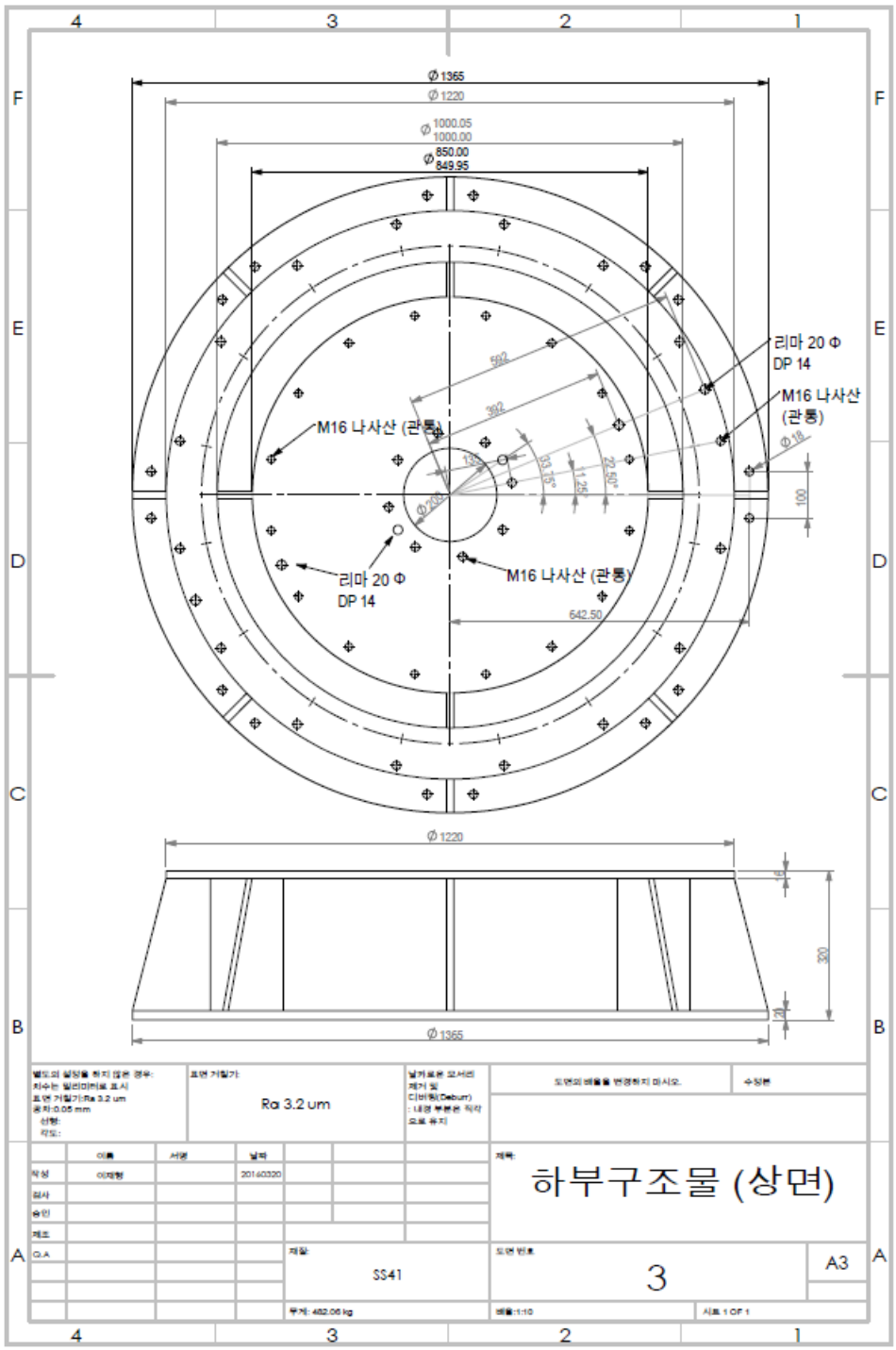

Figure 2.15 Drawing of a Part of SNU Compressor

holes, bellmouth, ogive, and filter system have been simplified.

Figure 2.16 shows the result of the static structural analysis. The dominant deformation component is the axial deformation by the weight of the compressor. Radial and tangential deformation are minimal compared with the axial deformation. The maximum axial deformation is estimated to be -0.06 mm and the maximum von Mises stress is 9.62 MPa. Based on the yield strength of the material (SS41, 240 MPa), the safety factor of static components is calculated to be 25.21.

The structural analyses of rotating parts have been conducted for two different configurations. First, a single rotor disk configuration with real blade geometries has been calculated first to identify the load applied on the rotor and rotor disk components. After that, the calculations of the entire four stages rotating disk parts have been performed to validate the mechanical integrity of the assembled rotating parts. In this configuration, the rotor geometries have been replaced by cylinders with similar weight and span length to reduce computational costs. The entire calculations have been performed at 1,200 RPM, which is higher than the design speed (1,000 RPM). During the calculations, the target object has been set to be stationary for 10 seconds, and accelerating to 1,200 RPM for 190 seconds, and continue to rotate for 10 seconds.

The results of the rotating parts' structural analysis are presented in Figure 2.17. Figure 2.17 (a) and (b) represent those of a single rotor disk, (c) and (d) represent those of the entire rotating disk. The maximum deformation of a single rotor disk is 0.475 mm: 0.391 mm radial, 0.269 mm axial. Equivalent maximum von Mises stress is 48.78 MPa for the rotor disk, 88.18 MPa for the blades. Based on the yield strength of the material (276 MPa for 6061 T6, 503 MPa for 7075 T6), the safety factors of rotating components are calculated to be 5.66 for rotor disk and 5.70 for blades. Higher maximum von Mises stress is observed at rotor blades, and it is located at the corner of the supporting cylinder where

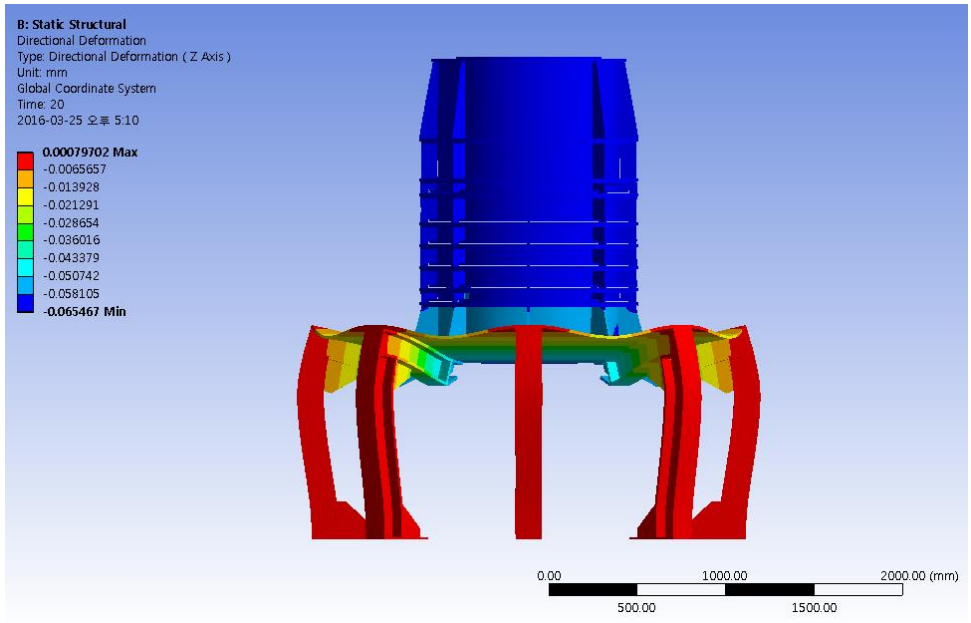

(a) Distribution of Axial Deformation

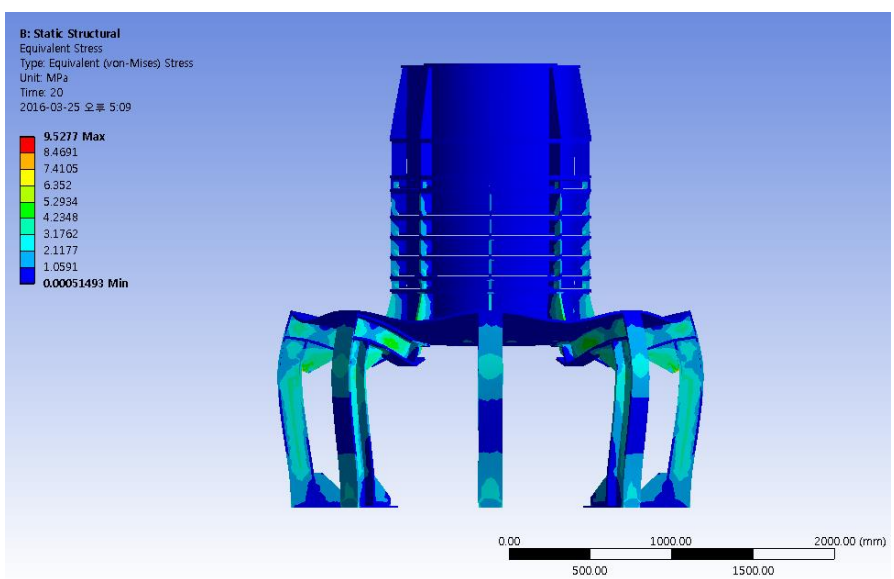

(b) Distribution of von Mises Stress

Figure 2.16 Static Structural Analysis of SNU Compressor

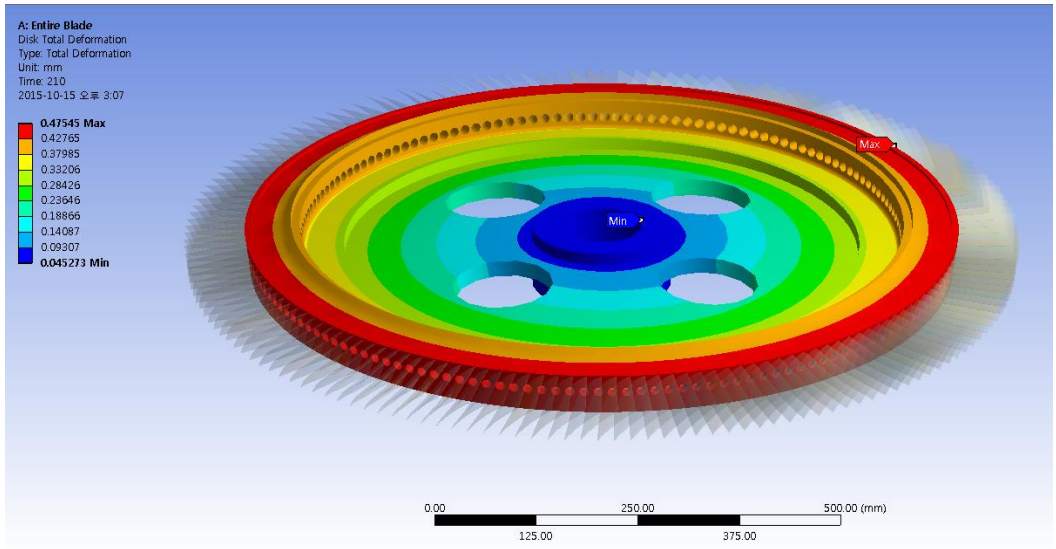

(a) Distribution of Radial Deformation

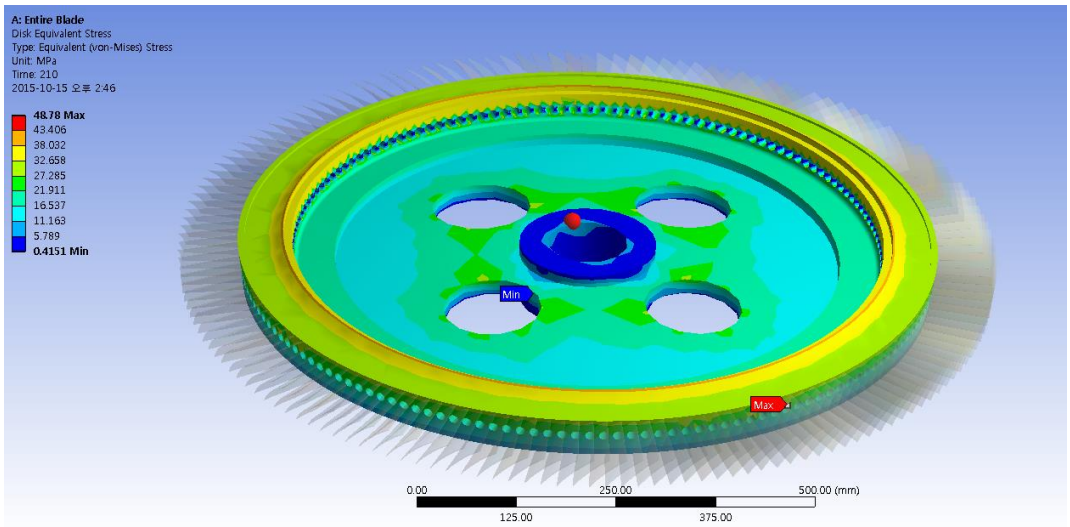

(b) Distribution of von Mises Stress of a Single Rotor Disk

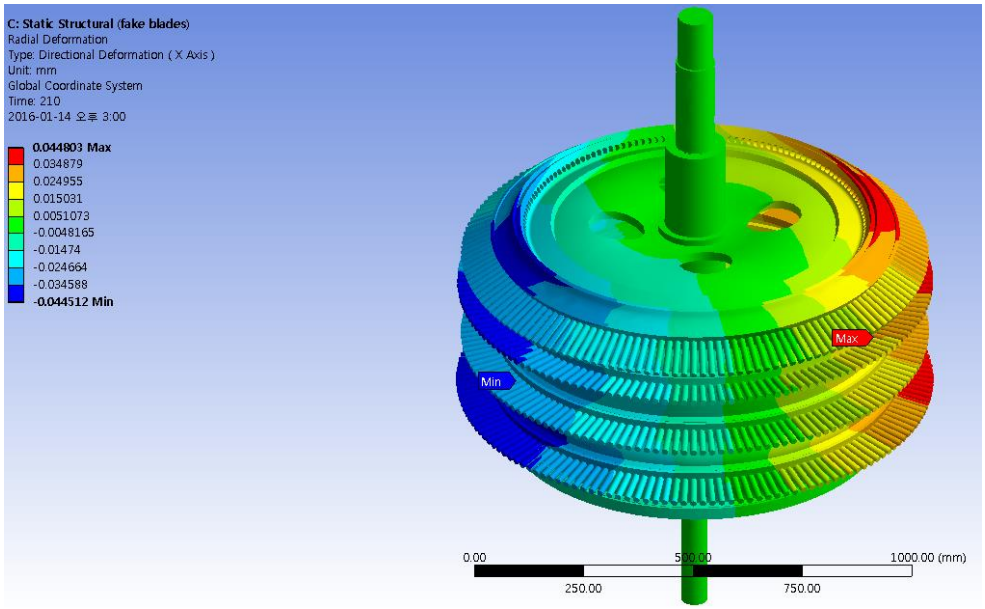

(c) Distribution of Radial Deformation

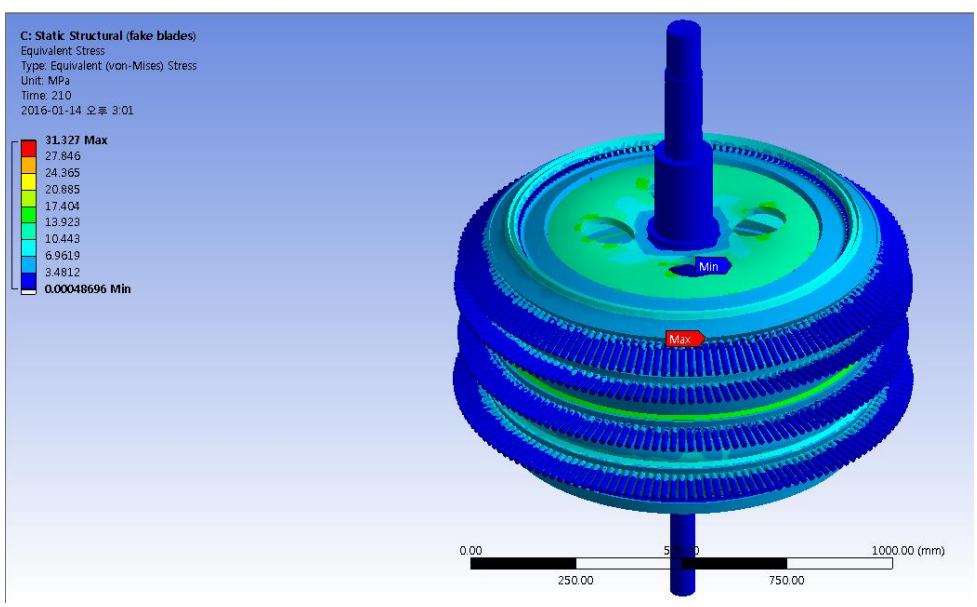

(d) Distribution of von Mises Stress of the Entire Rotating Part

Figure 2.17 Structural Analysis of the Rotating Parts of SNU Compressor

Table 2.6 Estimated Deformation, von Mises Stress and Safety Factor of SNU Compressor During Operation

Parameters	Static	Rotor Disk at 1,200 RPM (Entire)	Blades at 1,200 RPM
Max. Deformation (mm)	-0.06	0.10	0.10
von Mises Stress (MPa)	9.62	31.33	88.18
Safety Factor	25.21	8.81	5.70

the rotor blade and supporting cylinder rod meets perpendicularly. Therefore, a fillet has been applied at the corner to reduce the stress concentration at perpendicular geometries.

For the entire rotating part results, the maximum deformation of rotor disk has diminished to a maximum 0.010 mm: 0.044 mm radial, 0.090 mm axial. Equivalent von Mises stress is 31.33 MPa for the rotor disk. The safety factor of the rotor disk is calculated to be 8.81, which is higher than those of the single rotor disk result. Unlike the single rotor disk, which cannot support rotor disk axially, the combined structures can withstand the axial deformation of the rotor disk, therefore reducing axial and radial deformation.

Table 2.6 summarizes the deformation, von Mises stress, and safety factor of the SNU compressor. All results yield safety factor greater than one, suggesting that the compressor is within the elastic rage even at the increased rotation speed.

The modal analysis of rotating parts has been also performed using the ANSYS Mechanical. The calculation geometry is simplified to reduce computational costs and improve the convergence of calculations, as did in the structural analysis. Figure 2.18

Table 2.7 Estimated Modal Frequencies and Resonance Margin Rates at Each Mode

Modes	Frequency (Hz) / RPM	Resonance Margin Rate
1st	0.88 / 53.14	0.95
2nd	116.36 / 6981.61	5.98
3rd	166.72 / 10003.20	9.00

shows the calculation geometry, and table 2.7 shows the calculation results. The 1st mode is visible at 0.88 Hz (53.14 RPM), 116.36 Hz (6981.61 RPM) and 166.72 Hz (10003.20 RPM) for 2nd and 3rd modes, respectively. It is known that the system is considered to be stable if the resonance margin rate ϵ, shown in equation 2.7, is greater than 0.5.

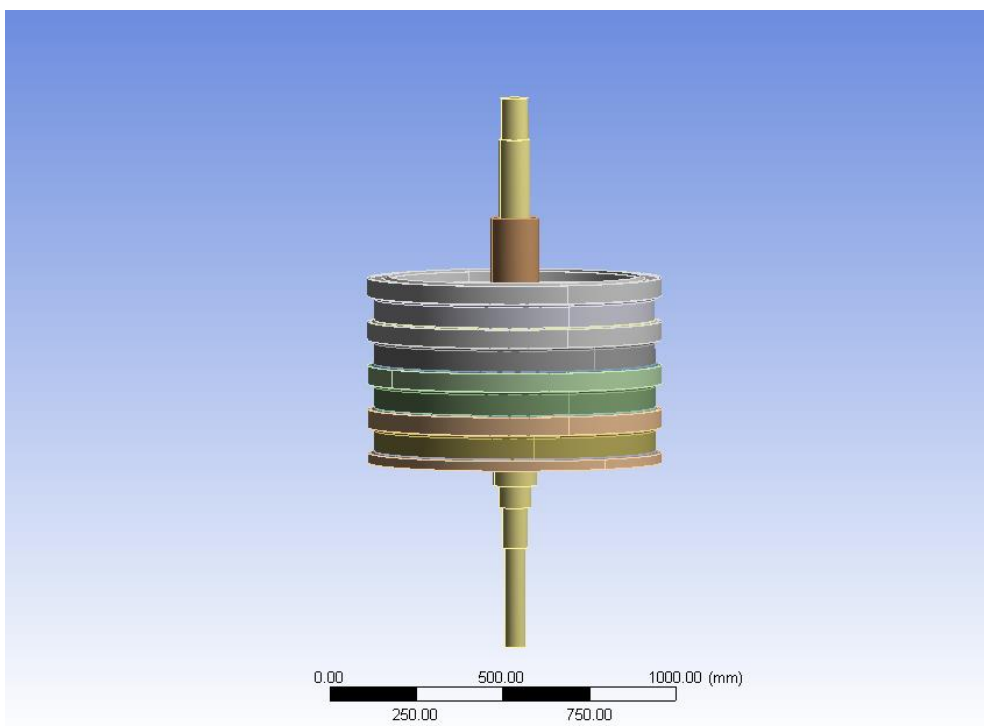

Figure 2.18 Modal Analysis of the Rotating Parts of SNU Compressor

$$\epsilon = \frac{|Rotation\ Speed - Natural\ Frequency|}{Rotation\ Speed} \quad (2.7)$$

All modes have resonance margin rates ϵ higher than 0.5 (0.95, 5.98, 9.00 for 1st, 2nd, 3rd), and are away from the designed operating speed (1,000 RPM). Thus, the designed compressor configuration is expected to be away from the natural frequency of rotating parts during the operation at the designed speed.

Combining the results of the static structural analysis, the rotating part analysis and the modal analysis of the designed compressor configuration, the safety factors of the entire parts except the blades are minimum 5.7, and the resonance margin rates of each mode are greater than 0.95. Therefore, it is expected that the designed compressor configuration is mechanically safe.

2.2.4 Powertrain of SNU Compressor

The powertrain is the set of components that generate and transfer the power required to operate the entire system. Figure 2.19 illustrates the schematic of the powertrain of SNU Compressor; it is composed of 1) a DC motor, which generates power, 2) gearbox that converts the horizontal rotation into the vertical rotation, 3) bearings to hold the rotating parts, and 4) torque limit couplings to transfer the power and protect the other rotational components from the sudden stop.

A 55 kW DC motor (Daedong Precision Machinery, DPFV-SH-H, No. 225B) has been installed horizontally to power the compressor system. The motor originally has been installed for the previous SNU LSRC and has been used for more than 10 years; the motor has been overhauled to replace the inner coils and magnets.

A gearbox (KIM, GD3872K) has been newly manufactured and installed to

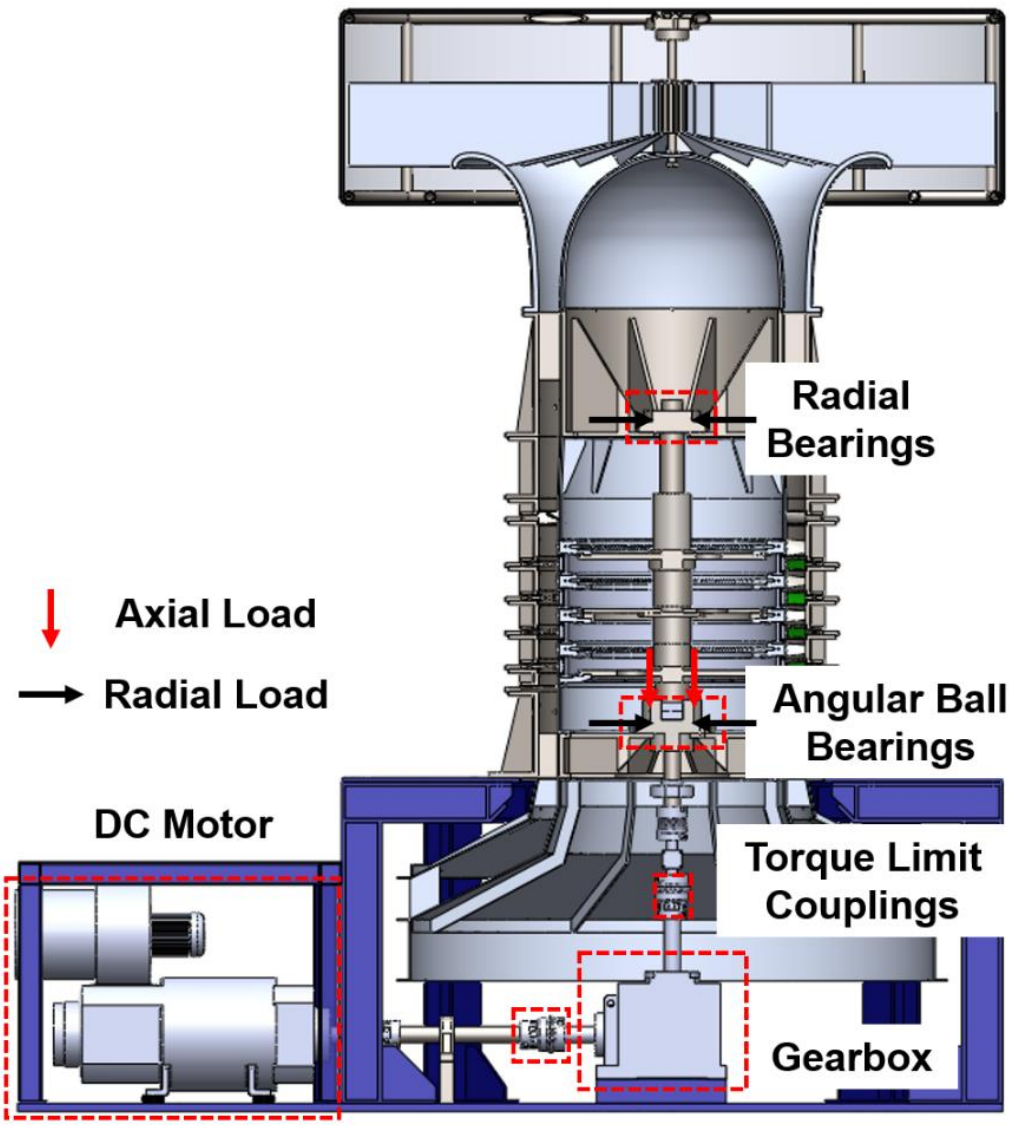

Figure 2.19 Schematic of Powertrain

convert the horizontal rotation of the motor into the vertical rotation. The gearbox is composed of plain gears and bevel gears. This gearbox uses an oil-bath cooling system to

cool down the gearbox, because the rotation velocity of the compressor is relatively low (1,000 RPM). ISO VG # 150-grade lubricant oil is selected as the lubricant.

Two different types of bearings have been selected and installed at the upper and the lower points of the main axis to withstand the rotating part of the compressor and ensure the durability of the powertrain. For the upper side, only radial loading is applied to the bearings. Therefore, two common radial type bearings (NTN, 6216) have been installed. For the lower side, both radial and axial loading are applied at bearings due to the weight of the rotation part of the compressor. Therefore, two angular ball type bearings (NTN, 7219 C) which can withstand both radial and axial loadings have been installed. The expected operating times of each bearing are 1.93×10^{9} hours, 4.93×10^{5} hours for the radial bearings and the angular ball bearings, respectively. The detailed procedures of selecting bearings are presented in Appendix A.

To prevent the rotating components from the sudden stop, two torque-limiting couplings have been installed between the DC motor and the gearbox, and between the gearbox and the compressor rotating parts. When the torque exceeding the limit of the couplings is applied on the couplings, the couplings disengage the mechanical connections between the rotating parts; the undamaged parts can continue their rotation with the remaining inertia. The torque limit of the couplings is set to the maximum capacity of the installed torquemeter, which is 500 N·m.

2.2.5 Manufacturing of the SNU Compressor

The manufacturing of the SNU compressor has been performed at Daehyun Protec, located at Guro-gu, Seoul, Republic of Korea. The entire components have been first machined by a lathe and finished by a 3-axis milling machine to achieve ± 0.05 mm

tolerance. SS41 (KS standard) structural steel has been used as the material for casings and internal rotor disks, and SCM1 (KS standard) Chromium-Molybdenum steel has been used for the main axis. To prevent rust, all steel components have been anodized with Nickel. The entire blades (rotor, stator, and IGV) have been manufactured by a 3-axis milling machine, using 7075-T6 Duralumin. The basement structures (base plate, supporting pillars, and cover plates) have been powder coated to prevent lust.

2.2.6 Installation, Test Running and Stabilization of SNU Compressor

After the manufacturing, the entire components have been examined to check their mechanical tolerances and surface roughness. The rotating parts have been assembled and tested at Daehyun Balancing, located at Guro-gu, Seoul, Republic of Korea, to check the balancing grade. The initial residual mass unbalance of the rotating parts is 29.90 g for the upper side (upstream), and 17.56 g for the lower side (downstream). The maximum residual unbalance is 47.46 g, which yields U_{res} of 20,170.5 g·mm and G 4.68. This value is higher than the ISO 1940-1 standard [63]; the standard requires that the level of the balancing of gas turbines should be less than G 2.5. Therefore to reduce the residual mass unbalance, the highest (upstream 1st rotor disk) and the lowest (downstream 5th rotor disk) surface of the rotating parts have been drilled to reduce the mass unbalance. The radius of balancing is ~ 350 mm. After the balancing procedure, the residual mass has been reduced to 0.40 g (upstream) and 0.77 g (downstream), which yielded the maximum residual mass of 1.17 g, U_{res} of 497.25 g·mm and G 0.12, satisfying the criteria G 2.5.

Using the hoists, the SNU compressor has been assembled at Turbomachinery Laboratory of Seoul National University. It has been tested for several months of stabilization, including the modification of design anomalies.

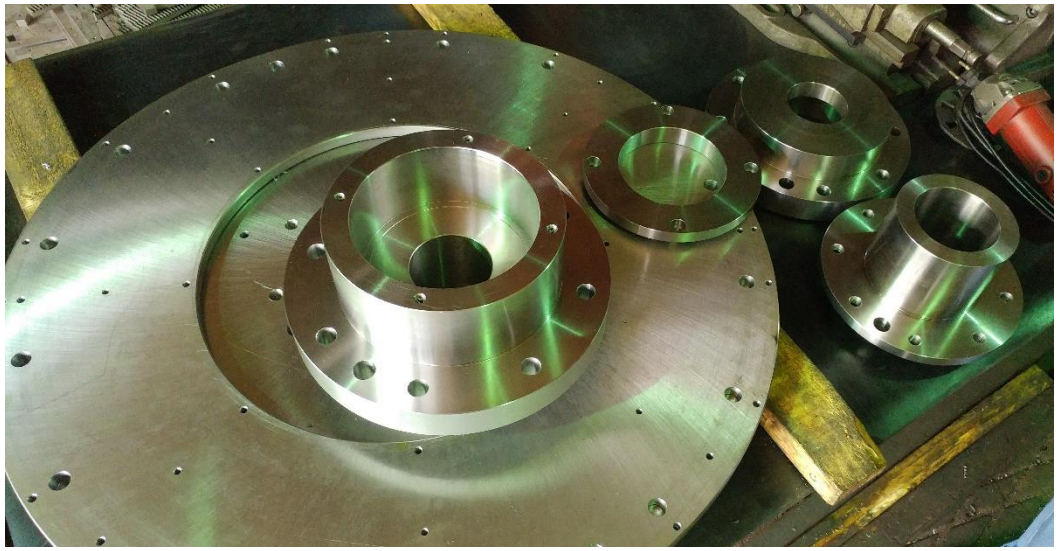

(a) Lathe-Machined Components Before Coating

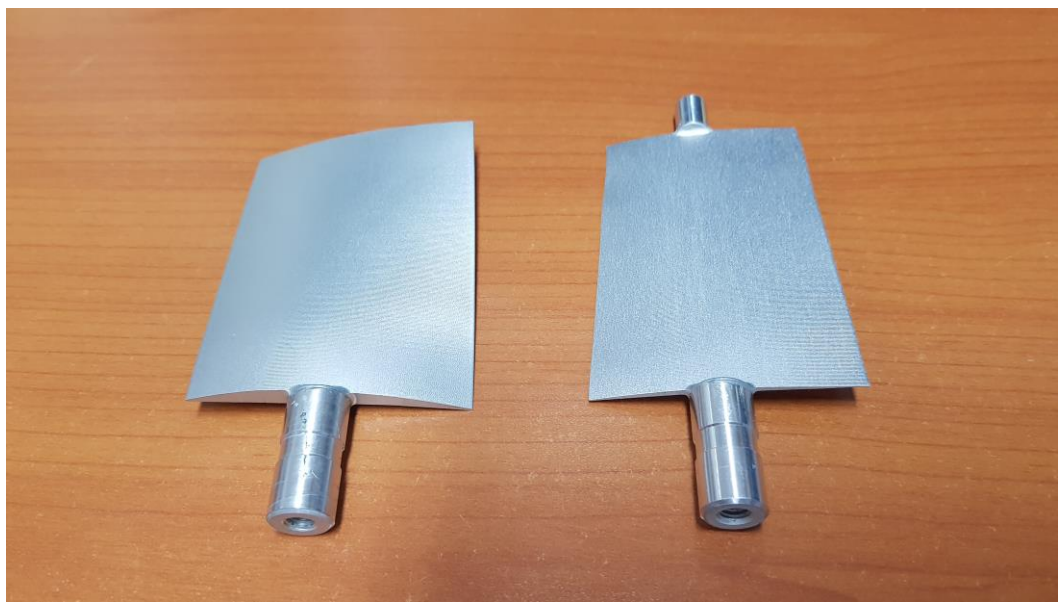

(b) 3-Axis Machined Rotor and Stator Blades

Figure 2.20 Picture of the Parts of SNU Compressor

Figure 2.21 Picture of Compressor Rotating Parts Installed at a Balancing Machine

2.3 Instrumentations of SNU Compressor

2.3.1 Variables, Parameters, and Sensors for Measuring Operating Conditions

To operate a compressor, operating conditions must be decided according to the measurements by the instruments. Table 2.8 illustrates the variables and parameters which define the operating condition of a compressor; flow coefficient (ϕ), a non-dimensionalized parameter representing the compressor mass flow rate, pressure coefficient (ψ), which is a non-dimensionalized parameter of the compressor pressure rise, isentropic efficiency (η), the ratio of input energy and the energy increase of the fluid passing a compressor, and RPM, the rotation speed of a compressor.

$$\phi = \frac{C_x}{U_{tip}} \tag{2.8}$$

$$\psi = \frac{P_{s,out} - P_{t,in}}{1/2\rho U_t^2} \tag{2.9}$$

$$\eta = \frac{\Delta H}{\tau\dot{\theta}} = \frac{\dot{m}c_p T_{t,in}\left\{\left(\frac{P_{t,out}}{P_{t,in}}\right)^{\frac{\gamma-1}{\gamma}} - 1\right\}}{\tau\dot{\theta}} \tag{2.10}$$

To measure these variables, $\dot{m}$, C_x (inlet axial velocity) and $\dot{\theta}$ are needed for ϕ, pressure difference (ΔP), density (ρ) and rotation speed ($\dot{\theta}$) are needed for ψ, inlet and outlet total pressure ($P_{t,in}$, $P_{t,out}$), $\dot{\theta}$, $\dot{m}$, inlet total temperature ($T_{t,in}$) and torque (τ) are needed for η.

For the SNU compressor, the inlet P_{atm} and T_{atm} vary because the compressor is an open-type. The variation of these parameters alter the actual mass flow rate at a fixed throttle position. To compensate the effect, the rotation speed *N* and the mass flow rate $\dot{m}$ are corrected at the equivalent values at the standard P_{atm} and T_{atm} (101.3 kPa, 15 °C), using the method of Cumpsty [2], which is shown in equations 2.11 and 2.22.

$$N_c = \frac{N}{\sqrt{T_{atm}/T_{ref}}} \tag{2.11}$$

$$\dot{m}_c = \dot{m}\frac{P_{ref}}{P_{atm}}\sqrt{\frac{T_{atm}}{T_{ref}}} \tag{2.12}$$

Furthermore, the humidity of the air varies these parameters. To compensate for the humidity effect, N and $\dot{m}$ are again corrected using the method of Bernadier et al. [68], which is shown in equations 2.13 ~ 2.16.

$$N_c^* = CF_n N_c \tag{2.13}$$

$$\dot{m}_c^* = CF_{\dot{m}}\dot{m}_c \tag{2.14}$$

$$CF_n = 0.6131AH + 0.9996 \tag{2.15}$$

$$CF_{\dot{m}} = 0.2521AH + 1.0000 \tag{2.16}$$

Figure 2.22 illustrates the measuring location of the parameters. First of all, an external barometer has been installed in the room where the SNU compressor is located. This device measures the atmospheric pressure (P_{atm}), temperature (T_{atm}) and relative humidity (RH). Next, $P_{t,in}, P_{s,in}$, $T_{t,in}$ and $\dot{m}$ are measured; $P_{t,in}$ and $P_{s,in}$ are measured by an upstream Pitot probe (United Sensor, PAA-8-KL). $T_{t,in}$ is measured by a RTD sensor with a signal conditioner (Omega Engineering, P-L series). $\dot{m}$ is calculated with the pressure difference between the upstream and the downstream of a calibrated bellmouth (see Appendix B for bellmouth calibration procedures and results) using a differential pressure transducer (MKS, 220DD, 10 torr full-scale). Sixteen static pressure taps with equal circumferential distance have been installed at the upstream and the downstream of each stages to measure the average stage pressure rise. A multi-channel gauge-type pressure transducer (Measurement Specialities, Netscanner 9116, 2.5 kPa full-scale) measures the pressure rise. A Kiel probe (United Sensors, KAA-8) and static pressure taps have been installed at the compressor outlet to measure the outlet total and

static pressure ($P_{t,out}$, $P_{s,out}$). An encoder (Baumer, HOG14) and a torquemeter (Unipulse, UTMII-500NM, 500 N·m full-scale) have been installed at the lower part of the main axis to measure the circumferential position of the rotor blades and τ. Another encoder (Baumer, EIL 580) has been installed at the DC motor to measure the $\dot{\theta}$.

To measure the vibration of the compressor, two accelerometers (PCB®, 352C34) have been installed on the lateral of the lower bearing housing, which is perpendicular to the main axis. These sensors have been connected to a DAQ board (National Instruments, PCI-4472), which has been installed at the motherboard of the control PC. A control box has been produced by Samduk Engineering, Sungnam, Republic of Korea to control the compressor $\dot{\theta}$, using the signal from EIL 580 encoder attached on the motor. This box has been connected to the control PC to enable the remote control of the entire compressor system. The detailed configuration of the sensor system of the SNU Compressor is illustrated in Figure 2.23, and the accuracies of the sensors are listed at Table 2.9.

2.3.2 Uncertainty of Operating Variables

The parameters constituting the operating variables have their own accuracies, affecting the total uncertainties of the measured variables. The following method has been used to calculate the uncertainties of each operating variables [69], which is shown in Equation 2.17.

$$u_{X_i} = \sqrt{b_{X_i}^2 + s_{X_i}^2} \tag{2.17}$$

$$\left(\frac{u_{r,95}}{r}\right)^2 = \sum_{i=1}^{N} \left(\frac{X_i}{r}\frac{\partial r}{\partial X_i}\right)^2 \left(\frac{u_{X_i}}{X_i}\right)^2 \tag{2.18}$$

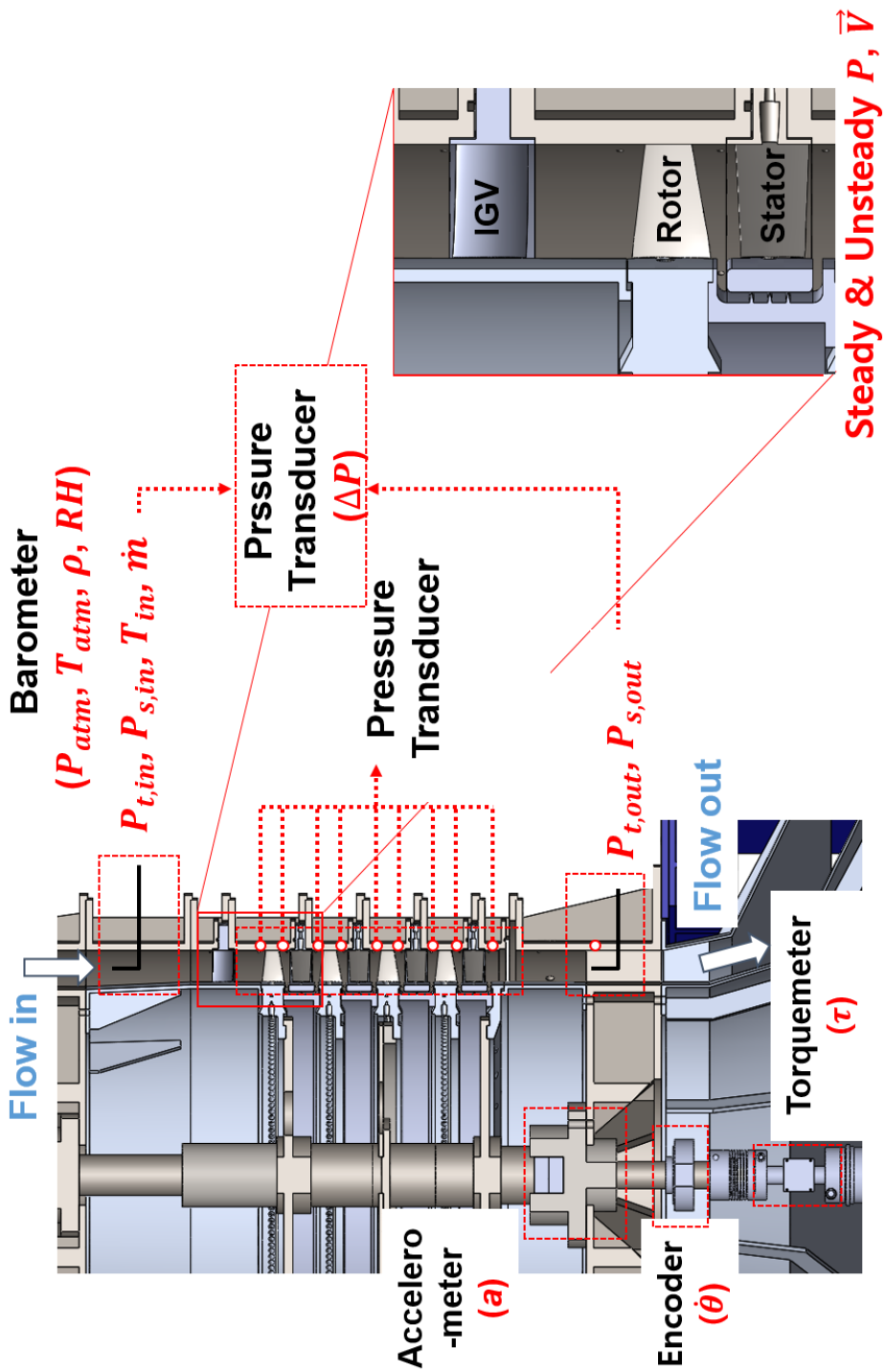

Figure 2.22 Schematic of Sensors Installed at SNU Compressor

Table 2.8 Variables and Parameters for the Operation

Variables	Definitions	Parameters Needed	
Flow Coefficient (ϕ)	$\frac{C_x}{U_t}$	$\dot{m}$	Mass Flow Rate
		$\dot{\theta}$	Rotation Speed
Pressure Coefficient (ψ)	$\frac{P_{s,out} - P_{t,in}}{1/2\rho U_t^2}$	ΔP	Pressure Difference
		ρ $(\frac{RT_{t,in}}{P_{t,in}})$	Density
		$\dot{\theta}$	Rotation Speed
Isentropic Efficiency (η)	$\frac{\Delta h}{\tau\dot{\theta}} = \frac{\dot{m}C_p T_{t,in}\left\{\left(\frac{P_{t,out}}{P_{t,in}}\right)^{\frac{\gamma-1}{\gamma}} - 1\right\}}{\tau\dot{\theta}}$	$P_{t,in}$	Inlet Total P
		$P_{t,out}$	Outlet Total P
		$\dot{\theta}$	Rotation Speed
		$\dot{m}$	Mass Flow Rate
		$T_{t,in}$	Inlet Temperature
		τ	Torque
RPM	rev/min	$\dot{\theta}$	Rotation Speed

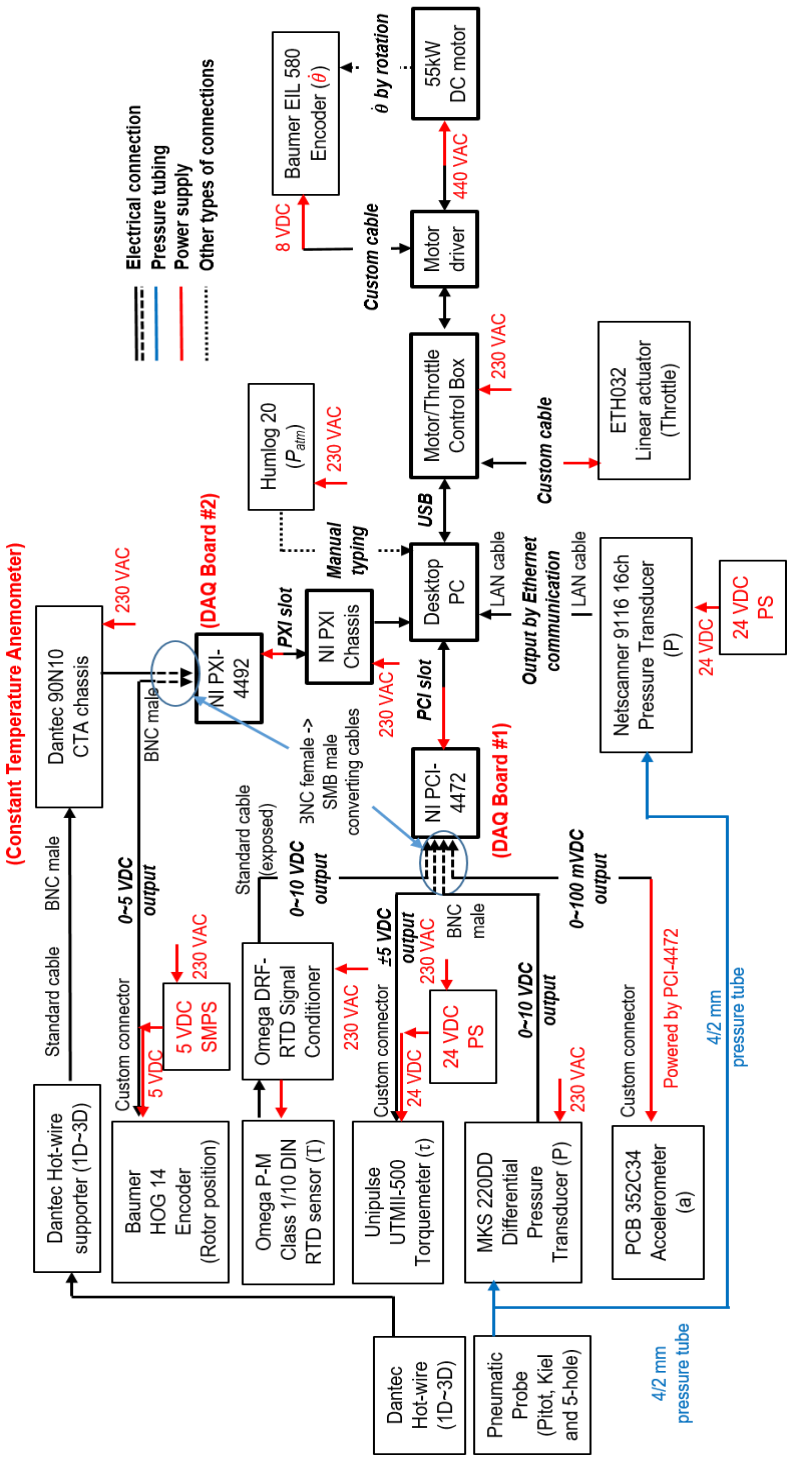

Figure 2.23 Schematic of the Detailed Sensor Configurations of SNU Compressor

Table 2.9 List of Sensors and Accuracies of each Parameter

Parameters	Sensors	Company	Accuracy
P_{atm}	Humlog 20	E+E Electronik	± 0.05 kPa
RH			± 2% RH
$T_{t,in}$	Class 1/10 R-M RTD	Omega Engineering	± 0.3 °C
$\dot{\theta}$	EIL 580	Baumer	± 0.2%
$\dot{m}$	Calibrated Bellmouth		± 0.70%
ΔP	220DD	MKS	± 0.15% Measured
P_s, P_t	Netscanner 9116	Measurement Spescial…..	± 3.75 Pa
τ	UTMII-500NM	Unipulse	± 0.15 N·m

Table 2.10 Uncertainties of Operating Variables

Variables	Uncertainties
ϕ	0.89%
ψ	0.44%
η	0.92%
$\dot{\theta}$	0.20%

Using the method [69], the uncertainties of each operating parameters are calculated to be the maximum 0.89% of $\dot{m}$, 0.91% of ϕ, 0.44% of ψ and 0.92% of η, which 95% confidence level.

2.3.3 Actuators and Traversing Systems of SNU Compressor

To maintain the operating conditions, and to measure the aerodynamic properties inside of the SNU compressor, instrumentations have been installed. Figure 2.24 shows one of four linear actuators which have been installed at the compressor throttle to control $\dot{m}$ and ϕ by varying the throttle opened area. These actuators are remote controlled by a software installed at the control PC. The accuracy of the linear actuator is $\pm$ 0.03 mm, which is expected to control the ϕ within the order of 0.001.

To measure the aerodynamic properties inside the compressor, the proper positioning of measuring sensors is necessary. Therefore, radial and circumferential traversing systems have been designed and installed at the compressor. Figure 2.25 and 2.26 display the picture of the actual radial and circumferential traversing systems; the radial traversing system is composed of three linear traverses (Velmex, Bislide) with an accuracy of 0.0762 mm (0.003") over the entire span (> 300 mm). These are aligned axial, radial and tangential to the SNU compressor, respectively to align the sensor at the exact cartesian coordinates. A rotary table has been installed at the radial traversing system to control the sensor yaw angle with an accuracy of 100 arc-second (1/36 degree). This radial traverse system can be installed at each stage including the IGV row.

In order to traverse the sensor circumferentially, the entire stator rows including the IGV are rotated to change the relative position between the stators and the stationary sensors. Each stator rows are connected to a supporting gear (gear A) with a radius larger than the compressor casings. To rotate the gear A, another five circular gears (gear B) are attached to a single shaft and connected to the gear A. At the bottom of the shaft, another gear (gear C) is connected to the gear D, which is attached at the axis of a step motor (Autonics, A200K-G599-GB10); Figure 2.26 shows the actual picture of the circumferential traversing system, including the gears. A controller (Autonics, PMC-

Figure 2.24 Linear Actuator Installed at the Throttle of SNU Compressor

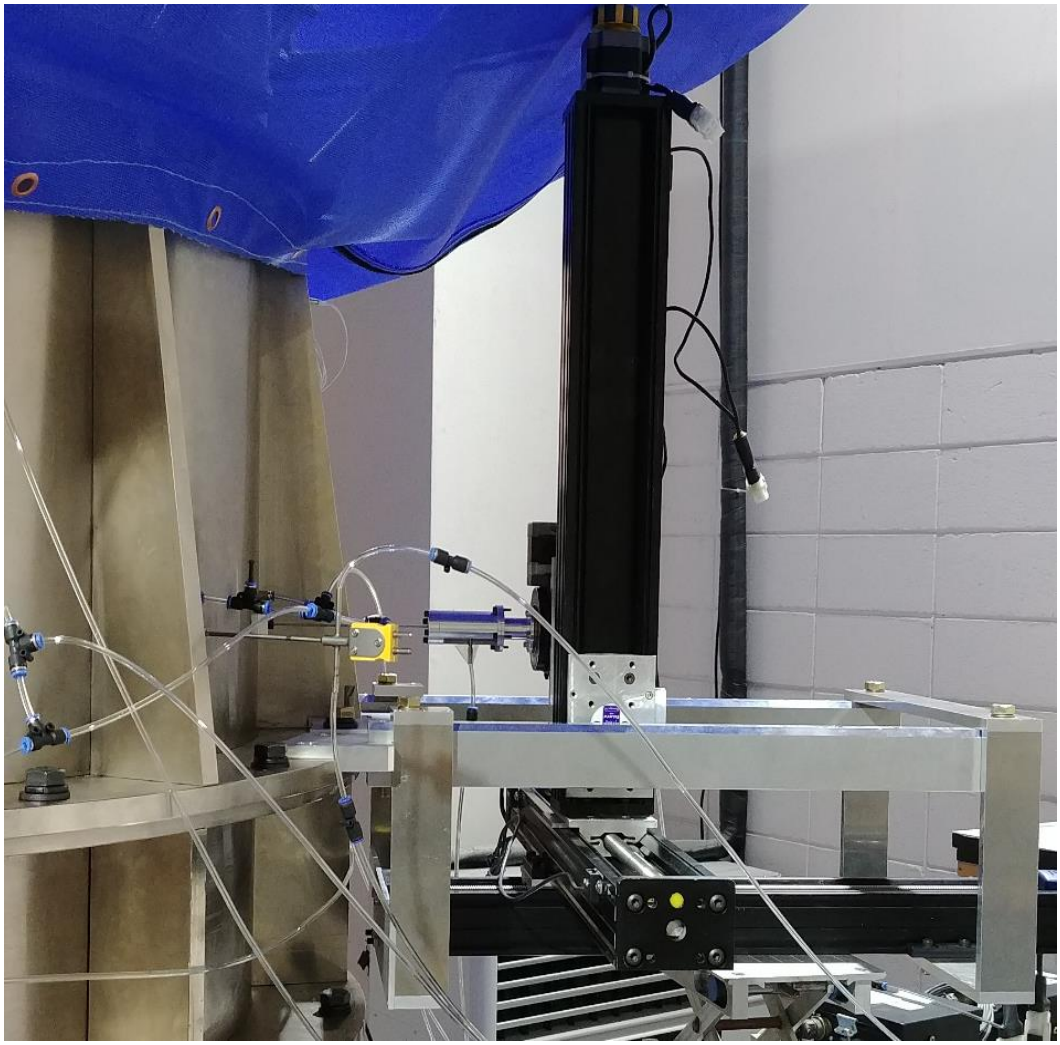

Figure 2.25 Radial Traverse System of SNU Compressor

2HSP-485) and a driver (Autonics, MD5-HF28) have been installed to control the step motor. The gear ratio of each set is 18.5 for gear A and B, 5.148 for gear C and D to amplify the torque applied on the stator rows. To avoid the clocking effect [70], the entire stator rows including IGV are rotated simultaneously.

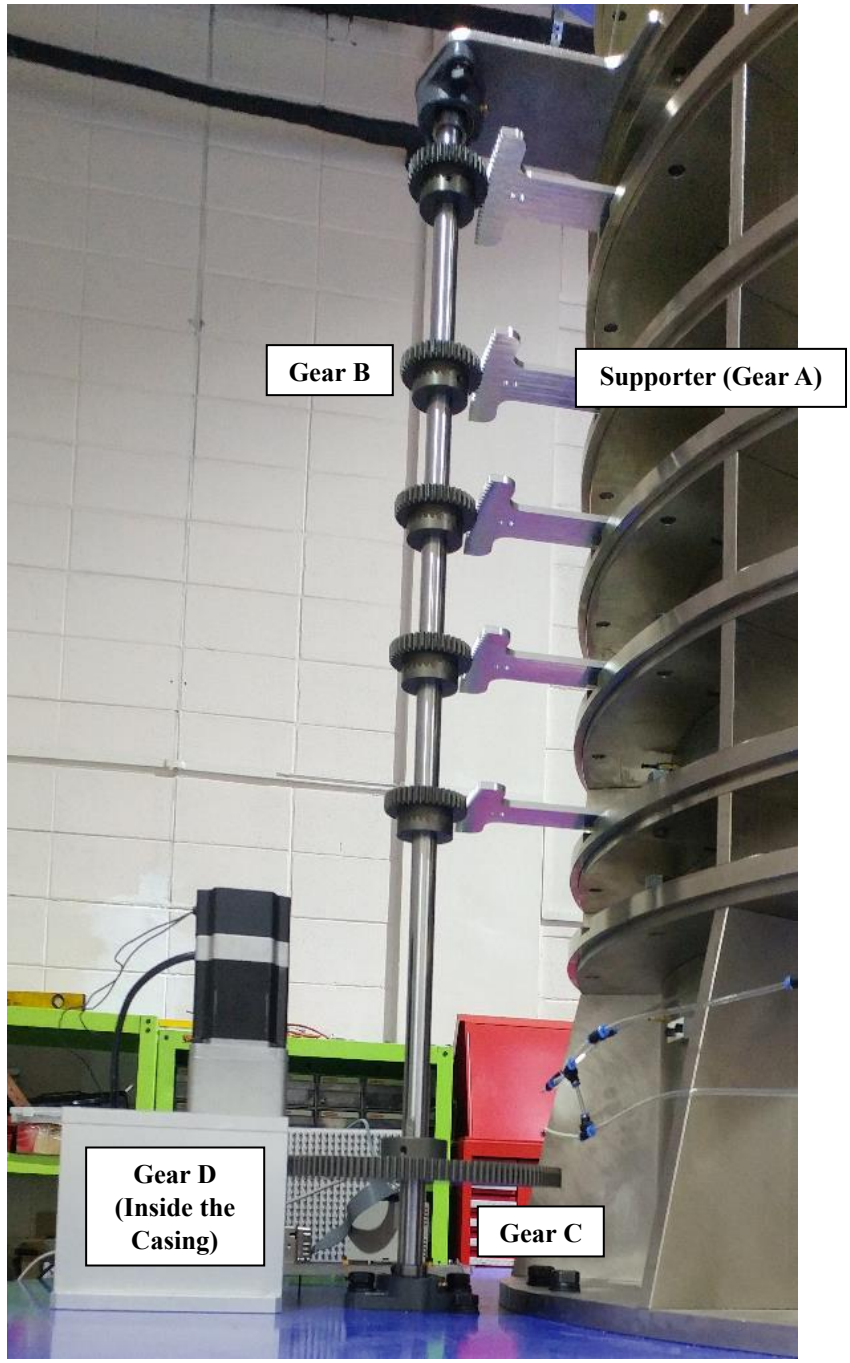

Figure 2.26 Circumferential Traversing System of SNU Compressor

2.4 Measuring Technique of 3D Velocity Vector

It is necessary to measure the unsteady velocity vectors inside the compressor in order to investigate the unsteady kinematics of a multistage shrouded stator flow. However, popular laser technics such as PIV or LDV cannot measure planes near the external casings or rotor disks due to the deflection of laser, and double or triple wire hot-wires have a poor spatial resolution (~ 5% of passage span) due to their large size.

Therefore, single 45° slanted hot-wires (Dantec Dynamics, 55P12), which has relatively small diameter (~ 2.67% of passage span), with a CTA anemometer module (Dantec Dynamics, 90C10) installed at a CTA frame (Dantec Dynamics, 90N10) have been used to measure the unsteady velocity vectors inside the SNU compressor. The encoder installed at the lower main axis (Baumer, model HOG14) has been used to synchronize the rotor circumferential position and the unsteady signals from the wires. Signals from the hot-wire and the encoder have been measured simultaneously for five seconds by a DAQ board (National Instruments, model PXI-4492) installed at a PXI chassis (National Instruments, PXIe-1071), with 200 kHz sampling rate (note that the blade passing frequency of 866.67 Hz). The encoder transmits a square wave signal per one revolution; after the signal, the wire raw voltage signals transmitted from a single rotor pitch have been collected. The measured data have been divided into 21 timesteps (0~100%) and ensemble averaged; approximately 80 signals have been obtained per a single timestep, for a single measuring point.

Three measurements with different yaw angles (40° interval) have been performed at a single measurement point to convert the raw-voltages into unsteady 3D velocity vectors, following the technique of Shin et al. [71]. First, three ensemble-averaged raw voltages at each yaw angles have been converted into effective velocity, U_{eff}, using the velocity-voltage relation deduced at 90° yaw angle; the velocity-voltage relation is curve

-fitted into 4th order polynomial equation (equation 2.19), which have been obtained prior to each measurement by a hot-wire calibrator (Dantec Dynamics, 90H02). The effect of the temperature on U_{eff} has been compensated according to the method of [72].

$$U_{eff} = a_4E^4 + a_3E^3 + a_2E^2 + a_1E + a_0 \tag{2.19}$$

To obtain the unsteady three-dimensional velocity components from the three U_{eff}, equations 2.20 ~ 2.22 have been used [71] (refer Figure 2.27 for coordinate systems).

$$\cos\theta_\alpha = \cos\theta_0 cos\theta_p cos\theta_y - sin\theta_0 sin\theta_p \tag{2.20}$$

$$\left(\frac{U_{eff}}{U}\right)^{0.45} = a_0 + a_1\alpha + a_2\theta_p + a_3U + a_4\alpha\theta_p + a_5\alpha U + a_6\theta_p U + a_7\theta_p^2 + a_8{\theta_\alpha}^2 + a_9{\theta_\alpha}^3 \tag{2.21}$$

$$\theta_{\alpha_2} = \theta_{\alpha_1} + 40° \tag{2.22}$$

$$\theta_{\alpha_3} = \theta_{\alpha_1} - 40° \tag{2.23}$$

Coefficients in the equation. 2.21 have been obtained from the pitch-yaw response of each single hot-wires in Appendix C. From the measurement of a single probe yaw angle, two equations (2.20 and 2.21) have been obtained, thus total six equations have been collected. These equations have been solved using MATLAB fslove function to obtain three unknowns, θ_{α_1}, U, θ_p (θ_{α_2} and θ_{α_3} can be derived using equation 2.23, and θ_y can be derived from equation 2.20). During this procedure, the fsolve function requires the initial guess of the θ_{α_1}, U, θ_p to solve the non-linear equations. Therefore, the θ_{α_1}, U, θ_p at the designed condition have been first used as initial guesses. The first fsolve solutions have been used as an initial guess of the second fsolve calculation to obtain the final unsteady three-dimensional velocity vector at a single point. To obtain the planar distribution of the unsteady three-dimensionial velocity vectors, the procedures have been

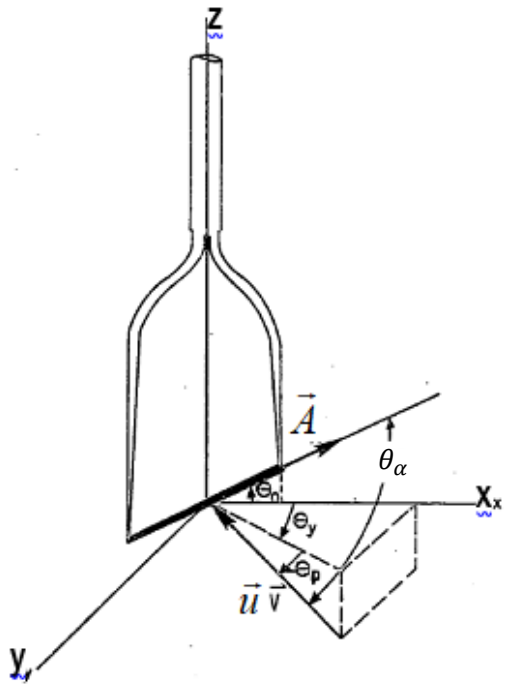

Figure 2.27 Coordinate System of Velocity Vector and Hot-Wire [71]

repeated at every measuring points with uncertainties (with 95% confidence interval) of 1.87% average, maximum 6.67% of $|\vec{U}|$, 1.52° and 1.29° for pitch and yaw angle of $\vec{U}$, respectively.

2.5 Measuring Planes and Conditions

Hot-wire measurements have been made at the upstream and the downstream of the 3rd stator passage of the SNU compressor, at three different operating conditions (design point (ϕ = 0.36, ϕ_d), near stall (ϕ = 0.32, 0.9 ϕ_d) and near choke (ϕ = 0.40, 1.1 ϕ_d)); Figure 2.28 and 2.29 shows the compressor map and the measuring planes of

Table 2.11 Operating Conditions of the Study

Operating Conditions	ϕ	ψ
Near Stall	0.32 (0.90 ϕ_d)	1.46 (1.12 ψ_d)
Design	0.36 (1.00 ϕ_d)	1.30 (1.00 ψ_d)
Higher Mass Flow	0.40 (1.11 ϕ_d)	0.94 (0.73 ψ_d)

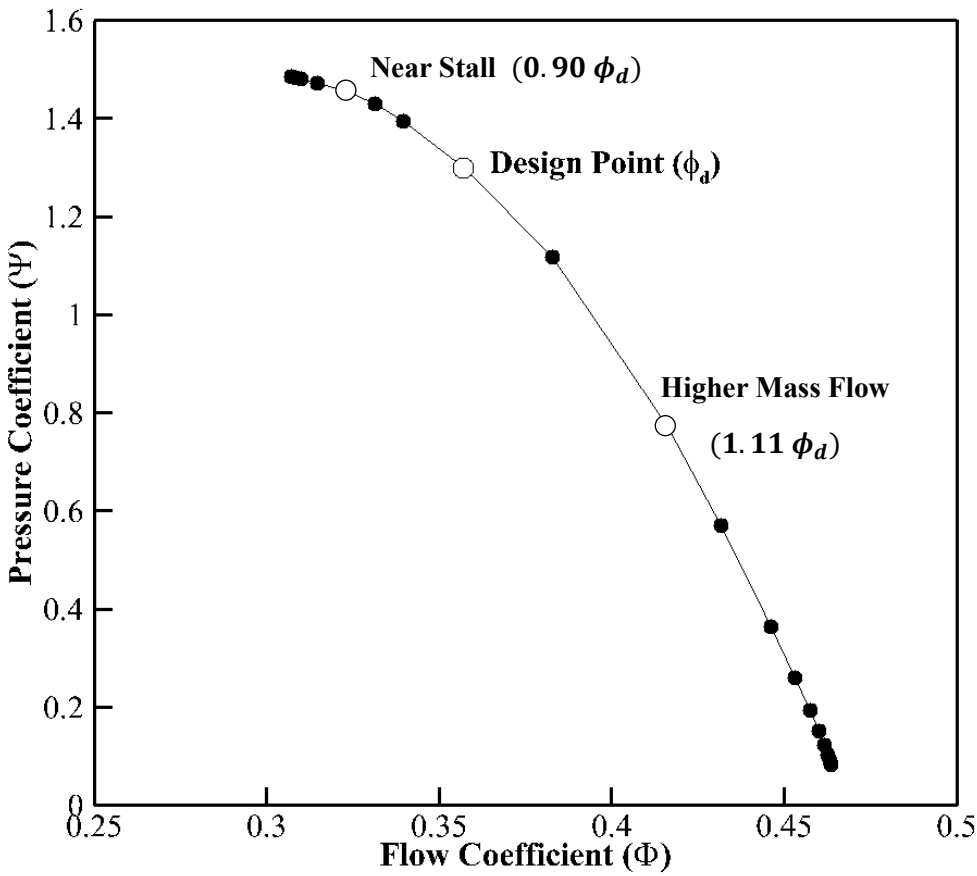

Figure 2.28 Compressor Map of SNU Compressor

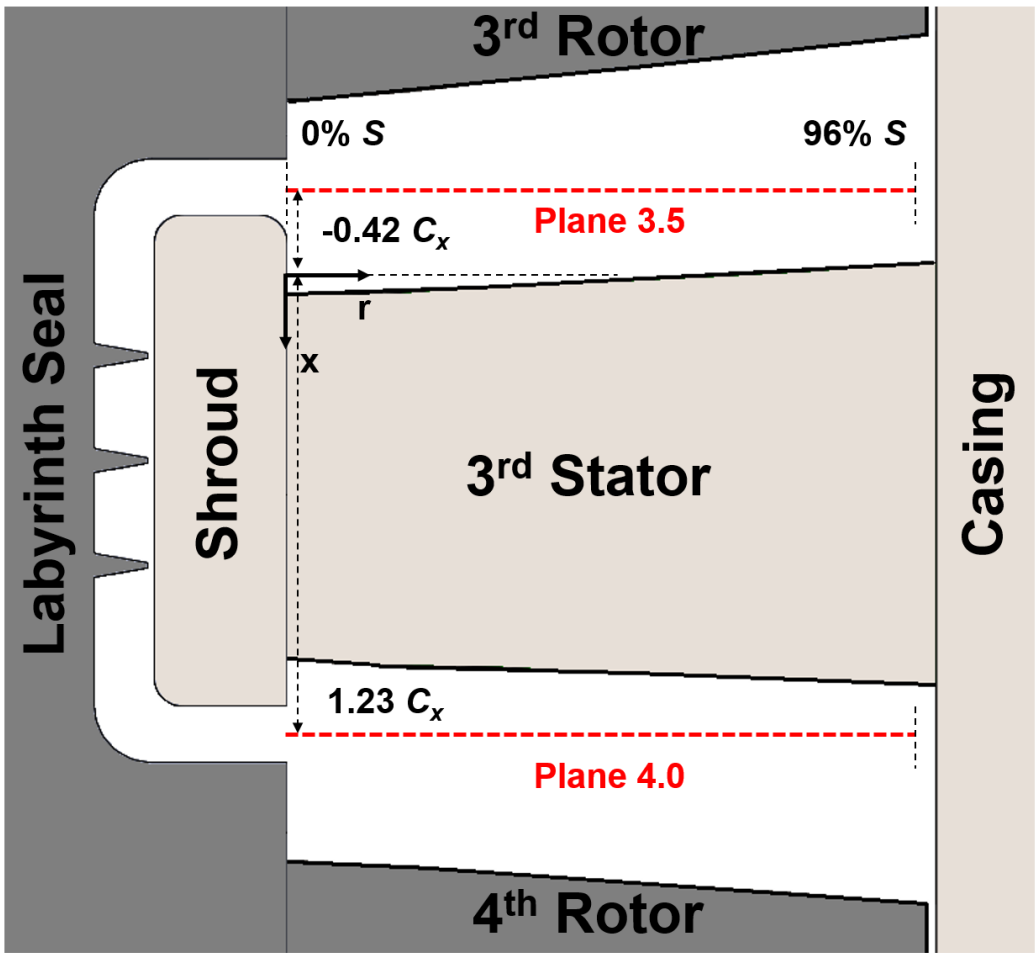

Figure 2.29 Measuring Planes of the Study

the SNU compressor, respectively. Plane 3.5 (upstream of the 3rd stator) is located 0.42 stator axial chord (C_x) upstream of the midspan leading edge (LE), and Plane 4.0 (downstream of the 3rd stator) is located 0.23 stator C_x downstream of the midspan trailing edge (TE). Both planes are located at the axial center of the cavities.

One stator pitch and 0 ~ 96% span from the hub have been measured at the

designed condition to investigate the detailed unsteady kinematics of shrouded stator flow: 21 equally spaced pitchwise measurement points and 37 spanwise points with intervals of 2.67% span, which yielded total 777 points for each plane. For the off-design conditions, one stator pitch and 0 ~ 50% span from the hub have been measured to focus on the effect of hub corner separation on the unsteady flow kinematics of the hubside shrouded stator flow. 21 equally spaced pitchwise measurement points and 37 spanwise points with intervals of 2% span ranging from 0~30% span and 3.33% span ranging from 30~50% span have been measured, which yielded total 462 points for the planes.

3. Unsteady Kinematics of Multistage Shrouded Stator Flow at Design Point

3.1 Unsteady Kinematics of the Flow Upstream of 3rd Stator

The periodic unsteady rotor wakes generate the unsteady kinematics of multistage shrouded axial compressor flow, which cause the variation of the aerodynamic properties. Plane 3.5 unsteady U_x/U_t, U_θ/U_t color contour distributions at design point (ϕ_d) are shown in Figures 3.1 and 3.2 to investigate the unsteady kinematics of multistage shrouded axial compressor flow. White dotted line in Figures. 3.1 and 3.2 represents the trailing edge (TE) of 3rd rotors axially extended downward, and the black dotted line represents the LE of a 3rd stator axially extended upward. Note that the locations of 3rd rotor wakes and TE of 3rd rotor does not coincide, due to the axial distance (0.33 rotor C_x at midspan) between the measuring plane (plane 3.5) and the midspan 3rd rotor TE.

An upstream 3rd rotor wake (Figure 3.1 (a), (b), (c)), and multiple 2nd stator wakes (Figure 3.1 (d), (e)) are observed (marked as 3rd RW and 2nd SW, respectively), which are distinguished by the low U_x and high U_θ regions. These are consistent with previous research [4, 20]. As discussed by Smith [8], the LE of the 3rd rotor shown in Figure 3.1 (a) ~ (c) splits the 2nd rotor wakes, creating the two different "chopped" 2nd rotor wakes located at the PE and SS of 3rd rotor wake, as shown in Figure 3.1, particularly Figure 3.1 (b); for convenience, the chopped 2nd stator wake segment at PS side of 3rd rotor wake will be called PS segments, and the wake at the SS will be called SS segments.

The width of the 3rd rotor wake is thicker at hubside, due to the hubside corner separation of the 3rd rotor. In addition, additional low U_x and U_θ regions are observed near the PS of the rotor wake tip region, which is caused by the tip clearance flow of the adjacent blade; the core of the tip clearance vortex (marked as TCV in Figure 3.1) has the lowest U_x, which is consistent with previous researches [4, 14, 71]. Furthermore, another low U_x region is observed near the casing region. Unsteady pressure measurement and numerical

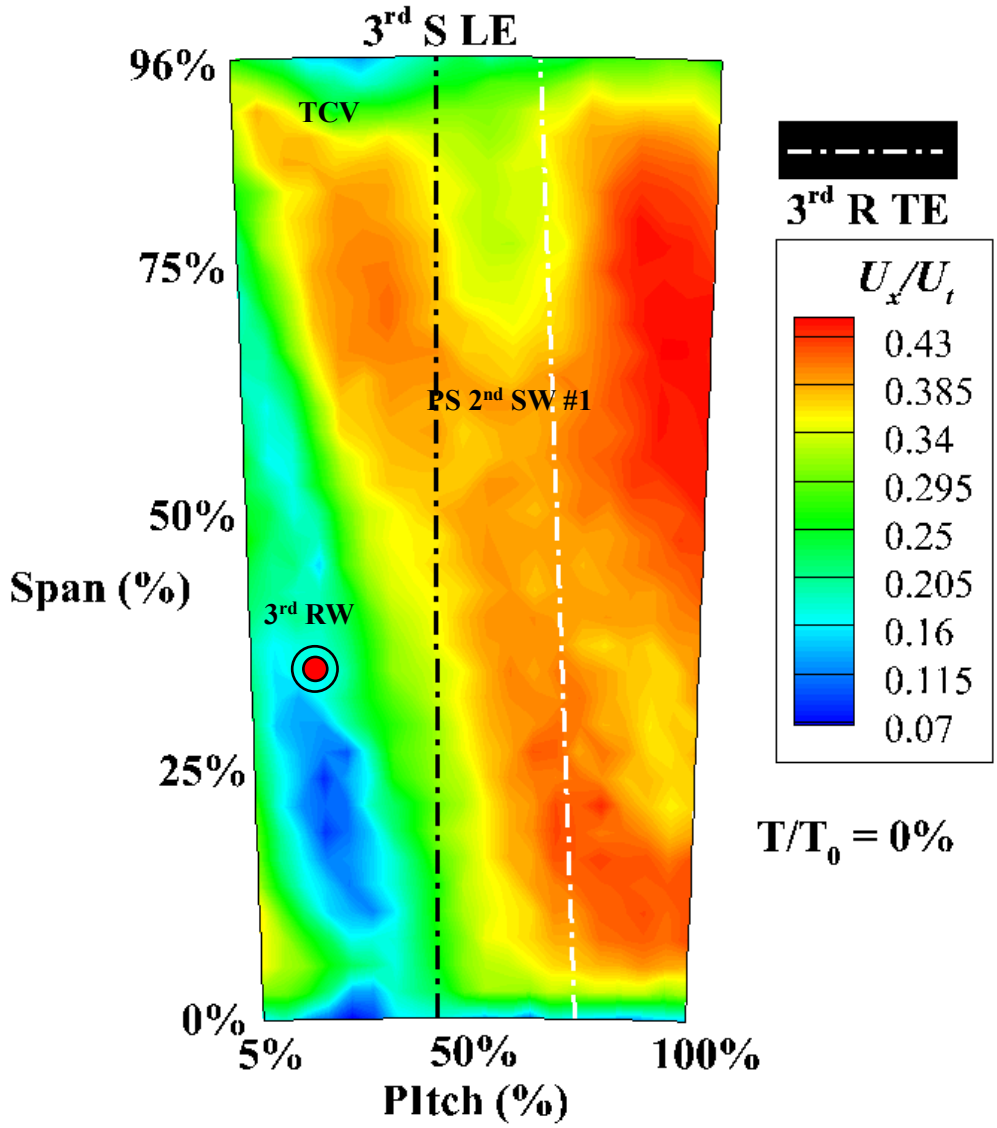

(a) Color Contour of U_x/U_t Distribution at Plane 3.5, T/T_0 = 0%, Design Point (ϕ_d)

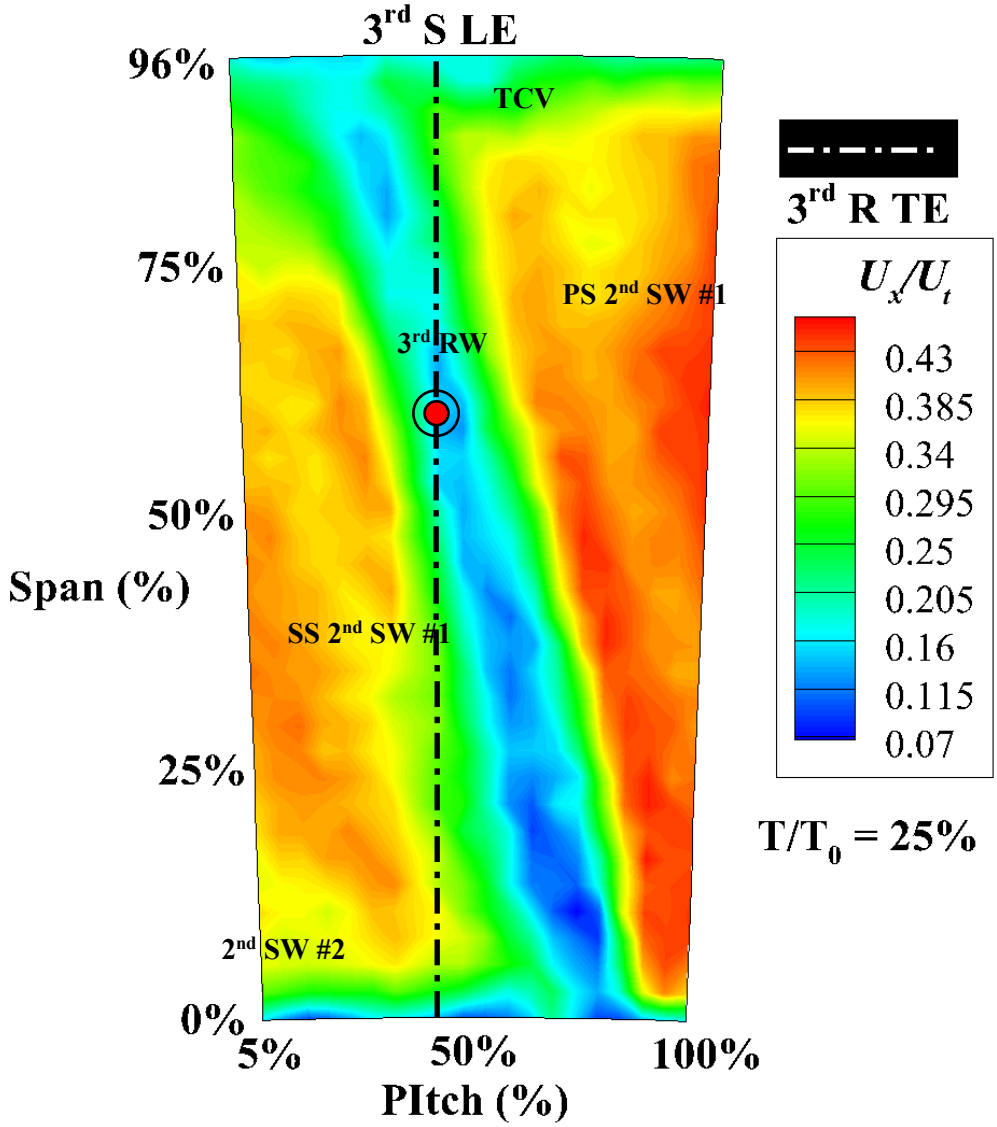

(b) Color Contour of U_x/U_t Distribution at Plane 3.5, T/T_0 = 25%, Design Point (ϕ_d)

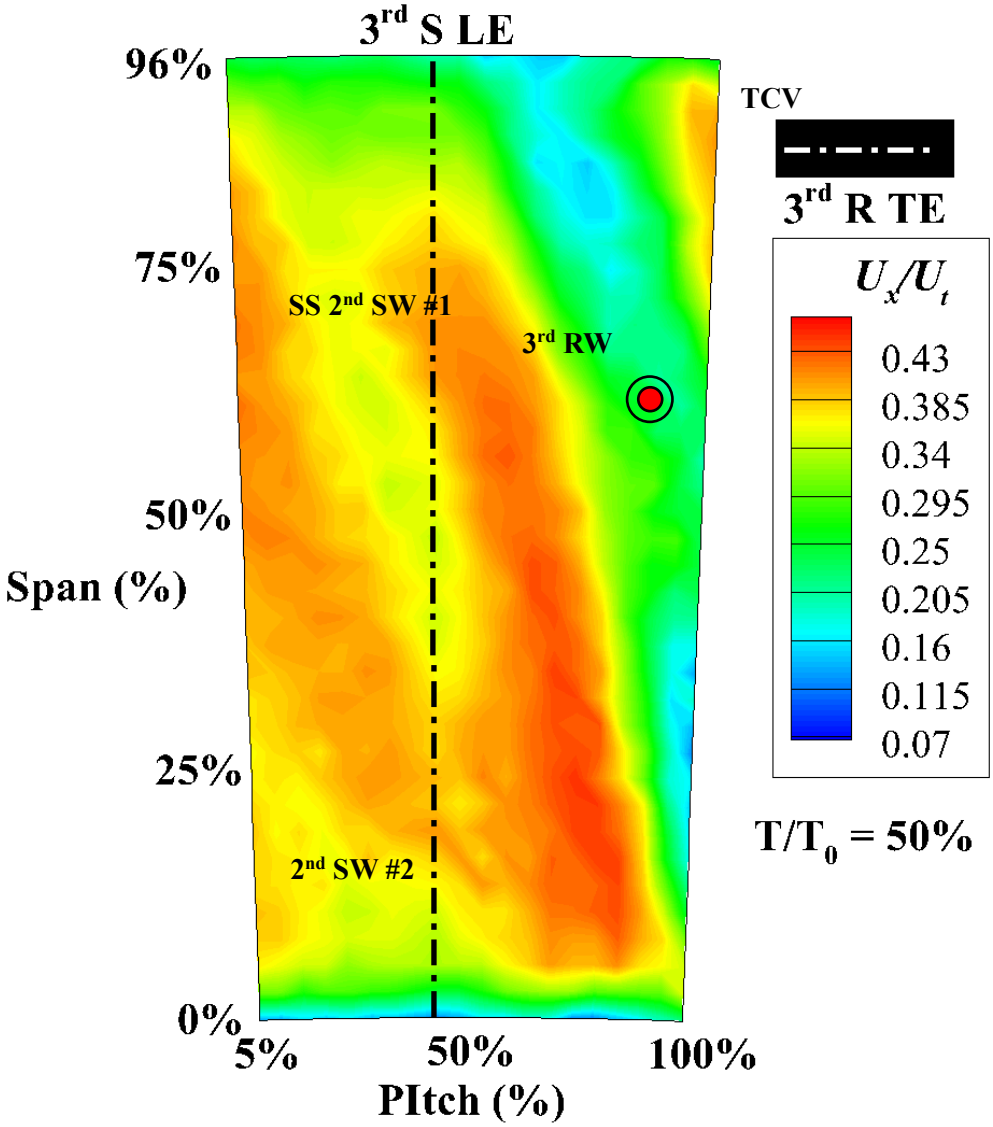

(c) Color Contour of U_x/U_t Distribution at Plane 3.5, T/T_0 = 50%, Design Point (ϕ_d)

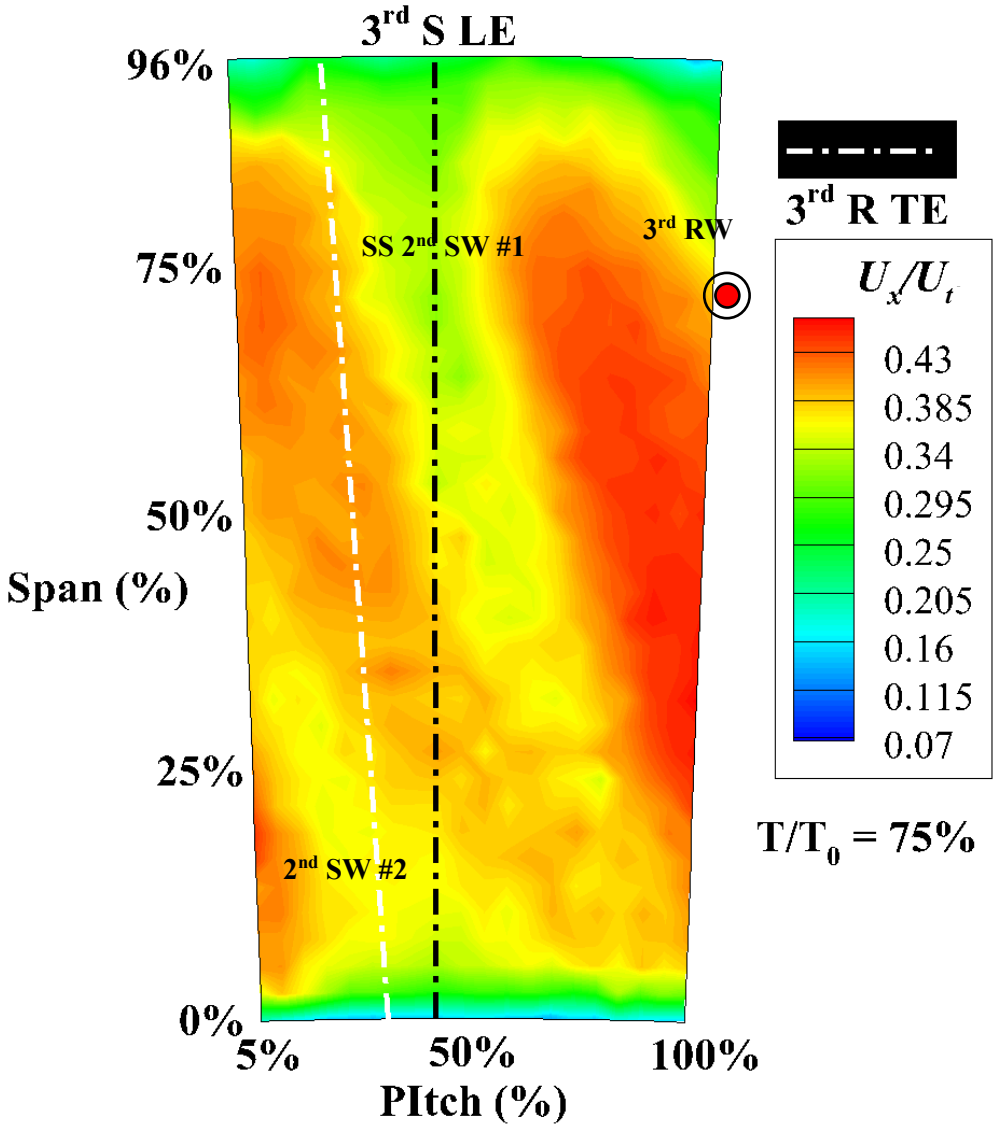

(d) Color Contour of U_x/U_t Distribution at Plane 3.5, T/T_0 = 75%, Design Point (ϕ_d)

Figure 3.1 Color Contour Plot of Instantaneous Axial Velocity Distribution at Plane 3.5, Design Point

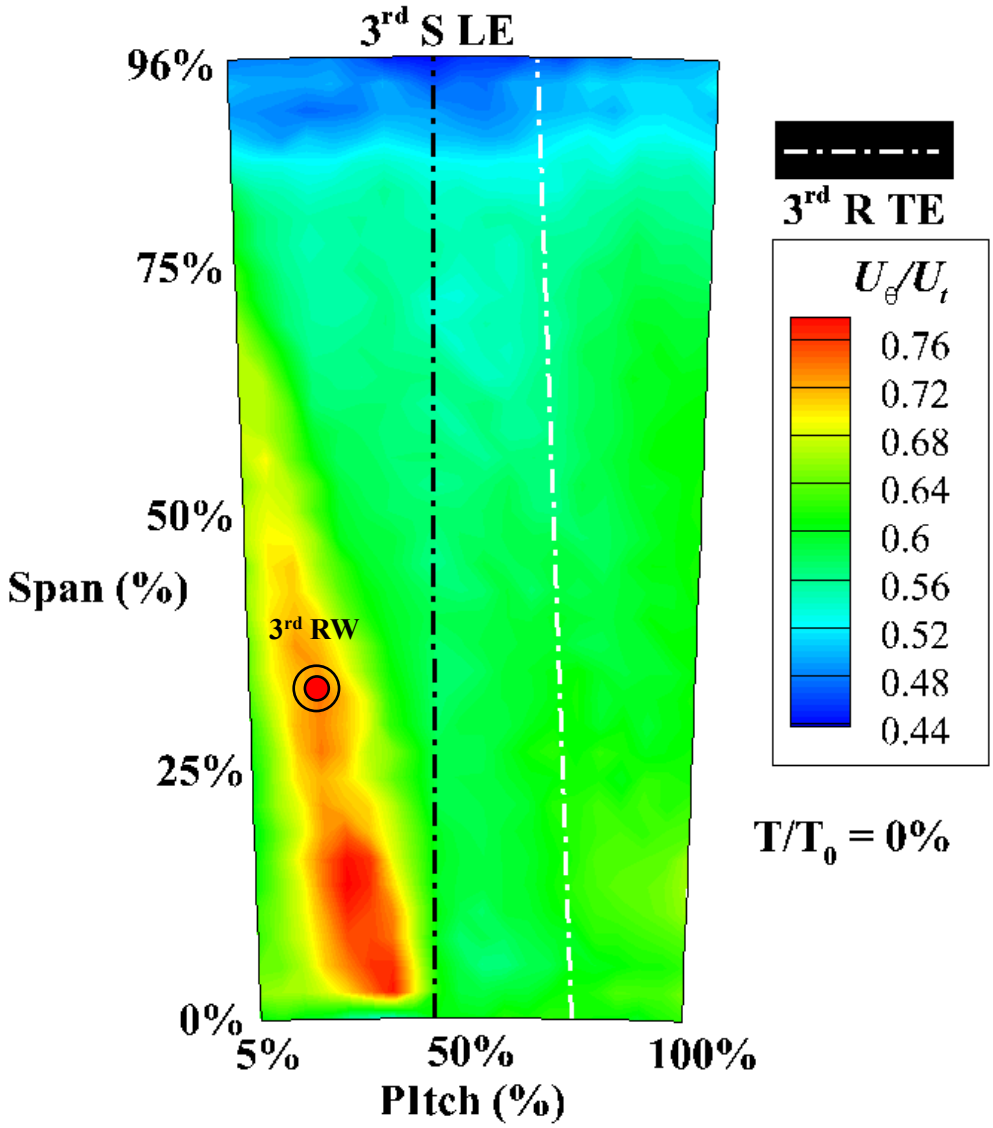

(a) Color Contour of U_θ/U_t Distribution at Plane 3.5, T/T_0 = 0%, Design Point (ϕ_d)

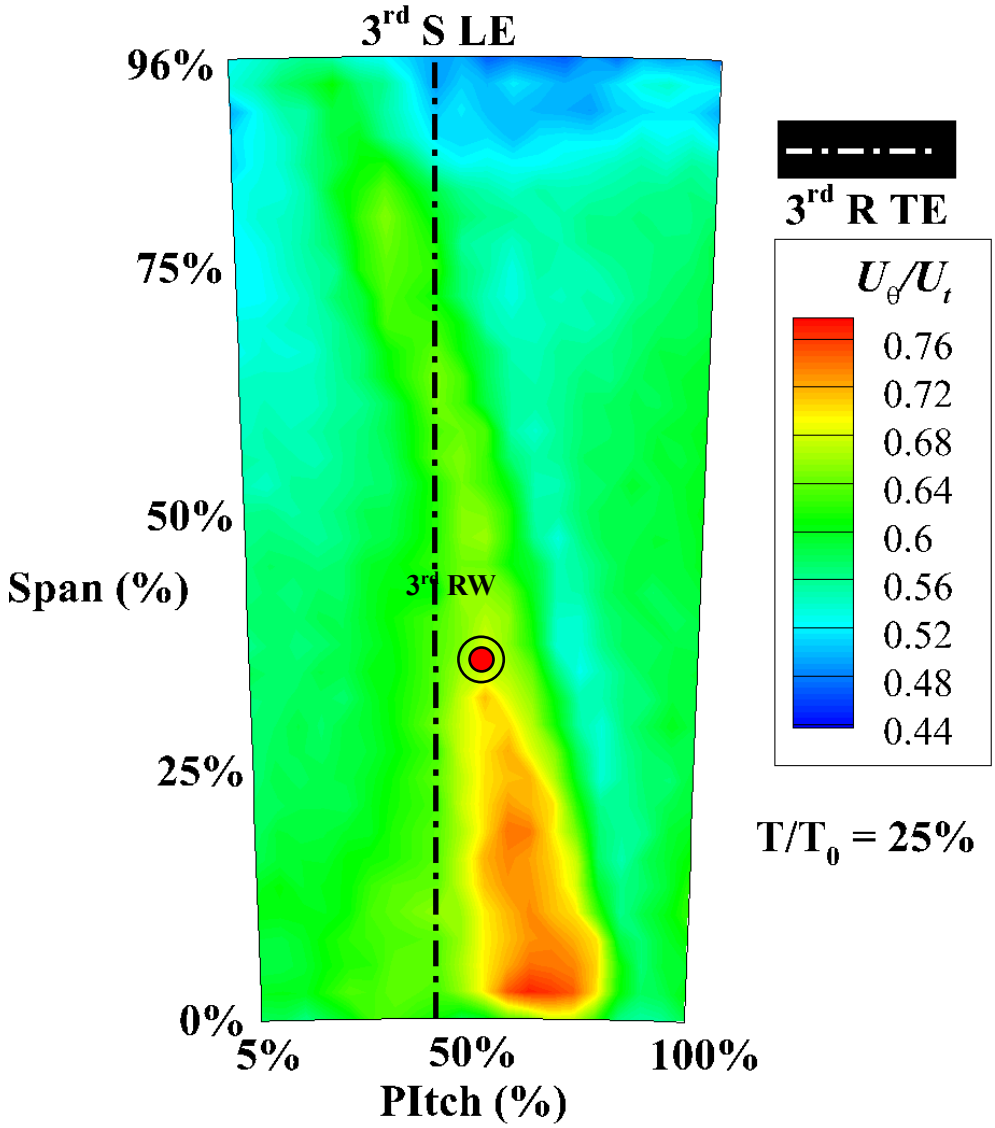

(b) Color Contour of U_θ/U_t Distribution at Plane 3.5, T/T_0 = 25%, Design Point (ϕ_d)

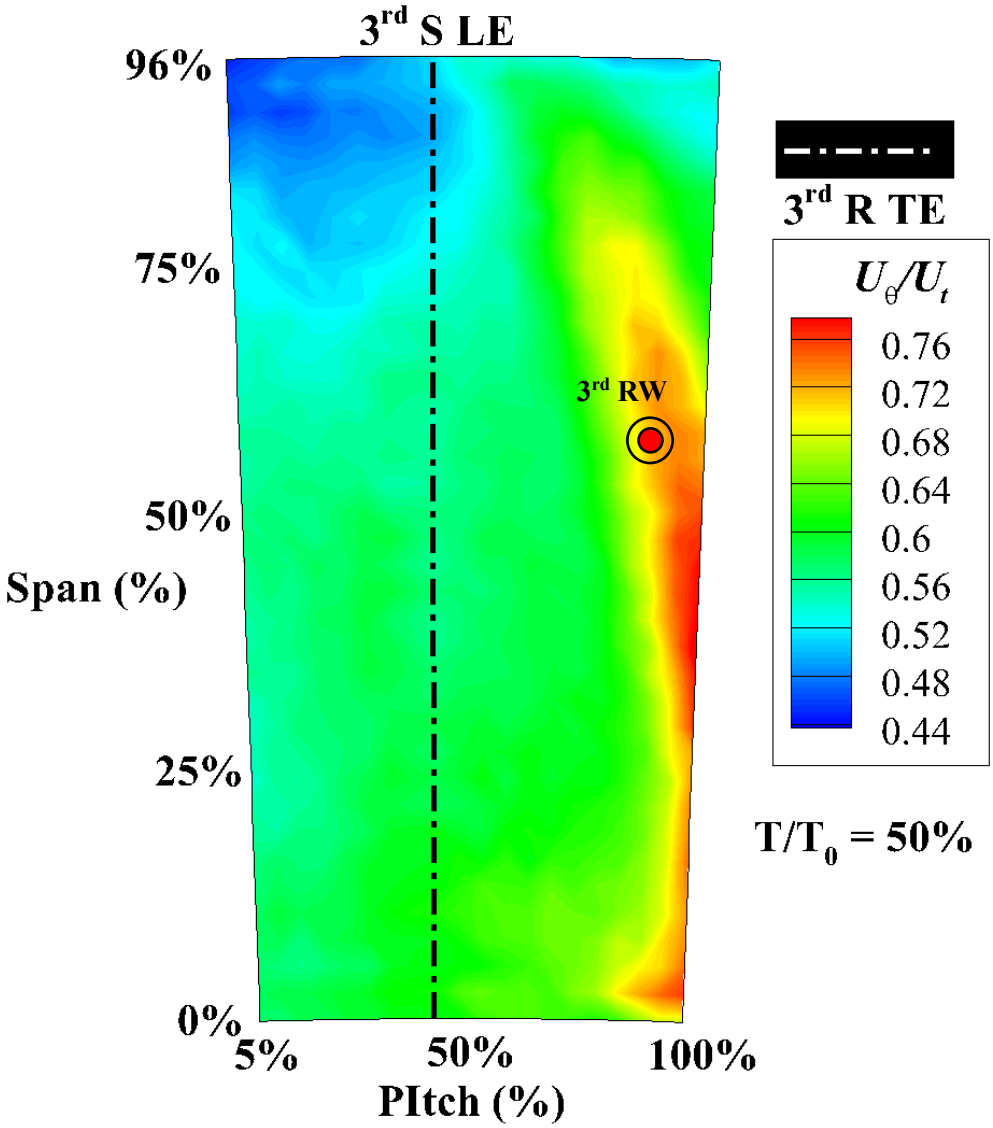

(c) Color Contour of U_θ/U_t Distribution at Plane 3.5, T/T_0 = 50%, Design Point (ϕ_d)

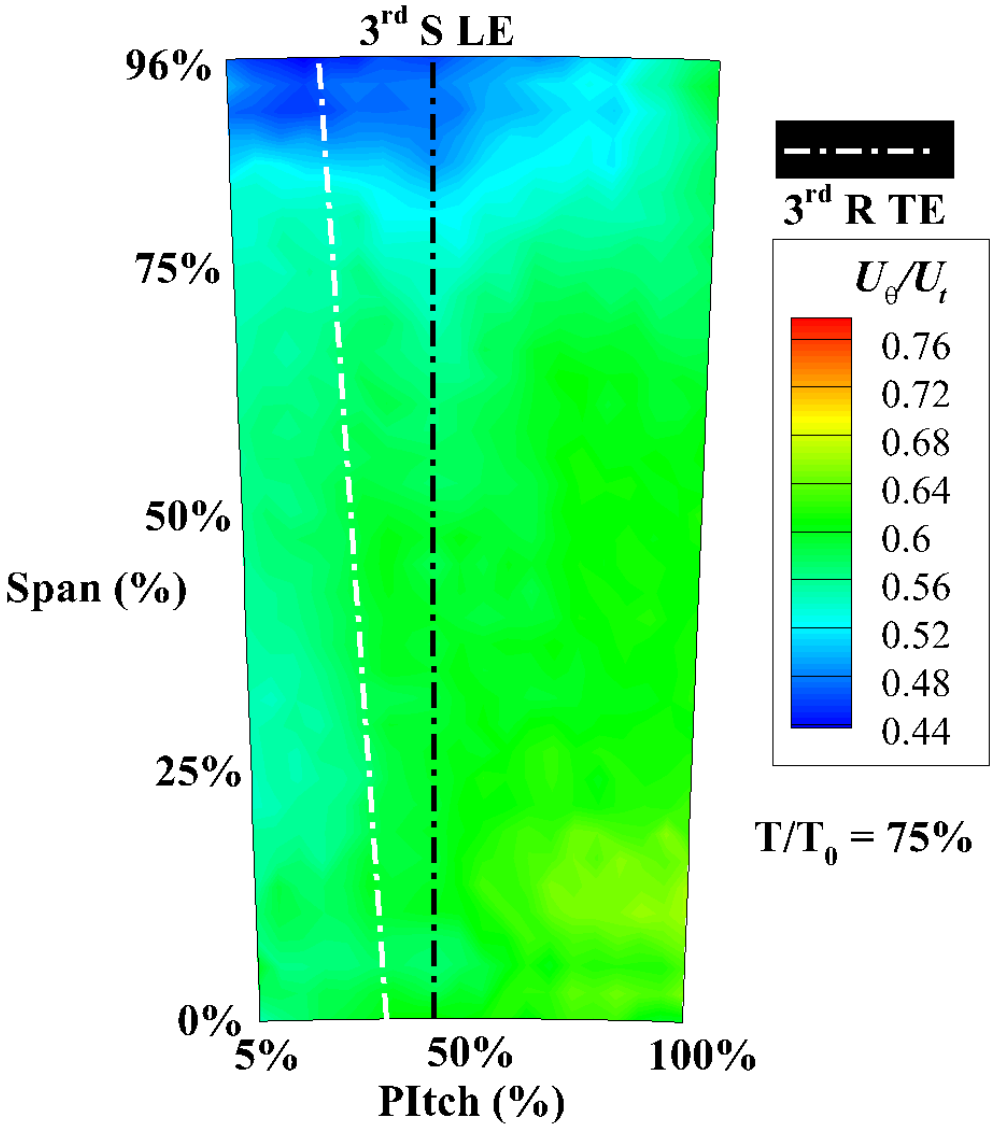

(d) Color Contour of U_θ/U_t Distribution at Plane 3.5, T/T_0 = 75%, Design Point (ϕ_d)

Figure 3.2 Color Contour Plot of Instantaneous Tangential Velocity Distribution at Plane 3.5, Design Point

simulation by Shin et al. [71] reported that this is caused by the interaction between the tip clearance flow and casing boundary layer. The magnitude of U_x of 2nd SW #1 near the tip region is lower, and it is thought to be the interaction with the low casing U_x region. Measurement by Lange et al. [4] and Mailach et al. [14] also found the widened stator wake width and lowered magnitude of stator wake U_x near the casing region.

The interaction between the 3rd rotor and 2nd stator wakes fluctuates the width and the magnitude of the velocity of the 3rd rotor wakes. At T/T_0 = 0%, the width of the rotor wake is wide (Figure 3.1 (a)), and the U_x at the wake region is higher than other time steps. These are due to the 2nd stator wakes, as illustrated in Figure 3.3 (a) (The 3rd rotor wake with a red circle in Figure 3.3 illustrates the 3rd rotor wake observed in Figure 3.1. The PS and SS segment of the 2nd stator will be decided based on this marked blade). At first, the 2nd stator SS segments (SS 2nd SW #1 in Figure 3.1 (a), 3.3 (a)) increases the suction side boundary layer thickness (BLD), widening the wake width [22, 23]. In addition, the PS segment of 2nd stator wake #2 is attached on the PS of rotor wake at this period; note that due to the difference of the streamwise velocity between the blade PS and SS, the wakes near the SS are transported faster, which causes the discontinuation between the rotor wake at stator PS and SS [8]. As a result, the width of the 3rd rotor wake PS is also widened, and the counter-clockwise vortex by the negative jet increases the streamwise velocity of 3rd rotor wake compared with other timesteps, which was introduced by Mailach et al. [13].

At T/T_0 = 25% (Figure 3.1 (b), 3.3 (b)), the PS segment of 2nd stator wake #2 is detached from the 3rd rotor wake, and SS segment of the 2nd stator wake #1 is beginning to be detached from the upstream third rotor wake. As a result, the width of the upstream 3rd rotor wake is decreased compared with T/T_0 = 0%. The PS segment of 2nd stator wake #1 is approaching to the measuring plane but is not affecting the 3rd rotor wake PS at the moment. In addition, the PS segment of 2nd SW #2 is exiting the measuring plane,

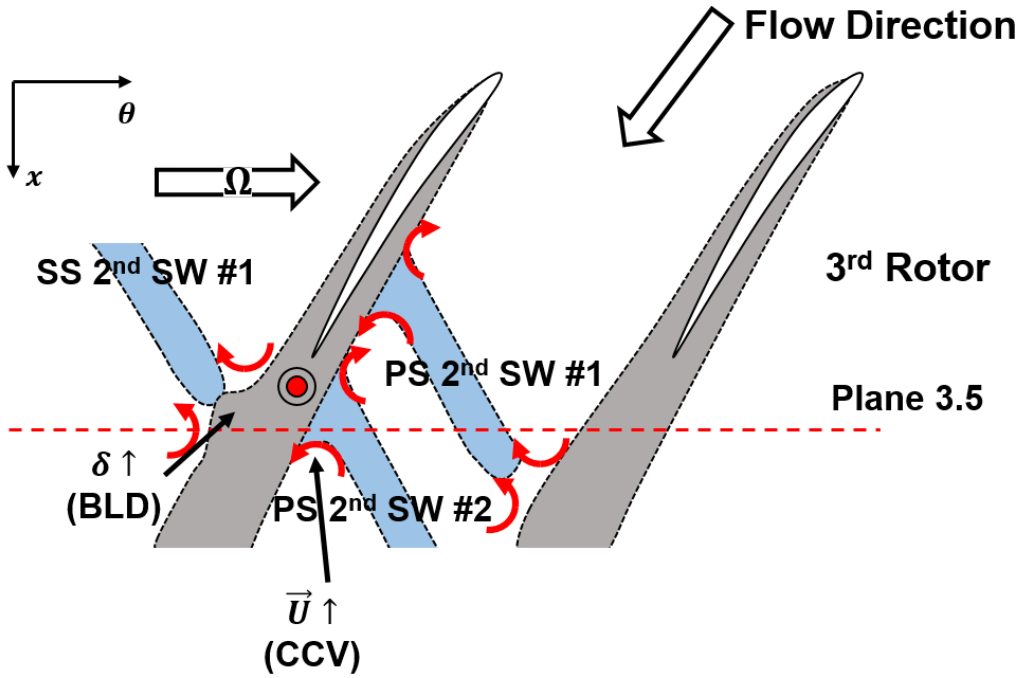

(a) Schematic of 3rd Rotor and 2nd Stator Wakes at T/T_0 = 0%

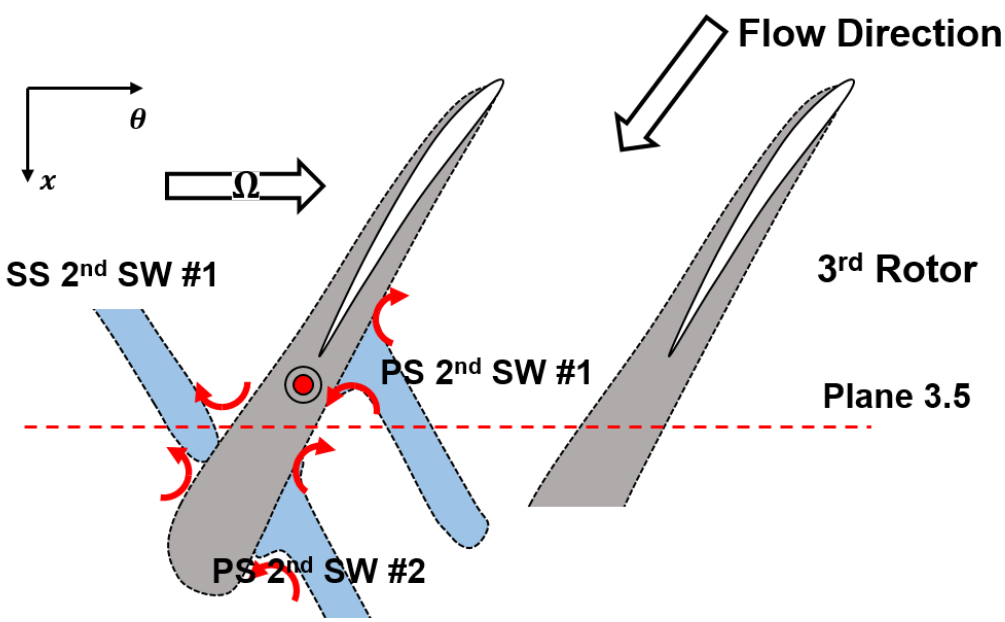

(b) Schematic of 3rd Rotor and 2nd Stator Wakes at T/T_0 = 25%

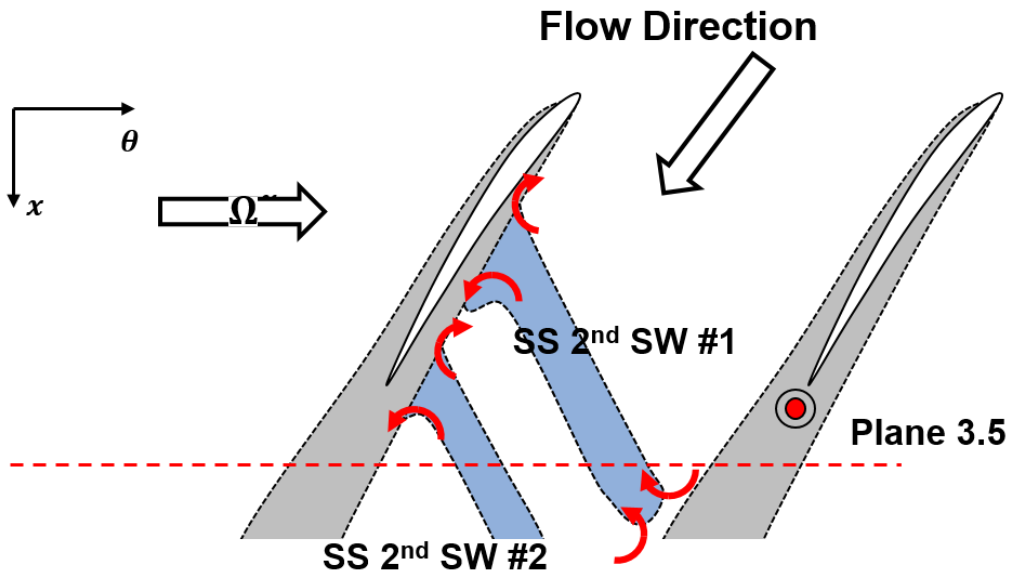

(c) Schematic of 3rd Rotor and 2nd Stator Wakes at T/T_0 = 50% and 75%

Figure 3.3 Schematics of the Interaction between 3rd Rotor and 2nd Stator Wakes

indicating that the clockwise vortex of 2nd SW #2 affects the 3rd rotor wake PS. As a result, the streamwise velocity of 3rd rotor wake PS is reduced, resulting in the decrease of wake U_x. These interactions with rotor wake and usptream stator wakes will be repeated, varying the width and the velocity of rotor wake.

In addition to the variance of 3rd rotor wake, the position of tip clearance flow fluctuates; comparing the location of TCV at T/T_0 = 0% and T/T_0 = 25% show that the location of TCV at T/T_0 = 25% is closer to the PS of the 3rd rotor. Mialach et al [14] reported that this is due to the clockwise and counterclockwise vortex of the upstream stator wakes; the vortices collide with the tip clearance flow, varying its magnitude direction as illustrated in Figure 1.8.

At T/T_0 = 50% and 75% (Figure 3.1 (c), (d), Figure 3.3 (c), (d)), the 3rd rotor wake

is outside the measurement plane. Two stator wakes (2nd SW #1 and #2) are observed and is not disturbed by the 3rd rotor wake. Another 3rd rotor wake will appear on the left side of the measuring plane, repeating the procedure mentioned above.

3.2 Unsteady Kinematics of the Flow Downstream of 3rd Stator

Unsteady kinematics of the downstream of the 3rd stator flow will be discussed next. The unsteady color contour of U_x/U_t, U_θ/U_t and absolute flow angle α distributions at Plane 4.0 are shown in Figures 3.4, 3.5 and 3.6, respectively. The white dotted line represents the leading edge (LE) of downstream 4th rotors axially extended upward, and the black dotted line represents the TE of 3rd stator axially extended downward. A distinctive low U_x and U_θ region, which is created by the 3rd stator wake (marked as 3rd SW), and the corner separation of the adjacent 3rd stator wake is observed at the entire period. In addition to these low U_x regions, another moving low U_x and high U_θ regions are observed at the stator passage throughout the entire timestep. Majority of the low U_x and high U_θ regions are created by the wakes of the 3rd rotors (marked as 3rd RW #1 and 2 in the Figures); the α distributions in Figure 3.6 show that the α is increased at the location of the 3rd rotor wakes, which are typical behavior of the rotor wakes inside the stator passages. These two wakes are transported downstream, and are merged with the 3rd stator wakes to create the variance of the width and U_x of 3rd stator wake, which will be discussed later. At the tip region, the magnitude of tipside 3rd rotor wake U_x and U_θ are lower, and the tipside width is higher compared with those of the midspan region. It is thought that the tip clearance flow of 3rd rotor is transported to the tip region, and is merged with the tipside 3rd rotor wake, which created the phenomenon.

In addition to the 3rd rotor wakes, another low U_x region is located between the two 3rd rotor wakes #1 and 2 at $T/T_0 = 0$ and 25%. (red dot in Figures 3.4 ~3.6). This region

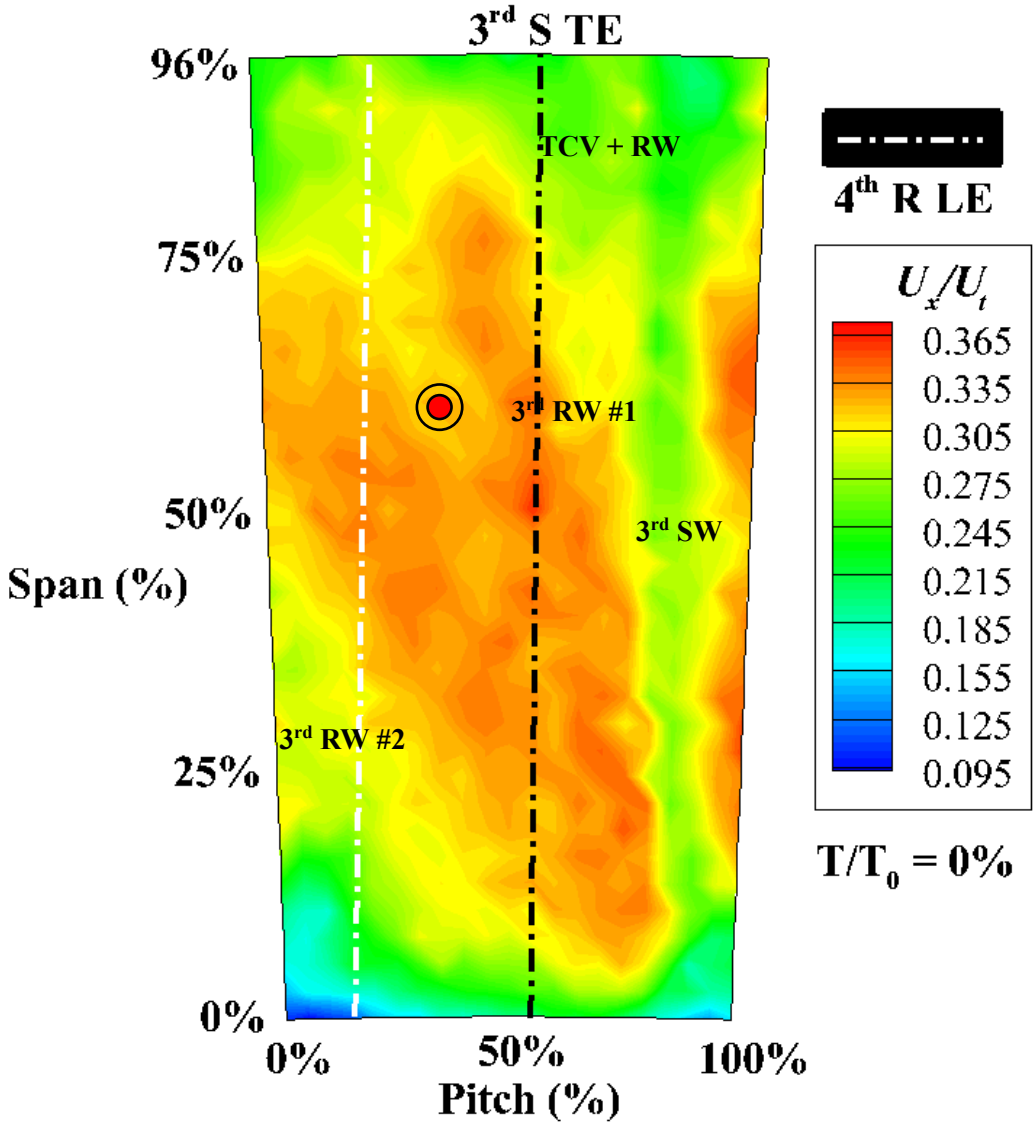

(a) Color Contour of U_x/U_t Distribution at Plane 4.0, T/T_0 = 0%, Design Point (ϕ_d)

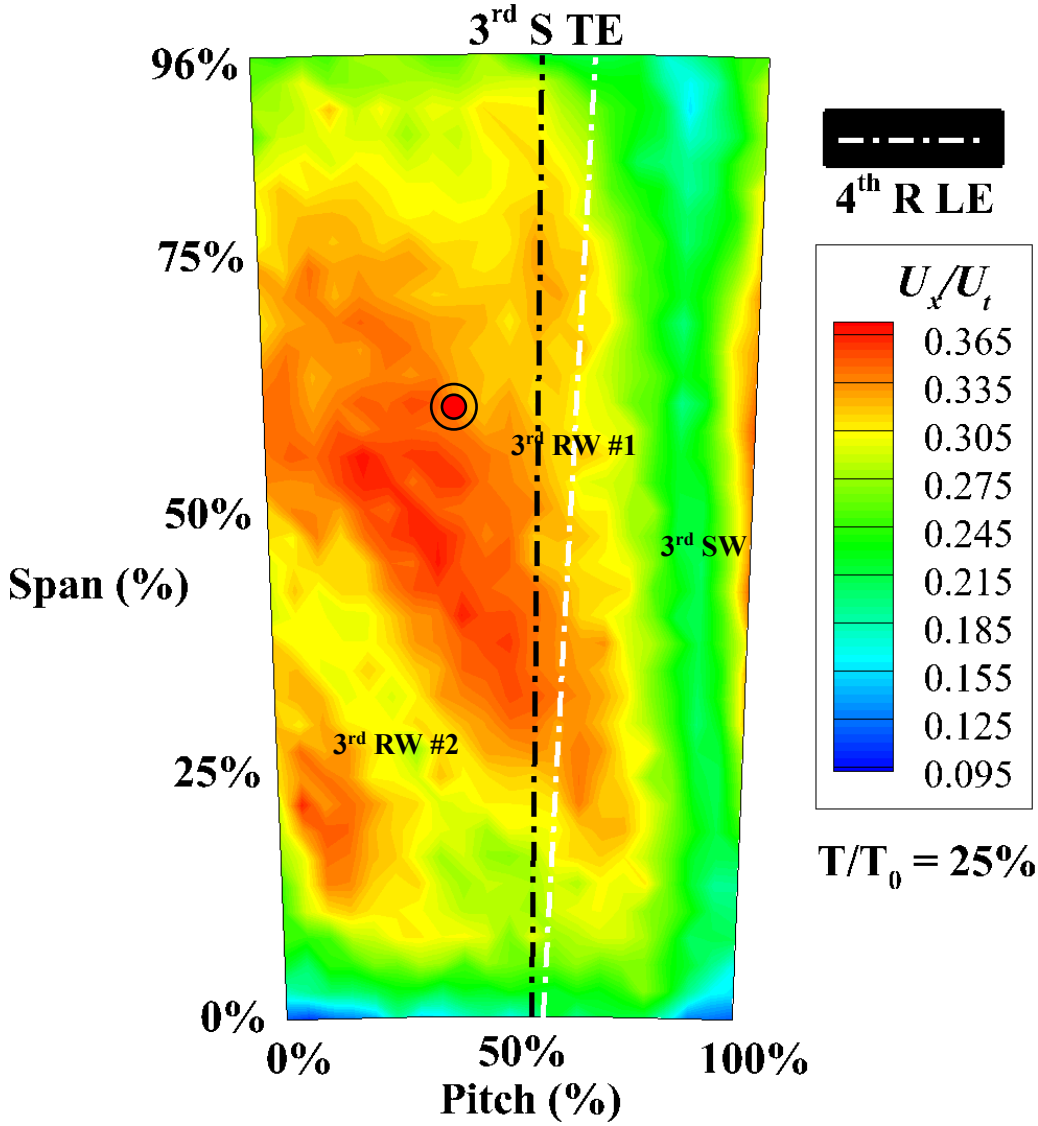

(b) Color Contour of U_x/U_t Distribution at Plane 4.0, T/T_0 = 25%, Design Point (ϕ_d)

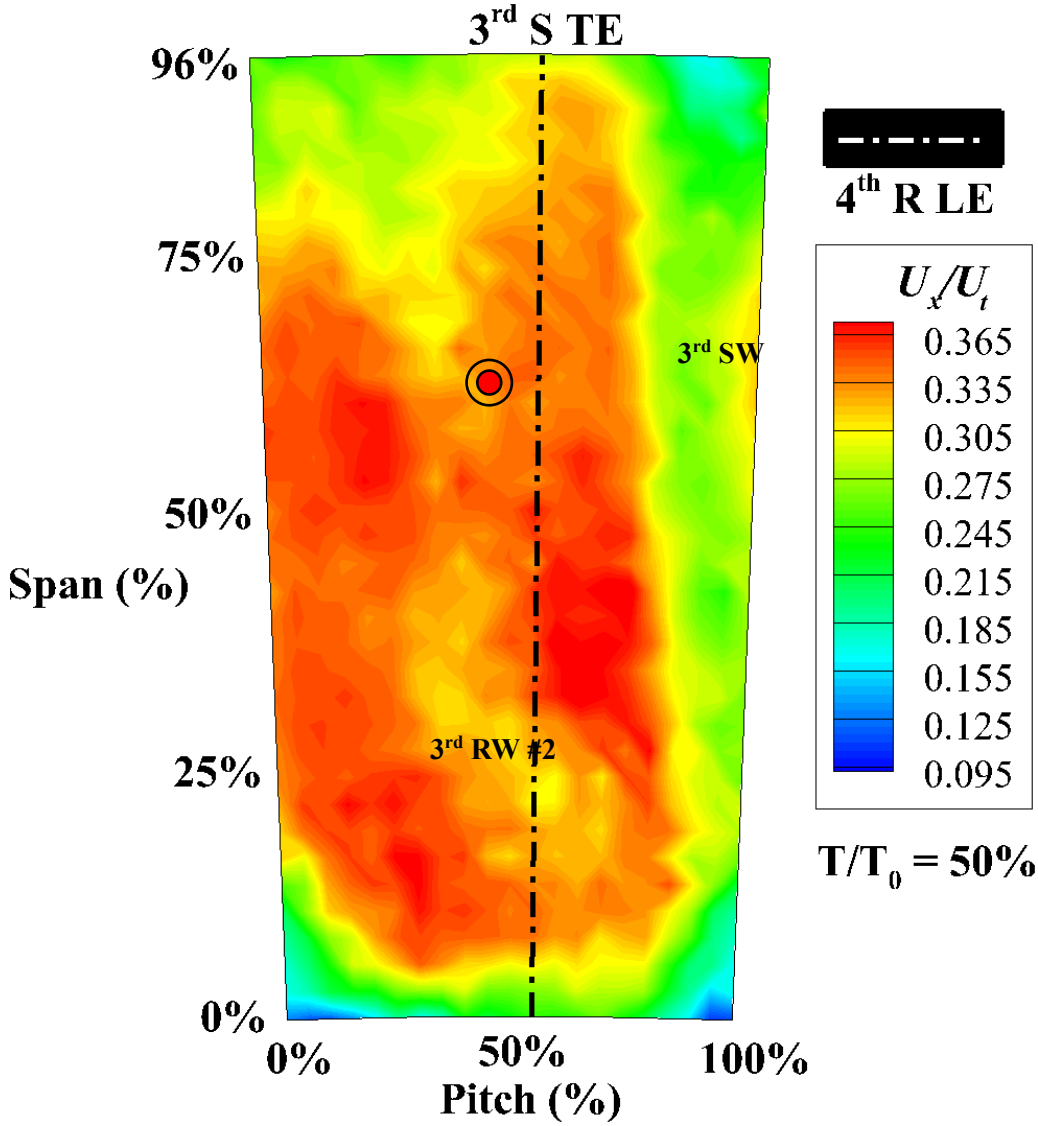

(c) Color Contour of U_x/U_t Distribution at Plane 4.0, T/T_0 = 50%, Design Point (ϕ_d)

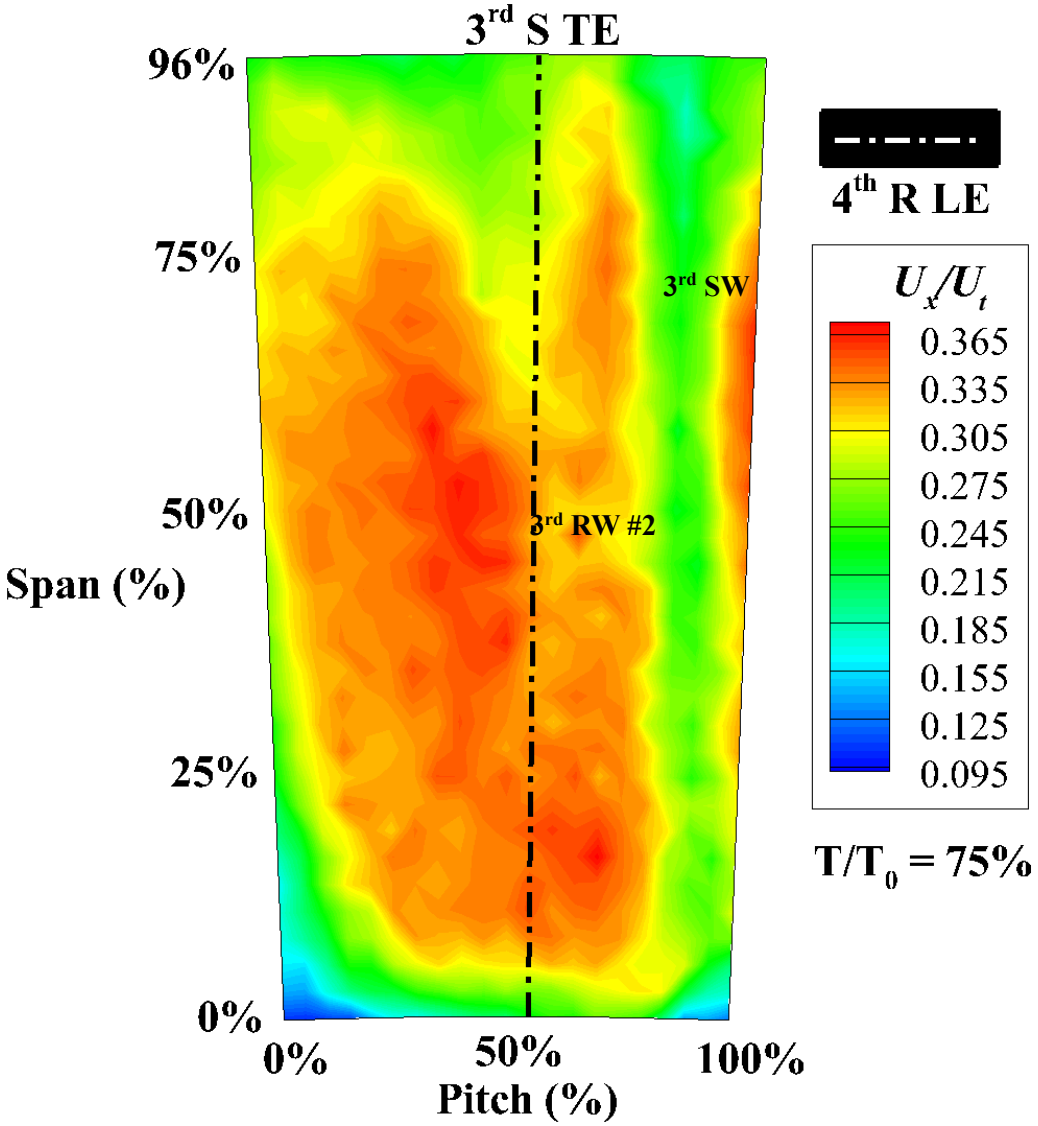

(d) Color Contour of U_x/U_t Distribution at Plane 4.0, T/T_0 = 75%, Design Point (ϕ_d)

Figure 3.4 Color Contour Plot of Instantaneous Axial Velocity Distribution at Plane 4.0, Design Point

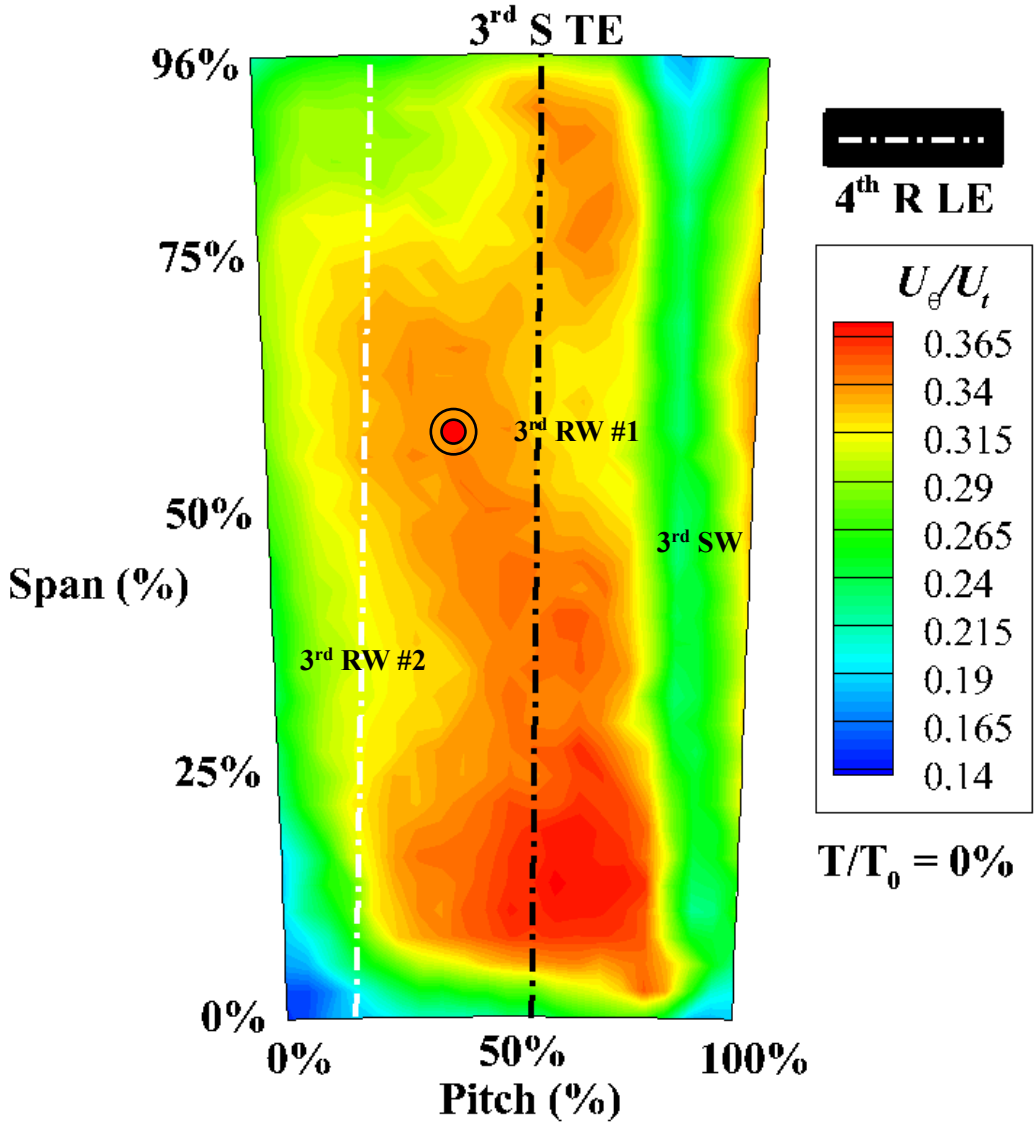

(a) Color Contour of U_θ/U_t Distribution at Plane 4.0, T/T_0 = 0%, Design Point (ϕ_d)

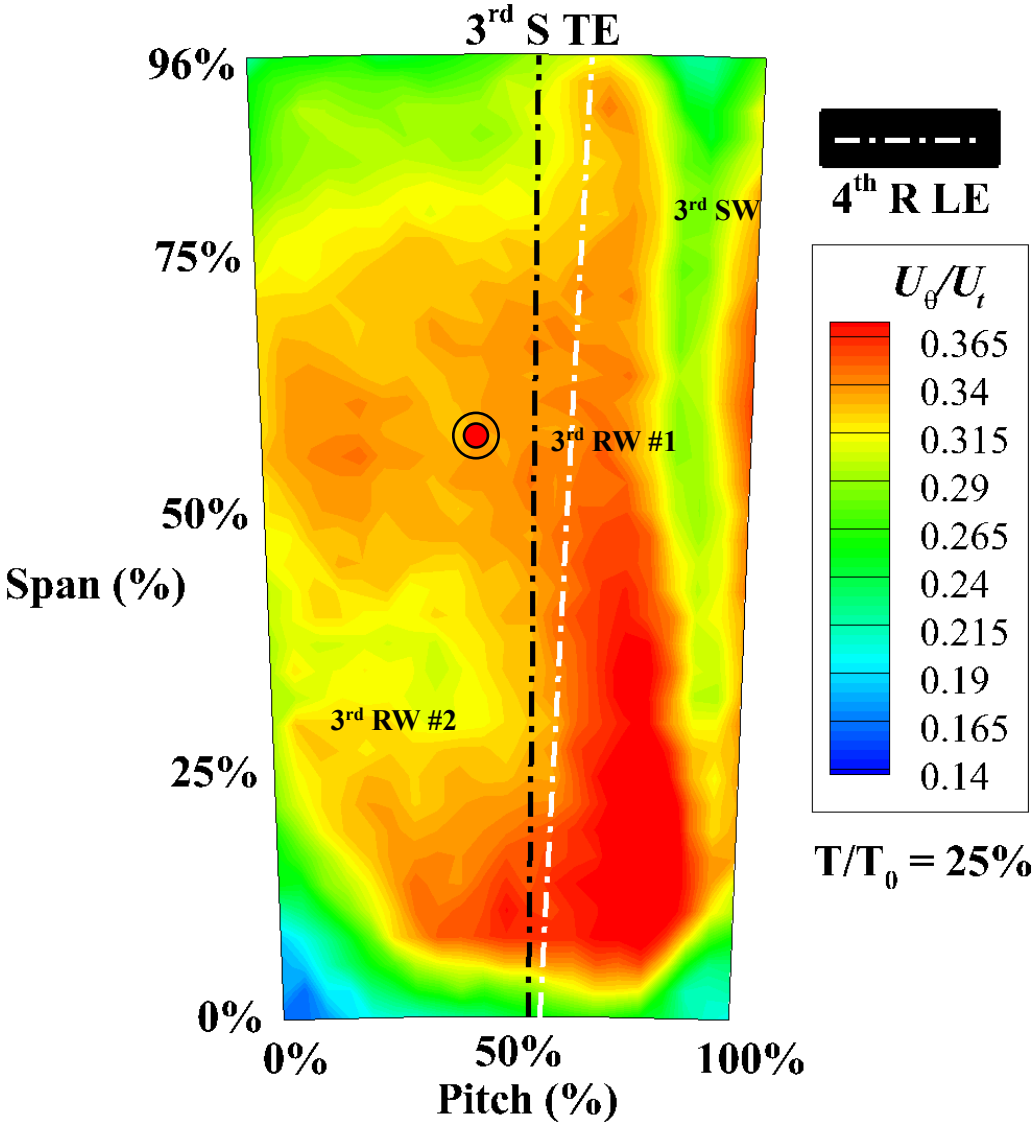

(b) Color Contour of U_θ/U_t Distribution at Plane 4.0, T/T_0 = 25%, Design Point (ϕ_d)

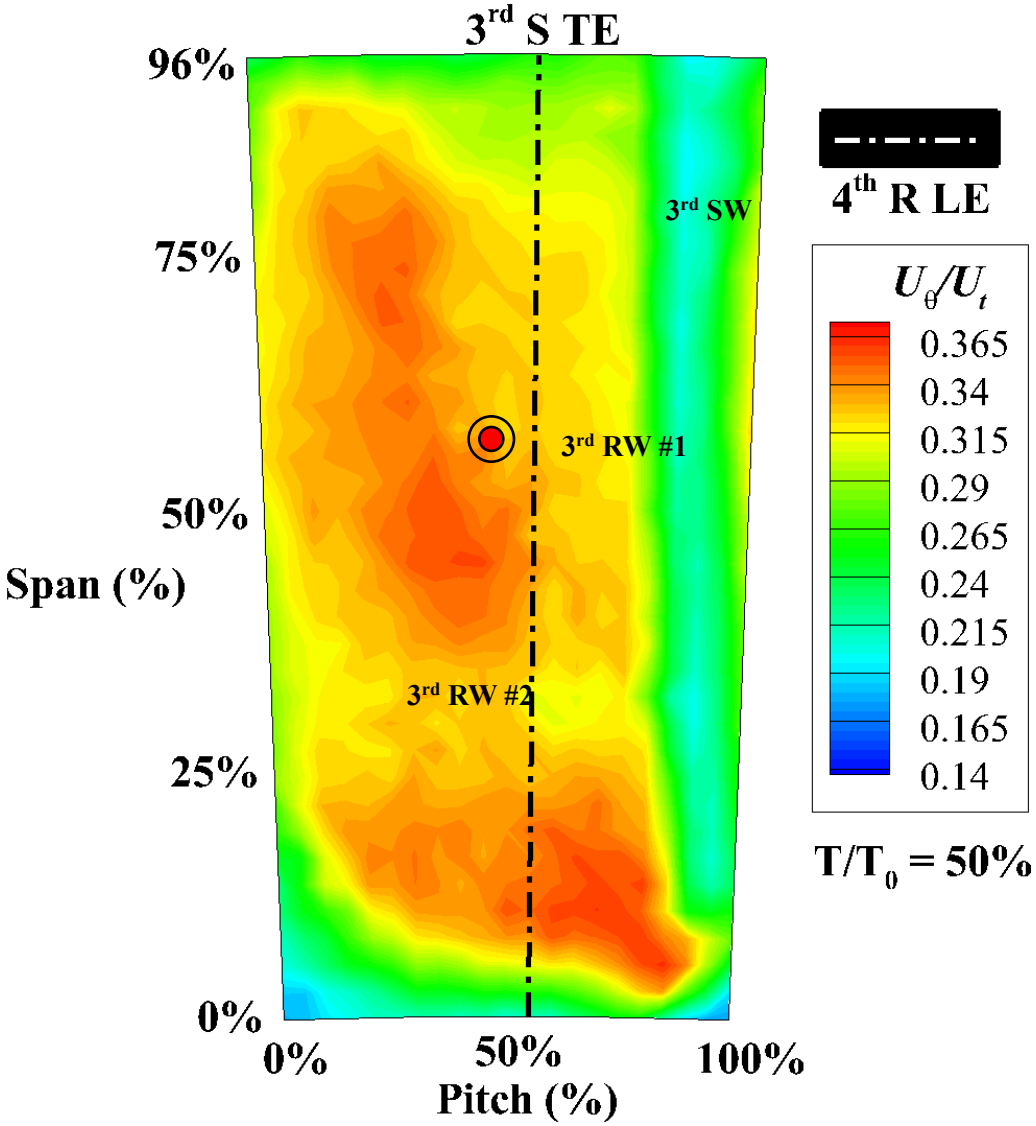

(c) Color Contour of U_θ/U_t Distribution at Plane 4.0, T/T_0 = 50%, Design Point (ϕ_d)

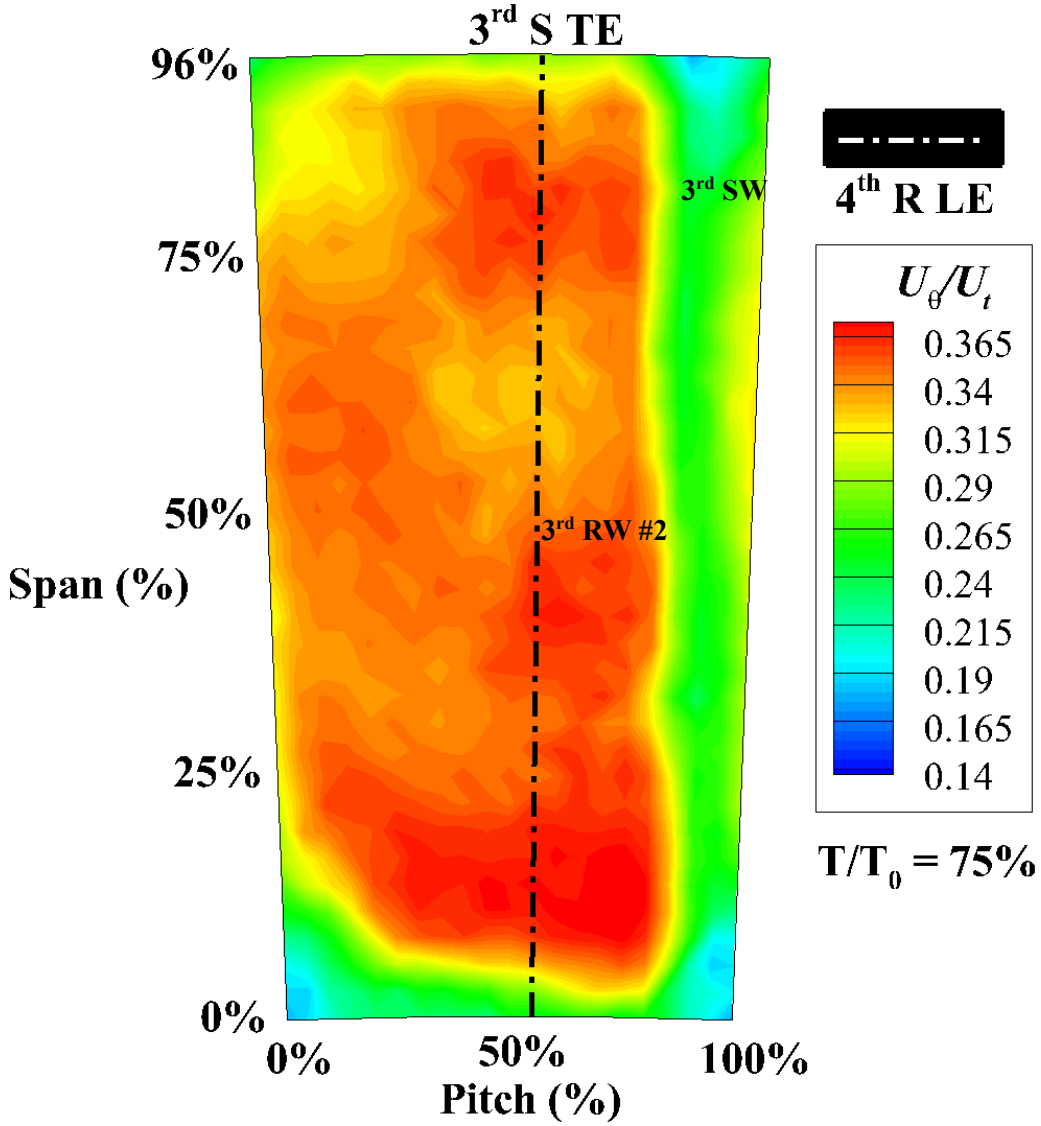

(d) Color Contour of U_θ/U_t Distribution at Plane 4.0, T/T_0 = 75%, Design Point (ϕ_d)

Figure 3.5 Color Contour Plot of Instantaneous Tangential Velocity Distribution at Plane 4.0, Design Point

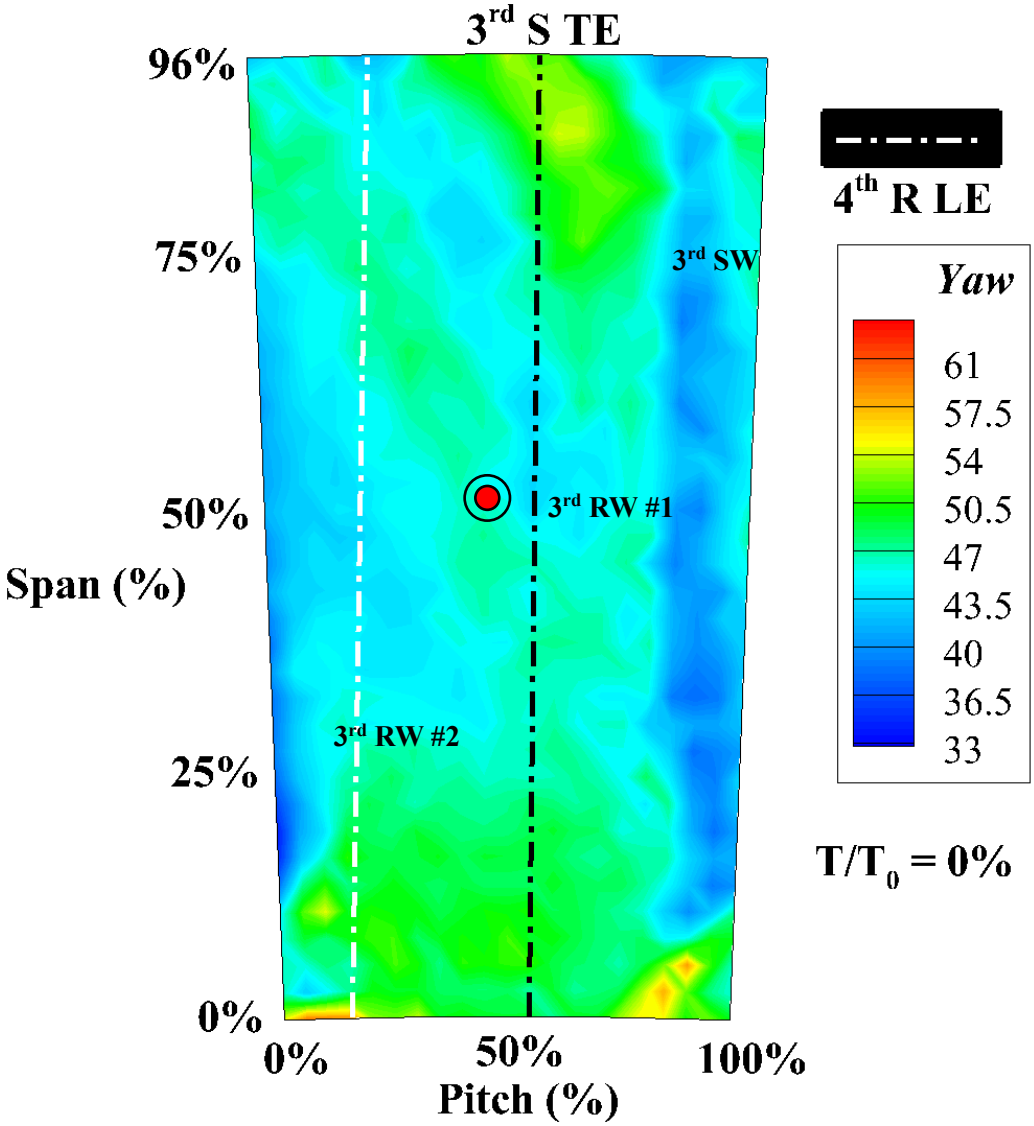

(a) Color Contour of α Distribution at Plane 4.0, T/T_0 = 0%, Design Point (ϕ_d)

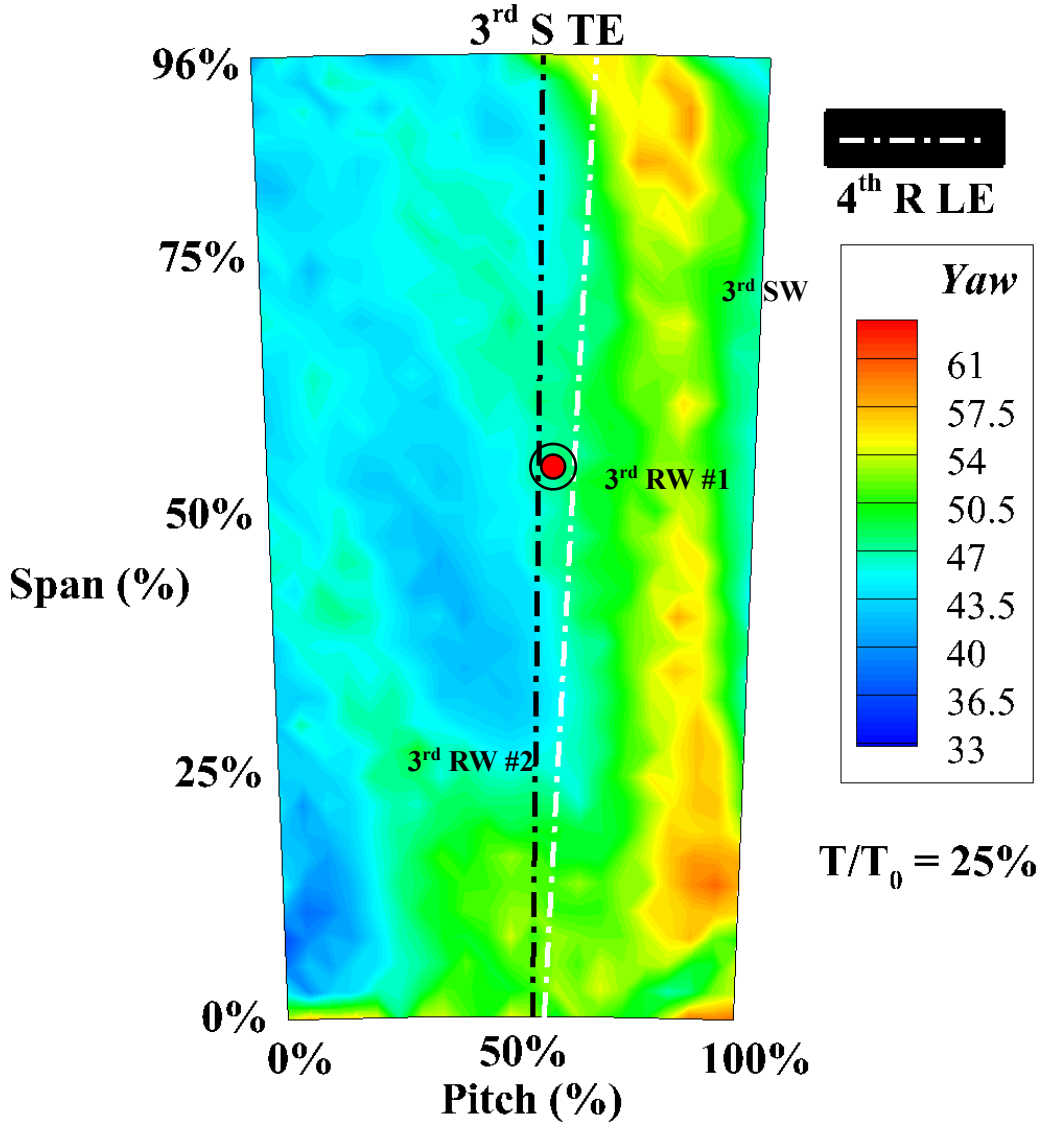

(b) Color Contour of α Distribution at Plane 4.0, T/T_0 = 25%, Design Point (ϕ_d)

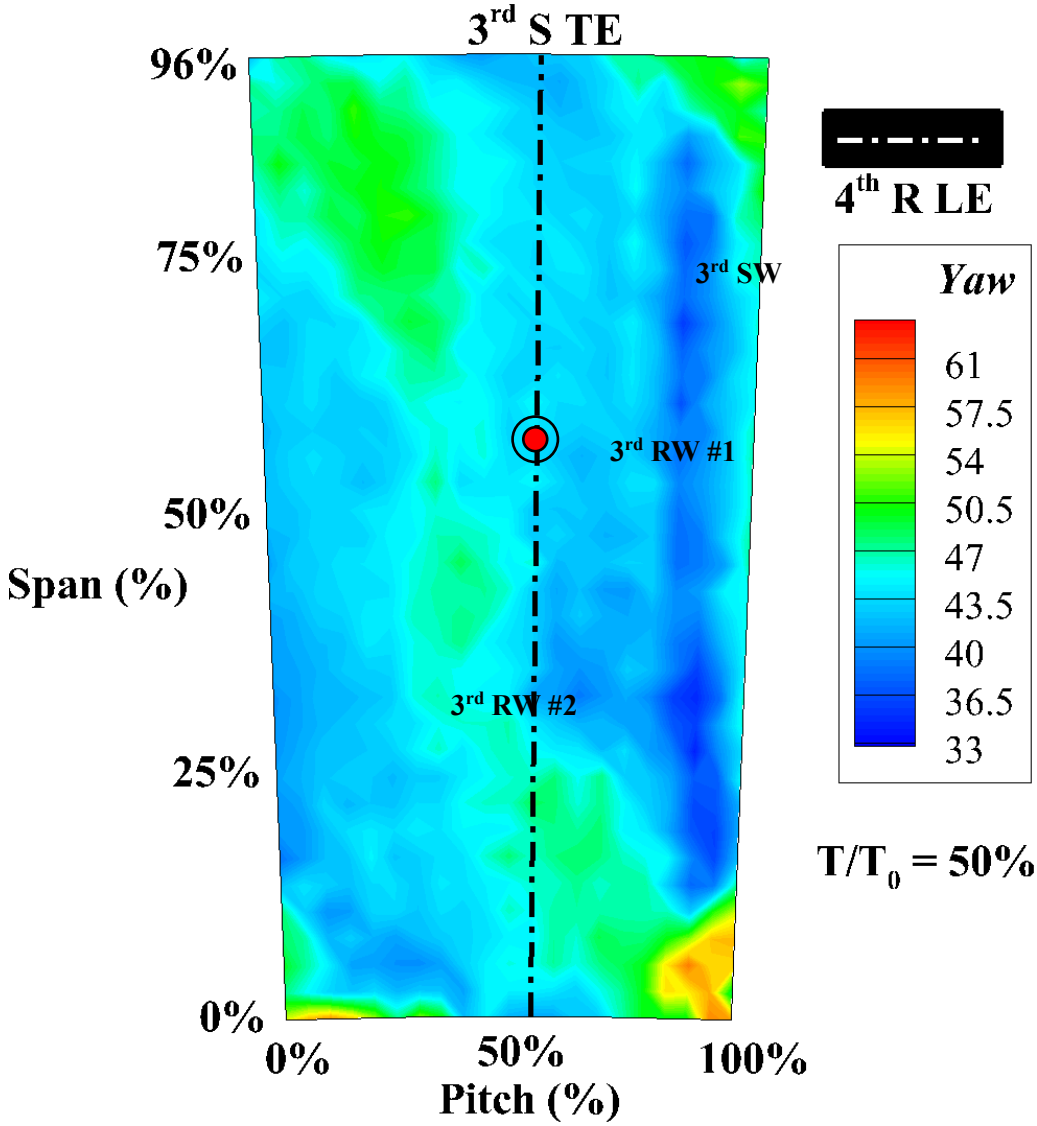

(c) Color Contour of α Distribution at Plane 4.0, T/T_0 = 50%, Design Point (ϕ_d)

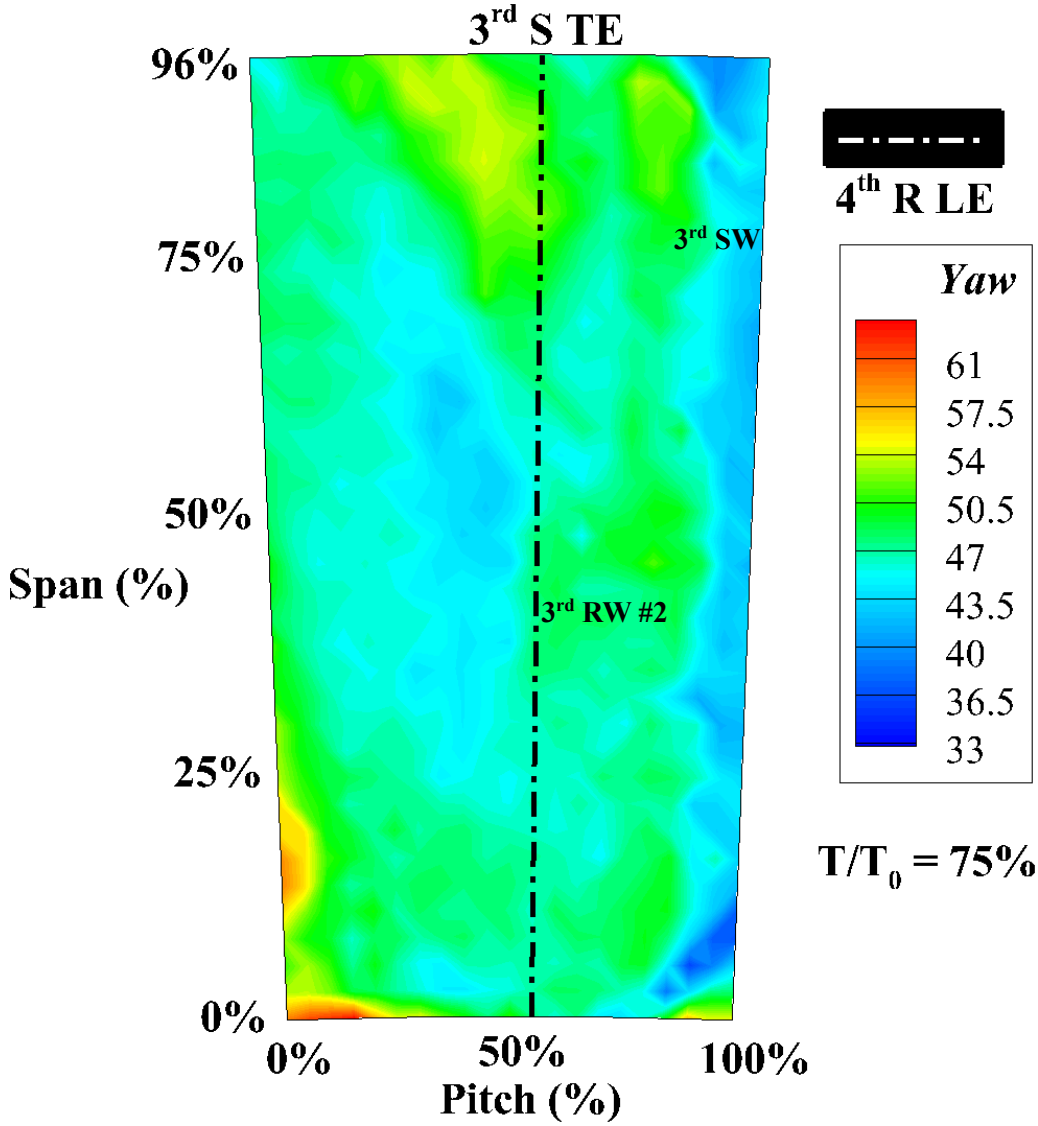

(d) Color Contour of α Distribution at Plane 4.0, T/T_0 = 75%, Design Point (ϕ_d)

Figure 3.6 Color Contour Plot of Instantaneous Flow Angle Distribution at Plane 4.0, Design Point

also has characteristics of the rotor wakes (reduced U_x and increased α). However, its tangential velocity U_θ is slower than that of the 3rd rotor wakes and is merged with the 3rd rotor wake #2 at T/T_0 = 50% and disappeared. If this low U_x region is the real 3rd rotor wake, then the passing frequency of the 3rd rotor wakes is doubled at the downstream of the 3rd stator, which is impossible. Therefore, it is evident that this low U_x region is not the 3rd rotor wake. This pseudo-wake can be explained by the recirculation between two 3rd rotor wakes due to the negative jet phenomenon [13], as illustrated in Figure 3.7. The counter-clockwise recirculation created by the CCV of 3rd rotor wake #1 alters the direction of the passage flow, reducing the U_x and increasing the α of the passage flow; a pseudo-wake region is created between the two 3rd rotor wakes by this recirculation. As the 3rd rotor wakes are transported downstream, the counter-clockwise recirculation does not affect the measuring plane, and the attenuation of the 3rd rotor wakes attenuate the magnitude of the negative jet, CCV and recirculation. Due to this, the pseudo-wake is weakened and eventually disappeared.

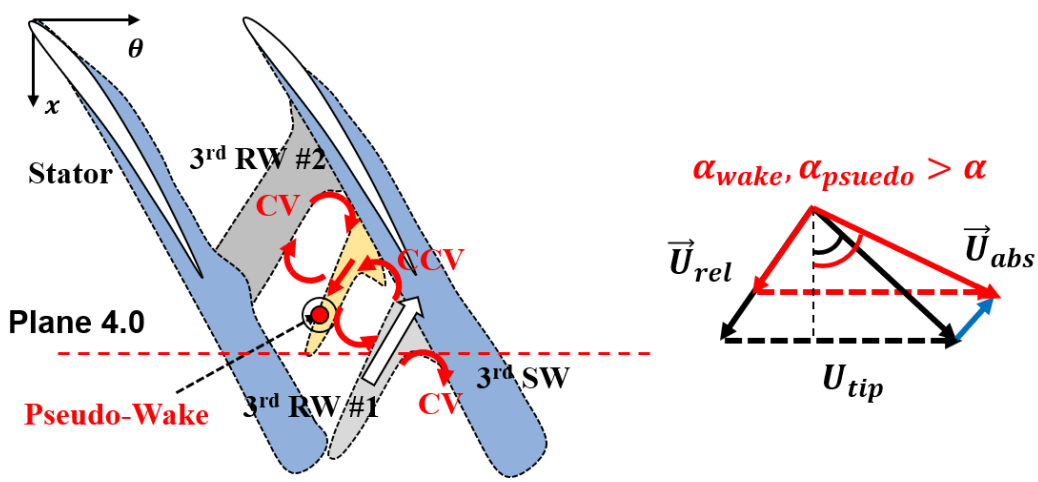

Figure 3.7 Schematic of 3rd Rotor, Stator Wakes and Psuedo-Wake inside a 3rd Stator Passage

The 3rd rotor wakes are transported downstream, varying the unsteady flow structure of the 3rd stator passage. At T/T_0 = 0%, three distinctive regions with lower U_x and higher α are located at the PS of a 3rd stator wake, the periphery of hubside corner separation and midpitch region due to the 3rd rotor wake #1, 2 and the pseudo-wake two 3rd rotor wakes (3rd RW #1 and #2) respectively. The width of 3rd corner separation is widened as the 3rd rotor wake #2 is close to the separation, which is similar to the boundary layer distortion by the rotor wake at the midspan [22, 23]. In addition, additional tipside low U_x and U_θ regions are observed, which is presumed to be caused by the 3rd rotor tip clearance flow.

At T/T_0 = 25%, the position of 3rd rotor wake # 1 and 2 are shifted towards the PS of 3rd stator wake at plane 4.0. The width of 3rd stator wake is wider compared with T/T_0 = 0%, due to the merge of the 3rd rotor wake #1 and the PS of 3rd stator wake. Experimental investigations by Lange et al. [4] and Mailach et al. [23] also observed the variation of the width and the magnitude of rotor wake due to the 'superposition' of upstream stator wake and rotor wake. In addition, the region with the highest α is located at the PS of the 3rd stator wake. This can be explained by the clockwise vortex created by 3rd rotor wake #1, as illustrated in Figure 3.7; as 3rd rotor wake #1 approaches nearby the PS of 3rd stator wake, the clockwise vortex created by the negative jet of 3rd rotor wake #1 shifts the direction of the fluid towards the PS of 3rd stator wake #1, increasing the tangential velocity component. As a result, the α is highest.

At T/T_0 = 50%, the position of 3rd rotor wake # 1 and 2 are shifted further towards the PS of 3rd stator wake at plane 4.0. The width of the hubside corner separation is reduced because the 3rd rotor wake #2 is moved towards the PS of 3rd stator wake at Plane 4.0, and does not affect the periphery of the corner separation. In addition, the width of the 3rd stator wake is reduced because the 3rd rotor wake #1 is leaving the measurement plane. As a result,

the counter-clockwise vortex of 3rd rotor wake #1 is affecting the PS of 3rd stator wake at plane 4.0, altering the direction of the flow at the location to reduce the α; reduced α is observed at the PS of 3rd stator wake in Figure 3.6, T/T_0 = 50%.

At T/T_0 = 75%, the 3rd rotor wake #1 is outside the measuring plane and the 3rd rotor wake #2 is further attenuated; color contours of U_x in Figure 3.4 (d) shows that the width of 3rd rotor wake #2 is reduced, and its U_x is increased. However, the contours also show the increased width of hubside corner separation of adjacent 3rd stator wake and the width of adjacent 3rd stator wake itself. This is due to the emergence of another 3rd rotor wake (3rd rotor wake #3) near the SS of 3rd stator blade; the existence of rotor wake distorts the SS boundary layer and the periphery of corner separation, widening the width of the adjacent 3rd stator wake. In addition, the α near the adjacent 3rd stator wake is increased due to the emerging 3rd rotor wake.

3.3 Variation of Aerodynamic Properties Downstream of 3rd Stator

This unsteady kinematics of the 3rd shrouded stator flow creates the timewise variation of aerodynamic properties, due to the different magnitude and the direction between the velocity vectors of the 3rd rotor wakes and the 3rd stator passage flow. The timewise variations of U'_x and U'_θ, indicating the difference between the instantaneous U and time-averaged $\overline{U}$ at plane 3.5 and 4.0, 50% span are presented in Figure 3.8, which show the increased U_x and decreased U_θ by the 3rd rotor wakes. At plane 3.5, the local minimum of U'_x and a local maximum of U'_θ, indicating the center of the 3rd rotor wakes, are moving towards the positive pitch direction, which is the rotating direction. However, at plane 4.0, the local U'_x minimum and the local U'_θ maximum are mainly observed at the PS and SS of 3rd stator wake. These are due to the combination of the 1) negative jet phenomenon, which pushes the 3rd rotor wakes towards the PS of the 3rd stator to

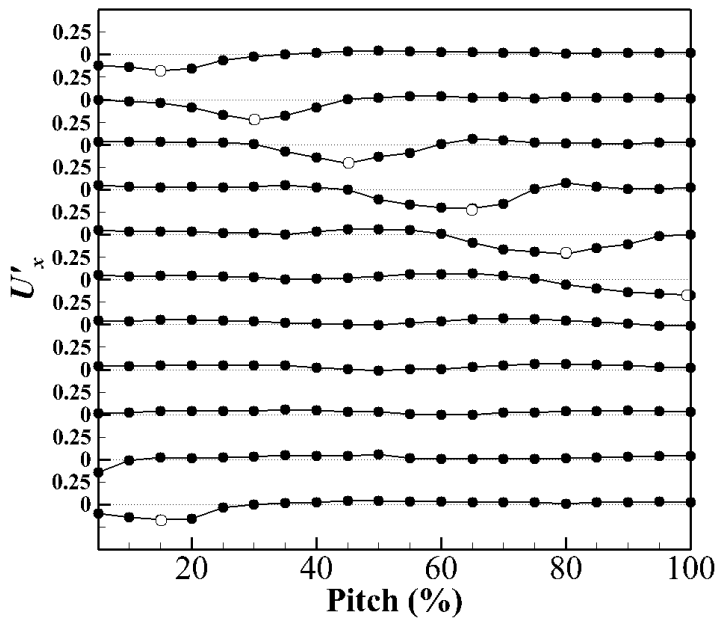

(a) Timewise Variation of Pitchwise U'_x Distribution at 50% S, Plane 3.5, ϕ_d

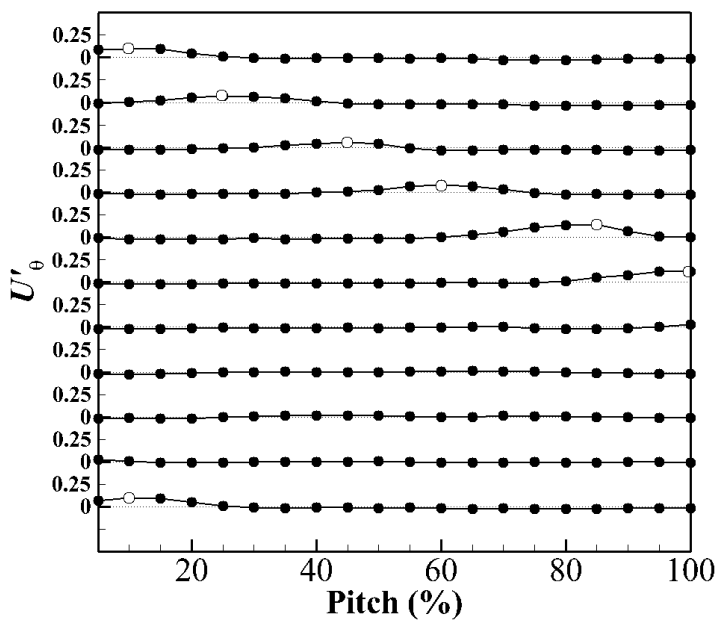

(b) Timewise Variation of Pitchwise U'_θ Distribution at 50% S, Plane 3.5, ϕ_d

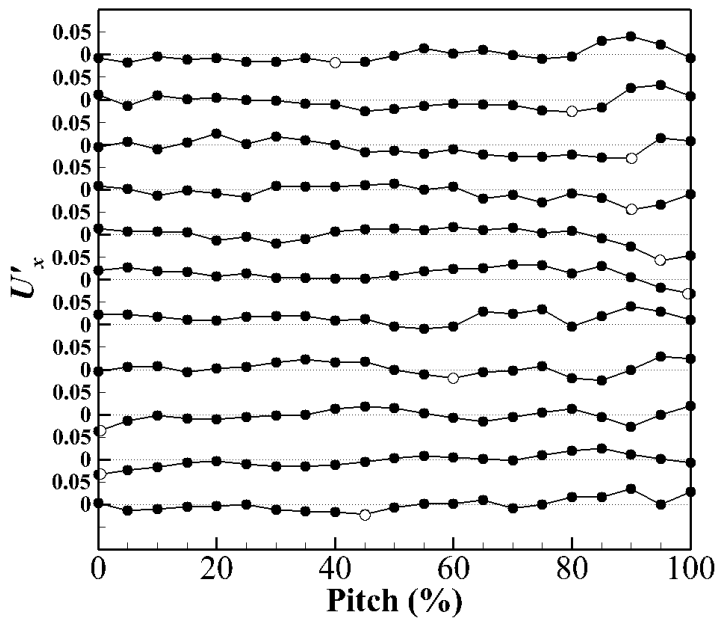

(c) Timewise Variation of Pitchwise *U'x* Distribution at 50% S, Plane 4.0, ϕ_d

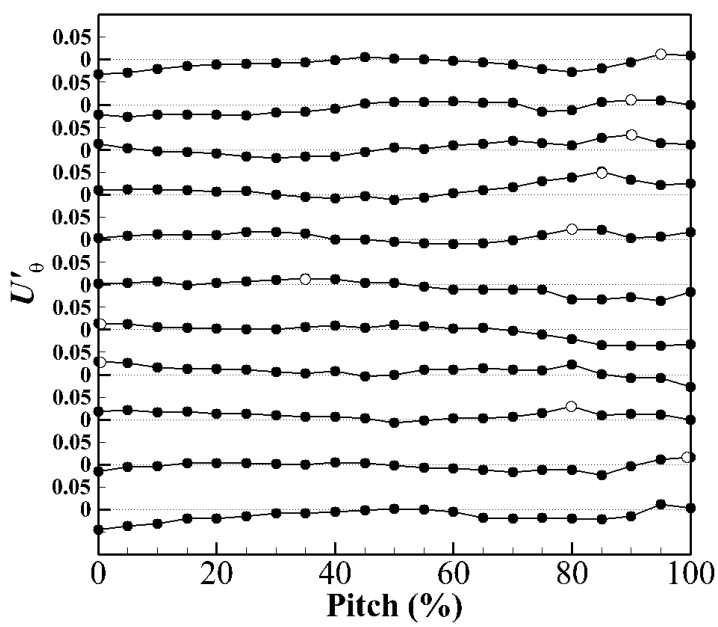

(d) Timewise Variation of Pitchwise *U'θ* Distribution at 50% S, Plane 4.0, ϕ_d

Figure 3.8 Timewise Variation of Midspan Pitchwise *U'* Distribution at Design Point

concentrate the velocity disturbances at the PS of 3rd stator, 2) the distortion of SS boundary layer of 3rd stator due to the recirculation created by the 3rd rotor wakes, which creates the velocity disturbances at the SS of 3rd stator, 3) the attenuation of the velocity disturbances by the wake stretching phenomenon, which suppresses the velocity disturbances at the stator midpitch region.

These velocity disturbances by the 3rd rotor wakes create the variation of the aerodynamic properties. Figure 3.9 presents the unsteady variation of the ratio A_b/A of the blocked region A_b and the area A of the entire passage (0 ~ 96% span, 0 ~ 100% pitch), which is equivalent to blockage, and mass-averaged α ($\overline{\alpha}^M$) of the entire passage at plane 4.0; Khalid et al. [21] suggested that the unsteadiness of velocity vector lead to the reduction of mass flow rate and the change of the α, blocking the passage flow; this concept can be quantified using the term "blockage". The magnitude of A_b/A is defined following the definition of Khalid et al. [21], which is defined in equation 1.1, and the value of the

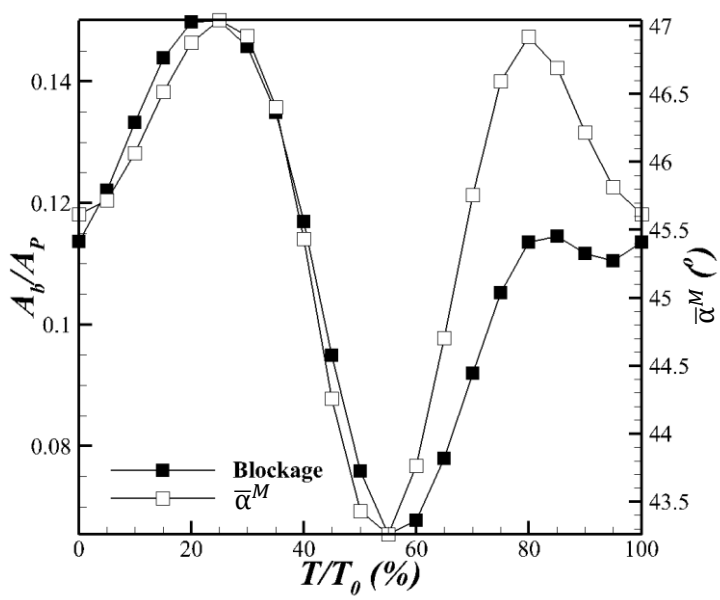

Figure 3.9 Timewise Variation of Blockage and Absolute Flow Angle at Plane 4.0

velocity at the boundary U_δ is arbitrary set to be the 99% of the time-averaged, mass-averaged U_x of the 50% span. A local maximum at T/T_0 = 20% and a local minimum at T/T_0 = 55% are observed for the blockage, whereas two local maximums at T/T_0 = 25% and T/T0 = 80% and a local minimum at T/T_0 = 55% are observed for the $\overline{\alpha}^M$.

At T/T_0 = 25%, when both the blockage and the $\overline{\alpha}^M$ are near the local maximum, the 3rd rotor wake #1 is merged with the PS of the 3rd stator wake (refer Figures 3.4 ~3.6), reducing the U_x of 3rd stator wake and increasing the $\overline{\alpha}^M$ near the PS of 3rd stator wake, as discussed in section 3.2. In addition to that, the hubside of 3rd rotor wake #2 is located at the middle of the passage, further reducing the hubside U_x and increasing $\overline{\alpha}^M$. As a result, A_b/A and $\overline{\alpha}^M$ are the highest at this period, creating the local maximum of the two variables at T/T_0 = 20%.

Between T/T_0 = 25% and 50%, the 3rd rotor wake #1, which creates the local maximum of both parameter at T/T_0 = 25%, is transported downstream, reducing the width and $\overline{\alpha}^M$. In addition to that, 3rd rotor wake #2 is attenuated as it travels downstream. Due to these, after T/T_0 =25% both the A_b/A and the $\overline{\alpha}^M$ are reduced, leading to the local minimum of the two variables near T/T_0 = 50%.

After T/T_0 = 50%, the local minima of each variable, the 3rd rotor wake #1 is outside the measuring plane and the 3rd rotor wake #2 is further attenuated. However, the 1) widened the width of hubside corner separation of adjacent 3rd stator wake and 2) the width of adjacent 3rd stator wake itself increase the overall blockage and the $\overline{\alpha}^M$ after T/T_0 = 50%. This continues until the 3rd rotor wake #3, attached at the adjacent 3rd stator wake and its corner separation, is detached at T/T_0 = 85%. After the detachment, the width of corner separation, and the adjacent 3rd stator wake are again reduced, decreasing the A_b/A and absolte $\overline{\alpha}^M$.

4. Effect of Corner Separation on Unsteady Kinematics and Flow Properties

The tip clearance flow and the hub corner separation alter the tip and hubside flow, creating the spanwise variation of the aerodynamic properties. Figure 4.1 shows the spanwise variations of time-averaged, pitchwise-averaged blockage and α; higher blockage and α at the hubside and tip regions are observed due to the corner separation and the 3rd rotor tip clearance flow. Furthermore, these can affect the unsteady kinematics of stator flow. It has been observed from the previous studies that the tip clearance flow can be considered as a widened rotor wake [37]; this interacts with 1) the casing boundary layer to widen the low momentum at the region [38], and 2) the upstream stator wake to alter its direction and the magnitude of velocity, varying the casing static pressure, tip incidence angle and blockage [4, 14].

Not only that, previous researches hinted that the hubside corner separation can

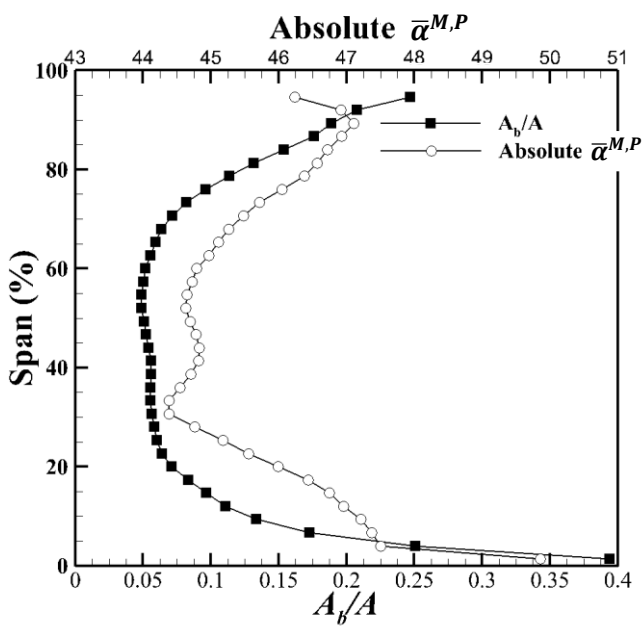

Figure 4.1 Spanwise Variation of Blockage and Flow Angle at Plane 4.0

also affect the unsteady kinematics of shrouded stator flow. Poensgen and Gallus [17, 18] observed the increased unsteadiness at the periphery of the hub corner separation due to the upstream rotor wake, but the center of the corner separation was not affected by the wake. This indicates that the corner separation blocks the wake, similar to the steady measurements by Joslyn and Dring [30], which can create the unsteady hubside radial movements as suggested by Sanders et al. [11]. However, no previous researches have focused the effect of hubside corner separation on the unsteady kinematics of multistage shrouded stator flow. Therefore, the unsteady kinematics of multistage shrouded stator flow related to the hubside corner separation of the shrouded stator will be discussed in this section.

4.1 Radial Movements Created by 3rd Rotor Wakes and Hubside Corner Separation

The color contour of U_r/U_t and secondary velocity vector $\vec{U} - \vec{U}_{|avg,E|}$ at Plane 3.5 and 4.0 are discussed in this chapter to investigate the unsteady radial movements and their hubside unsteady flow kinematics. The radial movements of the upstream 3rd stator will be discussed first; Figure 4.2 shows the color contour of U_r/U_t and $\vec{U} - \vec{U}_{|avg,E|}$ distribution at Plane 3.5. A region with positive U_r is observed from 0% to 50% span, ~75% pitch, which coincides with the 3rd rotor wake. Next to the wake, a passage vortex and counter-rotating vortex are located, which are typical hubside secondary flow.

At the hubside of the 3rd rotor wake, a region with local positive U_r is observed at the ~10% span, ~85% pitch. The magnitude of the positive U_r is about 0.18 U_t, which is too high to be generated by vortical structures. At this period, the 2nd stator wake #2 is detached from the PS of 3rd rotor wake, and the 2nd stator wake #1 is away from the 3rd rotor wake. Therefore, it can be presumed that the hubside passage flow passing along the

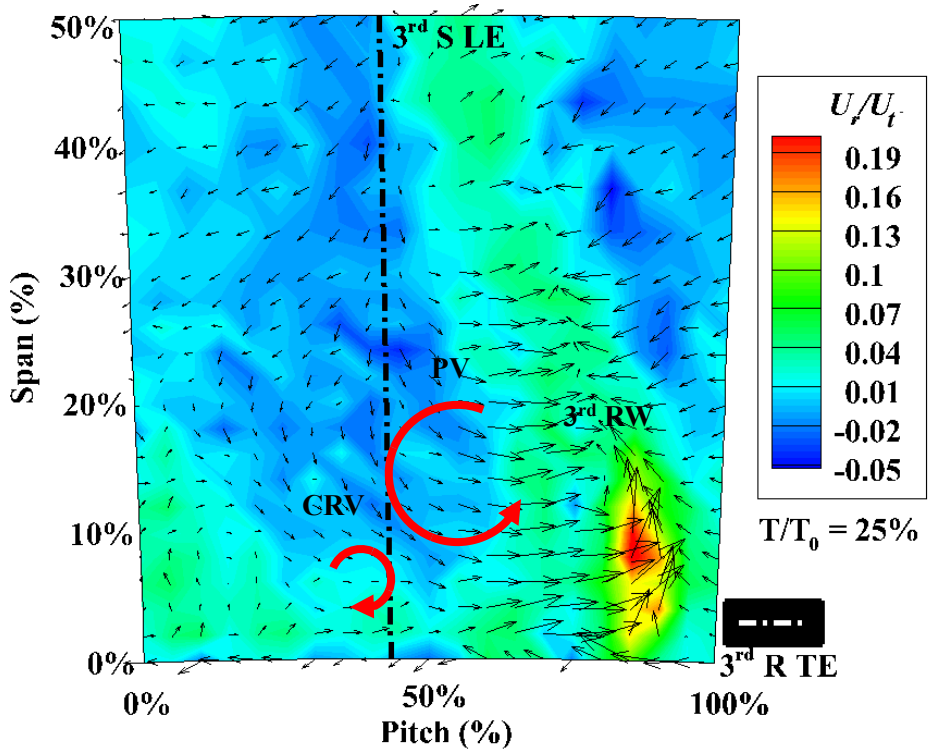

Figure 4.2 Color Contour Plot of Instantaneous Radial Velocity and Secondary Velocity Vector Distribution at Plane 3.5, Design Point, T/T_0 = 25%

PS of 3rd rotor wake created this radial movement, as illustrated in Figure 4.3.

1) The concave surface of the rotor blade makes the passage flow at PS flows along the PS of the 3rd rotor.

2) By the slip velocity, the relative direction of PS 2nd SW #2 is perpendicular to the PS surface, which acts as a blockage to the passage flow on the PS surface.

3) The blockage at the hubside is thicker due to the corner separation of the 2nd stator wake #2.

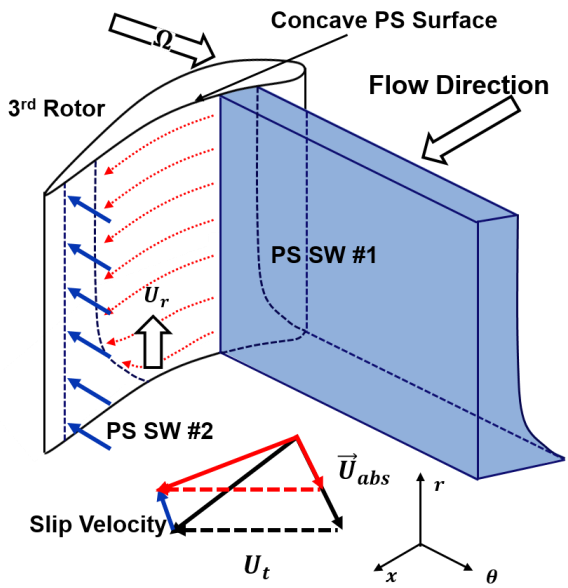

Figure 4.3 Schematic of the Hubside Rotor Passage Radial Movement

4) This thicker hubside blockage alters the hubside passage flow towards the tip region, creating the radial movement.

To assess the effect of this radial movement on the hubside aerodynamic properties, the pitchwise distribution of U_x/U_t, U_θ/U_t, and U_r/U_t at Plane 3.5, 85% pitch (where the radial movement is observed), T/T_0 = 25%, are presented in Figure 4.4. Compared with the pitchwise and timewise averaged value, Increased U_θ by the 3rd wake is observed at the hubside ranging from 0 to ~10% span, suggesting that the 3rd rotor wake is affecting up to ~10% span. The U_x is also reduced due to the 3rd rotor wake, however, their range (~20%) is outside the effect of the 3rd rotor wake (~10%). At the same time, U_r distribution shows that U_r is increased at 0% ~ 20% span; the positive hubside radial movement transported the low hubside axial momentum fluid, reducing the U_x at the region. It is expected that this radial movement enhances the mixing between the passage flow and

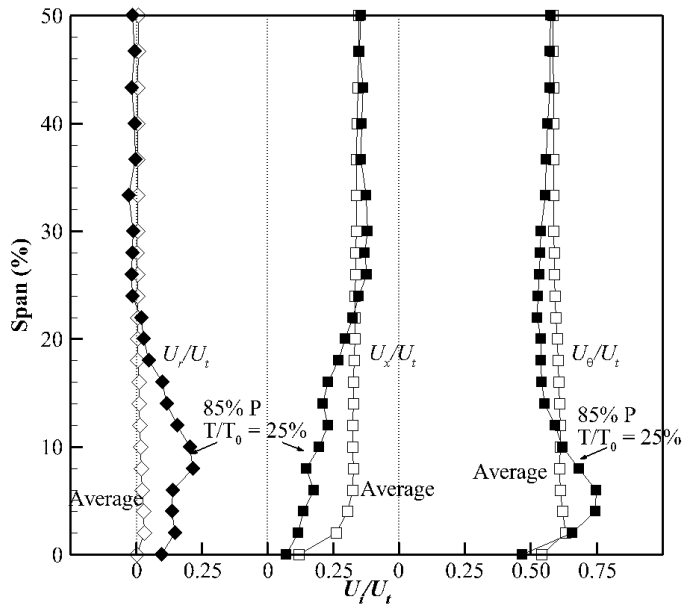

Figure 4.4 Radial Distribution of Velocity Component at Plane 3.5, 85% *P*, *T/T₀* = 25%, Design Point

the hubside flow, increasing the mixing loss.

The radial movements at the downstream of the 3rd stator will be discussed next. The color contour of U_r/U_t and secondary velocity vector $\vec{U} - \vec{U}_{|avg,E|}$ distributions at Plane 4.0, T/T_0 = 50% are shown in Figure 4.5. A typical passage vortex (PV) is observed near the periphery of corner separation, and two positive U_r regions are observed at the PS of 3rd stator wake (marked as 1) in Figure 4.5) and at the hubside SS of 3rd stator wake (marked as 2) in Figure 4.5), respectively. The positive radial movement 1) at the PS of 3rd rotor wake is observed ranging from 0% to 50% span of the 3rd stator wake when the 3rd rotor wake is merged with the PS of the 3rd stator. This radial movement can be explained

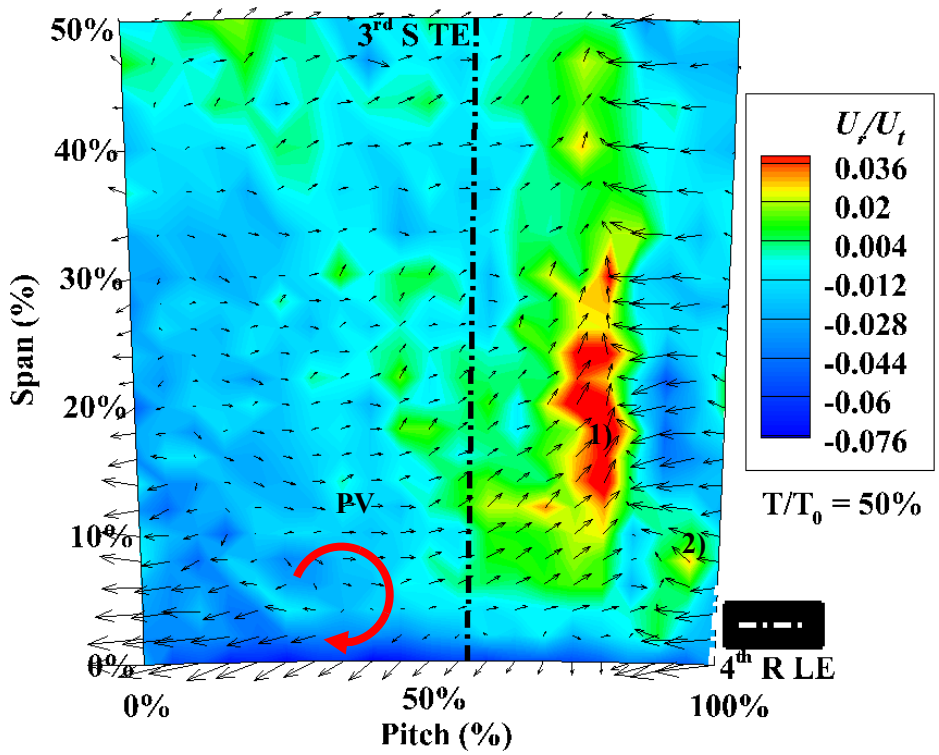

Figure 4.5 Color Contour Plot of Instantaneous Radial Velocity and Secondary Velocity Vector Distribution at Plane 4.0, Design Point, T/T_0 = 50%

as follows;

1) The rotor blades of modern axial compressors are twisted, including the SNU compressor. As a result, the axial projection of the rotor blade onto the radial-tangential plane is not parallel to the radial direction (spanwise).

2) Due to this rotor geometry, the 3rd rotor wake is angled to the spanwise direction, as observed in Figure 3.4.

3) This angled rotor wake is transported to the PS of 3rd stator wake by the negative jet and, is merged with the 3rd stator wake.

4) This collision with the angled and stationary wakes creates the radial movements. Its direction is towards the tip region (positive U_r) because the hubside of the 3rd rotor wake collides first.

Another positive radial movement 2) located at the hubside SS of 3rd stator wake, inside the corner separation of 3rd stator wake, is first generated as the hubside part of radial movement 1). This hubside radial movement 1) is penetrating the hubside 3rd rotor wake and is located inside the corner separation, which is contrary to the midspan region. The hubside corner separation is responsible for this penetration; at the hubside, the static pressure P_s of the 3rd stator wake is lower due to the corner separation. This enables the 3rd rotor wake penetrates the center of the corner separation.

The positive radial movement at the hubside SS of stator wake was also reported by Wellborn [50]; he observed the positive radial movement at the identical location (hubside SS of stator wake) from his unsteady measurements at increased loading. Kim [47] also found the radial movement at the hubside SS of the shrouded stator from his steady calculations. They both concluded that this phenomenon is caused by the hubside secondary flows and reported that the cavity flow can be re-ingested into the mainstream passage due to these flows.

4.2 Reduced Attenuation of Velocity Disturbances by 3rd Rotor Wake due to Corner Separation

It is known from the previous studies that the velocity disturbances created by rotor wakes induce the unsteadiness of aerodynamic properties inside the axial compressor [4, 8-20, 22-24]. These are attenuated due to the viscous mixing and the wake stretching inside the stator passage by the elongation of wake fluid component. [8, 10, 11, 22-24]. At

the axial gap between the rotor and the stator row, the attenuation by the viscous mixing dominates, creating the exponential decay of the rotor wake with respect to the axial position [19]. Due to this, the attenuation by the mixing is increased if the axial gap is widened [22, 23, 25]. Inside the stator passage, the attenuation by the wake stretching has the higher percentage compared with the viscous mixing [10], and the ratio of the velocity disturbances upstream and downstream of the stator blade is inversely proportional to the ratio between the inlet and exit passage width [8, 10]. However, the effective width of the hubside of the shrouded stator is limited by the corner separation [30], suggesting that the effective width of the shrouded stator is reduced. This can affect the attenuation of the wake by wake stretching, as illustrated in Figure 4.6; reduced effective width decreases the elongation of the fluid component perpendicular to the streamline, which results in reduced attenuation of rotor wakes and increased hubside velocity disturbance compared with the

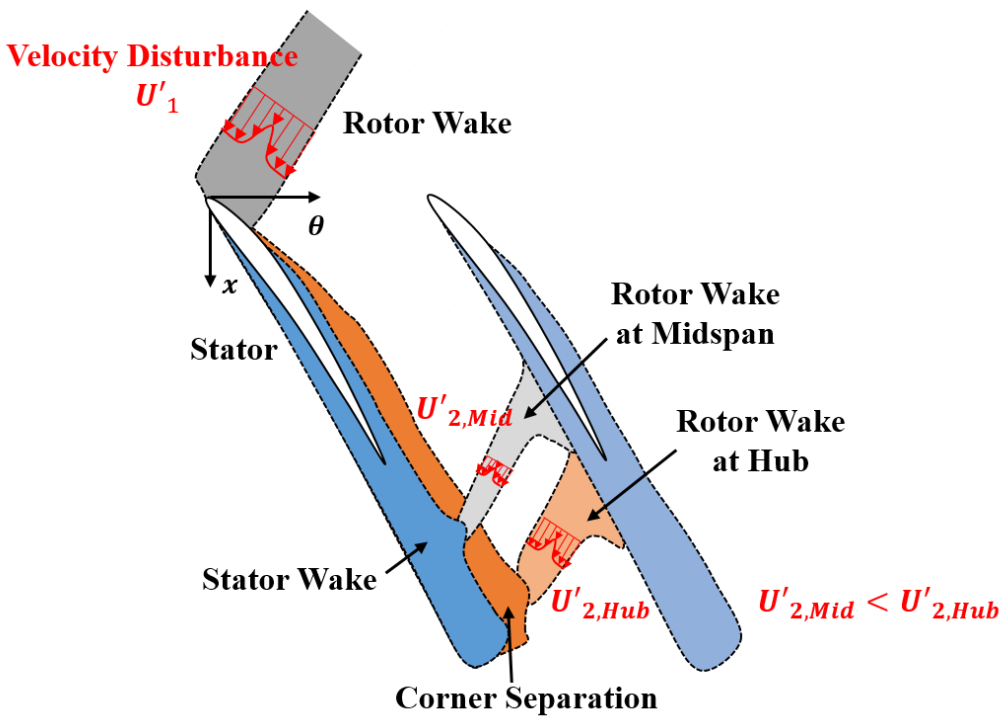

Figure 4.6 Schematic of Rotor Wakes inside a Hubside Shrouded Stator Passage

midspan region.

To assess the effect of the corner separation on the attenuation of the rotor wake, the velocity disturbances by 3rd rotor wakes are quantified using the timewise variations of U_x' and U_θ', which is the difference between the instantaneous U and the time-averaged U at a single point. The maximum U_θ' and the minimum U_x' at 10%, 50%, and 90% span are plotted versus timewise at both plane 3.5 and 4.0 in Figure 4.7 and 4.8, respectively. The minimum U'_x and maximum U'_θ at 50% and 10% span at plane 3.5 (Figure 4.7) show positive $U'_{\theta,\,max,}$ and negative $U'_{x,\,min}$ at the location of the 3rd rotor wake, which are typical behavior of rotor wakes. The $U'_{\theta,max}$ and $U'_{x,min}$. are close to zero at T/T_0 = 60 ~ 80% due to the disappearance of 3rd rotor wake. The phase of the U' at 10% span is faster than that of 50% span due to the angled rotor wake relative to spanwise direction, as discussed in Section 4.1. The magnitude of $U'_{\theta,max}$ and negative $U'_{x,min}$ are higher at 10% span. Furthermore, at T/T_0 = 35%, the $U'_{x,min}$ at 10% span shows local minimum contrary to that of 50% span. This is due to the hubside positive radial movement created by 2nd stator wake, which was discussed in section 4.1. By this movement, the hubside fluid with low axial momentum is transported towards tipside up to ~20%, further reducing the wake U_x, and $U'_{x,min}$.

The $U'_{\theta,max}$ and $U'_{x,min}$ at 90% span show qualitatively identical behavior, but their phases are different and the magnitude of $U'_{\theta,max}$ and $U'_{x,min}$ are lower. It is thought that the velocity disturbances by the 3rd rotor wake is dampened due to the low U_x and U_θ region by the interaction between the tip clearance flow and the casing boundary layer, which was observed by Shin et al. [71],

The timewise variation of $U'_{\theta,max}$ and $U'_{x,min}$ at each span, Plane 4.0 in Figure 4.8 show qualitatively identical behavior. The magnitude of the U' are reduced compared with the upstream due to the attenuation of the 3rd rotor wake as the rotor wake passes the 3rd

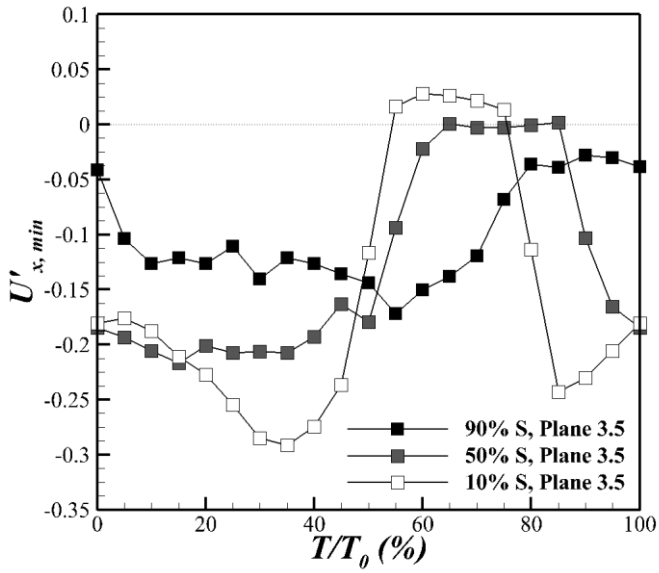

(a) Timewise Variation of Minimum U'_x at Plane 3.5

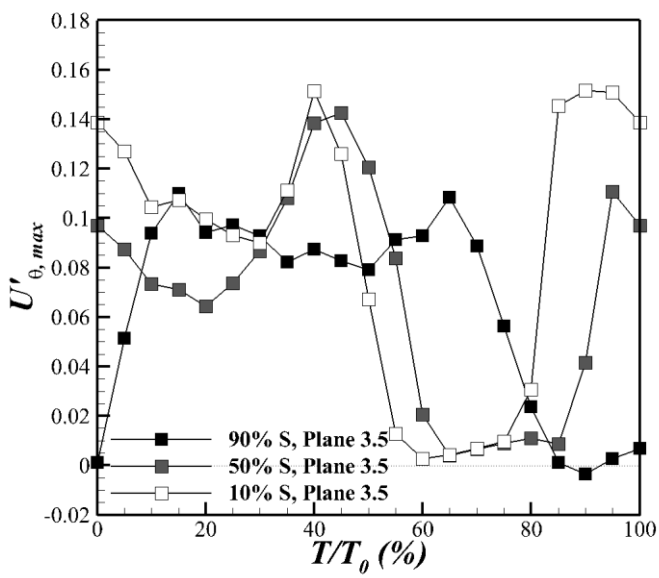

(b) Timewise Variation of Maximum U'_θ at Plane 3.5

Figure 4.7 Timewise Variation of Minimum U'_x and Maximum U'_θ at Plane 3.5

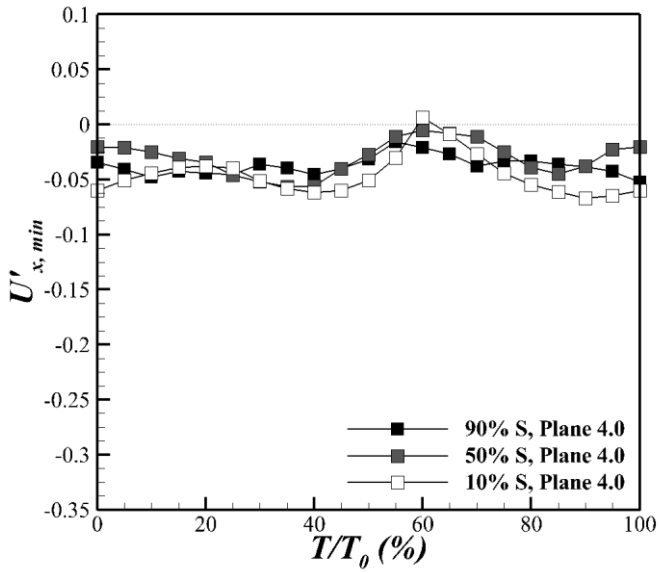

(a) Timewise Variation of Minimum U'_x at Plane 4.0

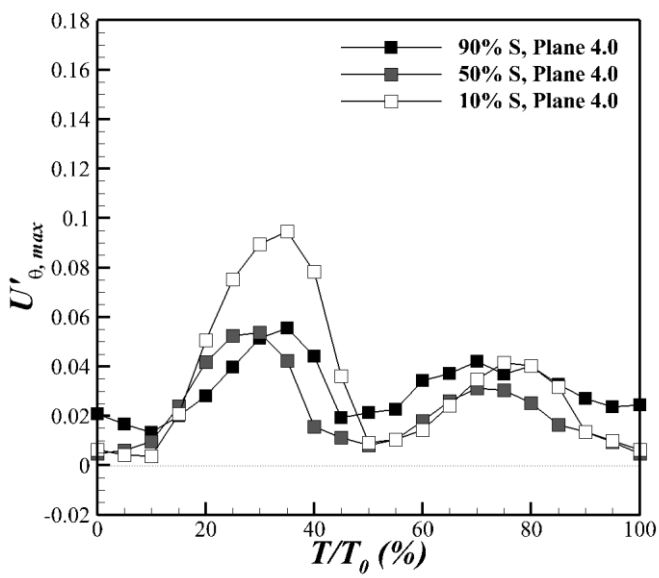

(b) Timewise Variation of Maximum U'_θ at Plane 4.0

Figure 4.8 Timewise Variation of Minimum U'_x and Maximum U'_θ at Plane 4.0

stator passage. In Figure 4.7 (b), the timewise variation of $U'_{\theta,max}$ shows two local peaks at T/T_0 ~30% and 80%. For the first peak (T/T_0 ~ 30%), the maximum U'_θ is observed at the PS of 3rd stator due to the merge of the 3rd rotor wake #1 on the 3rd stator at the period (Figure 3.4 (b)). For the second peak (T/T_0 ~ 80%), it is observed at the periphery of corner separation at the adjacent 3rd stator due to the emergence of 3rd rotor wake at the SS of adjacent 3rd stator wake (Figure 3.4 (d)).

The rate of change of the velocity disturbances $(U'_{i,1}-U'_{i,2})/ U'_{i,1}$ of U, U_x and U_θ at each span are compared to assess the effect of the corner separation on the attenuation of 3rd rotor wake. Table 4.1 summarizes the value of U'_{max}, $U'_{x,min}$, $U'_{\theta,max}$, at plane 3.5 and 4.0, and the rate at each span. At 50% span, the U'_{max}, $U'_{x,min}$ and $U'_{\theta,max}$ are reduced by 63.1%, 74.8%, and 67.0%, respectively. At 90% span, U'_{max}, $U'_{x,min}$ and $U'_{\theta,max}$ are reduced by 29.2%, 69.3%, and 49.6%, respectively. However at 10% span, these values are reduced to 24.4%, 74.7%, and 37.7%, respectively; the 3rd wake is less attenuated at the hubside of the 3rd stator, which confirms the previous hypothesis that the corner separation would reduce the attenuation of the wake.

However, this rate of the wake attenuation includes the viscous mixing at the axial clearances between the rotor and stator; Schlichting and Gersten [73] theoretically calcu lated the decaying wake profile by the viscous mixing, and Stauter et al. [19] deduced a correlation of the decay rate of velocity disturbances by a rotor wake inside the axial clearance, using experimental results from a two-stage low-speed axial compressor. The decay rate is exponential, which is the function of the axial distance travelled non-dimensionalized by the axial chord length, as shown in equation 4.1.

$$\frac{U'_\theta(x)}{U'_{\theta 0}} = e^{-a(\frac{x}{C_x})} \qquad (4.1)$$

At the upstream of the 3rd stator, the axial distance between the plane 3.5

Table 4.1 Summary of U'_i at Plane 3.5 and Plane 4.0 and Decay Rate

Span	U'_i	U'_i at Plane 3.5	U'_i at Plane 4.0	$(U'_{i,1}-U'_{i,2})/ U'_{i,1}$ (%)
50%	U'_{max}	0.07988	0.029476	**63.10**
	$U'_{x,min}$	-0.22746	-0.05735	**74.79**
	$U'_{\theta, max}$	0.154171	0.050813	**67.04**
10%	U'_{max}	0.074534	0.056361	**24.38**
	$U'_{x,min}$	-0.3213	-0.08146	**74.65**
	$U'_{\theta, max}$	0.152018	0.094706	**37.70**
90%	U'_{max}	0.051605	0.036563	**29.15**
	$U'_{x,min}$	-0.17168	-0.05264	**69.34**
	$U'_{\theta, max}$	0.109913	0.055408	**49.59**

and the LE of the 3rd stator is shown at Figure 4.8: 0.346 C_x, 0.363 C_x and 0.395 C_x for the 10% span, 50% span, and 90% span, respectively. If the exponential constant 2.295 from the Stauter et al. [19] is applied, then the exact magnitude of the wake attenuation by the viscous mixing can be obtained, which enables the attenuation of the wake inside the 3rd stator passage; The axial chord difference yields decay rate at 10% span 3.84% lower, and 7.67% higher compared with 50% span.

At the downstream of the 3rd stator, the axial distance between the Plane 4.0 and the TE of the 3rd stator is 0.359 C_x, 0.317 C_x and 0.267 C_x at the 10% span, 50% span, and 90% span, respectively. This yields additional 10.03% decay of the 3rd rotor wake at 10% span and 12.21% less decay ratio at 90% span.

If the ratio of U'_2/ U'_1 at the upstream axial clearance between the plane 3.5 and the 3rd stator LE, 50% span is called $D_{vis,1}$, then the rates at the similar location, at 10% span and 90% span are $D_{vis,1}$/0.961 and 1.077 $D_{vis,1}$. In the same manner, if the ratio of U'_2/ U'_1 at the downstream axial clearance between the plane 4.0 and 3rd stator TE, 50%

span is called $D_{vis,2}$, then the decay rates at the similar location, at 10% span and 90% span are 1.100 $D_{vis,2}$ and $D_{vis,2}$/0.891, as illustrated in Figure 4.9. Combining these two yields $D_{vis,1}D_{vis,2}$ at the 50% span and 1.058 $D_{vis,1}D_{vis,2}$ at the 10% span and 0.960 $D_{vis,1}D_{vis,2}$; the viscous mixing is 5.80% increased at 10% span, and 4.21% reduced at 90% span owing to the different axial clearance. If the decay rate by the wake stretching inside the stator will be called D_{stator}, the total rates of U'_2/U'_1 between the plane 3.5 and 4.0 at each span location are equal to $D_{vis,1}D_{vis,2}D_{stator,\ 50\%\ S}$, 1.058 $D_{vis,1}D_{vis,2}D_{stator,\ 10\%\ S}$ and 0.960 $D_{vis,1}D_{vis,2}D_{stator,\ 90\%\ S}$ at 50% span, 10% span and 90% span, respectively; ~6% variation of the attenuation of the velocity disturbances by the viscous mixing is generated due to the spanwise variation of axial clearance.

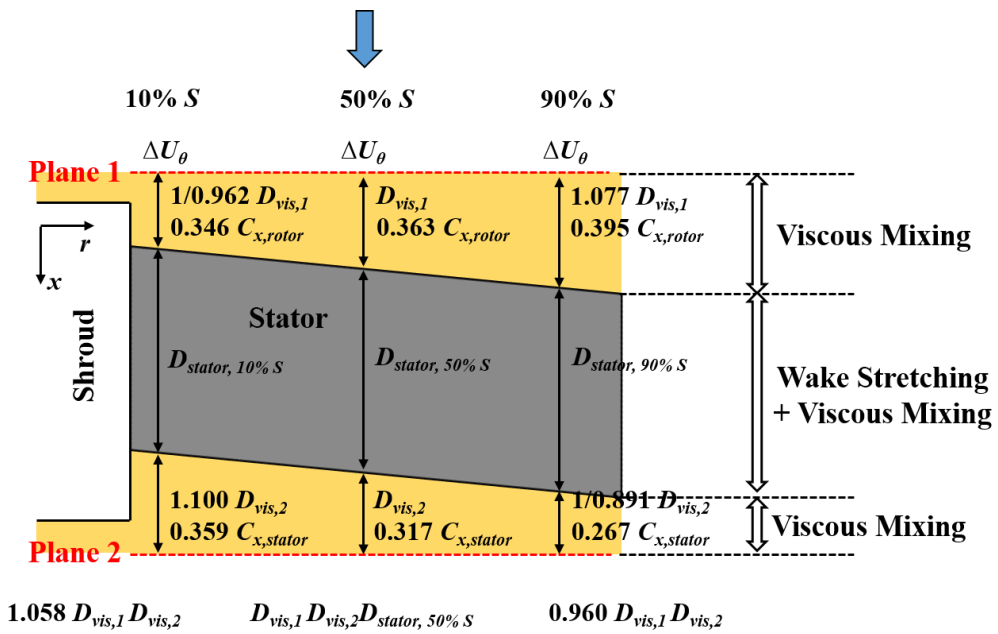

Figure 4.9 Axial Distance and Decay Rate Between the Measuring Planes and the 3rd Stator

This ~6% variation is lower than the difference of the total decay rate of the wake at the different spanwise direction (~30% at 10% span versus ~60% at 50% and 90%). Furthermore, the viscous mixing inside blade passages is ~1/6th order of that of the wake stretching [3]. Thus, it can be concluded that the reduced attenuation of the rotor wake at the hubside of the shrouded stator is due to the reduced wake attenuation, which is caused by the hubside corner separation blocking the passage.

4.3 Increased Variation of Hubside Unsteady Aerodynamic Properties

The existence of hubside corner separation of shrouded stator affects the aerodynamic properties of hubside passage flow. Figure 4.10 illustrates the comparison of the timewise variation of A_b/A, and $\boldsymbol{\alpha}^{M,P}$ at the hub (0~25% span), passage (25~75% span) and tip (75~96% span) regions. Both variables show qualitatively identical behavior with different magnitudes and phases; The magnitude of timewise-averaged $\overline{A_{b,local}}/A$ at Figure 4.10 (a) shows that the hubside $\overline{A_{b,hub}}/A$ is the highest (35.62% of the enitre $\overline{A_b}/A$), followed by the tipside $\overline{A_{b,tip}}/A$ (34.38%) and the passage $\overline{A_{b,pas}}/A$ (29.99%).

The passage blockage is mainly caused by the wake of the 3rd stator and 3rd rotors; as a result, the variation of the A_b/A is highest at the passage (-50.88% to 44.64% of $\overline{A_b}/A$), but the density of the blockage, which is defined as the ratio of the time-averaged $\overline{A_b}$ and the local passage area A_{local} ($\overline{A_b}/A_{pas}$), is the smallest (5.95%). At the hubside region, the corner separation increases the blocked area, increasing the density of the blockage $\overline{A_b}/A_{hub}$. In addition, reduced attenuation of 3rd rotor wake further reduces the hubside U_x of 3rd stator wake, further increasing the local blockage outside the corner separation. The hubside blockage density $\overline{A_b}/A_{hub}$ is 15.30%, which is 2.57 times of the $\overline{A_b}/A_{pas}$. Due to the higher level of hubside A_b/A, the variation of hubside A_b/A is reduced (-39.78% to 30.95%

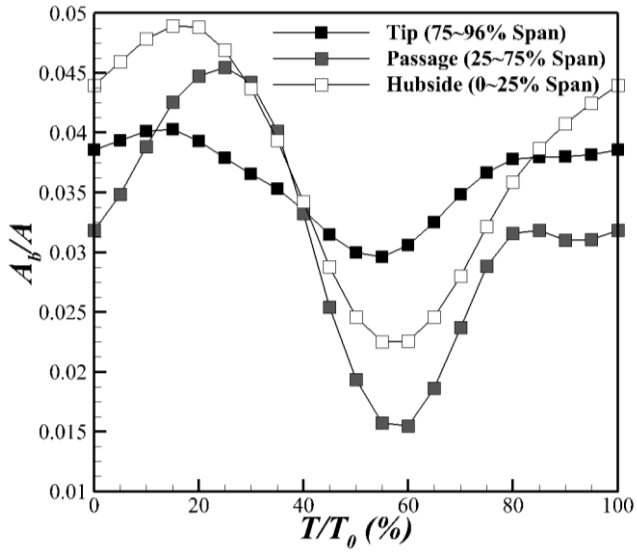

(a) Blockage at Hubside (0~25% Span), Midspan (25~75% Span) and Tip (75~96% Span), Plane 4.0

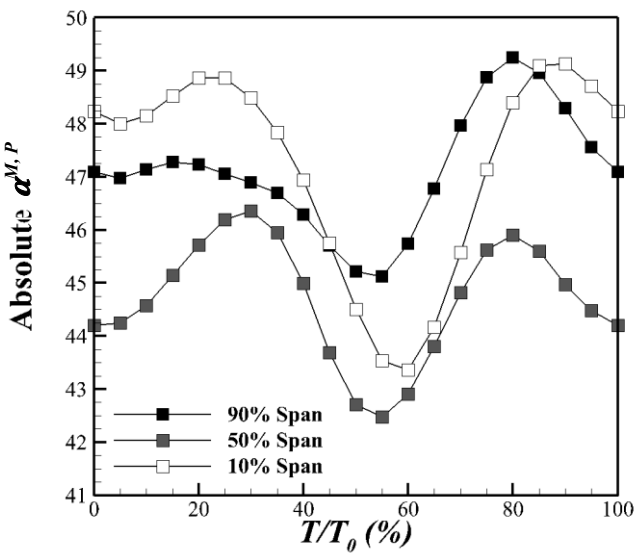

(b) Timewise Variation of $\alpha^{M,P}$ at 10%, 50% and 90% Span, Plane 4.0

Figure 4.10 Variation of Blockage and Flow Angle at Different Span, Plane 4.0

of $\overline{A_b}/A$) compared with the midspan region. At the tip region, the existence of the low momentum region near the tip due to the tip clearance flow and casing boundary layer increases the blockage density $\overline{A_b}/A_{tip}$ to 15.88%. These low momentum regions cover the entire span, decreasing the timewise variation of the blockage (from -17.89% to 11.76% of $\overline{A_b}/A$).

The timewise variations of $\boldsymbol{\alpha}^{M,P}$ at 10%, 50% and 90% Span, Plane 4.0 are shown in Figure 4.10 (b); the timewise averaged value of $\overline{\alpha^{M,P}}$ is highest at 10% span (47.21°), followed by $\overline{\alpha^{M,P}}$ at 90% span (47.10 °), and $\overline{\alpha^{M,P}}$ at 50% span (44.69 °); it is known that due to the increased hubside blockage by corner separation the hubside passage flow is deflected, increasing the α compared with that of the midspan region [15, 30]. In addition to that, the variations of the $\alpha^{M,P}$ at each locations are -4.20% to 4.55%, -4.96% to 3.72%, and -8.17% to 4.05% for 90% span, 50% span, and 10% span, respectively. The variation is highest at 10% span; reduced attenuation of the hubside 3rd rotor wake increases the α at the hubside 3rd rotor wake compared with the midspan region, increasing the variation of the flow angle.

These variations of aerodynamic properties downstream of the 3rd shrouded stator are transported to the next stage rotor, affecting the unsteady rotor inlet flow. Figure 4.11 illustrates the timewise variations of rotor relative $i^{M,P}$ at Plane 4.0, 90%, 50% and 10% span; all distributions show qualitatively identical sinusoidal behavior, a local maximum at T/T_0 ~ 10% and a local minimum at T/T_0 ~ 60%, with different magnitudes and phases. The timewise, pitchwise, mass-averaged i ($\bar{i}^{M,P}$) at 90%, 50%, and 10% span are 68.15°, 61.39°, and 60.95°, respectively. At the local maxima of each span (T/T_0 ~ 10%), the blockage of the 3rd stator in Figure 4.10 is high. As a result, the U_x is low at this period, increasing the i, as illustrated in the velocity triangle of Figure 4.12. However, at the local minima (T/T_0 ~ 60%), the blockage of the stator blade is also the lowest, increasing the

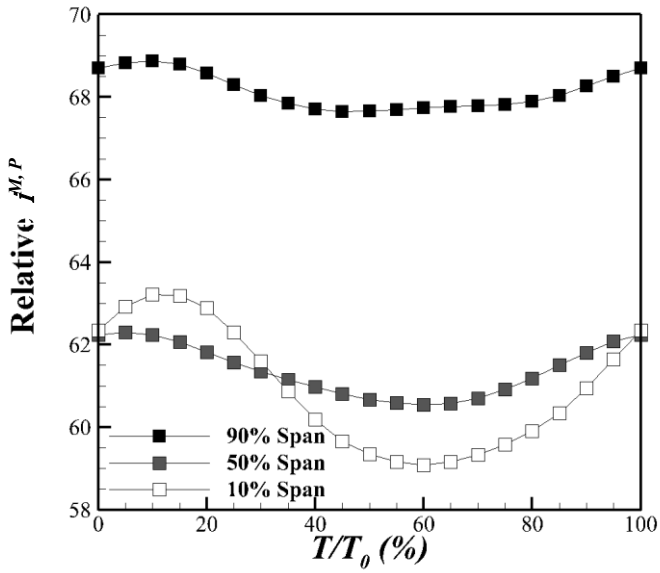

Figure 4.11 Variation of Rotor Relative Flow Angle at Different Span, Plane 4.0

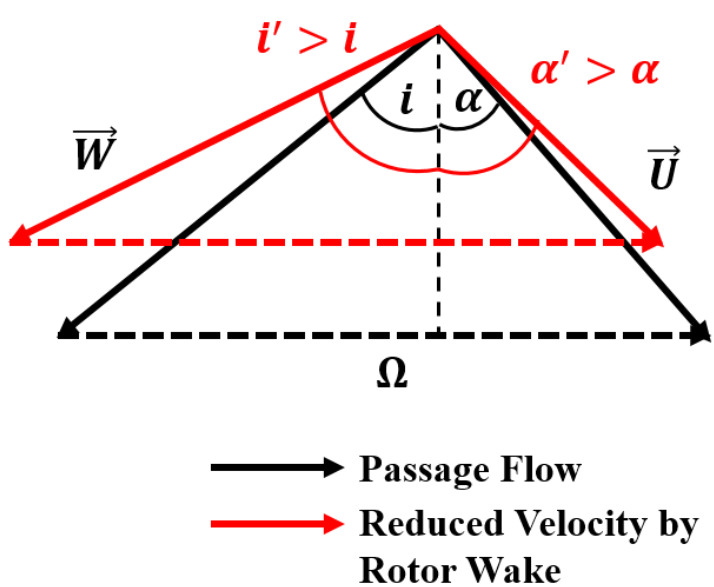

Figure 4.12 Schematic of Velocity Triangle Comparison

overall U_x, and reducing the i.

These relative flow angles vary from 0.51° to 0.73° at 90% span, -0.85° to +0.90° at midspan and -1.87 ° to +2.26 ° at 10% span. At 90% span, the rotor tip clearance flow increased the overall $\bar{\iota}^{M,P}$, but reduced the variation of the local relative flow angle, owing to the reduced variation of the blockage at tip region. Whereas for the 10% span region the variation of the relative flow angle is highest; higher velocity disturbances due to the reduced wake stretching by the corner separation triggered this variation. This can contribute to the lower operating range of shrouded configuration compared with cantilevered configuration [23, 25], which may trigger the earlier onset of the hubside stall by deviating the hubside flow from its designed condition.

5. Effect of Flow Coefficients on Unsteady Kinematics of Shrouded Stator Flow

The measurement of P_t distribution downstream of the shrouded stator by Joslyn and Dring [30] showed that the decrease of ϕ increased the hubside corner separation of a multistage shrouded stator. As previously shown in the previous sections, the hubside corner separation of shrouded stator reduces the wake stretching of the upstream rotor wake and induces additional secondary flows. Therefore, the variation of width and the magnitude of hubside corner separation can affect the hubside unsteady flow structures. Therefore, to assess the effect of ϕ on hubside corner separation and its impact on the unsteady kinematics of hubside shrouded stator flow, unsteady three-dimensional velocity measurements covering 0~50% of span have been conducted at two different ϕ : near stall (0.90 ϕ_d) and a higher flow rate (1.11 ϕ_d) cases.

5.1 Unsteady Kinematics of Shrouded Stator Flow at Near Stall Case

The near stall cases (0.90 ϕ_d) will be discussed first. Figures 5.1, 5.2 and 5.3 illustrate the U_x/U_t, U_θ/U_t and U_r/U_t distributions at plane 3.5, respectively. White dotted line in Figures 5.1, 5.2 and 5.3 represents the trailing edge (TE) of 3rd rotors axially extended downward, and the black dotted line represents the LE of a 3rd stator axially extended upward. U_x/U_t and U_θ/U_t distributions show that compared with the ϕ_d cases, the widths of the upstream third rotor and upstream second stator wakes are wider in the spanwise direction, which are typical behavior at a reduced flow rate. Passage and counter-rotating vortices are visible at SS of third rotor wake at T/T_0 = 50%, and U_r/U_t distribution show that the passage positive U_r caused by the interaction with the 2nd stator wake is also generated at the PS of rotor wake (marked as 1) in Figure 5.3 (a)), but the magnitude is weaker, and the location is shifted towards the tip. In addition, negative U_r

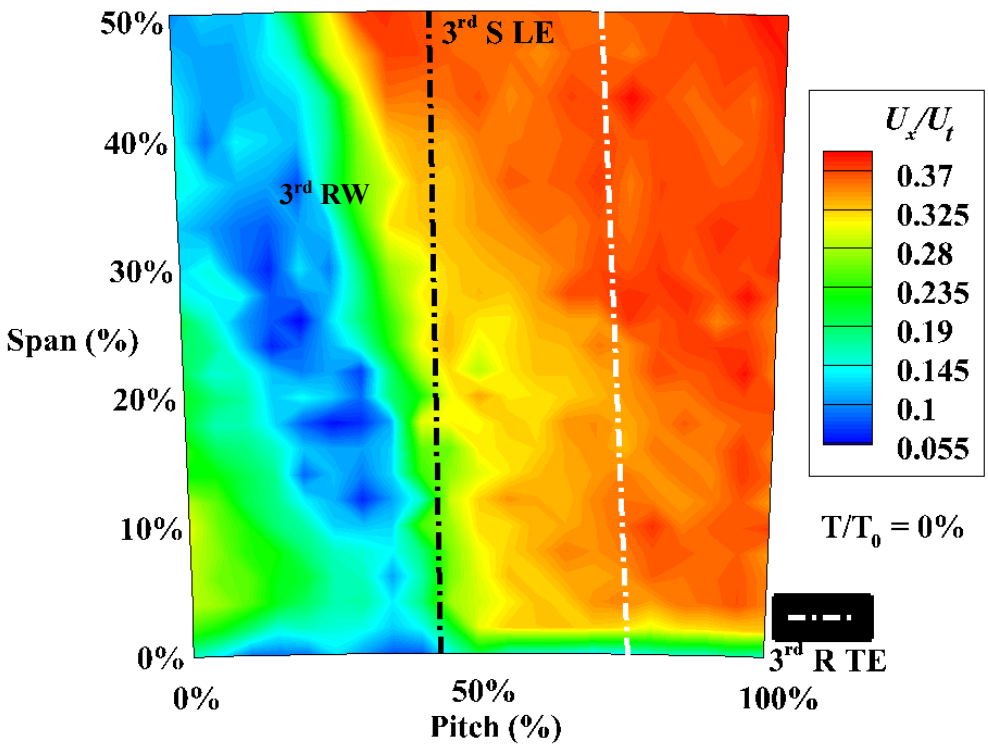

(a) Color Contour of U_x/U_t Distribution at Plane 3.5, T/T_0 = 0%, Near Stall Point (0.9 ϕ_d)

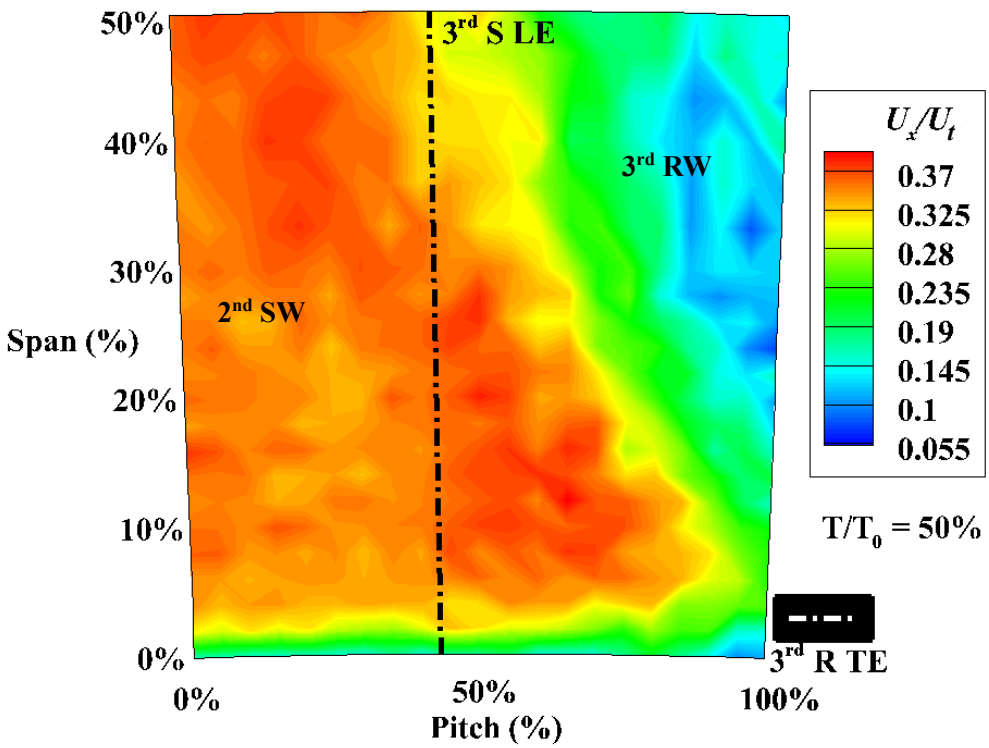

(b) Color Contour of U_x/U_t Distribution at Plane 3.5, T/T_0 = 50%, Near Stall Point (0.9 ϕ_d)

Figure 5.1 Color Contour Plot of Instantaneous Axial Velocity Distribution at Plane 3.5, Near Stall Point

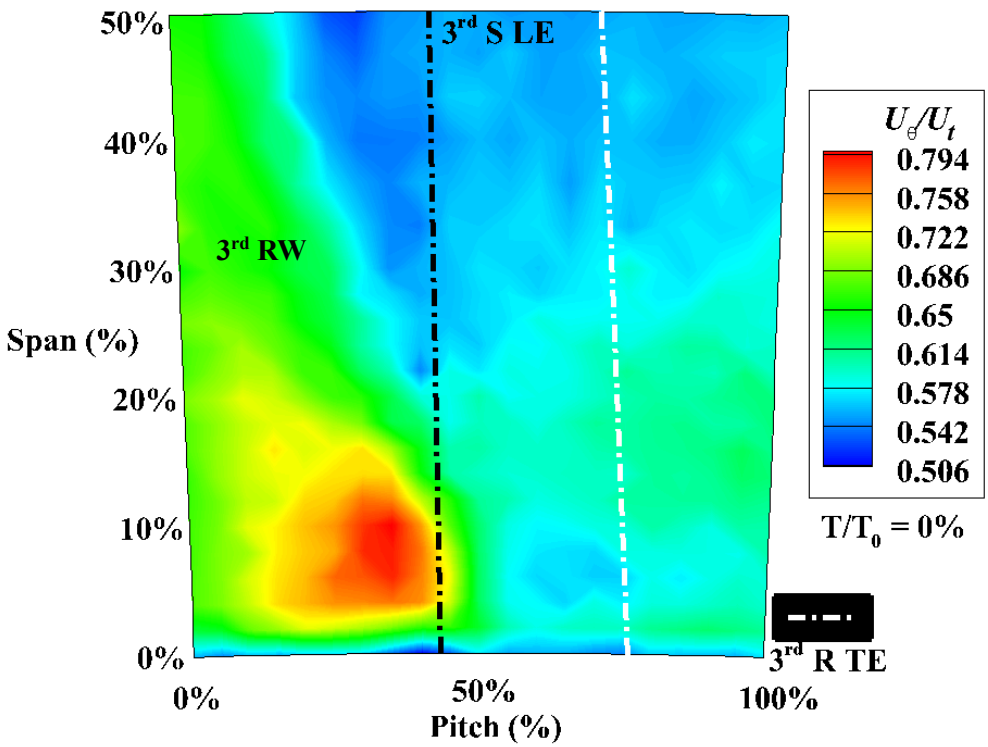

(a) Color Contour of U_θ/U_t Distribution at Plane 3.5, T/T_0 = 0%, Near Stall Point (0.9 ϕ_d)

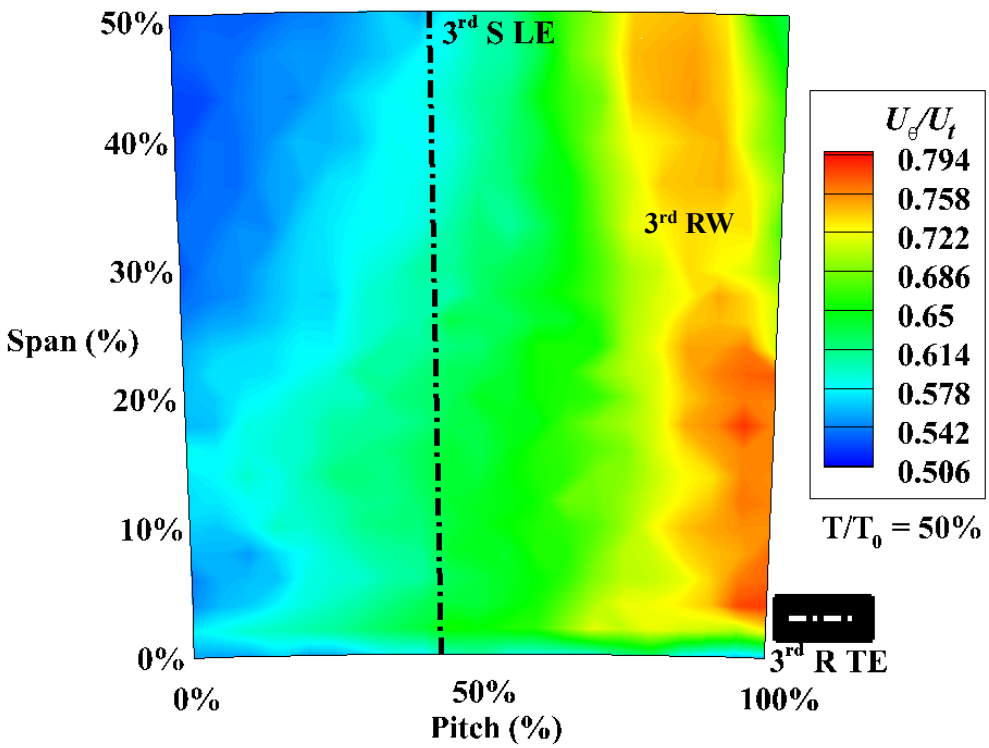

(b) Color Contour of U_θ/U_t Distribution at Plane 3.5, T/T_0 = 50%, Near Stall Point (0.9 ϕ_d)

Figure 5.2 Color Contour Plot of Instantaneous Tangential Velocity Distribution at Plane 3.5, Near Stall Point

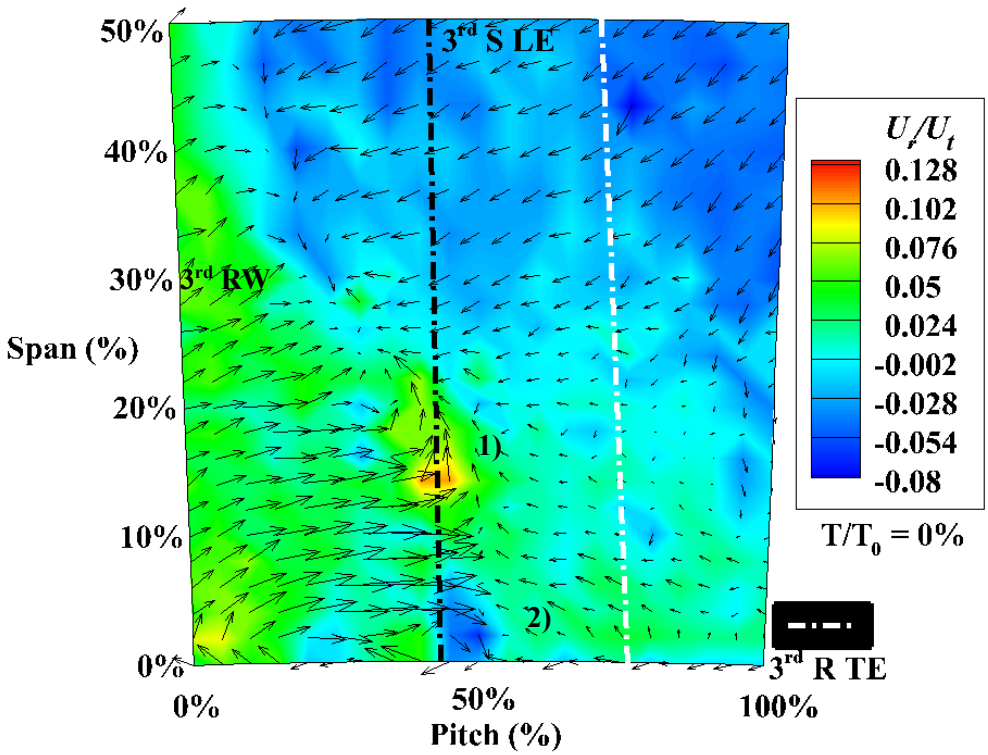

(a) Color Contour of U_r/U_t and Secondary Velocity Vector $\vec{U} - \vec{U}_{|avg,E|}$ Distribution at Plane 3.5, T/T_0 = 0%, Near Stall Point (0.9 ϕ_d)

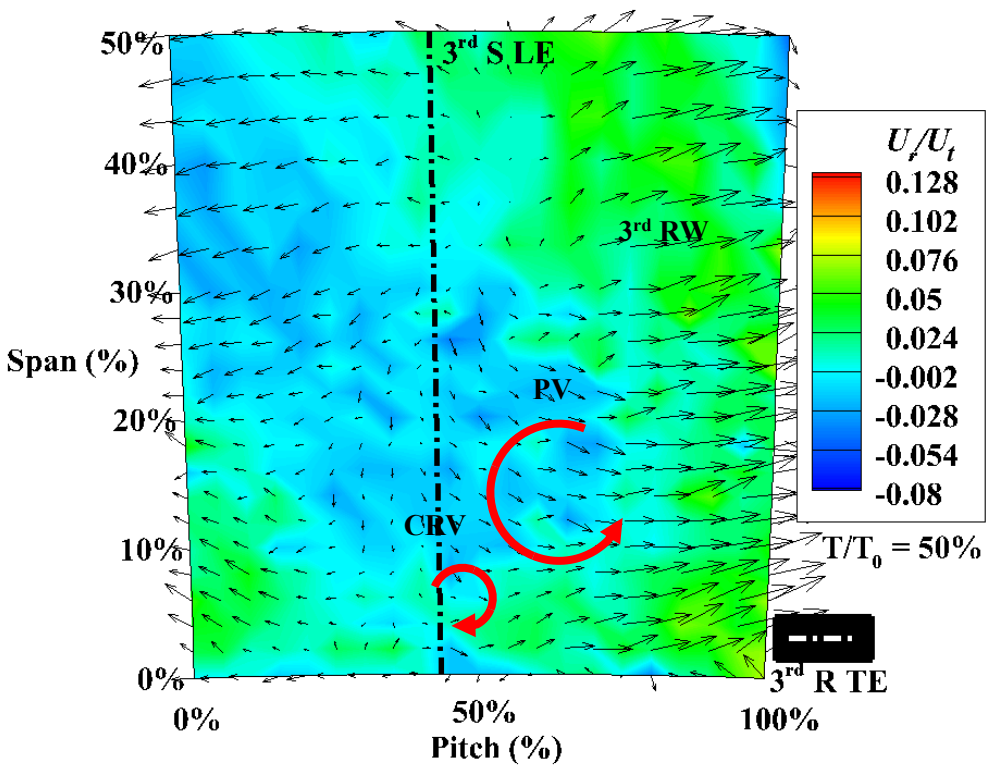

(b) Color Contour of U_r/U_t and Secondary Velocity Vector $\vec{U} - \vec{U}_{|avg,E|}$ Distribution at Plane 3.5, T/T_0 = 50%, Near Stall Point (0.9 ϕ_d)

Figure 5.3 Color Contour Plot of Instantaneous Radial Velocity and Secondary Velocity Vector Distribution at Plane 3.5, Near Stall Point

is observed at the rotor wake PS, 50% *P*, near 0% span (marked as 2) in Figure 5.3 (a)), which are related to the interaction between the cavity and mainstream flow; Wellborn [50]'s experimental and numerical data showed that near the leading edge of the shrouded stator, the static pressure P_s is high. At this high P_s region, negative radial velocity is observed at the increased loading condition, which suggests that the high P_s suppressed the egress of the upstream cavity, creating the ingress. In a similar manner, the high P_s of 3rd rotor PS suppressed the egress of the upstream cavity flow near the TE of the 3rd rotor, creating the negative U_r near the 3rd rotor PS at Plane 3.5 [74]. This phenomenon is also observed at the ϕ_d cases but is observed inside the upstream cavity [74]. Higher blade loading at 0.9 ϕ_d may trigger this negative movement at the mainstream passage.

Downstream unsteady velocity distribution at near-stall cases will be discussed next. Figures 5.4, 5.5 and 5.6 illustrates the U_x/U_t, U_θ/U_t and U_r/U_t distributions at Plane 4.0, 0.90 ϕ_d, respectively. The white dotted line represents the leading edge (LE) of downstream 4th rotors axially extended upward, and the black dotted line represents the TE of 3rd stator axially extended downward. Similar to the upstream cases, the widths of third stator wake and corner separation are wider than the ϕ_d case, as observed by the steady measurements by Joslyn and Dring [30]. Secondary movements, observed in the ϕ_d case, are also visible in U_r/U_t distributions, such as the passage vortex, the positive U_r at the PS of stator wake by the merge of 3rd rotor and stator wakes (marked as 1) in Figure 5.6), and positive U_r at the center of the corner separation region by the penetration of 3rd rotor wake (2) in Figure 5.6 (b)).

To sum up, the hubside unsteady kinematics of shrouded stator flow at near-stall case is qualitatively similar to that of ϕ_d cases. However, the locations and the magnitudes of the unsteady flow phenomena are different, owing to the larger corner separation.

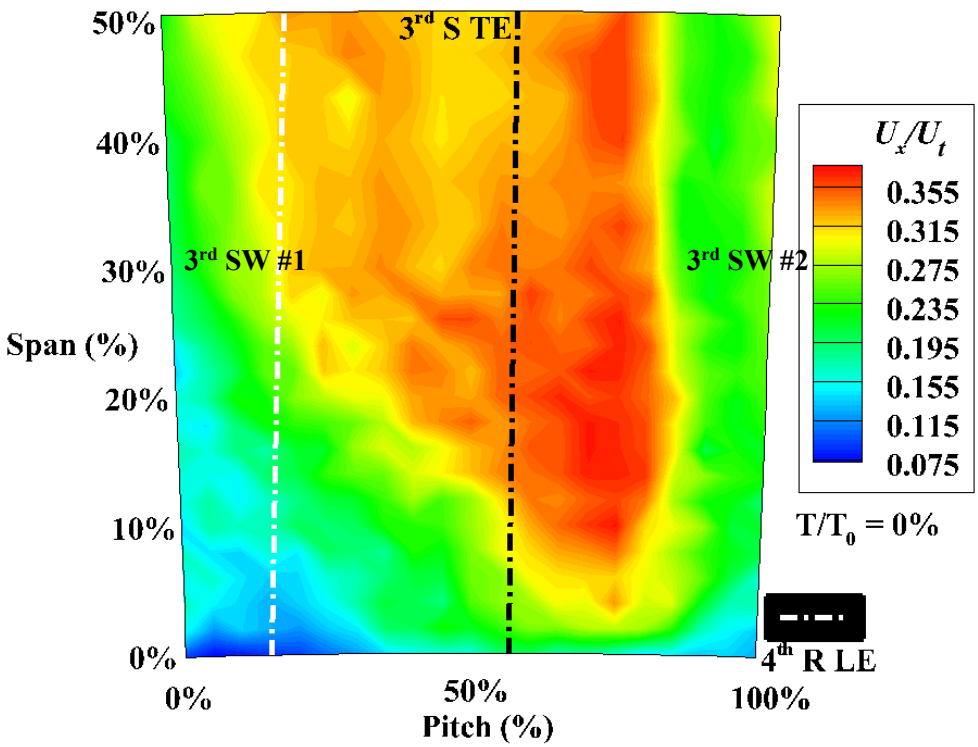

(a) Color Contour of U_x/U_t Distribution at Plane 4.0, T/T_0 = 0%, Near Stall Point (0.9 ϕ_d)

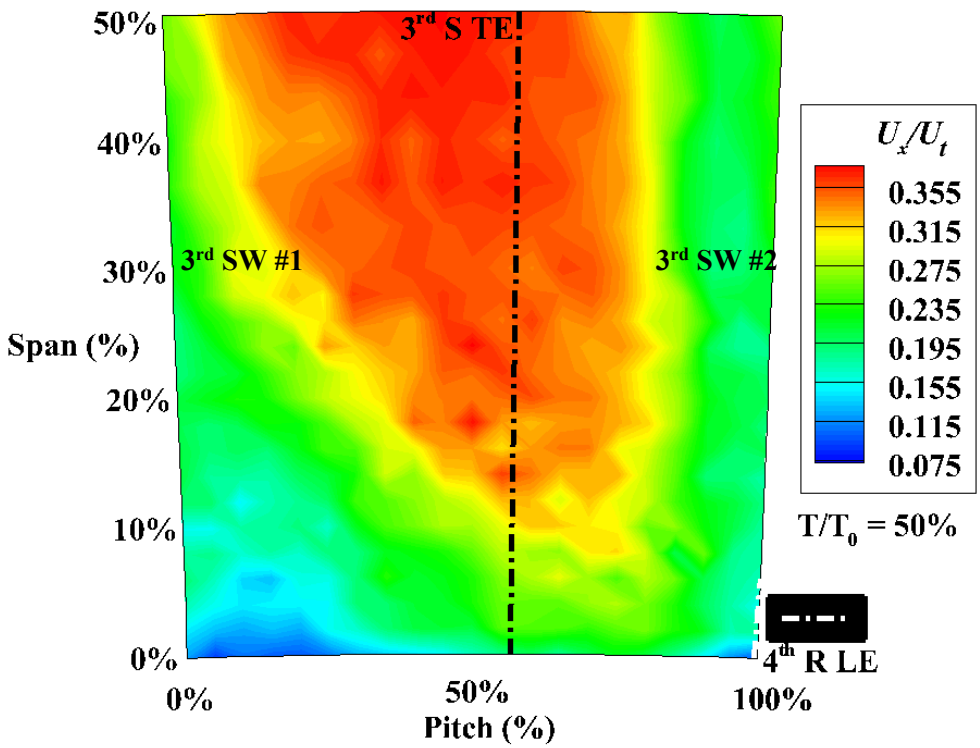

(b) Color Contour of U_x/U_t Distribution at Plane 4.0, T/T_0 = 50%, Near Stall Point (0.9 ϕ_d)

Figure 5.4 Color Contour Plot of Instantaneous Axial Velocity Distribution at Plane 4.0, Near Stall Point

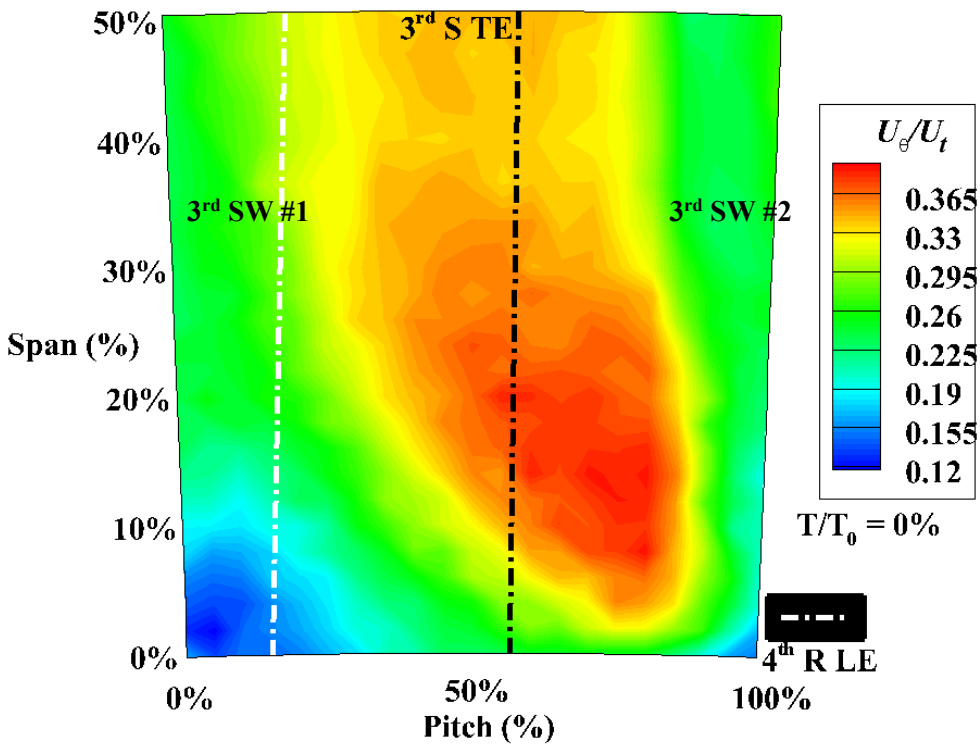

(a) Color Contour of U_θ/U_t Distribution at Plane 4.0, T/T_0 = 0%, Near Stall Point (0.9 ϕ_d)

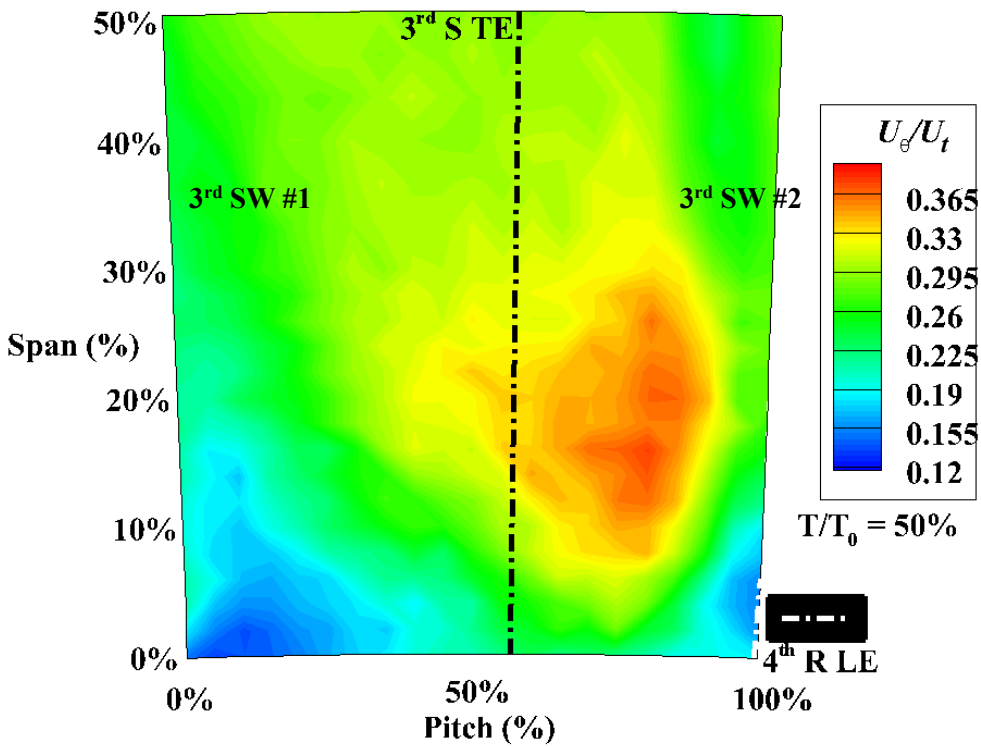

(b) Color Contour of U_θ/U_t Distribution at Plane 4.0, T/T_0 = 50%, Near Stall Point (0.9 ϕ_d)

Figure 5.5 Color Contour Plot of Instantaneous Tangential Velocity Distribution at Plane 4.0, Near Stall Point

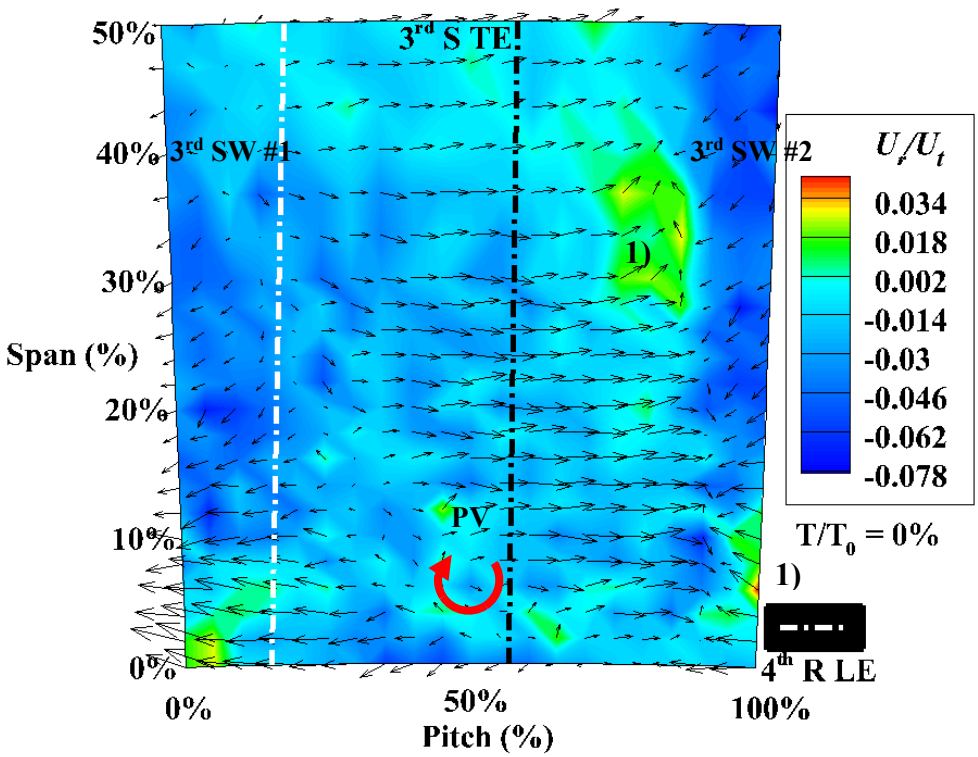

(a) Color Contour of U_r/U_t and Secondary Velocity Vector $\vec{U} - \vec{U}_{|avg,E|}$ Distribution at Plane 4.0, T/T_0 = 0%, Near Stall Point (0.9 ϕ_d)

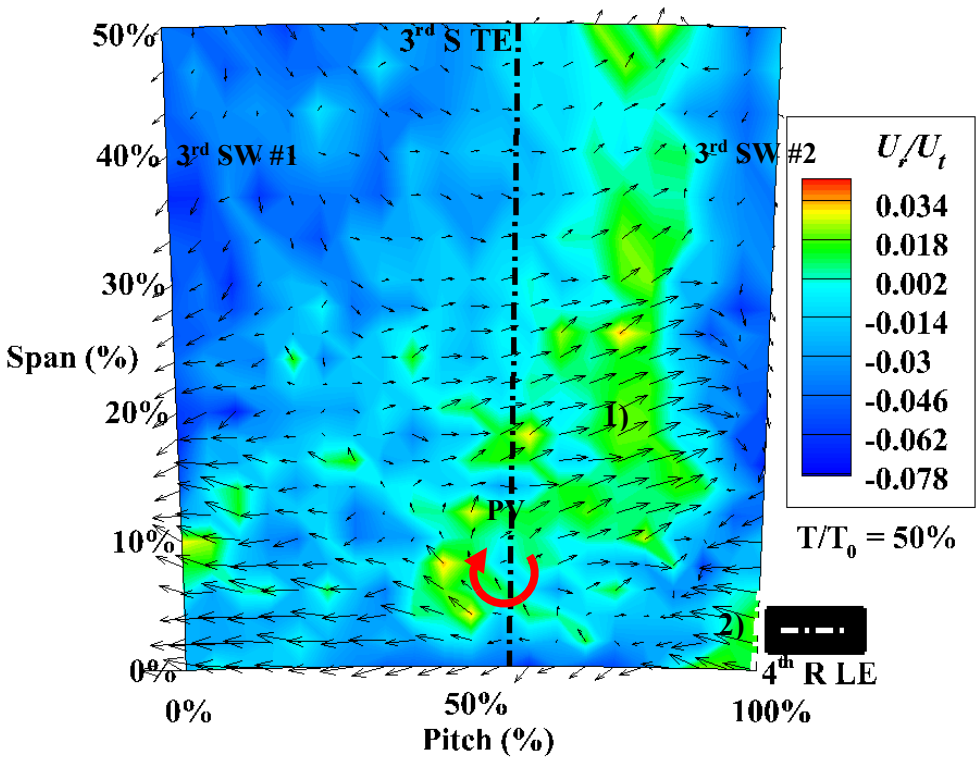

(b) Color Contour of U_r/U_t and Secondary Velocity Vector $\vec{U} - \vec{U}_{|avg,E|}$ Distribution at Plane 4.0, T/T_0 = 50%, Near Stall Point (0.9 ϕ_d)

Figure 5.6 Color Contour Plot of Instantaneous Radial Velocity and Secondary Velocity Vector Distribution at Plane 4.0, Near Stall Point

5.2 Unsteady Kinematics of Shrouded Stator Flow at Higher Flow Rate Case

Unsteady kinematics of shrouded stator flow at a higher flow rate will be discussed next. Figures 5.7, 5.8 and 5.9 show plane 3.5 U_x/U_t, U_θ/U_t and U_r/U_t distributions at 1.11 ϕ_d, respectively. White dotted line represents the trailing edge (TE) of 3rd rotors axially extended downward, and the black dotted line represents the LE of a 3rd stator axially extended upward. U_x/U_t and U_θ/U_t distributions show that compared with the ϕ_d cases, the width of wakes is narrower than the design case, which is again typical behavior at an increased flow rate. The locations of the 2nd stator wakes are changed, and the passage vortex and the counter-rotating vortex are barely visible near the SS of 3rd rotor wake. U_r/U_t distribution show that the hubside passage positive U_r caused by the interaction with the 2nd stator wake is also generated at the PS of rotor wake (marked as 1) in Figure 5.9 (a)), but its magnitude is reduced; at high flow rate, the widths of the hubside corner separation of 2nd stator is reduced, blocking the hubside passage flow and to create weaker radial movement.

Figure 5.10, 11 and 12 show plane 4.0 U_x/U_t, U_θ/U_t and U_r/U_t distributions at 1.11 ϕ_d. The white dotted line represents the leading edge (LE) of downstream 4th rotors axially extended upward, and the black dotted line represents the TE of 3rd stator axially extended downward. The overall unsteady flow kinematics are qualitatively identical to the other two cases; wakes of the 3rd rotor and stator, hub corner separation from the adjacent 3rd stator, and passage vortex are visible. However, the width of wakes and corner separation are narrower, and the radial movement at the PS of the 3rd stator wake by the interaction between the 3rd rotor and stator wakes (marked as 1) in Figure 5. 12 (b)) is reduced.

In addition, the positive radial movement at the center of the corner separation of the 3rd rotor is disappeared; U_θ/U_t distribution in Figure 5.11 show no dented region by

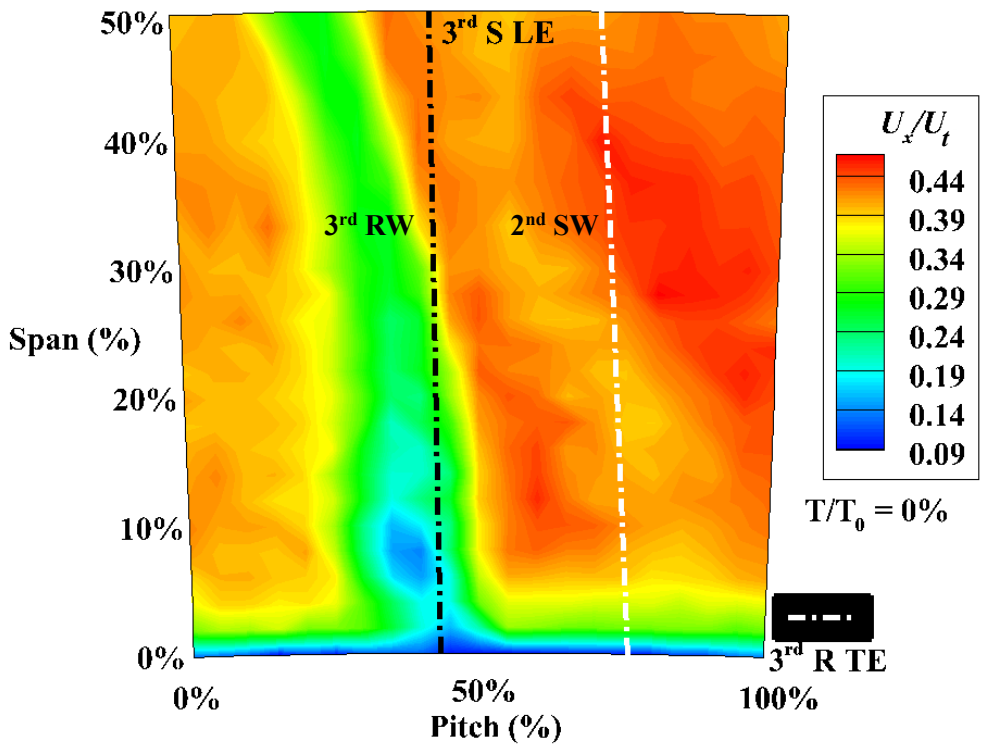

(a) Color Contour of U_x/U_t Distribution at Plane 3.5, T/T_0 = 0%, Higher Flow Rate Point (1.11 ϕ_d)

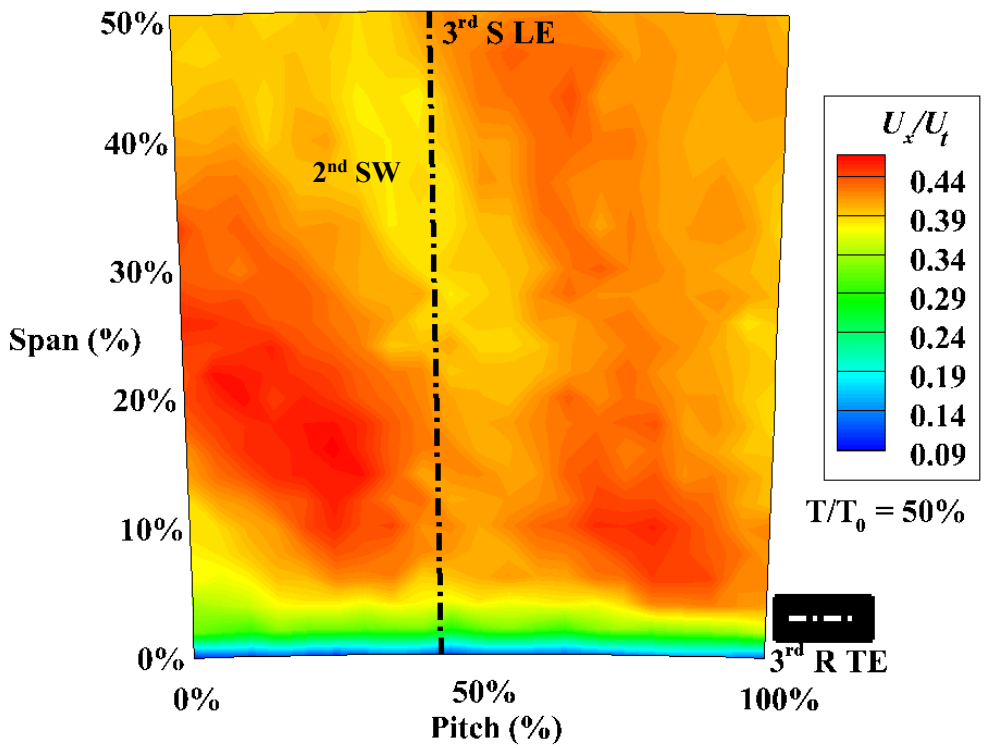

(b) Color Contour of U_x/U_t Distribution at Plane 3.5, T/T_0 = 50%, Higher Flow Rate Point (1.11 ϕ_d)

Figure 5.7 Color Contour Plot of Instantaneous Axial Velocity Distribution at Plane 3.5, Higher Flow Rate Point

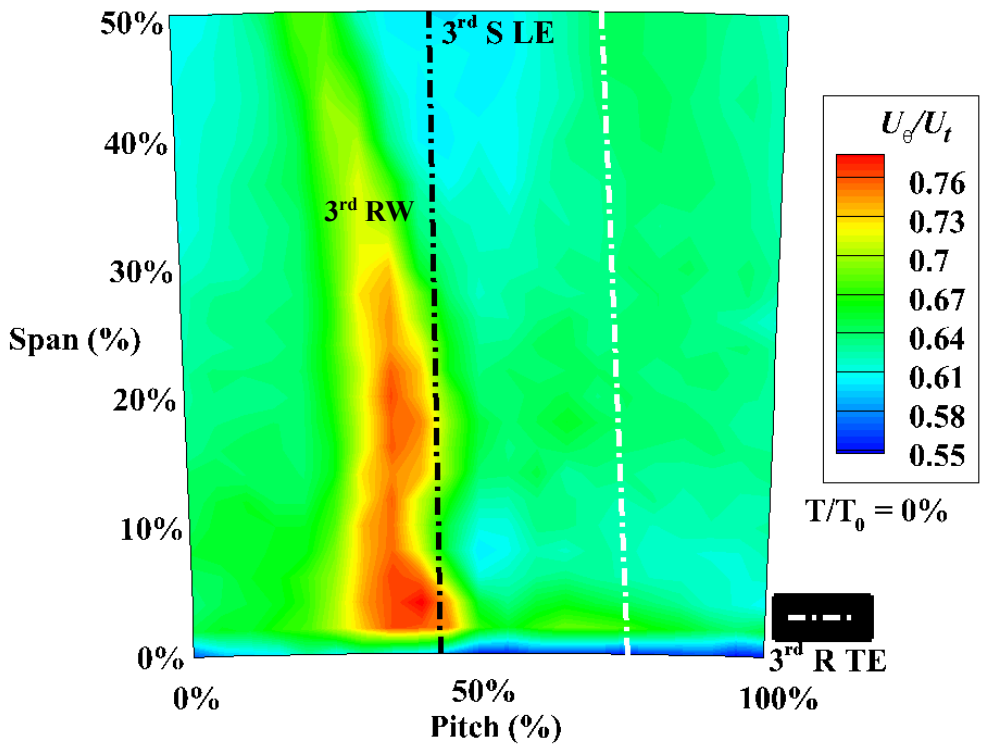

(a) Color Contour of U_θ/U_t Distribution at Plane 3.5, T/T_0 = 0%, Higher Flow Rate Point (1.11 ϕ_d)

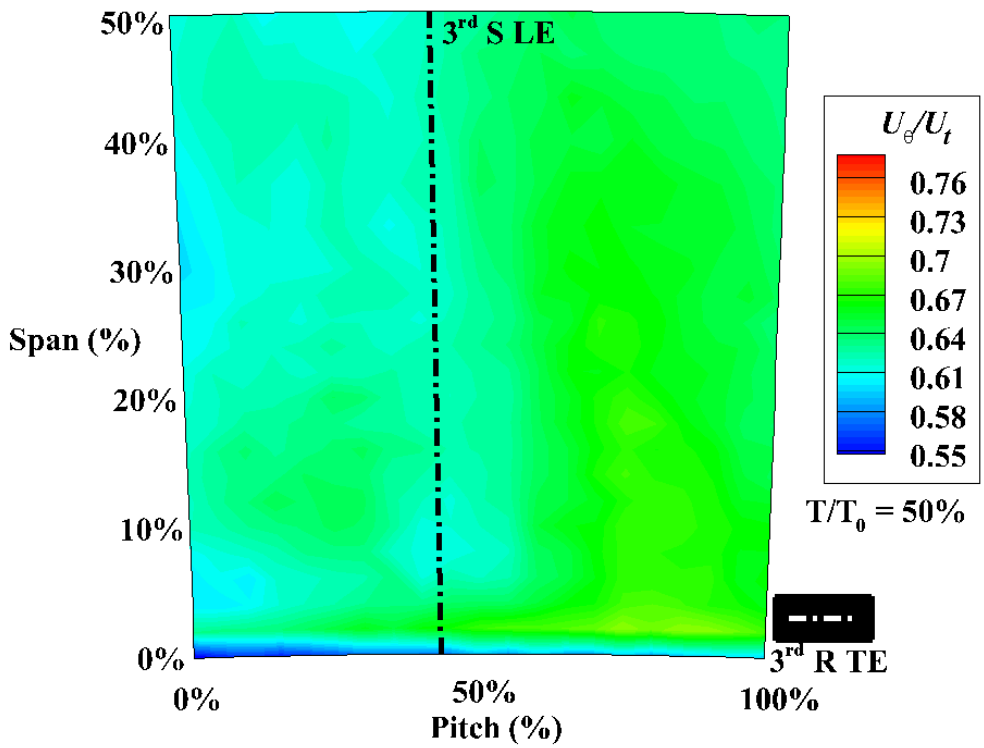

(b) Color Contour of U_θ/U_t Distribution at Plane 3.5, T/T_0 = 50%, Higher Flow Rate Point (1.11 ϕ_d)

Figure 5.8 Color Contour Plot of Instantaneous Tangential Velocity Distribution at Plane 3.5, Higher Flow Rate Point

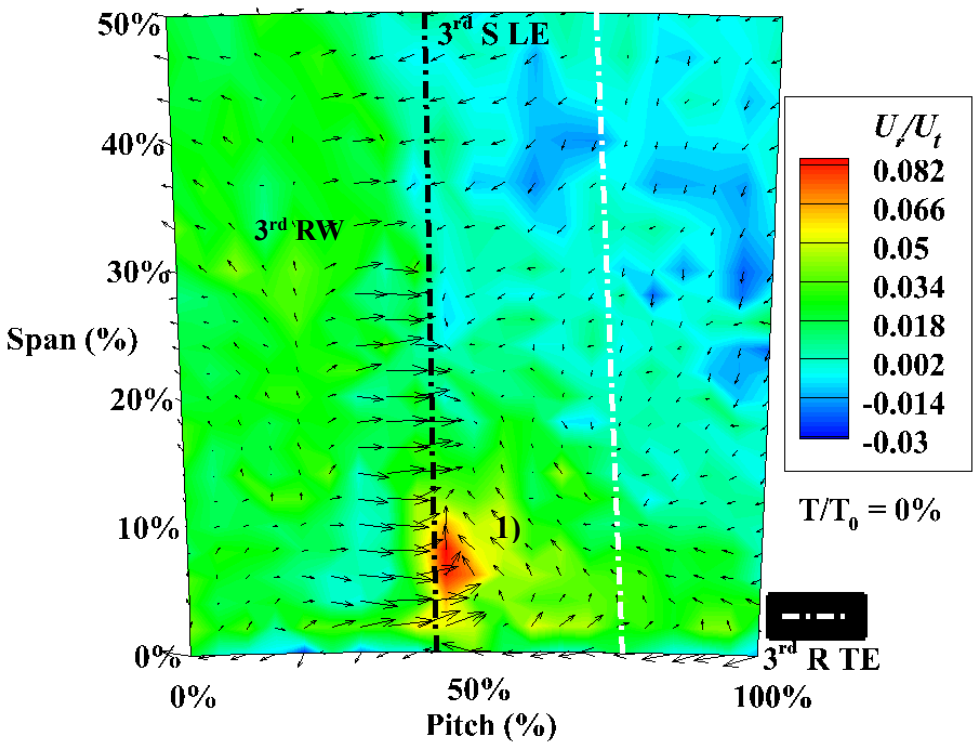

(a) Color Contour of U_r/U_t and Secondary Velocity Vector $\vec{U} - \vec{U}_{|avg,E|}$ Distribution at Plane 3.5, T/T_0 = 0%, Higher Flow Rate Point (1.11 ϕ_d)

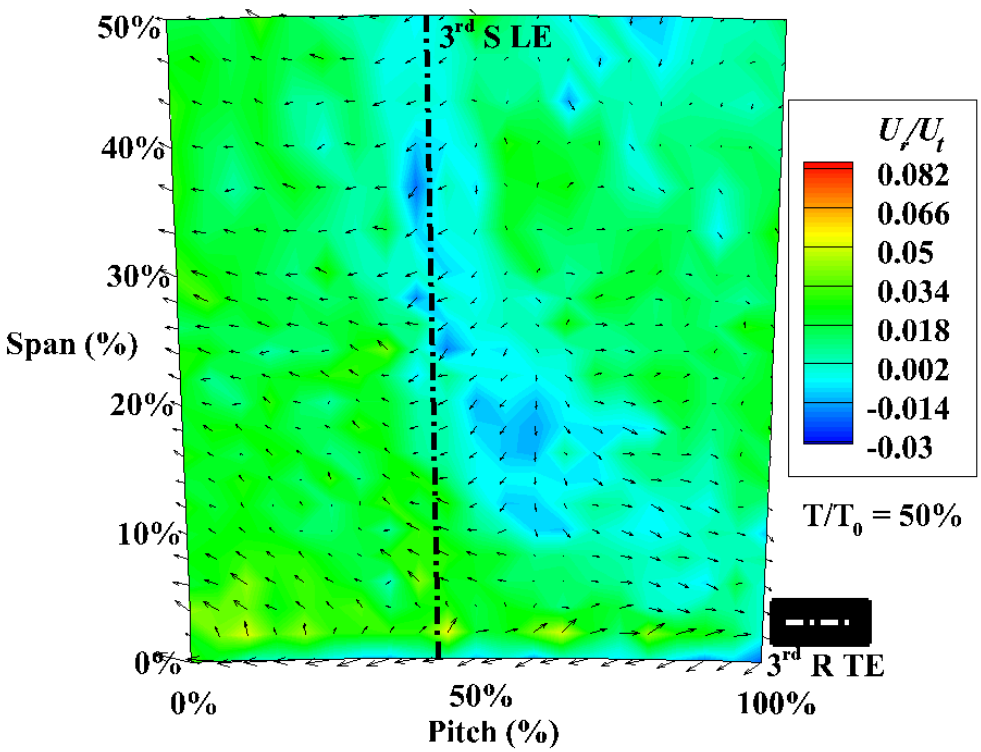

(b) Color Contour of U_r/U_t and Secondary Velocity Vector $\vec{U} - \vec{U}_{|avg,E|}$ Distribution at Plane 3.5, T/T_0 = 50%, Higher Flow Rate Point (1.11 ϕ_d)

Figure 5.9 Color Contour Plot of Instantaneous Radial Velocity and Secondary Velocity Vector at Plane 3.5, Higher Flow Rate Point

the upstream 3rd rotor wake at the hubside of the 3rd stator wake, suggesting that the 3rd rotor wake does not penetrate the hubside stator wake. Reduced corner separation of the 3rd stator at higher flow coefficient case increased the hubside P_s, preventing the 3rd rotor wake from the penetration.

The hubside unsteady kinematics of shrouded stator flow at an increased flow rate showed the reduced width of wakes and corner separation. As a result, the magnitudes of secondary flow structures generated by the interaction between rotor and stator wakes are reduced, and certain unsteady behavior is disappeared due to the decreased hubside corner separation of the shrouded stator.

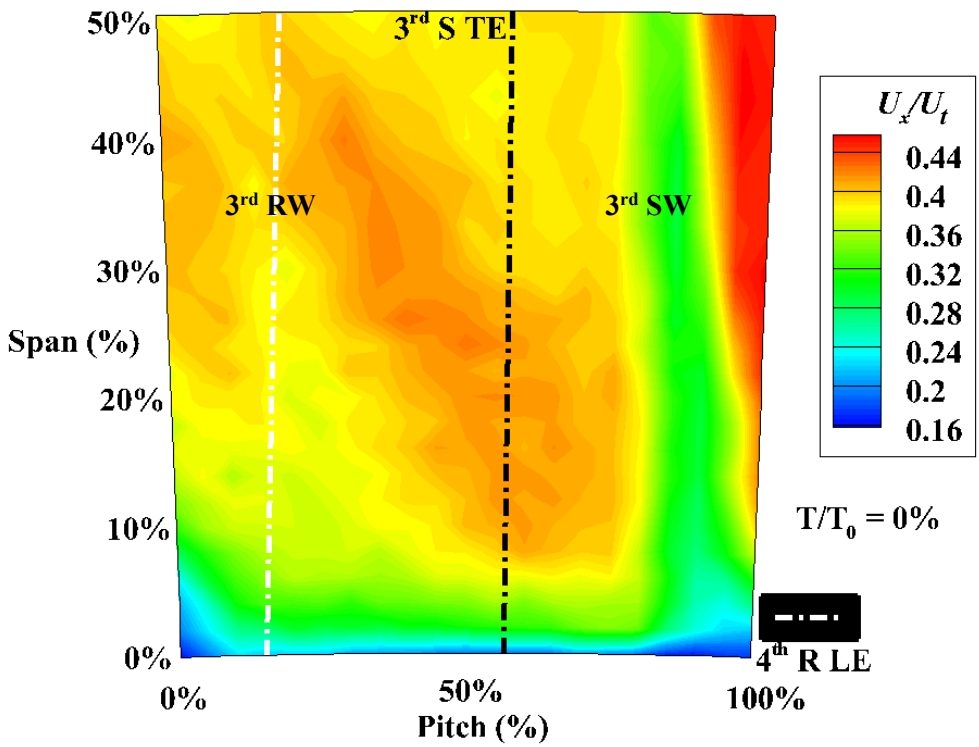

(a) Color Contour of U_x/U_t Distribution at Plane 4.0, T/T_0 = 0%, Higher Flow Rate Point (1.11 ϕ_d)

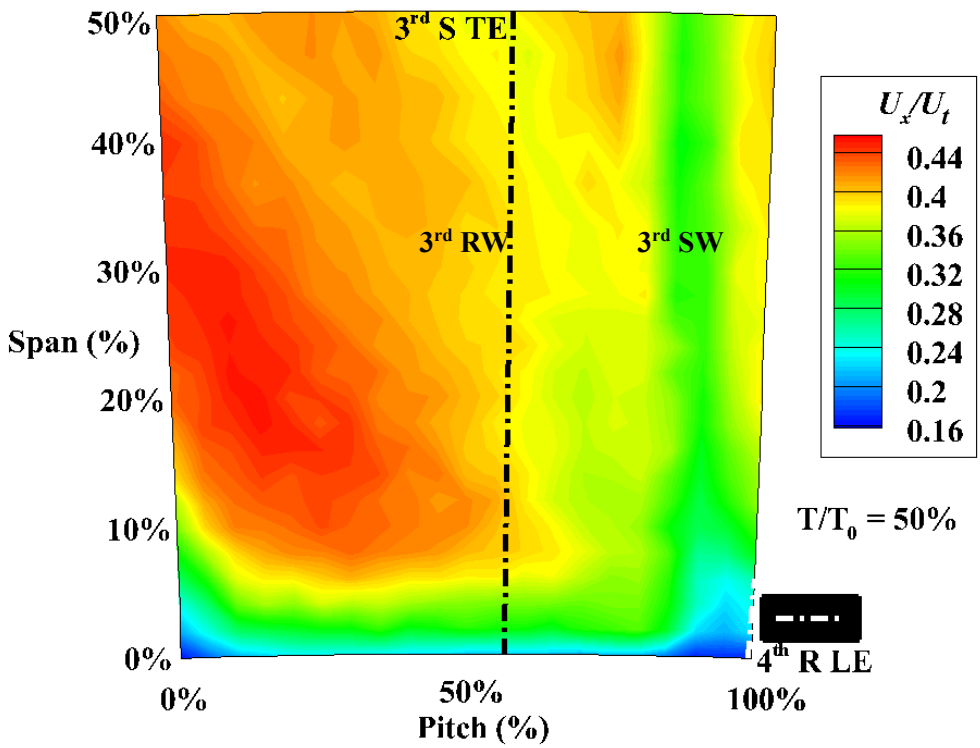

(b) Color Contour of U_x/U_t Distribution at Plane 4.0, T/T_0 = 50%, Higher Flow Rate Point (1.11 ϕ_d)

Figure 5.10 Color Contour Plot of Instantaneous Axial Velocity Distribution at Plane 4.0, Higher Flow Rate Point

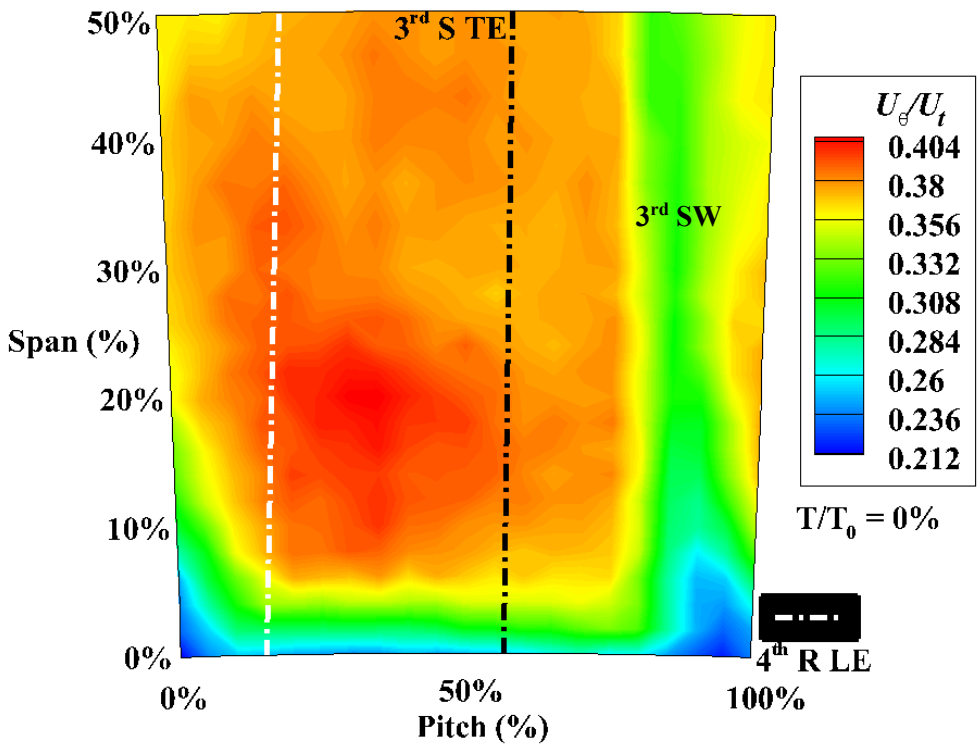

(a) Color Contour of U_θ/U_t Distribution at Plane 4.0, T/T_0 = 0%, Higher Flow Rate Point (1.11 ϕ_d)

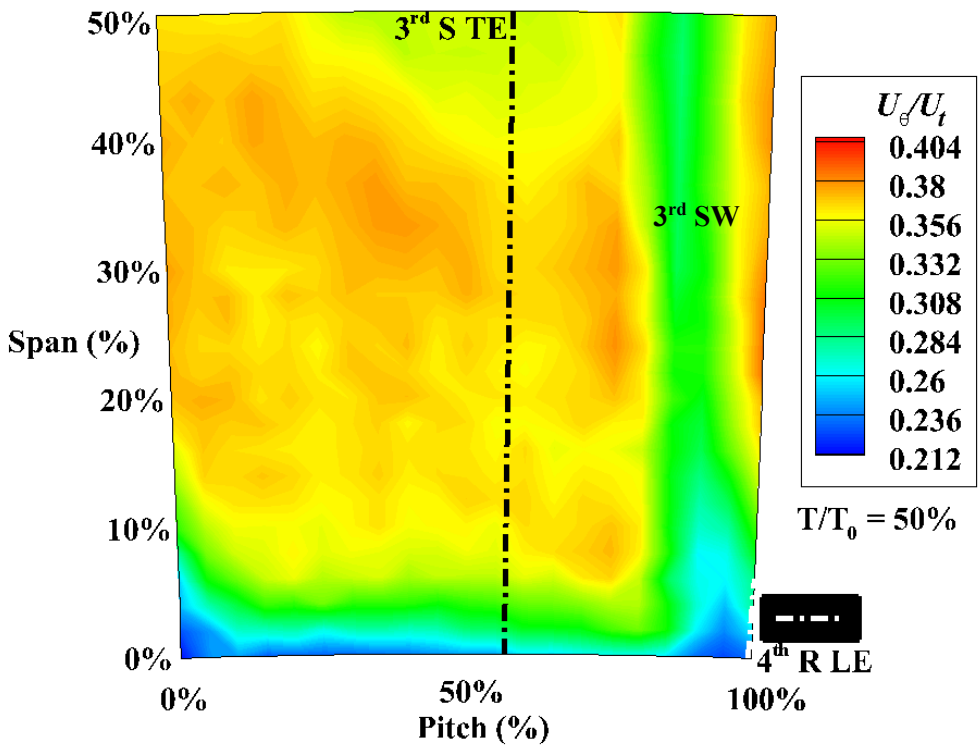

(b) Color Contour of U_θ/U_t Distribution at Plane 4.0, T/T_0 = 50%, Higher Flow Rate Point (1.11 ϕ_d)

Figure 5.11 Color Contour Plot of Instantaneous Tangential Distribution at Plane 4.0, Higher Flow Rate Point

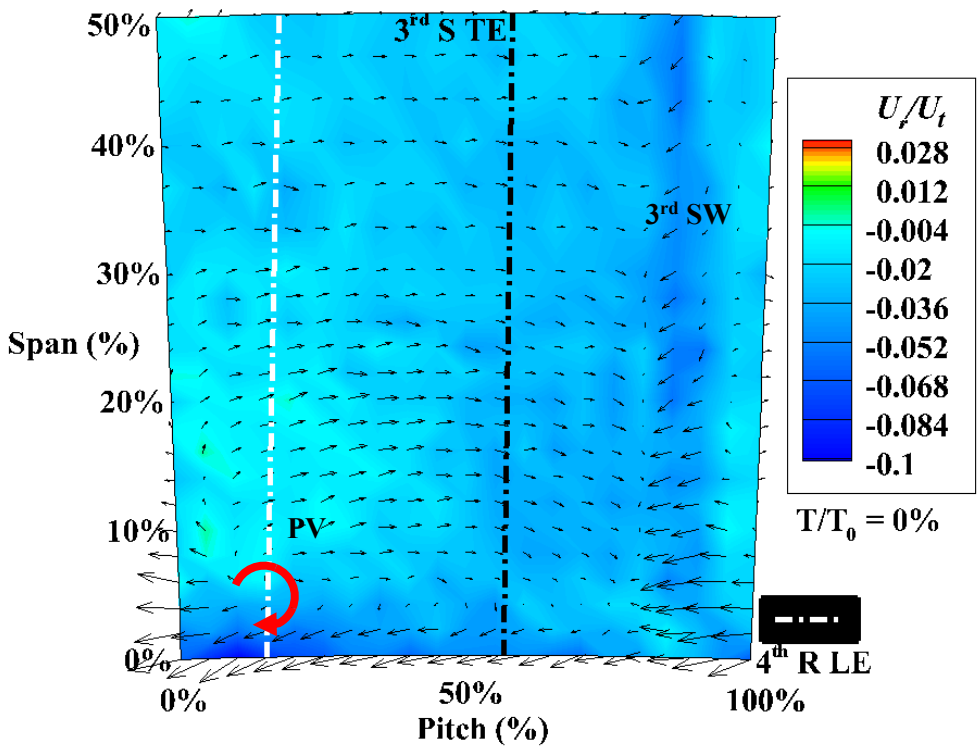

(a) Color Contour of U_r/U_t and Secondary Velocity Vector $\vec{U} - \vec{U}_{|avg,E|}$ Distribution at Plane 4.0, T/T_0 = 0%, Higher Flow Rate Point (1.11 ϕ_d)

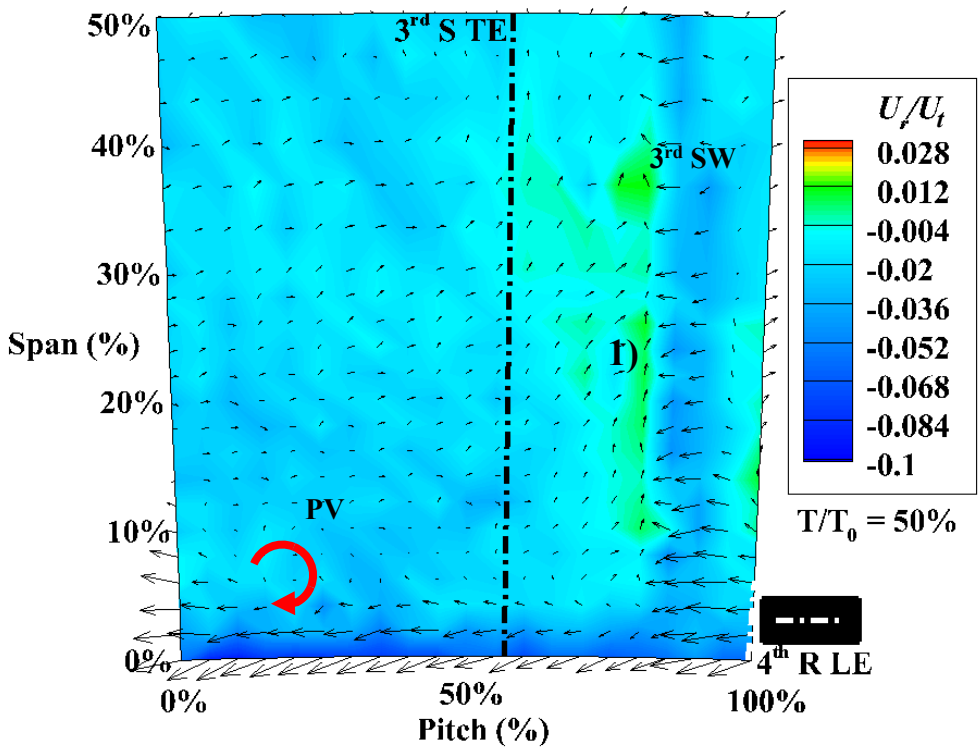

(b) Color Contour of U_r/U_t and Secondary Velocity Vector $\vec{U} - \vec{U}_{|avg,E|}$ Distribution at Plane 4.0, T/T_0 = 50%, Higher Flow Rate Point (1.11 ϕ_d)

Figure 5.12 Color Contour Plot of Instantaneous Radial Velocity and Secondary Velocity Vector Distribution at Plane 4.0, Higher Flow Rate Point

6. Discussions

6.1 Comparison of the Unsteady Kinematics of Hubside Stator Flow with Different Stator Configuration

The unsteady flow structure of the shrouded stator shows periodic behavior caused by the interaction between the rotor and stator wakes. At the upstream of the 3rd stator, the merge of the 3rd rotor and 2nd stator wake varies the width and velocity of 3rd rotor wake. Tip clearance flow of 3rd rotor creates low axial and tangential momentum region at the tip due to the interaction with the casing boundary layer. In addition, radial movement of hubside passage flow adjacent to PS of 3rd rotor wake is observed, which is caused by thickened hubside 2nd stator wake.

At the downstream of the 3rd stator, similar to the upstream case 3rd rotor varies the width and velocity of 3rd stator wake. The strength of 3rd rotor wake is higher at tip and hub region, and as a result velocity fluctuation, there are higher compared with midspan cases. For the tip region, the interaction between 3rd rotor wake and tip clearance flow increases the velocity fluctuation. In addition to widened tipside 3rd rotor wake, the additional low-momentum region is observed between 3rd rotor wakes, which is presumed to be caused by either tip leakage flow stem from the latter chord of the 3rd rotor, or double tip leakage flow. For the hubside region, the hubside corner separation reduced the effective passage, decreasing the wake stretching phenomenon. As a result, hubside 3rd rotor wake is attenuated less, having higher velocity disturbances. Finally, the collision between the 3rd rotor and 3rd stator wake creates a radial movement of passage flow.

Comparing the unsteady flow structure of hubside shrouded stator with other known unsteady flow structures show the unique feature of hubside shrouded stator. For the midspan case (Figure 6.1 (a)), the wake stretching inside the stator passage reduces the velocity disturbances by the rotor wake. However, the stator suction side is distorted by

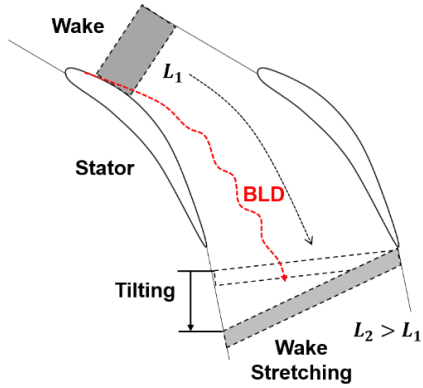

(a) Midspan

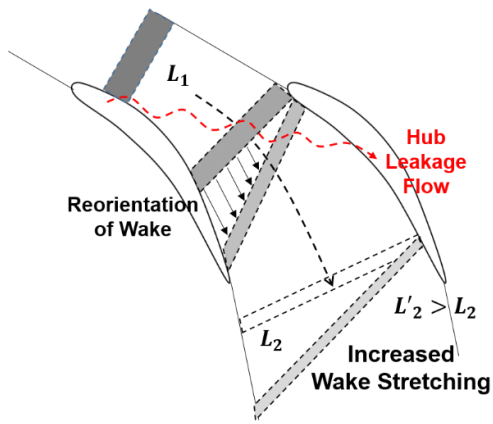

(b) Hubside, Cantilevered Stator Configuration [5]

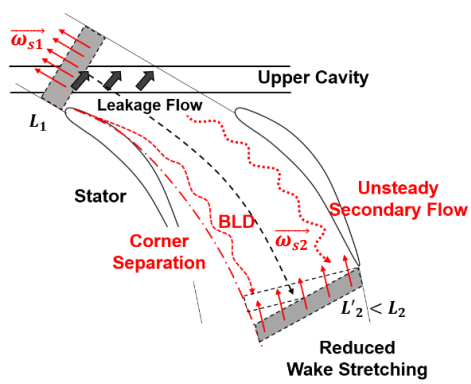

(c) Hubside, Shrouded Stator Configuration

Figure 6.1 Schematic of Unsteady Kinematics of Hubside Flow Depending on Stator Configurations

the BLD, increasing the suction side boundary layer thickness. For the tip region, the tip clearance flow of the upstream rotor can be considered as widened stator wake with a different direction [5, 22, 37], thus wake stretching reduces the velocity disturbances by the rotor tip clearance flow. At the hubside, the upstream wake of cantilevered configuration (Figure 6.1 (b)) is re-oriented by the hub leakage flow, stretching the rotor wake 15% longer than at midspan [5].

6.2 Effect of 3rd Rotor Wake on Hubside Vorticity Kinematics of Shrouded Stator

At the upstream of the shrouded stator, the hubside axial and tangential momentum are reduced due to the egress of the labyrinth seal leakage flow via the upstream cavity [44]. This is shown in the spanwise distribution of the timewise-averaged velocity components in Figure 4.4; without the upstream wake, the thickened boundary layer by the leakage flow enters the stator passage, reducing the hubside U_x and U_θ at Plane 3.5 up to ~8% span. These create the radial gradients $\frac{\partial U_x}{\partial r}$ and $\frac{\partial U_\theta}{\partial r}$, and resulting $\overrightarrow{\omega_\theta}$ and $\overrightarrow{\omega_x}$ at the upstream of the 3rd stator (the exact expression of $\vec{\omega}$ in cylindrical coordinate is $\vec{\omega} = \left(\frac{\partial u_\theta}{\partial x} - \frac{1}{r}\frac{\partial u_x}{\partial \theta}\right)\hat{r} + \left(\frac{\partial u_x}{\partial r} - \frac{\partial u_r}{\partial x}\right)\ \hat{\theta} + \frac{1}{r}\left(\frac{\partial u_r}{\partial \theta} - \frac{\partial (r u_\theta)}{\partial r}\right)\hat{x}$; the magnitude of U_r is about 1/10 order of the U_r and U_θ, and the circumferential gradient is negligible at the outside the upstream 3rd rotor wake. Therefore, the value of $\frac{\partial U_x}{\partial r}$ and $\frac{\partial U_\theta}{\partial r}$ can be approximated as $\overrightarrow{\omega_\theta}$ and $\overrightarrow{\omega_x}$, respectively). The ratio between the magnitude of $\frac{\partial U_x}{\partial r}$ and $\frac{\partial U_\theta}{\partial r}$ at 0% span at time-averaged, pitchwise-averaged condition is about 3:2, which is perpendicular to the stator inlet angle. As a result, the perpendicular $\vec{\omega}_p$ is entering the 3rd stator, as can be seen in Figure 6.2 (a). Perpendicular $\vec{\omega}_p$ by the boundary layer is tilted inside the stator passage, and as a result streamwise vorticity $\overrightarrow{\omega_s}$ is generated [75], which

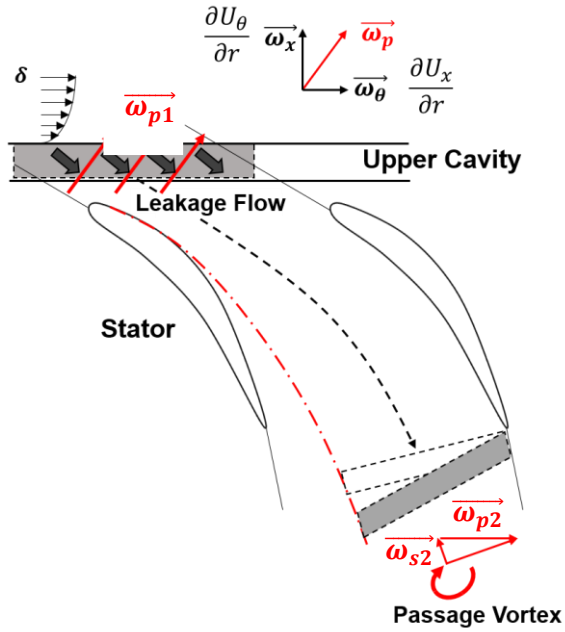

(a) Without the Upstream Rotor Wake

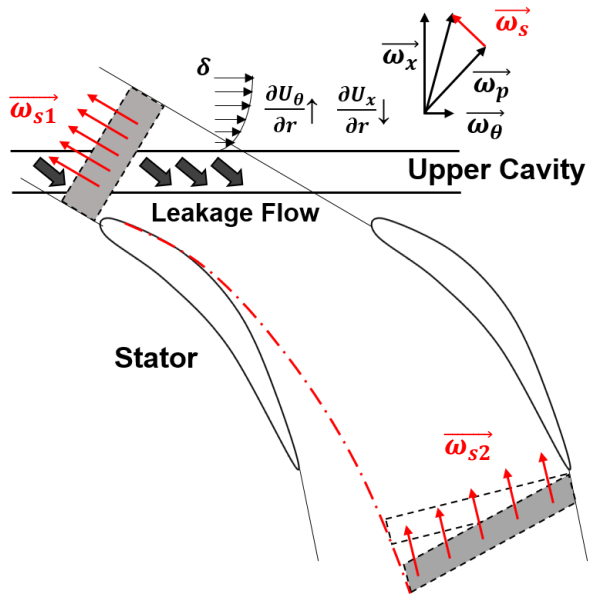

(b) With the Upstream Rotor Wake

Figure 6.2 Schematic of the Hubside Vorticity Kinematics of Shrouded Stators

creates the passage vortex. This is the typical behavior of the boundary layer inside the blade passage.

With the presence of the upstream 3rd rotor wake, the radial gradients $\frac{\partial U_x}{\partial r}$ and $\frac{\partial U_\theta}{\partial r}$ at 0% span change (refer Figure 4.4); reduced U_x and increased U_θ of the 3rd rotor wake reduces $\frac{\partial U_x}{\partial r}$ and increases $\frac{\partial U_\theta}{\partial r}$. As a result, reduced $\overrightarrow{\omega_\theta}$ and increased $\overrightarrow{\omega_x}$ create inlet streamwise vorticity $\overrightarrow{\omega_s}$, as shown in Figure 6.2 (b). The wake stretching should decrease the magnitude of this streamwise $\vec{\omega}$, however due to the reduced hubside wake stretching by the corner separation, the reduction of streamwise $\vec{\omega}$ will be lower. This inlet streamwise $\vec{\omega}$ can enhance the mixing to degrade the compressor performance.

6.3 Impact of Hubside Corner Separation on Hubside Unsteady Kinematics of Shrouded Stator Flow and Aerodynamic Properties

It is well known from the previous researches that the aerodynamic properties inside the multistage turbomachines vary by the upstream wake [8, 10-20]; a study conducted by Sanders and Fleeter [12] showed that the relative Mach number deficit by rotor wake and the variation of downstream stator incidence angle were varied, ranging from 13.6% to 17.7% and -15° to +1.9° (-6.7° on average), respectively. These caused the averaged incidence angle of the downstream stator to vary by 2.8°, deviating the passage flow from its designed conditions. This order of the variation of α is similar to the transient deviation of operating conditions from its design point; steady measurements by Wellborn and Okiishi [28] reported that 3 ~ 5° increase of α upstream and downstream of a multistage shrouded stator was observed if the operating point of compressor was moved from peak efficiency (ϕ = 0.395) to increased loading (ϕ = 0.350). Therefore, it can be perceived that the variation of aerodynamic properties by the rotor deviates the flow condition from its

design conditions, which are usually obtained using steady assumptions due to the complexity of the design process, and limitations of computing power; Denton [76] introduced the general approach of the turbomachinery design steps in seven steps, starting from specifying overall parameters to one-dimensional mean-line calculations, 2D axisymmetric throughflow calculations, quasi-3D blade to blade calculations and multistage viscous calculations. However, the actual unsteady flow causes the unwanted change of compressor characteristics, such as operating range, performances, aerodynamic properties transported to downstream blade row.

This impact of the variation of aerodynamic properties is higher at the hubside of the shrouded stator, where the existence of corner separation reduces the attenuation of the upstream rotor wake, as shown in Figure 4.7, 4.8, 4.10. In addition to that, hubside corner separation induces the additional positive radial movements of hubside flow at the upstream and downstream of the shrouded stator, further decreasing the hubside axial momentum. This indicates that the detrimental effect of unsteady rotor wake is amplified at the hubside of the shrouded stator, deviating the hubside flow from its designed flow condition higher compared with the midspan region. Furthermore, it is expected that the beneficial effect of the unsteady flow on the compressor performances at the hubside of the shrouded stator will be reduced or may even be detrimental to the performances; unsteady RANS simulations by Valkov [22] showed that at the midspan, combining both the wake stretching and boundary layer distortion yields ~0.2% increased efficiency compared with the steady cases. However, the detrimental unsteady structure of shrouded stator by the hubside corner separation decreases the beneficial effects on the efficiency from the hub to ~25% of span to deteriorate the unsteady performances of the shrouded stator.

6.4 Recommendations for Compressor Design

Of all the unsteady flow structures which affect the compressor, the wake stretching affects the performance beneficially. Thus, to maximize the wake stretching it is recommended to reduce the axial gap between rotor and stator rows; Stauter et al. [19] showed from their LDV measurements that the upstream rotor wakes decay exponentially with respect to the axial distances traveled, which is the result of the viscous mixing of the rotor wake. In addition, simulations of Van Zante et al. [10] and Valkov [22] showed increased loss by increasing the axial gap due to the increased viscous mixing at the axial gap and reduced wake stretching inside the stator passage.

However, the unsteady flow structures at the hubside or tip region reduce this beneficial wake stretching, which is related to the hubside corner separation. 1) Reduced effective flow path induces the decrease of wake stretching, 2) the periphery of corner separation is affected by boundary layer distortion, and 3) additional unsteady secondary flow structures are presumed to be generated by the interaction between the corner separation and the upstream wakes. This increase the variations of aerodynamic properties, which can lower the operating range of shrouded configuration compared with cantilevered configuration [23, 25] to trigger the earlier onset of hubside stall.

In addition to the detrimental effect of the steady performances of hubside corner separation, which have been studied by many researchers [25-27, 43, 44], the hubside corner separation of shrouded configurations further reduce the unsteady performances. This is due to the labyrinth seal leakage flow concentrated at the hubside SS of shrouded stator blades [28, 43, 44, 47-49]. Therefore, the hubside corner separation should be minimized to reduce this detrimental effect, and it is advised that the methods reduce the hubside corner separation, such as endwall contouring [77], active control of the hubside fluid using by means of blowing/suction [78], etc.

7. Summary of the Study

7.1 Conclusions

Unsteady kinematics of a multistage shrouded stator flow has been investigated experimentally to investigate the effect of corner separation on the unsteady kinematics of hubside stator flow and the variations of aerodynamic properties. Single 45^{o} slanted hot-wires have been used to measure planar unsteady three-dimensional velocity vector distributions inside a four-stage low speed shrouded axial compressor. The data have been ensemble-averaged to obtain the timewise variation of velocity vectors upstream and downstream of the shrouded 3rd stator. The unsteady kinematics of shrouded stator flow has been studied, which have found that the behavior of rotor wakes inside the stator passage consistent with previous researches, such as the fluctuation of stator wake width and the attenuation of rotor wake due to the wake stretching phenomenon. In addition, the study has shown that the hubside corner separation of a multistage shrouded axial compressor alters the hubside unsteady kinemics of shrouded stator flow and the magnitude of the variation of hubside aerodynamic properties. The measurements have shown that;

I. The width and the velocity disturbances of 3rd stator wake varied by the merge with 3rd rotor wakes. Due to the attenuation of the 3rd rotor wake and the negative jet of the rotor wakes, the velocity disturbances by the wakes are more pronounced near the PS of the 3rd stator wake. Between the two 3rd rotor wakes, a pseudo-wake region is observed, which is presumed to be created by the recirculation due to the negative jet of the 3rd rotor wakes.

II. The periphery of the hubside corner separation is fluctuated by the 3rd rotor wake, similar to the distortion of the stator suction side boundary layer by the upstream rotor wake.

III. The hubside corner separation of shrouded stator induces the hubside radial movements upstream and downstream of the shrouded stator. At the upstream, the hubside width of 2nd stator wake is wider, deflecting the passage flow flowing on the convex 3rd rotor PS. This transports the hubside low axial momentum fluid towards the positive spanwise direction. At the downstream, the hubside corner separation lowers the static pressure, forcing the 3rd rotor wake to penetrate the 3rd stator wake. This penetration of 3rd rotor wake transports the radial movement, which was created by the merge between rotor and stator wakes, inside the center of corner separation.

IV. The increased blockage by the hubside corner separation reduced the effective width, decreasing the elongation of wake fluid component perpendicular to the streamwise direction. This reduces the wake stretching inside the stator passage, causing wider rotor wake width and higher velocity disturbances compared with the midspan region.

V. The attenuation of the upstream rotor wake inside the stator passage was reduced at the hubside region of the shrouded stator. The absolute, axial and tangential velocity disturbances at the 50% span are reduced by 63.10%, 74.79%, and 67.04%, respectively. However, at the 10% span, the disturbances are reduced by 24.38%, 74.65%, and 37.70%.

VI. The higher hubside velocity disturbances by the corner separation create a higher variation of aerodynamic properties at the hubside region. The timewise variation of blockage and the flow angle downstream of 3rd stator showed higher timewise-averaged values and the degree of variation at the hubside. This higher variation of the hubside region is transported downstream, varying the hubside rotor inlet condition higher compared with the midspan region.

VII. Unsteady velocity measurements at off-design conditions show the variation of hubside flow structures. For near-stall cases, qualitative similar flow structures are observed. The magnitude and the width of the structures are changed by the enlarged corner separation and wake width. For higher mass flow rate cases, the strengths of secondary flow structures are lower, and the positive radial U_r at the hubside, SS of third stator wake is not observed. Reduced corner separation and narrower rotor and stator wake are responsible.

VIII. The unsteady kinematics of shrouded stator flow has shown that the hubside corner separation can reduce the performances and the stability of the multistage shrouded axial compressors. It is advised that the hubside corner separation should be minimized to reduce the detrimental effect if shrouded stator configuration is used.

6.4 Recommendations for the Future Work

The unsteady kinematics of a multistage shrouded axial compressor flow has been investigated in this study. Based on the conclusions of the study, the following subjects are suggested for future investigations.

I. The study showed that the attenuation of the wake is reduced at the hubside of the shrouded stator. Therefore, it is expected that the unsteady hubside performance of the shrouded stator is reduced. Unsteady P_t measurement can quantify the reduced wake stretching on the compressor performances.

II. The measuring planes of this study are away from the LE or TE of the target third stator. Therefore, the origin of the unsteady flow structures of 3rd stator passages discussed in the study, such as the positive Ur, are conjectures based on the measurements. Therefore, streamwise unsteady measurements of $\vec{U}$ and P_t inside the stator passage, or unsteady numerical calculations are required to validate these unsteady behaviors.

III. Wellborn [50] showed that the unsteady passage flow can affect the upstream and downstream cavity flow structures. Lim [77] further investigated the unsteady cavity flow structures by the passage flow, explaining the unsteady cavity flow kinematics. However, the resolution of the Lim's measurement is not fine enough; it is possible that additional secondary flow structures are not observed by his measurements, which can increase the mixing inside cavities. Finer measurements or numerical simulations at the area are required.

IV. In this study measurements upstream and downstream of stator have been performed, and the kinematics of hubside unsteady flow structure of shrouded stator is presented. It is possible that inside the stator passage, additional

secondary flow structures can be generated. Numerical calculations of the stator passage with the presence of the incoming perturbations by the upstream wake will be adequate to observe the flow structures inside the stator passage.

References

[1] “GE’s HA Gas Turbine Fleet,” General Electric Power, Retrieved from https://www.ge.com/power/gas/gas-turbines/h-class.

[2] Cumpsty, N. A., 2004, *Compressor Aerodynamics*, Krieger, Florida, USA.

[3] Camp, T. R., Day, I. J., 1998, “A Study of Spike and Modal Stall Phenomena in a Low-Speed Axial Compressor,” *Journal of Turbomachinery*, Vol. 120 (3), pp. 393-401.

[4] Lange, M., Rolfes, M., Mailach, R., Schrapp, H., 2018, “Periodical Unsteady Atip Clearance Vortex Development in a Low Speed Axial Research Compressor at Different Tip Clearances,” *Journal of Turbomachinery*, Vol. 140 (3), 031005.

[5] Montomoli, F., Naylor, E., Hodson, H. P., Lapworth, L., 2013, “Unsteady Effects in Axial Compressors: A Multistage Simulation,” *Journal of Propulsion and Power*, Vol. 29 (5), pp. 1001-1008.

[6] Gbadebo, S. A., Cumpsty, N. A., Hynes, T. P., 2005, “Three-Dimensional Separations in Axial Compressors,” *Journal of Turbomachinery*, Vol. 127 (2), pp. 331-339.

[7] Praisner, T. J., Smith, C. R., 2006, “The Dynamics of the Horseshoe Vortex and Associated Endwall Heat Transfer—Part I: Temporal Behavior,” *Journal of Turbomachinery*, Vol. 128 (4), pp. 747-754.

[8] Smith, L. H. Jr., 1966, “Wake Dispersion in Turbomachines,” *Journal of Basic Engineering*, Vol. 88 (3), pp. 688-690.

[9] Kerrebrock, J. L., Mikolajczak, A. A., 1970, “Intra-Stator Transport of Rotor Wakes and Its Effect on Compressor Performance,” *Journal of Engineering for Power*, Vol. 92 (4), pp. 359-368.

[10] Van Zante, D. E., Adamczyk, J. J., Strazisar, A. J., Okiishi, T. H., 1997, “Wake Recovery Performance Benefit in a High-Speed Axial Compressor,” ASME Turboexpo 1997, 97-GT-535.

[11] Sanders, A. J., Papalia, J., Fleeter, S., 2002, “Multi-Blade Row Interactions ina Transonic Axial Compressor: Part I - Stator Particle Image Velocimetry (PIV) Investigation,” *Journal of Turbomachinery*, Vol. 124 (1), pp. 10-18.

[12] Sanders, A. J., Fleeter, S., 2001, “Multi-Blade Row Interactions in a Transonic Axial Compressor: Part II - Rotor Wake Forcing Function & Stator Unsteady Aerodynamic Response,” ASME Turboexpo 2001, 2001-GT-0269.

[13] Mailach, R., Lehmann, I., Vogeler, K., 2008a, “Periodical Unsteady Flow Within a Rotor Blade Row of an Axial Compressor - Part I: Flow Field at Midspan,” *Journal of Turbomachinery*, Vol. 130 (4), 041004.

[14] Mailach, R., Lehmann, I., Vogeler, K., 2008b, “Periodical Unsteady Flow Within a Rotor Blade Row of an Axial Compressor - Part II: Wake-Tip Clearance Vortex Interaction,” *Journal of Turbomachinery*, Vol. 130 (4), 041005.

[15] Schultz, H. D., Gallus, H. E., Lakshminarayana, B., 1990a, “Three-Dimensional Separated Flow Field in the Endwall Region of an Annular Compressor Cascade in the Presence of Rotor-Stator Interaction Part 1 - Quasi-Steady Flow Field and Comparison with Steady-State Data,” *Journal of Turbomachinery*, Vol. 112 (4), pp. 669-678.

[16] Schultz, H. D., Gallus, H. E., Lakshminarayana, B., 1990b, “Three-Dimensional Separated Flow Field in the Endwall Region of an Annular Compressor Cascade in the Presence of Rotor-Stator Interaction Part 2 - Unsteady Flow and Pressure Field,” *Journal of Turbomachinery*, Vol. 112 (4), pp. 679-688.

[17] Poensgen, H. D., Gallus, H. E., Lakshminarayana, B., 1991a, “Three-Dimensional Wake Decay Inside of a Compressor Cascade and Its Influence on the Downstream unsteady Flow Field : Part I - Wake Decay Characteristics in the Flow Passage,” *Journal of Turbomachinery*, Vol. 113 (2), pp. 180-189.

[18] Poensgen, H. D., Gallus, H. E., Lakshminarayana, B., 1991b, “Three-Dimensional Wake Decay Inside of a Compressor Cascade and Its Influence on the Downstream

unsteady Flow Field : Part II - Unsteady Flow Field Downstream of the Stator," *Journal of Turbomachinery*, Vol. 113 (2), pp. 190-197.

[19] Stauter, R. C., Dring, R. P., Carta, F. O., 1991, "Temporally and Spatially Resolved Flow in a Two-Stage Axial Compressor: Part I – Experiment," *Journal of Turbomachinery*, Vol. 113 (2), pp. 219-225.

[20] Ernst, M., Michel, A., Jeschke, P., 2011, "Analysis of Rotor-Stator-Interaction and Blade-to-Blade Measurements in a Two Stage Axial Flow Compressor," *Journal of Turbomachinery*, Vol. 113 (4), pp. 600-607.

[21] Khalid, S. A., 1995, "The Effects of Tip Clearance on Axial Compressor Pressure Rise," Ph. D Thesis, Massachusetts Institute of Technology.

[22] Valkov, T. V., 1997, "The Effect of Upstream Rotor Vortical Disturbances on the Time-Average Performance of Axial Compressor Stators," GTL Report #227.

[23] Valkov, T. V., Tan, C. S., 1999, "Effect of Upstream Rotor Vortical Disturbances on the Time-Averaged Performance of Axial Compressor Stators: Part 1—Framework of Technical Approach and Wake-Stator Blade Interactions," *Journal of Turbomachinery*, Vol. 121 (3), pp. 377-386.

[24] Hah, C., 2017, "Impact of Wake Dispersion on Axial Compressor Performance," ASME Turboexpo 2017, GT2017-63020.

[25] Swaboda, M., Ivey, P. C., Wenger, U., Gummer, V., 1998, "An Experimental Examination of Cantilevered and Shrouded Stators in a Multistage Axial Compressor," ASME Turboexpo 1998, 98-GT-282.

[26] Campobasso, M. S., Mattheiss, A., Wenger, U., Amone, A., Boncinelli, P., 1999, "Complementary Use of CFD and Experimental Measurements to Assess the Impact of Shrouded and Cantilevered Stators in Axial Compressors," ASME Turboexpo 1999, 99-GT-208.

[27] Lange, M., Mailach, R., Vogeler, K., 2010, “An Experimental Investigation of Shrouded and Cantilevered Compressor Stators at Varying Clearance Sizes,” ASME Turboexpo 2010, GT2010-22106.

[28] Wellborn, S. R., Okiishi, T. H., 1996, “Effects of Shrouded Stator Cavity Flows on Multistage Axial Compressor Aerodynamic Performances,” NASA Contract Report 198536.

[29] Yoon, S., Selmeier, R., Cargill, P., Wood, P., 2014, “Effect of the Stator Hub Configuration and Stage Design Parameters on Aerodynamic Loss in Axial Compressors,” ASME Turboexpo 2014, GT2014-26905.

[30] Joslyn, H. D., Dring, R. P., 1985, “Axial Compressor Stator Aerodynamics,” *Journal of Engineering for Gas Turbines and Power*, Vol. 107 (2), pp. 485-493.

[31] Dring, R. P., Spear, D. A., 1991, “The Effects of Wake Mixing on Compressor Aerodynamics,” *Journal of Turbomachinery*, 113(4), pp. 600-607.

[32] Mailach, R., Vogeler, K., 2004a, “Aerodynamic Blade Row Interactions in an Axial Compressor - Part I : Unsteady Boundary Layer Development,” *Journal of Turbomachinery*, Vol. 133 (1), 011027.

[33] Mailach, R., Vogeler, K., 2004b, “Rotor-Stator Interactions in a Four-Stage Low-Speed Axial Compressor - Part I: Unsteady Profile Pressures and the Effect of Clocking,” *Journal of Turbomachinery*, Vol. 133 (1), 011027.

[34] Sirakov, B. T., Tan, C. S., 2003, “Effect of Unsteady Stator Wake-Rotor Double-Leakage Tip Clearance Flow Interaction on Time-Average Compressor Performance,” *Journal of Turbomachinery*, Vol. 125 (3), pp. 465-474.

[35] Meyer, R. X., 1958, “The Effect of Wakes on the Transient Pressure and Velocity Distributions in Turbomachines,” *Transaction of ASME*, Vol. 80, pp. 1544-1552.

[36] Soranna, F., Chow, Y., Uzol, O., Katz, J., 2006, “The Effect of Inlet Guide Vanes Wake Impingement on the Flow Structure and Turbulence Around a Rotor Blade,” *Journal of Turbomachinery*, Vol. 128 (1), pp. 82-95.

[37] Valkov, T. V., Tan, C. S., 1999b, “Effect of Upstream Rotor Vortical Disturbances on the Time-Averaged Performance of Axial Compressor Stators: Part 2 - Rotor Tip Vortex/Streamwise Vortex-Stator Blade Interactions,” *Journal of Turbomachinery*, Vol. 121 (3), pp. 387-397.

[38] Shin, H. W., Solomon, W., Wadia, A., 2008, “Transonic Fan Tip-Flow Features Revealed by High Frequency Response Over-Tip Pressure Measurements,” ASME Turboexpo 2008, GT2008-50279.

[39] Jefferson, J. L., Turner, R. C., 1958, “Some Shrouding and Tip Clearances Effects in Axial Flow Compressors,” *International Shipbuilding Progress*, Vol. 5 (42), pp. 78-101.

[40] Mahler, F. H., 1972, *Advanced Seal Technology*, Pratt and Whitney Aircraft Division Technical Report, PWA-4372.

[41] Freeman, C., 1985, “Effect of Tip Clearance Flow on Compressor Stability and Performance,” von Karman Institute for Fluid Dynamics Lecture Series, 1985-05.

[42] Heidegger, N. J., Hall, E. J., Delancy, R. A., 1996, “Parameterized Study of High-Speed Compressor Seal Cavity Flow,” AIAA Paper 96-2807.

[43] Wellborn, S. R., Okiishi, T. H., 1999, “The Influence of Shrouded Stator Cavity Flows on Multistage Compressor Performance,” *Journal of Turbomachinery*, Vol. 121 (3), pp. 486-497.

[44] Demargne, A. A., Longley, J. P., 2000, “Aerodynamic Interaction of Stator Shroud Leakage and Mainstream Flows in Compressors,” ASME Turboexpo 2000, 2000-GT-570.

[45] Wisler, D. C., 1988, *Advanced Compressor and Fan Systems*, GE Aircraft Engines, Cincinnati, Ohio, USA.

[46] Ludwig, L., 1978, "Gas Path Sealing in Turbine Engines," *Seal Technology in Gas*

Turbine Engines, AGARD Publications, Neuilly Sur Seine France, Apr.; also NASA TM 73890.

[47] Kim, J., 2011, "Effects of Seal Cavity Flows on the Aerodynamic Performance in a Shrouded Compressor Stator Passage," Ph. D Thesis, Seoul National University.

[48] Marty, J., Aupoix, B., 2013, "Interaction of Shrouded Stator Flow and Main Flow and Its Influence on Performances of a Three-Stage High Pressure Compressor," *Journal of Power and Energy*, Vol. 226 (4), pp. 489-500.

[49] Kato, D., Yamagami, M., Tsuchiya, N., Komada, H., 2011, "The Influence of Shrouded Stator Cavity Flows on the Aerodynamic Performance of a High-Speed Multistage Axial Compressor," ASME Turboexpo 2011, GT2011-46300.

[50] Wellborn, S. R., 2001, "Details of Axial-Compressor Shrouded Stator Cavity Flows," ASME Turboexpo 2001, 2001-GT-0495.

[51] Yun, Y. I., Porreca, L., Kalfas, A. I., Song, S. J., Abhari, R. S., 2008, "Investigation of Three-Dimensional Unsteady Flows in a Two-Stage Shrouded Axial Turbine Using Stereoscopic PIV-Kinematics of Shroud Cavity Flow," *Journal of Turbomachinery*, Vol. 130 (1), 011021.

[52] Denton, J. D., 2010, "Some Limitations of Turbomachinery CFD," ASME Turboexpo 2010, GT2010-22540.

[53] Wisler, D. C., 1980, "Core Compressor Exit Stage Study Volume 2 : Data and Performance Report for the Baseline Configurations." NASA Technical Report, NASA-CR-159498.

[54] Wasserbauer, C. A., Weaver, H. F., Senyitko, R. G., 1995, "NASA Low-Speed Axial Compressor for Fundamental Research," NASA Technical Memorandum 4635.

[55] Clemen, C., Schrapp, H., Gümmer, V., Müller, R., Künzelmann, M., Vogeler, K., 2008, "Design of a Highly-Loaded Four-Stage Low-Speed Research Compressor," ASME Turboexpo 2008, GT2008-50254.

[56] Pfau, A., 2003, “Loss Mechanisms in Labyrinth Seals of Shrouded Axial Turbines,” Ph. D Thesis, Swiss Federal Institute of Technology Zürich.

[57] Brandstetter, C., Wartzek, F., Werner, J., Schiffer, H. P., Heinichen, F., 2015, “Unsteady Measurements of Periodic Effects in a Transonic Compressor with Casing Treatments,” ASME Turboexpo 2015, GT2015-42394.

[58] Lim, H., Bae, H., Lim, Y., Song, S. J., Kang, S., Yang, S., 2011, “Injection Profile Effects on Low Speed Axial Compressor Stability Enhancement,” *Journal of Mechanical Science and Technology*, Vol. 25 (6), pp. 1501-1507.

[59] Hong, Y. S., Chang, T. C., 2002, “A Comprehensive Review of Tolerancing Research,” *International Journal of Production Research*, Vol. 40 (11), pp.2425-2459.

[60] Back, S. C.. Hobson, G. V., Song, S. J., Milsaps, K. T., 2012, “Effects of Reynolds Number and Surface Roughness Magnitude and Location on Compressor Cascade Performance,” *Journal of Turbomachinery*, Vol. 134, 051013.

[61] Back, S. C., Sohn, J. H., Song, S. J., 2010, “Impact of Surface Roughness on Compressor Cascade Performance,” *Journal of Fluids Engineering*, Vol. 132, 064502.

[62] Song, S. J., Sohn, J. L., Kim, T. S., 2007, “Final Report on the Effects of Compressor Fouling on Gas Turbine Performance and Diagnosis,” Korea Midland Power, Co. Ltd., Seoul, Technical Report No. R-2005-0-016.

[63] “Mechanical Vibration – Balance Quality Requirements for Rotors in a Constant (Rigid) State – Part 1: Specification and Verification of Balance Tolerances, Second Edition,” ISO 1940-1:2003(E).

[64] Childs, P. R. N., 2004, *Mechanical Design 2nd Edition*, Elsevier, Oxford, Great Britain.

[65] Denecke, J., Färber, J., Dullenkopf, K., Bauer, H. J., 2005, “Dimensional Analysis and Scaling of Rotating Seals,” ASME Turboexpo 2005, GT2005-68676.

[66] Flores, D., Seume, J. R., 2014, “Selecting Cavity Geometries for Improving the Aerodynamic Performance of an Axial Compressor,” ASME Turboexpo 2014, GT2014-25328.

[67] Chupp, R. E., Hendricks, R. C., Lattime, S. B., Steinetz, B. M., 2006, “Sealing in Turbomachinery,” *Journal of Propulsion and Power*, Vol. 22 (2), pp. 313-349.

[68] Berdanier, R. A., Smith, N. R., Fabian, J. C., Key, N. L., 2015, “Humidity Effects on Experimental Compressor Performance – Corrected Conditions for Real Gases,” *Journal of Turbomachinery*, Vol. 137, 031011.

[69] Coleman, H. W., Steele, W. G., 2009, *Experimentation, Validation, and Uncertainty Analysis for Engineers 3rd Edition*, Wiley, New Jersey, USA.

[70] Key, N. L., Lawless, P. B., Fleeter, S., 2009, “An Experimental Study of Vane Clocking Effects on Embedded Compressor Stage Performance,” *Journal of Turbomachinery*, Vol. 132 (1), 011018.

[71] Shin, H. W., Whitfield, C. E., Wisler, D. C., 1994, “Rotor-Rotor Interaction for Counter-Rotating Fans, Part 1: Three-Dimensional Flowfield Measurements,” *AIAA Journal*, Vol. 32 (11), pp.2224-2233.

[72] *Streamline®/ Streamware® Installation & Users guide, Vol.3*, Dantec Dynamics, Denmark, Retrieved from https://www.dantecdynamics.com/.

[73] Schlichting, H., Gersten, K., *Boundary Layer Theory*, 8th Revised and Extended Edition, Springer-Verlag Berlin Heidelberg New York.

[74] Lim, S., 2018, “Unsteady Flow Measurement in a Shrouded Stator Cavity of Multistage Axial Compressor,” MS Thesis, Seoul National University.

[75] Greitzer, E. M., Tan, C. S., Graf, M. B., 2004, *Internal Flow*, Cambridge University Press, Cambridge, United Kingdom

[76] Denton, J. D., 2017, “MULTALL – An Open Source, CFD Based, Turbomachinery Design System,” ASME Turboexpo 2017, GT2017-63993.

[77] Dorfner, C., Hergt, A., Nicke, E., Moenig, R., 2010, “Advanced Nonaxisymmetric Endwall Contouring for Axial Compressors by Generating an Aerodynamic Separator – Part I: Principal Cascade Design and Compressor Application,” *Journal of Turbomachinery*, Vol. 133 (2), 021026.

[78] Hecklau, M., Wiederhold, O., Zander, V., King, R., Nitsche, W., Huppertz, A., Swoboda, M., 2011, “Active Separation Control with Pulsed Jets in a Critically Loaded Compressor Cascade,” *AIAA Journal*, Vol. 49 (8), pp. 1729-1739.

[79] *Rolling Bearings*, NSK Catalogue No. E1102m, NSK, Japan, Retrieved from http://www.nsk.com.

[80] *Technical Report*, NSK Catalogue No. E728g, NSK, Japan, Retrieved from http://www.nsk.com.

[81] *Ball and Roller Bearings*, NTN Catalog A-1000-XI, NTN, Japan, Retrieved from http://www.ntnamericas.com/en/.

Appendix A. Procedure for Selecting Bearings

To select the bearing, the loading applied on the bearings, the applications of machines used, operating hours, and the lifetime of bearings have to be considered. These parameters are evaluated to guarantee the durability of the selected bearings.

Two types of bearings are used in SNU compressor. Two radial ball bearings (NTN, 6219) are installed at the upper side of the rotor axis to withstand the radial load, and two angular ball bearings (NTN, 7219C) are installed at the lower side of the rotor axis to withstand both the radial and axial load. For the radial load, it is assumed to be the centrifugal force generated by the mass imbalance [63], at a condition of 1,200 RPM, ISO 1940-1 G 2.5. In this condition, the residual U_{res} is calculated to be 8978.93 g·mm, which yields the center of mass 19.89 μm away from the center of rotation. This imbalance generates 141.79 N of the centrifugal force. For the axial load, the mass of the rotating parts is 451.33 kg. This yields the 4427.55 N of the axial load.

These estimated loads are compared with the load rating of bearings, which is an empirical parameter related to the actual load applied on the bearings. For the standard radial ball bearings, the radial load determines the load rating of the bearings. However, the sum of the radial and axial loads applied on the bearings determine the load rating of the angular ball bearings; the combined load needs to be converted into the equivalent load P_b applied on the bearings, shown in equation A.1.

$$P_b = XF_R + YF_A \quad \text{(A.1)} \quad [79,81]$$

X, Y – Empirical load coefficient

F_R – Radial loading

F_A – Axial loading

Dynamic Equivalent Load $P = XF_r + YF_a$

Contact Angle	$if_0F_a^*/C_{or}$	e	Single, DT				DB or DF			
			$F_a/F_r \leqq e$		$F_a/F_r > e$		$F_a/F_r \leqq e$		$F_a/F_r > e$	
			X	Y	X	Y	X	Y	X	Y
15°	0.178	0.38	1	0	0.44	1.47	1	1.65	0.72	2.39
	0.357	0.40	1	0	0.44	1.40	1	1.57	0.72	2.28
	0.714	0.43	1	0	0.44	1.30	1	1.46	0.72	2.11
	1.07	0.46	1	0	0.44	1.23	1	1.38	0.72	2.00
	1.43	0.47	1	0	0.44	1.19	1	1.34	0.72	1.93
	2.14	0.50	1	0	0.44	1.12	1	1.26	0.72	1.82
	3.57	0.55	1	0	0.44	1.02	1	1.14	0.72	1.66
	5.35	0.56	1	0	0.44	1.00	1	1.12	0.72	1.63
25°	—	0.68	1	0	0.41	0.87	1	0.92	0.67	1.41
30°	—	0.80	1	0	0.39	0.76	1	0.78	0.63	1.24
40°	—	1.14	1	0	0.35	0.57	1	0.55	0.57	0.93

*For i, use 2 for DB, DF and 1 for DT

Static Equivalent Load $P_0 = X_0F_r + Y_0F_a$

Contact Angle	Single, DT		DB or DF	
	X_0	Y_0	X_0	Y_0
15°	0.5	0.46	1	0.92
25°	0.5	0.38	1	0.76
30°	0.5	0.33	1	0.66
40°	0.5	0.26	1	0.52

Single or DT mounting
When $F_r > 0.5F_r + Y_0F_a$ use $P_0 = F_r$

Figure A.1 Dynamic and Static Equivalent Load Chart of Angular Ball Bearings [79]

The selected angular ball bearings are aligned in duplex tandem (DT) configuration, which yields 0.44 and 1.47 of X and Y, respectively. This yields the equivalent load p 6570.89 N.

To check the validity of the selected bearings, the empirical speed and life factors f_n and f_h are calculated based on the rotation speed [78, 80], bearing load ratings and equivalent load applied on the bearings. f_n is calculated by using the relation between f_n

and the rotation speed, which is shown in Figure A.2, yielding f_n 0.3. f_h is calculated using the f_n, bearing load ratings and equivalent load applied on the bearings, as shown below.

$$f_h = \frac{C_b}{P_b} f_n \qquad \text{(A.2) [79, 81]}$$

C_b – Bearing load rating (N)

P_b – Equivalent bearing load (N)

This yields the f_h 155.34 for radial ball bearings, 9.86 for angular ball bearings. According to the empirical life factor chart, shown in Figure A.3, the machines used continuously and with high-reliability should have the life factor higher than 6, which is lower than the factor of the selected bearings. Thus, the selected bearings can withstand the estimated loading of the compressor.

The estimated lifespan of the selected bearings will be discussed next. The following formula is suggested by a bearing maker [79].

$$L = \frac{10^6}{60N}\left(\frac{C_b}{P_b}\right)^3 \qquad \text{(A.3) [79, 80]}$$

L – Life span (hr)

N – RPM

This yields the life span L 1.93×10^9 hours and 4.93×10^5 hours for the radial ball bearings and angular ball bearings, respectively.

Finally, the cooling method and the life span of the bearing lubricant will be discussed. By the rotation and the resulting friction, the temperature of the bearing is increased during the operation. Lubricant or oil are applied inside the bearings to reduce the friction; The recirculating oil system has higher maximum rotating speed and better cooling capability compared with lubricant, which requires manual apply on the bearings,

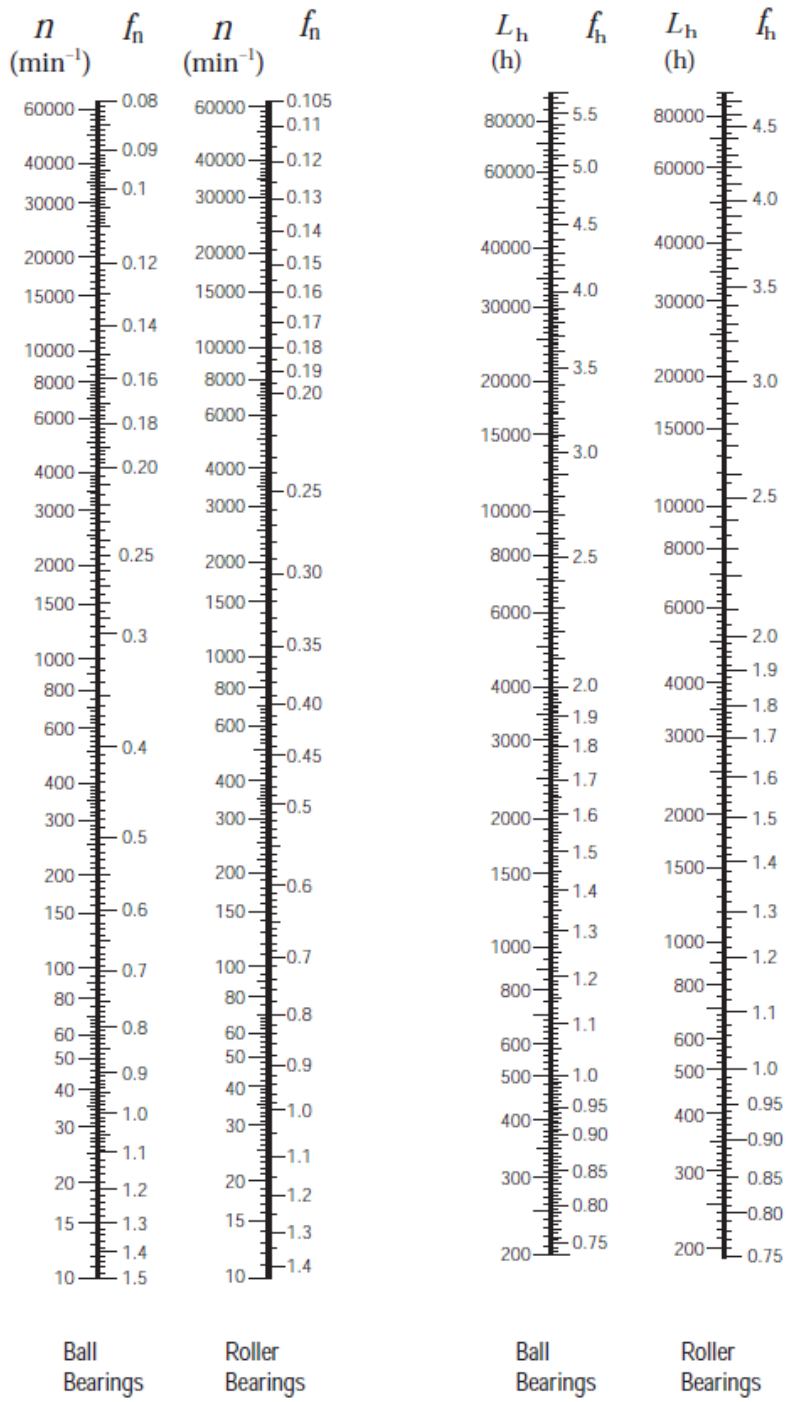

Figure A.2 Rotation Speed, Fatigue Life Factor and Life of Ball Bearings [79]

Table 5. 1 Fatigue Life Factor f_h for Various Bearing Applications

Operating Periods	Fatigue Life Factor f_h				
	~3	2~4	3~5	4~7	6~
Infrequently used or only for short periods	· Small motors for home appliances like vacuum cleaners and washing machines · Hand power tools	· Agricultural equipment			
Used only occasionally but reliability is important		· Motors for home heaters and air conditioners · Construction equipment	· Conveyors · Elevator cable sheaves		
Used intermittently for relatively long periods	· Rolling mill roll necks	· Small motors · Deck cranes · General cargo cranes · Pinion stands · Passenger cars	· Factory motors · Machine tools · Transmissions · Vibrating screens · Crushers	· Crane sheaves · Compressors · Specialized transmissions	
Used intermittently for more than eight hours daily		· Escalators	· Centrifugal separators · Air conditioning equipment · Blowers · Woodworking machines · Large motors · Axle boxes on railway rolling stock	· Mine hoists · Press flywheels · Railway traction motors · Locomotive axle boxes	· Paper making machines
Used continuously and high reliability is important					· Waterworks pumps · Electric power stations · Mine draining pumps

Figure A.3 Fatigue Life Factor for Various Bearing Applications [79]

but is more expensive and requires complex bearing housings, recirculation system, and coolers, which is redundant for the design RPM (1,000) of the SNU compressor. Lubricant is applied manually on each bearing, and to ease the refitting of grease without the complete disassemble, a grease fitting is installed at the lower bearing housing. The lifespan of the applied grease is estimated by equation A.3

$$\log L_g = 6.54 - 2.6\frac{N}{N_{max}} - \left(0.025 - 0.012\frac{N}{N_{max}}\right)T_b \qquad \text{(A.3) [79, 80]}$$

L_g – the Life span of grease [hr]

N – Bearing RPM

N_{max} – Maximum bearing speed [rev/min]

T_b – Temperature of bearing [°C]

The maximum rotation speed of the selected bearings is 4,800 RPM and 4,500 RPM for the angular type and radial type, respectively. This yields the L_g 2.65×10^4 and 2.51×10^4, respectively.

Table A.1 summarizes the parameters of the selected bearings. It is estimated that the bearings can withstand at least 4.93×10^5 hours, and the grease can withstand at least 2.51×10^4 hours, which is over 20,541 days for the bearings and 1,054 days for the lubricant. Therefore, it can be concluded that the selected two bearings are appropriate for the operation of the SNU Compressor.

Table A.1 Parameters of Selected Bearings

Parameters	Upper	Lower
Type	Radial Ball Bearing	Angular Ball Bearing
Company	NTN (Japan)	
Bearing #	6219	7219C
P_b (N)	141.79	6570.89
C_b (N)	7.34×10^4 [81]	2.16×10^5 [79]
N_{max} (RPM)	4,500	4,800
F_n	0.30	0.30
F_h	155.34	9.86
L (hr)	1.93×10^9	4.93×10^5
L_g (hr)	2.51×10^4	2.65×10^4

Appendix B. Procedure of Bellmouth Calibration for Measuring Mass Flow Rate

To measure the mass flow rate $\dot{m}$ of the compressor, a pre-calibrated bellmouth and an ogive system is generally used. This method correlates the $\dot{m}$, which is measured by the radial distribution of the U_x, and the pressure difference ΔP across the upstream and downstream of the bellmouth.

To correlate the $\dot{m}$ and ΔP, the following method is used. Because the bellmouth does not add nor subtract work from the incoming fluid, the P_t inlet and outlet of the bellmouth should be similar. Therefore, equation B.1 ~ B.5 are valid at the flow passing through the bellmouth:

$$P_{t,1} = P_{s,1} + \frac{1}{2}\rho U_1^2 = P_{s,2} + \frac{1}{2}\rho U_2^2 = P_{t,2} \tag{B.1}$$

$$\dot{m}_1 = \rho A_1 U_1 = \rho A_2 U_2 = \dot{m}_2 \tag{B.2}$$

Substituting U_{in} by putting (B. 2) into (B. 1) yields:

$$P_{s,1} - P_{s,2} = \frac{1}{2}\rho U_2^2 \left(1 - \left(\frac{A_2}{A_1}\right)^2\right) \tag{B.3}$$

$$\Delta P = P_{s,1} - P_{s,2} = \frac{1}{2\rho}\rho^2 A_2^2 U_2^2 \left(\frac{1}{A_2^2} - \frac{1}{A_1^2}\right) = \frac{1}{2\rho}\left(\frac{1}{A_2^2} - \frac{1}{A_1^2}\right)\dot{m}^2 \tag{B.4}$$

$$\dot{m} = \sqrt{2/\left(\frac{1}{A_2^2} - \frac{1}{A_1^2}\right)} \cdot \sqrt{\rho} \cdot \sqrt{\Delta P} \propto C_d \sqrt{\rho} \cdot \sqrt{\Delta P} \tag{B.5}$$

Therefore, a linear relationship exists between the $\dot{m}$, and $\sqrt{\rho} \cdot \sqrt{\Delta P}$. $\dot{m}$ can be measured by the radial and circumferential U_x, and $\sqrt{\Delta P}$ can be measured by static pressure measurements upstream and downstream of the bellmouth.

For $\dot{m}$, measuring the radial distribution of U_x at a fixed circumferential location can yield the different $\dot{m}$, because of the non-uniformity of the entering flow. Therefore,

to identify the flow non-uniformity, circumferential measurements of the bellmouth static P_s has been performed conducted, which is shown in Figure B.1. The circumferential P_s distribution indicate that the P_s non-uniformity is the biggest at 60° (1.96 % of inlet dynamic head), and 0.79% of inlet dynamic head on average. Compared with the result of previous SNU LSRC (maximum 7.03%, average 3.39%) the inlet non-uniformity of the SNU compressor is improved and considered to be uniform. Therefore, radial distributions of U_x at a fixed circumferential location has been used to $\dot{m} - \Delta P$ relation.

To measure the radial distributions of U_x at a fixed circumferential location, a single straight hot-wire (Dantec dynamics, 55P11) and a CTA anemometer module (Dantec Dynamics, 90C10) installed at a CTA frame (Dantec Dynamics, 90N10) has been used.

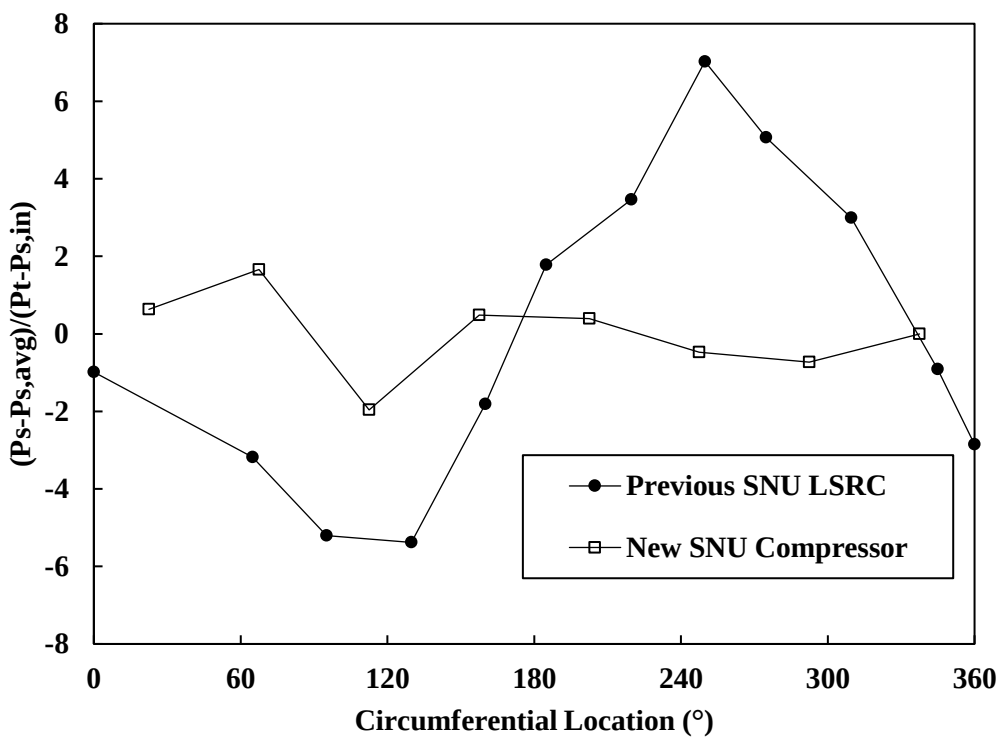

Figure B.1 Circumferential Static Pressure Non-Uniformity of Previous SNU LSRC and SNU Compressor

This probe has been calibrated by a hot-wire calibrator (Dantec Dynamics, 90H02) prior to the measurements. The radial traversing system which was introduced in Section 2.3.3 has been used to traverse the sensors radially. The measured radial U_x distributions have been converted into $\dot{m}$, using the atmospheric P_{atm} and T_{atm} which have been recorded by a barometer (E+E Electronik, HUMLOG 20).

To measure the $\sqrt{\Delta P}$ upstream and downstream of the bellmouth, 16 static pressure taps has been installed upstream and downstream of the bellmouth. Each static pressure tap has been connected to each other with pneumatic pipes to average the P_s signal. These averaged P_s signals have been measured by a differential pressure transducer (MKS, 220DD, 10 torr FS).

These parameters have been measured repeatedly at different throttle positions to obtain the relationship between $\dot{m}$ and $\sqrt{\rho} \cdot \sqrt{\Delta P}$. Figure B.2 illustrates the measured relationship. The linear interpolation of the two parameters yields the relationship as follows:

$$\dot{m} = 0.413009\sqrt{\rho} \cdot \sqrt{\Delta P} + 0.147121 \quad \text{(B.6)}$$

Maximum 0.70% error exists between the actual $\dot{m}$ and $\dot{m}$ calculated by the correlation.

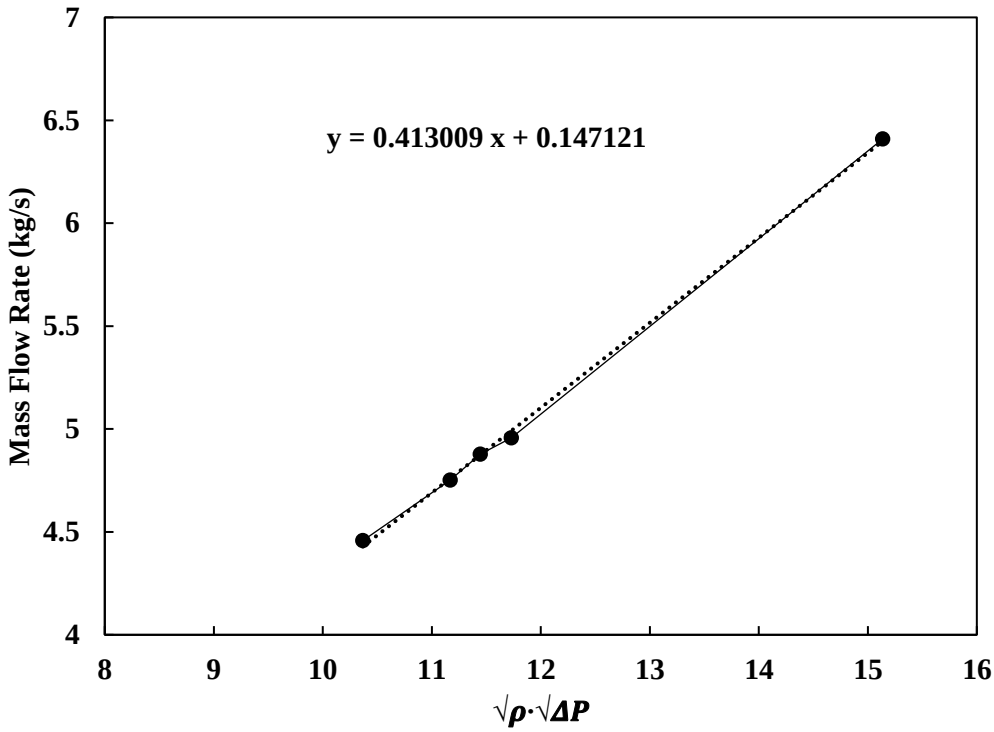

Figure B.2 Relationship between $\dot{m}$ and $\sqrt{\rho} \cdot \sqrt{\Delta P}$

Appendix C. Pitch and Yaw Angle Response of Hot-Wires Used for the Experiments

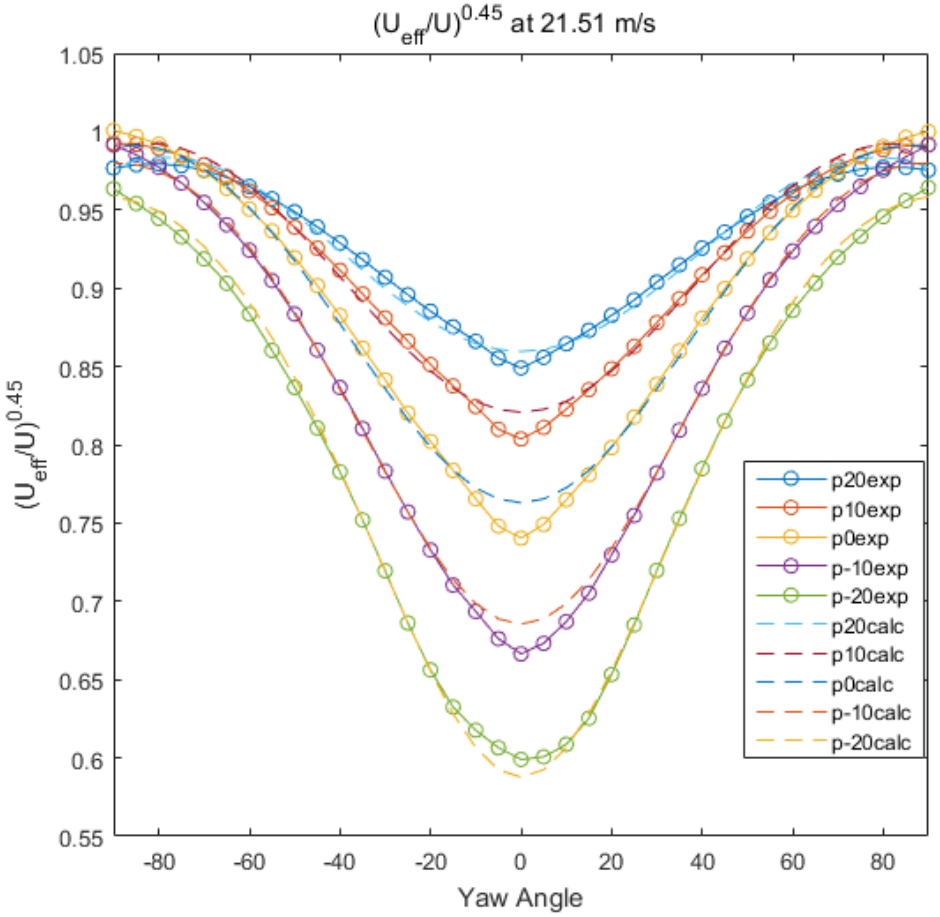

Figure C.1 Pitch and Yaw Angle Response of Hot-Wire #1 (Serial 98811, 55P12) at 21.51 m/s

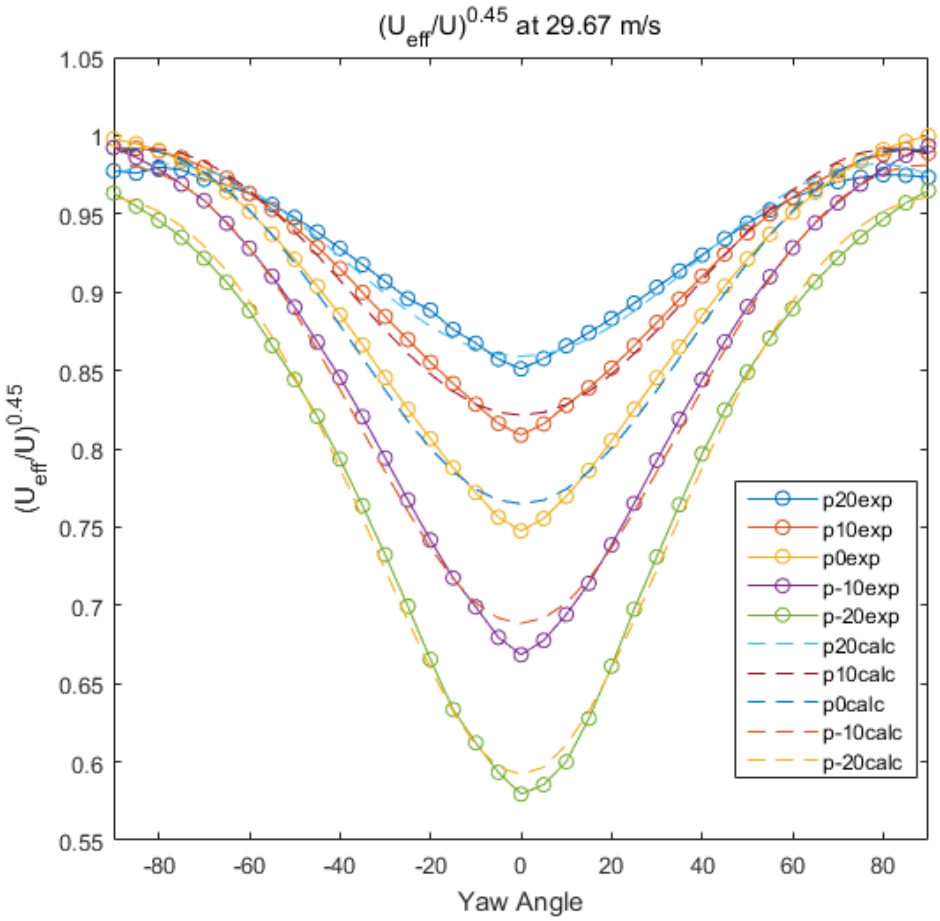

Figure C.2 Pitch and Yaw Angle Response of Hot-Wire #1 (Serial 98811, 55P12) at 29.67 m/s

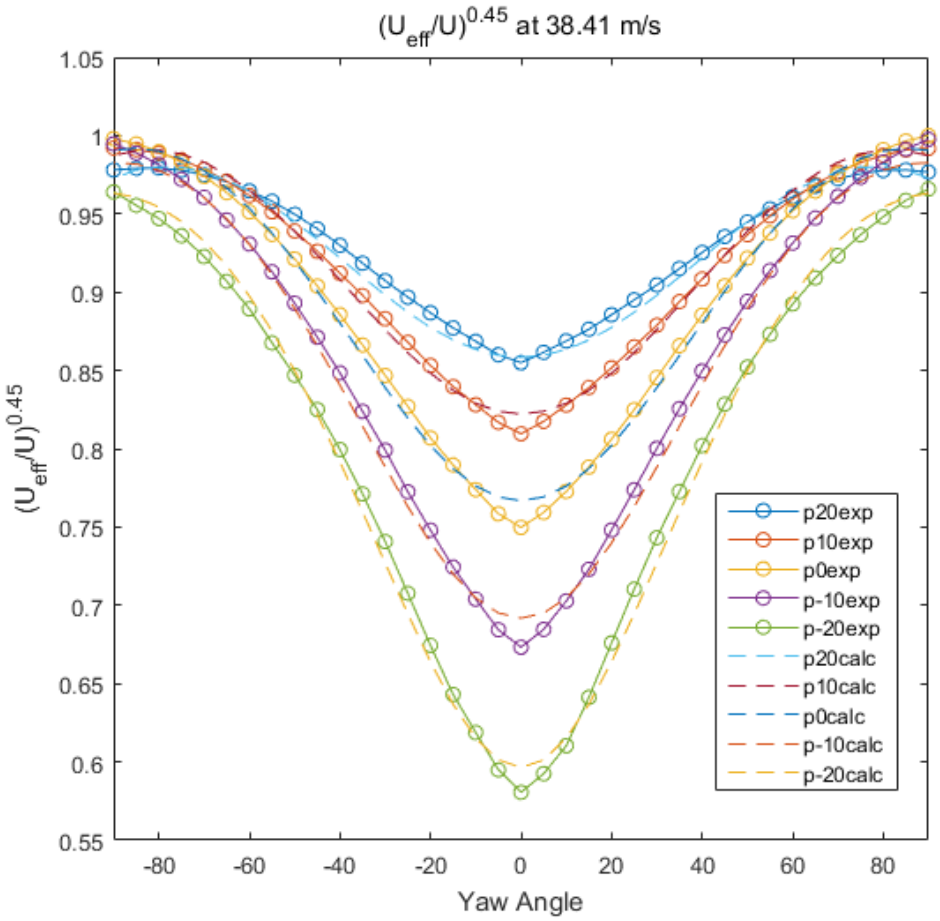

Figure C.3 Pitch and Yaw Angle Response of Hot-Wire #1 (Serial 98811, 55P12) at 38.41 m/s

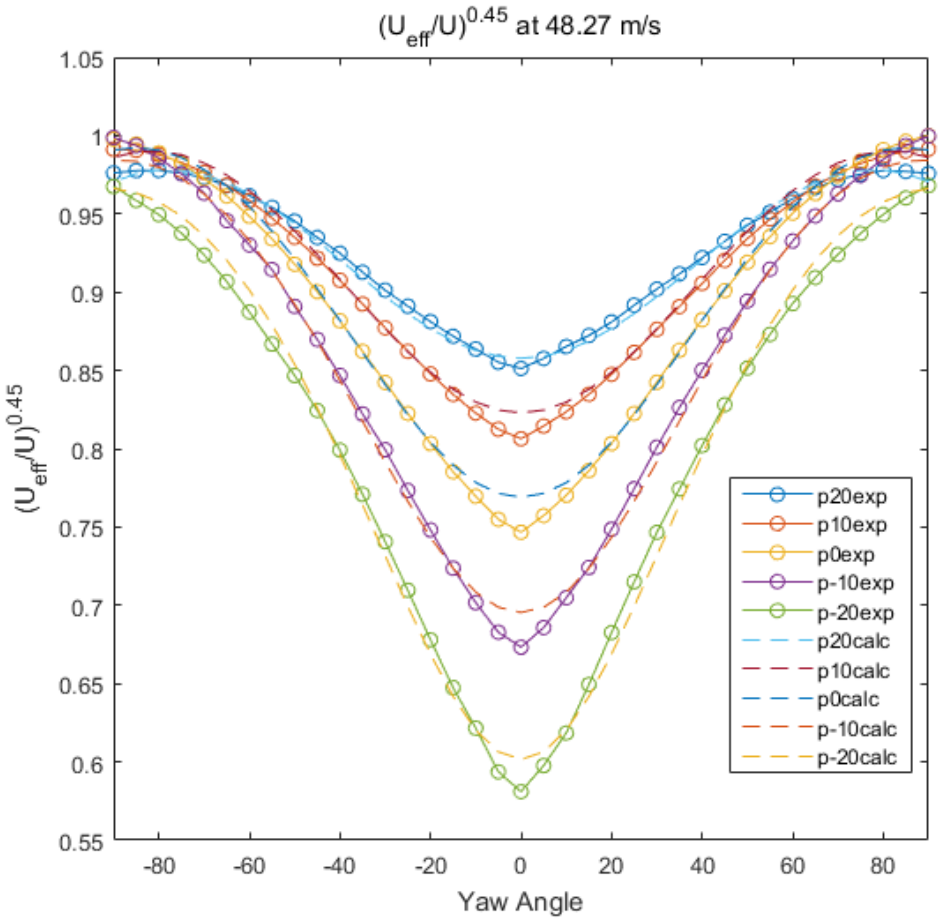

Figure C.4 Pitch and Yaw Angle Response of Hot-Wire #1 (Serial 98811, 55P12) at 48.27 m/s

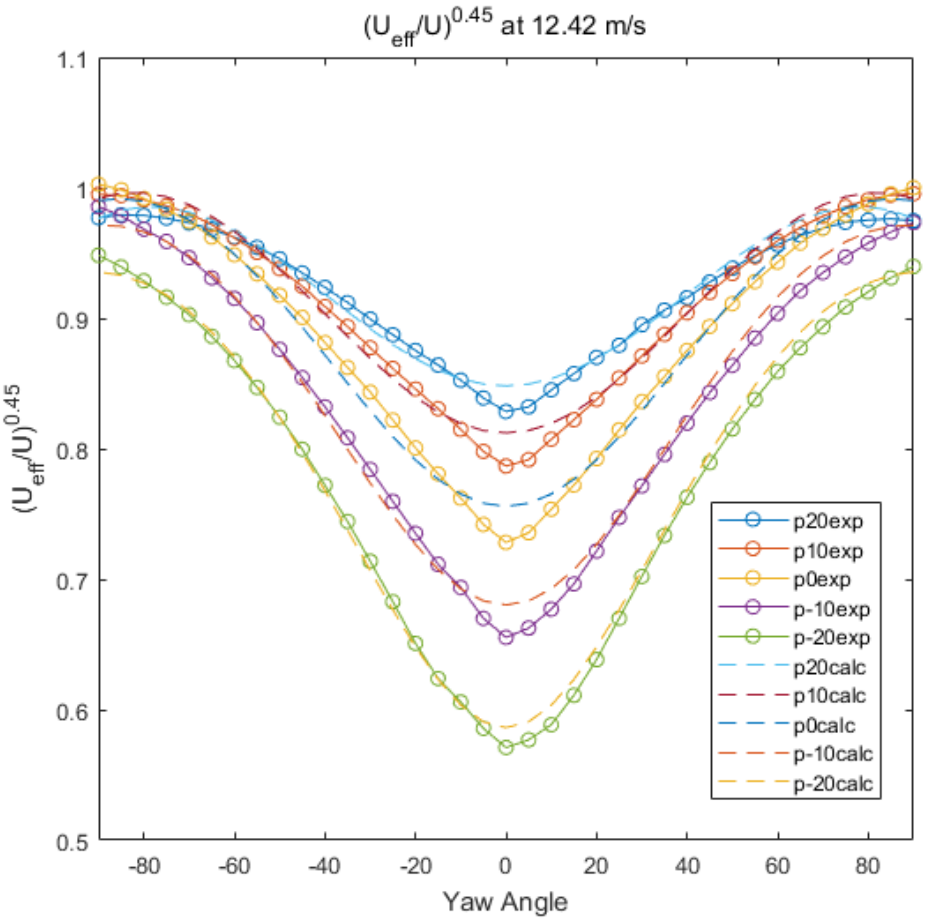

Figure C.5 Pitch and Yaw Angle Response of Hot-Wire #2 (Serial N/A, 55P12) at 12.42 m/s

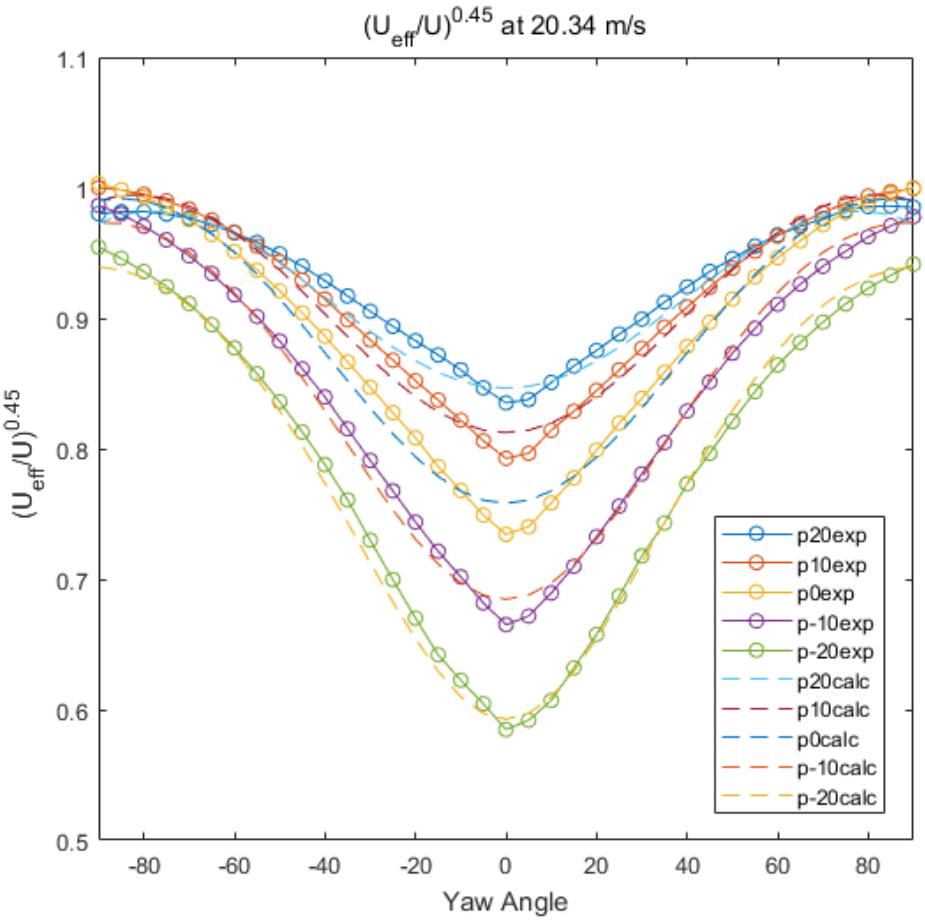

Figure C.6 Pitch and Yaw Angle Response of Hot-Wire #2 (Serial N/A, 55P12) at 20.34 m/s

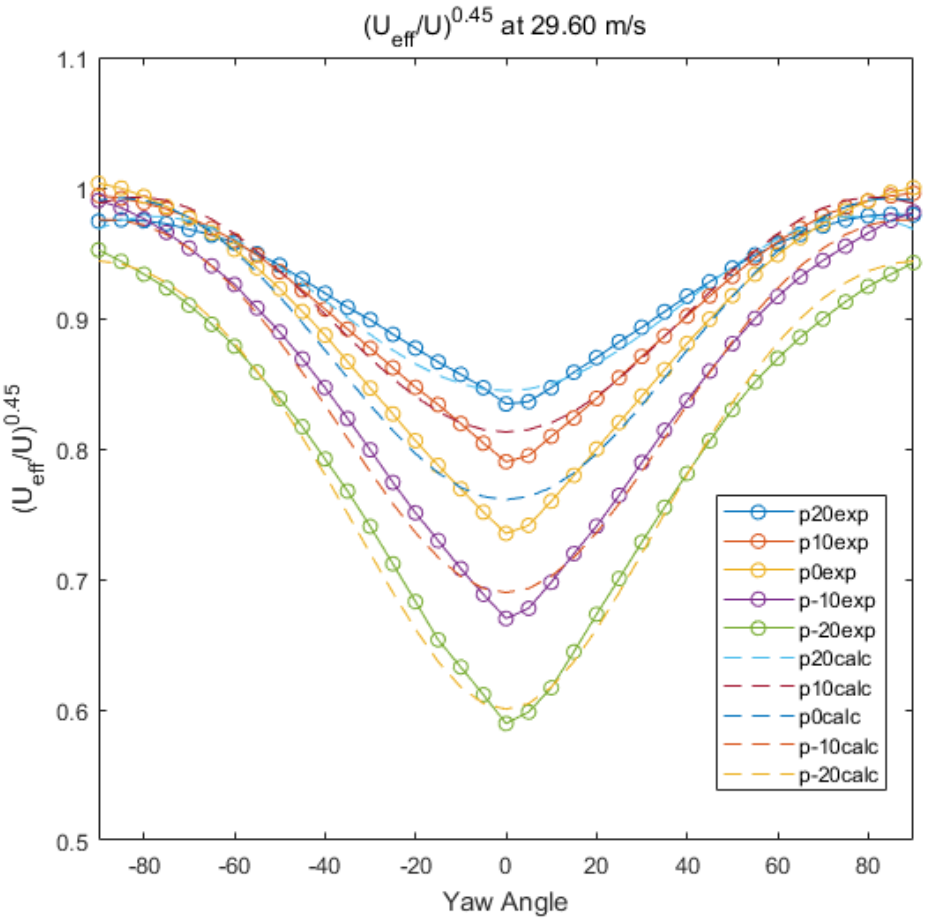

Figure C.7 Pitch and Yaw Angle Response of Hot-Wire #2 (Serial N/A, 55P12) at 29.60 m/s

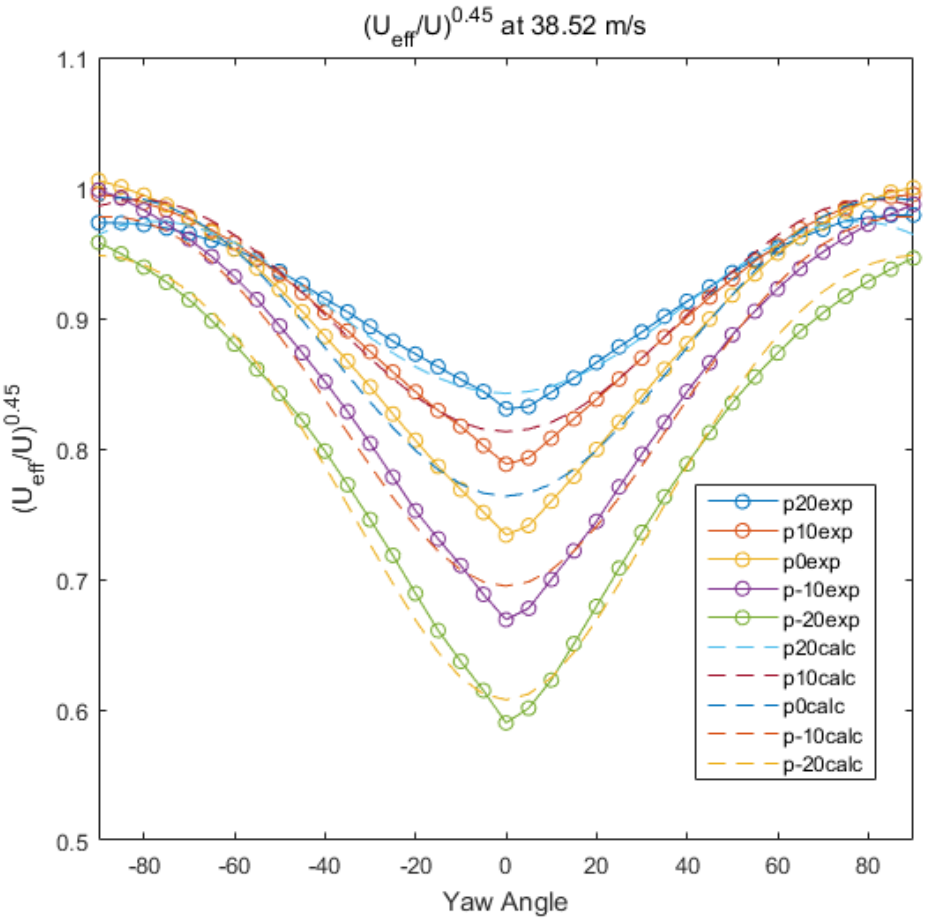

Figure C.8 Pitch and Yaw Angle Response of Hot-Wire #2 (Serial N/A, 55P12) at 38.52 m/s

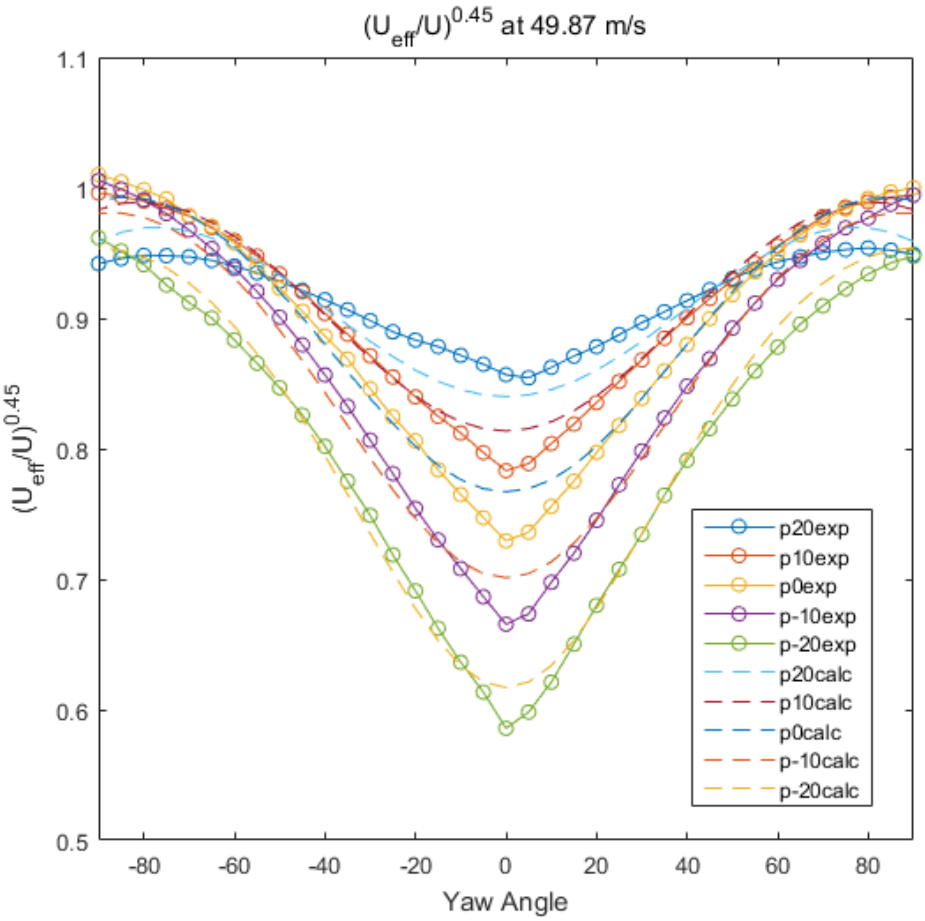

Figure C.9 Pitch and Yaw Angle Response of Hot-Wire #2 (Serial N/A, 55P12) at 49.87 m/s

요약 (국문초록)

다단 압축기 슈라우드형 정익 허브의 유동 구조가 상단 동익 후류에 미치는 영향을 파악하기 위해 저속 4단 슈라우드형 축류 압축기의 3단 정익 상단 및 하단에서의 비정상 속도 분포를 핫와이어를 이용하여 최초로 측정하였다.

상단 동익 후류의 폭과 강도는 상단 정익 후류와의 상호작용으로 인해 변동한다. 두 동익 후류 사이에는, 동익 후류로 인해 생긴 순환류로 인해 동익 후류와 유사하게 보이는 유동 구조가 형성된다. 동익 후류로 인해 생긴 유동의 시간에 따른 변화는 유동의 점성과 후류의 늘어남으로 인해 완화된다.

다단 슈라우드형 정익의 허브 모서리 유동 박리는 정익 허브의 비정상 운동학에 영향을 준다. 유동 박리가 허브의 유효 면적을 줄여, 동익 후류의 완화를 억제한다. 또한, 유동 박리로 인해 슈라우드형 정익 상/하단에서 추가적인 반경방향 움직임이 형성된다. 이로 인해 동익 후류로 인한 유동의 시간에 따른 변화의 크기가 증가하여, 유동의 공력 성질이 시간에 따라 변하게 되며, 디자인 공력 조건에서 벗어난다.

압축기의 운전 조건을 바꿀 시 허브의 비정상 유동구조가 변화한다. 낮은 유량에서 운전했을 시, 후류와 모서리 유동 박리의 폭은 늘어나지만, 비정상 유동구조는 설계 운전조건에서의 경우와 정성적으로 동일하다. 높은 유량에서 운전했을 시, 모서리 유동 박리의 폭과 강도가 감소하여, 다른 운전 조건에서 보였던 모서리 박리 안에서의 반경방향 움직임이 사라진다.

주요어 : 축류 압축기, 슈라우드형 정익, 동익, 비정상 운동학, 후류, 허브, 모서리 박리,

학 번 : 2012-23183